

ENGINEERING AND ARCHITECTURE SCIENCES Theory, Current Researches and New Trends 4

ENGINEERING AND ARCHITECTURE SCIENCES

Theory, Current Researches and
New Trends 4

E d i t o r

Assoc. Prof. Dr. Gülden SANDAL ERZURUMLU

ISBN: 978-9940-46-094-5

2022



ENGINEERING AND ARCHITECTURE SCIENCES

Theory, Current Researches and New Trends 4

Editor

Assoc. Prof. Dr. Gülden SANDAL ERZURUMLU

Editor
Assoc. Prof. Dr. Gülden SANDAL ERZURUMLU

First Edition •© March 2022 /Cetinje-Montenegro

ISBN • 978-9940-46-094-5

© copyright All Rights Reserved

web: www.ivpe.me

Tel. +382 41 234 709

e-mail: office@ivpe.me



Cetinje, Montenegro

PREFACE

Although Engineering and Architecture are two separate disciplines, positive results emerge only when they act together.

As the needs on a global scale increase, the need for the mentioned branches becomes more evident.

As Charles Eames stated, “Recognizing the need is the primary condition of design.” Evaluating the researches and the results together in line with the needs will make the problem or solution be evaluated from different perspectives and the emergence of new ideas.

This book offers researchers a different, interdisciplinary perspective on engineering and architecture.

This book, ENGINEERING AND ARCHITECTURE SCIENCES: Theory, Current Researches and New Trends, provides an academic forum for academics and researchers working in the fields of Engineering and Architecture. Studies of academicians and researchers working in different fields are evaluated in the book. I would like to thank the authors who supported the book with their studies and information, and IVPE Publishing House for bringing the studies together and presenting them.

Assoc. Prof. Gülden SANDAL ERZURUMLU

CONTENTS

| | |
|---|-----|
| PREFACE | I |
| CONTENTS | III |
| CHAPTER I | |
| CLUTTER MODELING AND MOVING TARGET DETECTION WITH PASSIVE BISTATIC RADAR FOR MILITARY USE | |
| İbrahim Ethem YILMAZ & Necmi Serkan TEZEL | 1 |
| CHAPTER II | |
| RENEWABLE ENERGY POTENTIAL OF ISTANBUL | |
| Haydar KEPEKÇİ | 27 |
| CHAPTER III | |
| PRIORITIZING OF WASTEWATER-TO-HYDROGEN PRODUCTION PROCESSES USING DIFFERENT MCDM TECHNIQUES: COMPARISON AND SENSITIVITY ANALYSIS | |
| Elanur ADAR | 44 |
| CHAPTER IV | |
| CHARACTERIZATION OF PERLITE AND EXPANDED PERLITE-BASED GEOPOLYMERS WITH DIFFERENT ANALYSIS TECHNIQUES | |
| Ceyda BİLGİÇ & Şafak BİLGİÇ | 71 |
| CHAPTER V | |
| USING OF SUPERHYDROPHOBICITY, SELF-CLEANING, LOW ADHESION, AND DRAG REDUCTION PROPERTIES IN GREEN ENGINEERING APPLICATIONS | |
| Ceyda BİLGİÇ & Şafak BİLGİÇ | 89 |
| CHAPTER VI | |
| PHYSICOCHEMICAL, MICROBIOLOGICAL AND ECOTOXICOLOGICAL CHARACTERIZATION OF HOSPITAL WASTEWATER | |
| Mahir İNCE & Handenur YAŞAR & Yasin Abdullah USLU & Elif İNCE | 104 |

CHAPTER VII

THE EFFECT OF TEMPERATURE AND Al CONTENT ON THE THERMO-ELECTRICAL, MICROSTRUCTURE AND MECHANICAL PROPERTIES OF Sn-Al ALLOYS

Fatma MEYDANERI TEZEL & Buket SAATÇI116

CHAPTER VIII

MEASUREMENT OF THERMAL CONDUCTIVITIES WITH LASER FLASH METHOD AND ELECTRICAL, MECHANICAL, AND MICROSTRUCTURE CHARACTERIZATION OF Bi-Sn, Bi-Sn-Zn AND Bi-Sn-Sb EUTECTIC ALLOYS

Fatma MEYDANERI TEZEL & İbrahim UZUN138

CHAPTER IX

EFFECT OF PLUG PARAMETERS ON THICKNESS VARIATION OF A THERMOFORMED PRODUCT USING PLUG ASSIST THERMOFORMING

Olçay EKŞİ & Ertuğ CABBAR160

CHAPTER X

THE EVALUATION OF STUDENT AWARENESS IN THE NEW BUILDING DESIGN STUDIO TEACHING PRACTICES IN HISTORICAL ENVIRONMENT

İlknur ACAR ATA & Merve ÖZKAYNAK171

CHAPTER I

CLUTTER MODELING AND MOVING TARGET DETECTION WITH PASSIVE BISTATIC RADAR FOR MILITARY USE¹

Research Assist. İbrahim Ethem YILMAZ* and
Prof. Dr. Necmi Serkan TEZEL**

*Department of Electric Electronic Engineering, Faculty of Engineering,
Karabük University, 78050, Karabük, Turkey,
E-mail: ibrahimethemyilmaz@karabuk.edu.tr,
ORCID ID: 0000-0001-7891-090X

**Department of Electric Electronic Engineering, Faculty of Engineering,
Karabük University, 78050, Karabük, Turkey,
E-mail: nstezel@karabuk.edu.tr,
ORCID ID: 0000-0002-9452-677X

1. Introduction

Radar (Radio Detection and Ranging) is a system that uses various electromagnetic waves to determine target detection and the range of that target. The system also find velocity, direction, elevation angle such parameter defined by the target. While the radar provides the acquisition of the relevant parameters, in operational point of view, radar principle is similar to sound-wave reflection. Unlike sound-wave reflection, radar uses much wider range of frequency for transmit energy in electromagnetic spectra. A portion of the reflected energy from the target evaluate by the system for determine target parameters.

It is possible to evaluate radar circuits according to the receiver and transmitter geometry. From this perspective, the type of radar where the receiver and transmitter circuits are in the same location is called monostatic radar. This type of radar uses its own transmitter for surveillance, target detection or any other purposes. The target distance to be determined is founded by calculating the time elapsed in this process as a result of the signal transmitted through the transmitting antenna reflecting from the target to the receiving antenna. On the other hand,

¹ This chapter is Master Thesis completed by Research Assist. İbrahim Ethem YILMAZ in January 2022.

there are radars with bistatic geometry, which have their own transmitter in the same way as monostatic radars, but whose geometry is different from the monostatic geometry, the positions of the receiving and transmitting antennas are not the same. In bistatic geometry, radar's receiving site (one antenna or multiple antennas) utilizes two signals; one of them is directly from transmitter and the other is reflected from the target. The target range is found by calculating the delay between the signals. Bistatic radars also have transmitter of its own. There are passive radars (PR) that operate in bistatic geometry however these radars do not have a transmitter of their own. This type of radar is also known as passive covert location (PCL) radar, passive covert radar (PCR). They take advantage of the illuminators of opportunity or non-cooperative illuminators that are already broadcasting and commonly commercial transmitters such as FM radio, Analog TV, digital audio broadcasting (DAB), digital video broadcasting-terrestrial (DVB-T), direct video broadcasting-satellite (DVB-S) TV, GSM telephone signals, Wi-Fi signals etc. Considering its features and different approach in application, passive radar has advantages and disadvantages compared to active radar systems. Passive radar potential attractions: Since the transmitters of the opportunity illuminators used are generally in high locations, therefore PR have broad coverage. The cost of system is much lower than active radar because it does not have any transmitter expenditure. Well suited for covert operations as the receiver does not emit signals. Difficulty of jamming against PR. Excess of illuminator of opportunity that can be used.

Disadvantages of PR systems: The computational overhead of adapting the waveform for radar purposes. Dependency on the transmission source. Direct Signal Interference (DSI) and Multipath Interference (MPI) effects because of continuous waveform of signal. Low range and doppler resolution for targets close to the baseline.

One of the biggest problems encountered while detecting targets in passive bistatic radar systems is the difficulty in detecting the weak echo signal reflected from the target due to the clutter function caused by environmental factors (sea waves, trees, skyscrapers etc.) [1]–[8]. In this study, clutter was filtered and used for target detection in a bistatic radar system using an FM illuminator as a transmitter.

1) A Short historical background of PR

The Daventry Experiment, the first passive radar experiment conducted by Robert Watson Watt and Arnold Wilkins in 1935, showed that radar detection of aircraft at useful ranges was possible by detecting the Heyford bomber aircraft at a range of 8 km via a BBC transmitter operating at 6 MHz [9]–[11]. It paved the way for the Chain Home radar

system, as it was shown as a potential solution against possible raids by the enemy. It will be the backbone of the British air defense system in World War II [12]. In the 1950s and 1960s, studies on passive bistatic radar were limited due to the insufficiency of data processing capability and information privacy policies during the cold war period [1], [11]. However, cooperative bistatic radar studies such as the American AN/FPS-23 early warning system and the AN/FPS-133 Air Force Space Surveillance System have been developed. These systems were produced for a certain purpose. Active monostatic radar was the mainstream of radar studies [13]. By the 1980s and 1990s, passive location began to increase its popularity in the fields of scientific and defense systems because of developments of data processing and the emergence more suitable receiver circuits. The use of television transmitters as an illuminator of opportunity can also be counted as a turning point [14]. In 1998, a passive radar system called Silent Sentry was developed by U.S. company Lockheed Martin Corporation. It is the first commercial PCR system [9]. This system based on FM radio illuminators and used for real-time tracking of multiple targets and detection [9], [11]. In the last 20 years, the interest in passive radar systems has increased with the advancement of technology and the developments of data processing. Systems such as PARADE, which uses the Russian P18 VHF observation radar as an illuminator, Occiu developed by the French C&T company, HA100 (name comes from the initials of Homeland Alert and 100 km detection range) by Thales, SELEX can be given as examples [9]. Many articles [2], [15]–[26] and books [11], [13], [27], [28] were published in the field of passive and/or bistatic radar study during this period. Nowadays, passive radar systems have become a field of study that attracts a lot of attention in both academic and industrial fields due to the features they provide. Factors such as its possibility of detecting stealth targets and its difficulty in detecting increase its potential to be an effective field for the homeland security [1].

3. Passive radar

It is important to understand the concept of bistatic radar (BR), as passive bistatic radars are an element of BR systems. Bistatic radars are systems with a geometry in which the receiving and transmitting antennas are in different locations. These systems use two different types of transmitters. The first of these is the transmitters specially allocated for BR, while the other is the transmitters that are currently broadcasting and are generally used for commercial purposes. Both of these two types of transmitter systems perform target detection by evaluating the echo signal reflected from the target, similar to the monostatic system, but passive systems that use currently broadcasting transmitter as an illuminator need

an antenna that receives the signal coming directly from the transmitter in the receiver side. Hence bistatic radar must have at least two receiving channels: reference and echo and they are called passive bistatic radar (PBR) or passive coherent location (PCL) because of this passive characteristic. The absence of its own transmitter and the difference in receiver and transmitter locations gives great advantages to PBR systems. Detection capability against stealth targets, difficulty of jamming etc. Signal processing difficulty created by the absence of a synchronized signal is a disadvantage of PBR Figure 1 shows the basic bistatic radar structure.

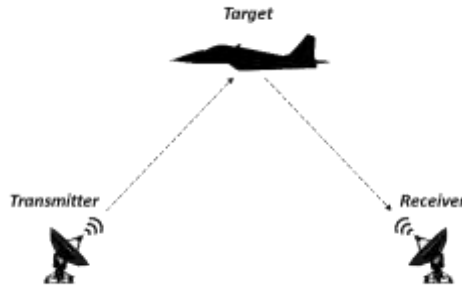


Fig. 1 Basic Bistatic Radar Structure.

Bistatic radars may differ according to the number of receivers and transmitters, illuminator types and signal modulation. These different features of systems given in Table 1.

Table 1 Different Features Used By Radar Systems

| Features | Different Types Used by BR |
|---------------------------------|-------------------------------------|
| Transmitter or Receiver Numbers | <i>Bistatic, Multistatic</i> |
| Cooperation of Illuminators | <i>Cooperative, Non-cooperative</i> |
| Signal Modulation | <i>FM, AM, OFDM, Unmodulated</i> |
| Operation of Signal | <i>Continuous Wave (CW), Pulsed</i> |

3.1 Bistatic radar geometry

In Figure 2, the bistatic radar geometry is depicted in Cartesian coordinates in the transmitter-receiver-target plane [1]. The figure includes receiver (R_x), transmitter (T_x) and target (T). The notations of above figure; R_T , R_R and L are distance between T_x and T , distance between R_x and T , distance between T_x and R_x or baseline, respectively. R_T , R_R and L are calculated by using Equation 1 in cartesian coordinates.

$$\begin{aligned}
R_T(t) &= \sqrt{(x(t) - x_t)^2 + (y(t) - y_t)^2 + (z(t) - z_t)^2} \\
R_R(t) &= \sqrt{(x(t) - x_r)^2 + (y(t) - y_r)^2 + (z(t) - z_r)^2} \\
L &= \sqrt{(x_t - x_r)^2 + (y_t - y_r)^2 + (z_t - z_r)^2}
\end{aligned} \tag{1}$$

δ is the angle between the target velocity vector and bistatic bisector. θ_T is transmitter-pointing angle and θ_R is receiver-pointing angle. The angle subtended at the target by the transmitter and receiver is β . It is called the bistatic angle and is defined by Equation 2.

$$\beta = \theta_T - \theta_R \tag{2}$$

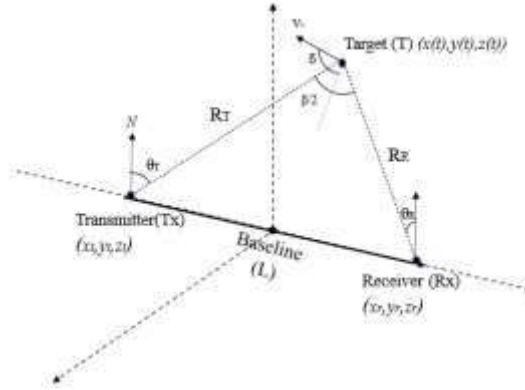


Fig. 2 Bistatic Radar Geometry.

3.2 Bistatic radar range and range resolution

The In bistatic radars, the bisatic range (R_B) is found by the difference between the indirect path $R_T + R_R$ and the direct path L , as can be defined in Equation 3.

$$R_B(t) = R_T(t) + R_R(t) - L \tag{3}$$

Bistatic range also calculated by multiplying τ which is the delay between reference signal and echo signal and the speed of light, as seen in Equation 4.

$$R_B = c \cdot \tau \tag{4}$$

Contours of the constant bistatic range ($R_T + R_R$) define an ellipse, with the transmitter and receiver located at the two focal points. Because of this reason, targets on the same ellipse have the same bistatic range. Its planar representation is given in Figure 3.

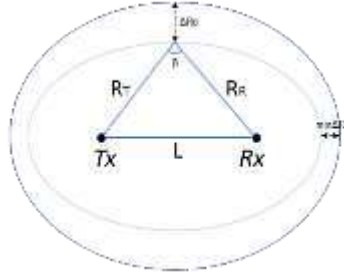


Fig. 3 Constant Bistatic Range Contours and Their Range Resolution Between Each Other.

Range resolution in bistatic radar is defined as the shortest distance at which two targets can be distinguished from each other. This distance appears as the distance between two concentric ellipses. Due to the shape of the ellipse, this distance changes depending on the β angle. As β approaches zero, the range resolution increases as the distance of ellipses decreases, while when it approaches 180 degrees, the range resolution decreases. The range resolution is shown in Figure 3. Monostatic and bistatic range resolutions are expressed in Equation 5 below, respectively.

$$\Delta R = \frac{c}{2BW}$$

$$\Delta R_B = \frac{c}{2\cos(\frac{\beta}{2})BW} \quad (5)$$

In Equation 5, ΔR is range resolution of monostatic radar, ΔR_B is range resolution of bistatic radar and BW is the signal bandwidth. Range resolution varies according to different illuminator types due to the effect of bandwidth.

3.3 Examination of mechanistic features

As with other radar forms, radar equation can be used to test the suitability of expected performance while designing bistatic radars [11], [27], [28]. Basic form of the radar equation for a radar with one transmitter can be written as in Equation 6 [11], [28].

$$\frac{P_R}{P_N} = \frac{P_T G_T}{4\pi R_T^2} \sigma_B \frac{1}{4\pi R_R^2} \frac{G_R \lambda^2}{4\pi} \frac{1}{kT_0 BW F} L_o \quad (6)$$

Where;

P_R = received signal power,

P_N = receiver noise power,

P_T = transmitted power,
 G_T = transmitter antenna gain,
 R_T = transmitter to target range,
 σ_B = target bistatic radar cross-section,
 R_R = target to receiver range,
 G_R = receiver antenna gain,
 λ = signal wavelength,
 k = Boltzmann's constant,
 T_0 = 290K, noise reference temperature,
 BW = receiver effective bandwidth,
 F = receiver effective noise figure,
 L_0 = system losses.

When converted to this simple form of the equation by adding pattern propagation factors (F_T, F_R), system losses (L_T, L_R), T_s (receiving system noise temperature) and B_N (receiver noise bandwidth), the SNR (signal to noise ratio), which is one of the important criteria for evaluating system performance, is obtained as in Equations 7.

$$SNR = \frac{P_T G_T G_R \lambda^2 \sigma_B F_T^2 F_R^2}{(4\pi)^2 k T_s B_N L_T L_R R_T^2 R_R^2} \quad (7)$$

If we say A to the variables that do not change with the range in Equation 7, we get Equation 8.

$$SNR = \frac{A}{R_T^2 R_R^2} \quad (8)$$

When Equation 8 is expressed in the polar coordinate system (r, θ) as in Equation 9 and consider its range dependency, it creates Cassini ovals for SNR as shown in Figure 4. Each curve represents a fixed SNR value. SNR values of two identical targets on the same oval are equal to each other.

$$SNR = \frac{A}{(r^2 + L^2/4)^2 - r^2 L^2 \cos^2 \theta} \quad (9)$$

3.4 Illuminators of opportunity

There are numerous types of currently broadcasting transmitters that can be used for the purpose of passive radar. When choosing the appropriate illuminator type, various properties have to be considered, such as transmitted power, frequency band, signal bandwidth, and

modulation according to the purpose of the passive radar system. Commonly used illuminator types for passive radar are mentioned below.

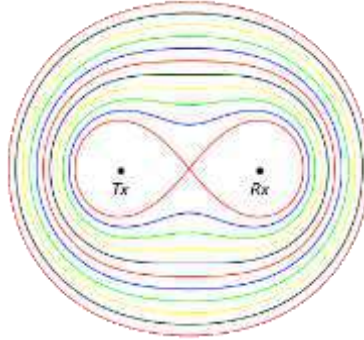


Fig. 4 Cassini ovals

3.4.1 Analog radio (FM)

FM broadcasting is a technology that uses frequency modulation and was invented by Edwin Howard Armstrong in 1922 to provide high quality sound transmission. FM radio is one of the frequently used and preferred illuminators in passive radar applications [15], [17], [19], [22], [25], [30], [31]. It operates between 88 MHz and 108 MHz frequency range. The transmitter powers can be reach 250 kW, so it provide long detection range or in other words FM signal provide large coverage area. One of the greatest disadvantage of FM radio as a source of illumination for radar, however, is the narrow gap of the signal bandwidth. In addition, the bandwidth of the FM signal changes in time due to the analog modulation applied. The nominal bandwidth of the signal is 150 kHz, with 200 kHz interchannel spacing. However, the instantaneous bandwidth of the signal strongly depends on the content of the used FM channel program. For speech, the bandwidth can be very narrow, which results in degraded range resolution [3], [20]. It is available in systems that increase bandwidth by using multiple channels in order to improve the range resolution [16].

3.4.8 Comparison of different transmitter types

In Chapter 3.4, different signal types used as illuminators in passive radar systems are mentioned. These illuminators should be chosen according to the purpose of the system to be used because of their different features that can create advantages and disadvantages. Table 2 shows the basic parameters of the different illuminators. The parameter

values of the signals may vary depending on the environmental conditions and the broadcast.

Table 2 Typical Parameters Of Different Transmitter Types.

| Transmission | Frequency Band | Bandwidth | $P_T G_T$ |
|----------------|------------------|-----------|-----------|
| FM | 88-108 MHz | 200 kHz | 250 kW |
| Analog TV | ~550 MHz | 5.5 MHz | 1 MW |
| DVB-T | 470-860 MHz | 7,6 MHz | 8-100 kW |
| DAB | 174-240 MHz | 1,5 MHz | 10 kW |
| DVB-S | 950-2150 MHz | 36 MHz | 2 kW |
| GSM (900,1800) | 935-960 MHz | 200 kHz | 320 W |
| Wi-Fi | 2,4 GHz or 5 GHz | 16 MHz | 200 mW |

When the parameters in Table 2 for FM radio signal are examined, having a high value in terms of signal power means a wide coverage area. Due to this feature, it is preferred for passive radar applications. However, having a relatively narrow bandwidth, which varies depending on the content of the broadcast, negatively affects the range resolution. Although analog TV has good values in terms of basic parameters, it is not widely used for passive radar purposes as it has been replaced by digital video broadcasting in most countries. DVB-T signal has high values in terms of range resolution due to its wide bandwidth. It is seen that it is suitable for passive radar purposes in terms of signal transmission power. However, the high frequency of the broadcast has a negative effect on the coverage area. When the DAB signal is evaluated, it has an average bandwidth, so the range resolution also has an average value. The fact that the signal strength is lower than the FM signal puts the FM signal ahead in terms of the width of the coverage area. The same can be seen for broadcast frequency. It is suitable for short range surveillance applications due to its GSM signal bandwidth and low signal power. Range resolution and coverage are low. The Wi-Fi signal has a good range resolution due to its high bandwidth. However, the low signal power allows it to be used only in short distance applications. Due to the low transmission power of the DVB-S signal, the target detection range is short. Due to its high bandwidth, it can be considered as a good illuminator in terms of range resolution.

4. Signal modelling and analysis

In this section, the geometry of the designed passive bistatic radar, the signal model detected by the receiver part, the proposed methods for clutter removal and pulse compression part are explained.

4.1 Geometry of the designed PBR

The proposed PBR system includes stationary receiver and transmitter parts. The geometry of the designed system is as in Figure 5.

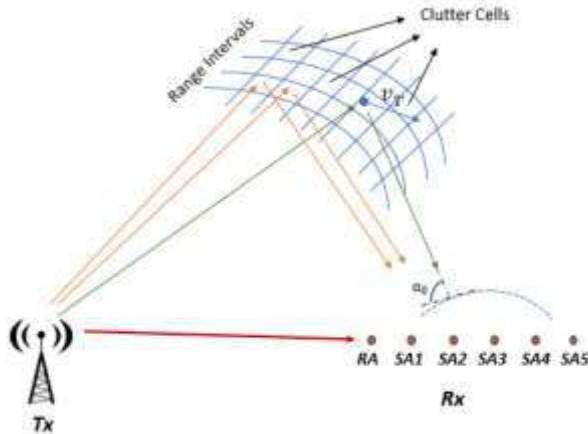


Fig. 5 Designed System Geometry.

The designed system has a PBR geometry in which the transmitter and receiver circuits are in fixed positions. Receiver circuit part consists of 5 antennas with fixed position and distance between antennas $d=1,5$ m. In Chapter 4, the effect on system goals will be shown by changing the number of antennas. One of the antennas on the receiving side is used by the FM illuminator of opportunity to receive the incoming signal directly and is called the reference antenna. The remaining antennas were used to detect the moving target in the vicinity. These antennas also play an important role in the clutter elimination phase.

The working diagram of the designed passive radar is as in Figure 6. Reflected signals from both the target and the clutter are obtained by the antennas SA1, SA2, SA3, SA4, SA5 which are used for surveillance purposes. After the synchronization between the antennas, the signals are digitized. The digitized signals are compressed and optimized by means of a matched filter. The clutter signal obtained from constant environmental factors is suppressed by beamforming. The doppler frequency parts where the suppressed clutter signal is present and target detection can be made are indicated by the improvement factor.

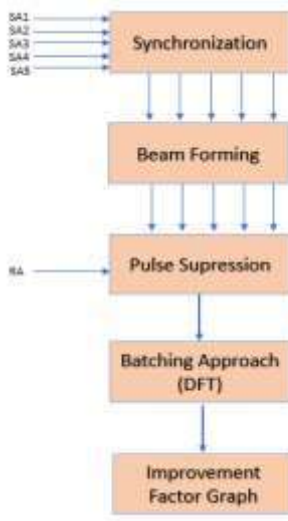


Fig. 6 Working diagram of the designed pbr.

4.2 Transmitted signal model

The signal received by the surveillance antennas is as in Equation 10.

$$x^{(n)}(t) = x_C^{(n)}(t) + x_T^{(n)}(t) + x_N^{(n)}(t) \quad (10)$$

The signal obtained by the designed system consists of the sum of $x_C^{(n)}(t)$, $x_T^{(n)}(t)$, $x_N^{(n)}(t)$ signals. The signal originating from clutter represented by $x_C^{(n)}(t)$, $x_T^{(n)}(t)$ is the echo signal reflected from the target and $x_N^{(n)}(t)$ is the noise signal. n represents the surveillance antennas SA1, SA2, SA3, SA4 and SA5.

4.2.1 Clutter signal

The clutter signal is formed by the reflection of the transmitted signal by stationary objects such as a house and skyscraper on the ground. The resulting signal reduces the target detection performance of the passive bistatic radar. The signal reflected from a single scatterer for each surveillance antenna is as in Equation 11.

$$x_0^{(SA1)}(t) = A_0 s(t - \tau_0)$$

$$x_0^{(SA2)}(t) = A_0 s(t - \tau_0) e^{j2\pi \frac{d}{\lambda} \cos \alpha_0}$$

$$x_0^{(SA3)}(t) = A_0 s(t - \tau_0) e^{j2\pi \frac{2d}{\lambda} \cos \alpha_0} \quad (11)$$

$$x_0^{(SA4)}(t) = A_0 s(t - \tau_0) e^{j2\pi \frac{3d}{\lambda} \cos \alpha_0}$$

$$x_0^{(SA5)}(t) = A_0 s(t - \tau_0) e^{j2\pi \frac{4d}{\lambda} \cos \alpha_0}$$

In Equation 11, A_0 is the complex amplitude, time t , and $s(t)$ denotes the signal emitted from the transmitter. τ_0 is the bistatic propagation delay and is calculated by equation 12.

$$\tau_0 = \frac{R_T + R_R - L}{c} \quad (12)$$

Equation 13 is obtained when the $x_0^{(SA1)}(t)$, $x_0^{(SA2)}(t)$, $x_0^{(SA3)}(t)$, $x_0^{(SA4)}(t)$, $x_0^{(SA5)}(t)$ signals received by the surveillance antennas are sampled with the sampling frequency F_s .

$$x_0^{(SA1)}[l] = A_0 s[l - l_{\tau_0}]$$

$$x_0^{(SA2)}[l] = A_0 s[l - l_{\tau_0}] e^{j2\pi \frac{d}{\lambda} \cos \alpha_0}$$

$$x_0^{(SA3)}[l] = A_0 s[l - l_{\tau_0}] e^{j2\pi \frac{2d}{\lambda} \cos \alpha_0} \quad (13)$$

$$x_0^{(SA4)}[l] = A_0 s[l - l_{\tau_0}] e^{j2\pi \frac{3d}{\lambda} \cos \alpha_0}$$

$$x_0^{(SA5)}[l] = A_0 s[l - l_{\tau_0}] e^{j2\pi \frac{4d}{\lambda} \cos \alpha_0}$$

l and l_{τ_0} are expressed by Equation 14 and Equation 15, respectively.

$$l = tF_s \quad (14)$$

$$l_{\tau_0} = \tau_0 F_s \quad (15)$$

The reference and surveillance signals synchronized by the receiving system, respectively, are divided into data parts, and related to the batching approach, the surveillance signal part is cross-linked to the reference part. Range/Doppler map is obtained by applying DFT (Discrete Fourier Transform) to the obtained matrix. In Equation 16, $s(t)$ is expressed by the result of the batching approach. The total time of sampling is called the CPI (Coherent Processing Interval).

$$s(t) = \sum_{b=0}^{B-1} s_b(t - bT) \quad (16)$$

where B is the number of pieces in a CPI and T is the duration of a piece. When it is assumed that a CPI consists of a total of B parts, the

signals received from the surveillance antennas are expressed by Equation 17.

$$\begin{aligned}
x_0^{(SA1)}[l, b] &= A_0 \sum_{b=0}^{B-1} s_b [l - bL_N - l_{\tau_0}] \\
x_0^{(SA2)}[l, b] &= A_0 \sum_{b=0}^{B-1} s_b [l - bL_N - l_{\tau_0}] e^{j2\pi \frac{d}{\lambda} \cos \alpha_0} \\
x_0^{(SA3)}[l, b] &= A_0 \sum_{b=0}^{B-1} s_b [l - bL_N - l_{\tau_0}] e^{j2\pi \frac{2d}{\lambda} \cos \alpha_0} \\
x_0^{(SA4)}[l, b] &= A_0 \sum_{b=0}^{B-1} s_b [l - bL_N - l_{\tau_0}] e^{j2\pi \frac{3d}{\lambda} \cos \alpha_0} \\
x_0^{(SA5)}[l, b] &= A_0 \sum_{b=0}^{B-1} s_b [l - bL_N - l_{\tau_0}] e^{j2\pi \frac{4d}{\lambda} \cos \alpha_0}
\end{aligned} \tag{17}$$

where L_N is the number of samples in a piece, which is obtained by equation 18.

$$L_N = TF_s \tag{18}$$

The surveillance antennas receive signals from multiple ranges. It must be taken into account that different angular spacings (ϕ_r) come from different angles of incidence (α). In addition, considering that the amplitudes are modeled with the Rayleigh distribution ($A_r(\alpha)$), $x_c(t)$ is expressed by the equation 19.

$$\begin{aligned}
x_c^{(SA1)}[l, b] &= \sum_{r=1}^R \int_{\phi_r} A_r(\alpha) \sum_{b=0}^{B-1} s_b [l - bL_N - l_{\tau_0}] d\alpha \\
x_c^{(SA2)}[l, b] &= \sum_{r=1}^R \int_{\phi_r} A_r(\alpha) \sum_{b=0}^{B-1} s_b [l - bL_N - l_{\tau_0}] e^{j2\pi \frac{d}{\lambda} \cos \alpha_0} d\alpha \\
x_c^{(SA3)}[l, b] &= \sum_{r=1}^R \int_{\phi_r} A_r(\alpha) \sum_{b=0}^{B-1} s_b [l - bL_N - l_{\tau_0}] e^{j2\pi \frac{2d}{\lambda} \cos \alpha_0} d\alpha \tag{19} \\
x_c^{(SA4)}[l, b] &= \sum_{r=1}^R \int_{\phi_r} A_r(\alpha) \sum_{b=0}^{B-1} s_b [l - bL_N - l_{\tau_0}] e^{j2\pi \frac{3d}{\lambda} \cos \alpha_0} d\alpha \\
x_c^{(SA5)}[l, b] &= \sum_{r=1}^R \int_{\phi_r} A_r(\alpha) \sum_{b=0}^{B-1} s_b [l - bL_N - l_{\tau_0}] e^{j2\pi \frac{4d}{\lambda} \cos \alpha_0} d\alpha
\end{aligned}$$

4.2.2 Target signal

In addition to the clutter signals from the surveillance antennas of the passive radar, the echo signal reflected from the target is also received. In the designed scenario, it is assumed that there is a target in the observation environment. In such a case, there will be no effect from other cells to the range range where the target is located. Since the target is in motion, the target's Doppler is calculated in Equation 11. The target

signal $x_T^{(n)}(t)$ received from the surveillance antennas is obtained by combining Equation 20 and Equation 17 as in Equation 21.

$$f_D = f_T(2\frac{v_T}{c} \cos \delta \cos(\beta/2)) \quad (20)$$

$$x_T^{(SA1)} = A_0 \sum_{b=0}^{B-1} S_b [l - bL_N - l_{\tau_0}] e^{j2\pi f_T (2\frac{v_T}{c} \cos \delta \cos \beta / 2) bT}$$

$$x_T^{(SA2)} = A_0 \sum_{b=0}^{B-1} S_b [l - bL_N - l_{\tau_0}] e^{j2\pi f_T (2\frac{v_T}{c} \cos \delta \cos \beta / 2) bT} e^{j2\pi \frac{d}{\lambda} \cos \alpha_0}$$

$$x_T^{(SA3)} = A_0 \sum_{b=0}^{B-1} S_b [l - bL_N - l_{\tau_0}] e^{j2\pi f_T (2\frac{v_T}{c} \cos \delta \cos \beta / 2) bT} e^{j2\pi \frac{2d}{\lambda} \cos \alpha_0}$$

$$x_T^{(SA4)} = A_0 \sum_{b=0}^{B-1} S_b [l - bL_N - l_{\tau_0}] e^{j2\pi f_T (2\frac{v_T}{c} \cos \delta \cos \beta / 2) bT} e^{j2\pi \frac{3d}{\lambda} \cos \alpha_0}$$

$$x_T^{(SA5)} = A_0 \sum_{b=0}^{B-1} S_b [l - bL_N - l_{\tau_0}] e^{j2\pi f_T (2\frac{v_T}{c} \cos \delta \cos \beta / 2) bT} e^{j2\pi \frac{4d}{\lambda} \cos \alpha_0} \quad (21)$$

4.2.3 Noise signal

Noise is the unwanted signals encountered in most electronic applications that occur randomly and statistically. Noise signals can come from the antenna to the receiving system or from the receiver's own circuits. The noise component $x_N^{(n)}(t)$ is modeled with AWGN (Additive White Gaussian Noise). AWGN is a basic noise model used in information theory to simulate the effect of many random processes occurring in nature. This noise is frequently used in radar, sonar, communication and signal processing applications. The sample noises generated for the surveillance antennas are shown in Figure 7.

4.3 Clutter cancellation

The passive radar system designed consists of fixed position receiver and transmitter parts. For this reason, stationary targets are located at 0 Hz in the Doppler space. Since stationary targets with Doppler frequency of 0 Hz express clutter, clutter removal was performed with a beamforming approach using a matched filter in the pulse suppression stage. The results obtained by the proposed methods are shown in section 5.

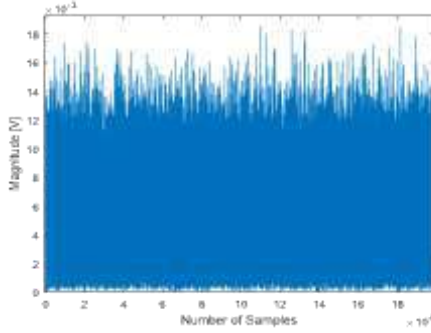


Fig. 7 Surveillance Antennas AWGN.

4.3.1 Beamforming

Beamforming is a digital technique that focuses the radar transmitter and receiver in a particular direction [21], [32]. The side to side direction is commonly referred to as the azimuth and the up and down direction as the elevation. Beamforming can be used to focus the radar over both azimuth and elevations. In the receive beamformer the signal from each antenna may be amplified by a different "weight." Different weighting patterns can be used to achieve the desired sensitivity patterns. A main lobe is produced together with nulls and sidelobes. As well as controlling the main lobe width (beamwidth) and the sidelobe levels, the position of a null can be controlled. This is useful to ignore noise or jammers in one particular direction, while listening for events in other directions. A similar result can be obtained on transmission. Each antenna element must have a delay, or phase adjustment, such that after this adjustment, all elements will have a common phase of the signal. If the angle $\alpha_0 = 0$, then all the elements will receive the signal simultaneously, and no phase adjustment is necessary. At a non-zero angle, each element will have a delay to provide alignment of the wavefront across the antenna array. Figure 8 shows the schematic representation of the proposed digital beamforming approach in the system.

Once each antenna element input is downconverted to baseband by a common clock and local oscillator, each antenna input is delayed by the correct amount so that the wave front arriving from a given direction is aligned. This delay can be digitally implemented by phase rotations, or multiplication by $W_i = e^{j\alpha_0 i}$.

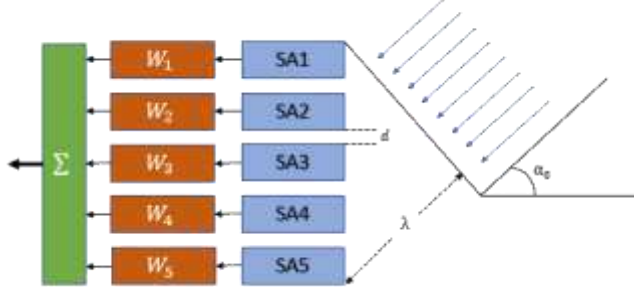


Fig. 8 Digital Beamforming Schematic.

For better side lobe control, the amplitude can also be varied, by using $W_i = A_i e^{j\alpha_0 i}$. By adaptively changing W_i for each antenna input, the beamforming can be accomplished. In the proposed PBR system, the selectivity determined by the angle of incidence in the receiver antennas by means of beamforming plays an important role in clutter removal and target detection. The phase shift can be express as Equation 22.

$$\alpha_n = \frac{2\pi}{\lambda} d(n-1) \sin \alpha_0 \quad (22)$$

Then the steering vector can be calculated as Equation 23.

$$a_n(\alpha_0) = e^{j\alpha_n} \quad (23)$$

Beamforming coefficient vector (W_n) express as Equation 24. ϕ_0 is represents the particular direction. If $\phi_0 = 0$ the beamforming coefficient vector $W_n = 1$.

$$W_n = e^{j\frac{2\pi d}{\lambda}(n-1) \sin(\phi_0)} \quad (24)$$

Then the radiation pattern of the receiver antennas can be express as Equation 25.

$$F_R(\alpha_0, W) = \sum_{n=1}^N W_n^* a_n(\alpha_0) = \frac{\sin(N\frac{\pi d}{\lambda} \sin \alpha_0)}{\sin(\frac{\pi d}{\lambda} \sin \alpha_0)} e^{j\frac{\pi d}{\lambda}(N-1)} \quad (25)$$

4.3.2 Pulse suppression

Active radar systems can control the signal transmitted to the receiver, since the transmitted signal is under the control of its own transmitter. However, passive radars do not have their own transmitting system, unlike active radars, so the waveform of the received signal must be changed. Matching filter is used to change the waveform of the signal and make it suitable.

The state of the received signal after pulse suppression is given in Equation 26.

$$\begin{aligned}
d^{(a)}[l, b] &= r^{(a)}[l, b] * h[l, b] & b \\
&= 0, \dots, B - 1 \\
&= IDFT\{DFT\{r^{(a)}[l, b]\} \odot DFT\{h[l, b]\}\} & (26)
\end{aligned}$$

where $*$ corresponds to convolution and \odot to element-based multiplication. $d^{(a)}[l, b]$ contains the pulse suppression version of each part of the signal. DFT represents discrete fourier transform and IDFT represents the inverse version of DFT.

4.3.3 Match filter

Matched filters are a basic tool in electrical engineering for extracting known wavelets from a signal that has been contaminated by noise [33]. In this section, the matched filter used in the pulse compression phase is explained. In signal processing, a matched filter is obtained by correlating a known delayed signal, or template, with an unknown signal to detect the presence of the template in the unknown transmitted signal. Matched filters are commonly used in radar, in which a known signal is sent out, and the reflected signal is examined for common elements of the transmitted signal. Pulse compression is an example of matched filtering. The unknown shape of the echo signals in passive bistatic radar is a main problem. The echo signals from the target and the disturbance take different forms with the addition of the Doppler effects. Moreover, the echo signal may even overlap with multiple Doppler frequencies. For example, both the Doppler frequencies of the rotor blades and the Doppler frequencies of the fuselage, as well as the radial velocity of the entire helicopter, are important in recognizing a helicopter. In practice, there must be a special matched filter for each Doppler frequency spectrum. The pulse compression is a radar specific form of the matched filter. This filter is most suitable if the received signal is the same as the sent signal. Here, the beamforming process applied to the signal comes into play. When used in conjunction with a compatible filter, the signal can be optimized for effective clutter cancellation and target detection.

5. Simulation results and discussion

The simulation of the PBR system based on the use of an FM radio transmitter as an illuminator was made using the MATLAB program. The simulation parameters are given in Chapter 5.1. A matched filter is used for pulse compression. In Chapter 5.2, the response of the designed 5 antenna system with beamforming and clutter removal at different CNR

values is shown. The results obtained are compared to show the effects of CNR on clutter cancellation. The proposed beamforming approach is evaluated by comparing the effect of CNR value on clutter and target detection capability. The response of the passive radar system designed in Chapter 5.3 is shown when four antennas, three surveillance and one reference, are used. Simulation results are given for different CNR values. The proposed beamforming approach is evaluated by comparing the effect of CNR value on clutter and target detection capability. In Chapter 5.4, the number of receiving antennas is reduced to three and tested for different CNR values. The proposed beamforming approach is evaluated by comparing the effect of different antenna numbers on clutter and target detection capability.

5.1 Simulation Parameters

The carrier frequency (f_T) of the received FM signal is 100 MHz. Therefore, the wavelength becomes 3 m from $\lambda = c / f_T$. The angular spacing is in the range 0 to π . The range interval number (R) is set to 100. The received signal was sampled with a sampling frequency (F_s) of 200 kHz. A CPI consists of a total of 100 parts. The duration (T) of each part is 0.5 ms. The distance between the surveillance antennas (d) is 1.5 m. The number of surveillance antennas (n) was changed to 3, 4 and 5 to observe its effect on the improvement factor. The CNR value was tested at different values such as 30, 40 and 50 dB, and its effect on clutter suppression was examined. All system parameters are given in Table 3.

Table 3 Simulation parameters and values of parameters.

| Symbol | Parameter | Values |
|-----------|--------------------------|-------------|
| f_T | Carrier frequency | 100 MHz |
| λ | Wavelength | 3 m |
| R | Range interval number | 100 |
| ϕ_r | Angular spacing | $[0, \pi]$ |
| F_s | Sampling frequency | 200 kHz |
| d | Distance between | 1,5 m |
| CNR | Clutter to noise ratio | 30-40-50 dB |
| B | Number of batches in CPI | 100 |
| L | Number of sample in one | 400 |
| T | Duration of one batch | 0,5 ms |
| n | Number of surveillance | 3-4-5 |

The improvement factor (IF) is an important evaluation criteria in PBR [34]. IF is the beneficial sign and clutter sign ratio at the output of the filter (here: Moving Target Echo/Stationary Target Echo) divided by the beneficial sign and noise sign ratio at the input of this filter, averaging over the desired target velocities. This definition covers not only the attenuation of fixed target echoes, but also the gain of Doppler frequency smeared fixed target echoes. In this section, the clutter cancellation and target detection capability of the PBR system is evaluated over IF. The effect of range resolution on IF should not be overlooked.

5.2 PBR System With Five Antennas

In this section, the improvement factor of the proposed five antenna PBR system is given for different CNR values. The response of the system for 30 CNR values is shown in Figure 9.a and in Figure 9.b zoomed in between 15 dB and -60 dB.

The Improvement Factor (IF) graph where the CNR value is 40 in the proposed PBR system with 5 antenna receivers is given in Figure 10.a and zoomed version of it given in Figure 10.b. The fact that the clutter rate has been increased is seen with the differences in the parts containing the moving targets, as the Doppler frequency is different from zero.

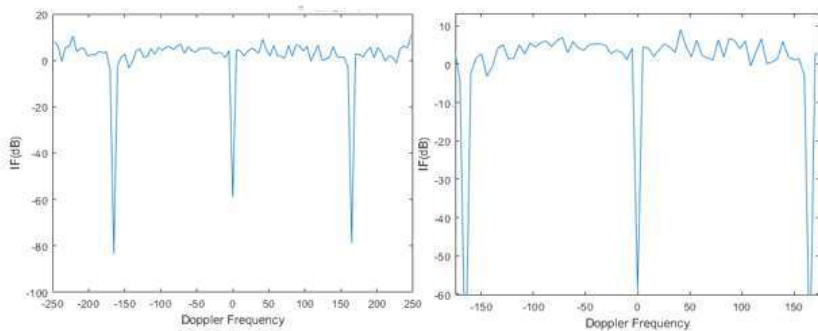


Fig. 9 IF of PBR system with CNR 30 and five receiver antennas. a) simulation results, b) zoomed version of the results.

The response of the system for 50 CNR values is shown in Figure 11.a and in Figure 11.b zoomed in between 20 dB and -45 dB.

When the Improvement Factor (IF) of the system is considered in the parts where the Doppler frequency is zero, it is seen that the clutter is effectively suppressed. For various CNR values, different IF values were obtained for clutter cancellation. The IF value, which is -60 dB at 30 CNR, decreases below -60 dB at 40 CNR and below -50 dB at 50 CNR.

The ratio of the clutter signal to the received signal affects the system performance negatively. Within three CNR values, the system is suitable for target detection.

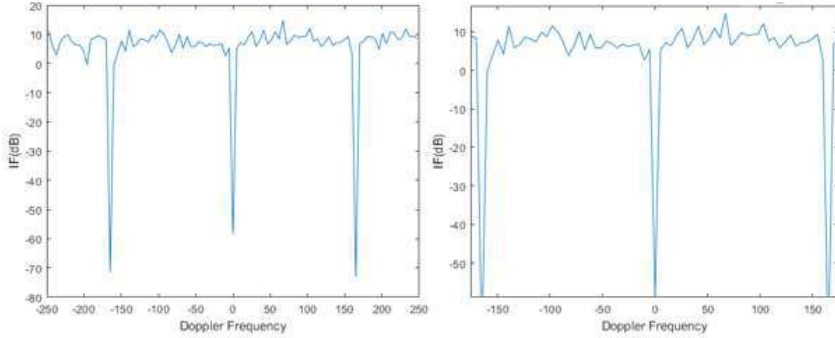


Fig. 10 IF of PBR system with CNR 40 and five receiver antennas. a) simulation results, b) zoomed version of the results.

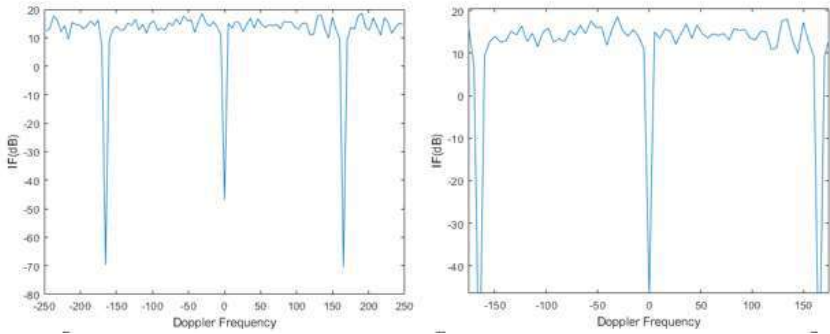


Fig. 11 IF of PBR system with CNR 50 and five receiver antennas. a) simulation results, b) zoomed version of the results.

5.3 PBR system with four antennas

In this section, the improvement factor of the proposed four antenna PBR system is given for different CNR values. The response of the system for 30 CNR values is shown in Figure 12.a and in Figure 12.b zoomed in between 12 dB and -58 dB.

The response of the system for 40 CNR values is shown in Figure 13.a and in Figure 13.b zoomed in between 12 dB and -58 dB. For various CNR values, different IF values were obtained for clutter cancellation. The IF value, which is about -55 dB at 30 CNR.

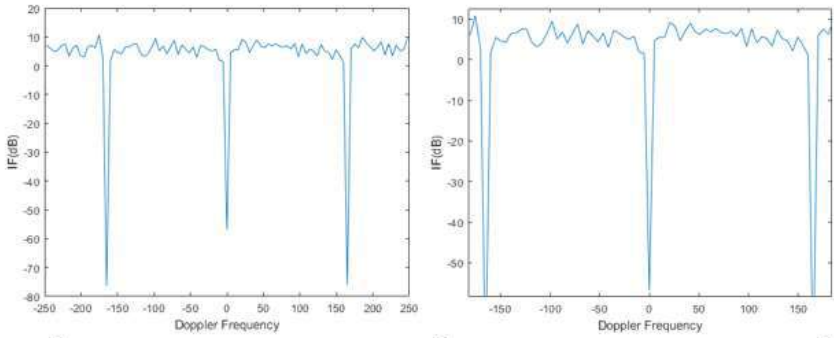


Fig. 12 IF of PBR system with CNR 30 and four receiver antennas. a) simulation results, b) zoomed version of the results.

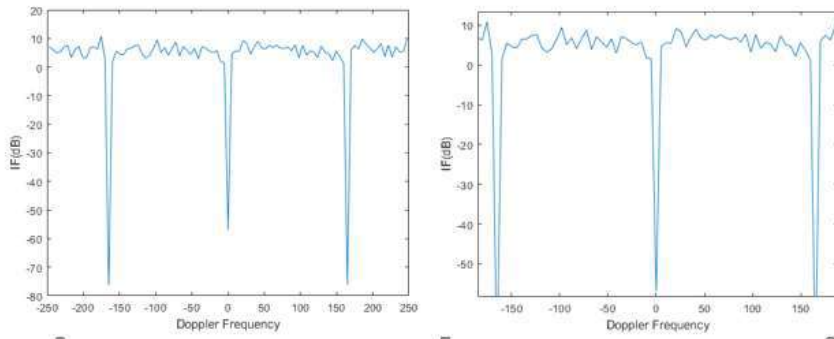


Fig. 13 IF of PBR system with CNR 40 and four receiver antennas. a) simulation results, b) zoomed version of the results.

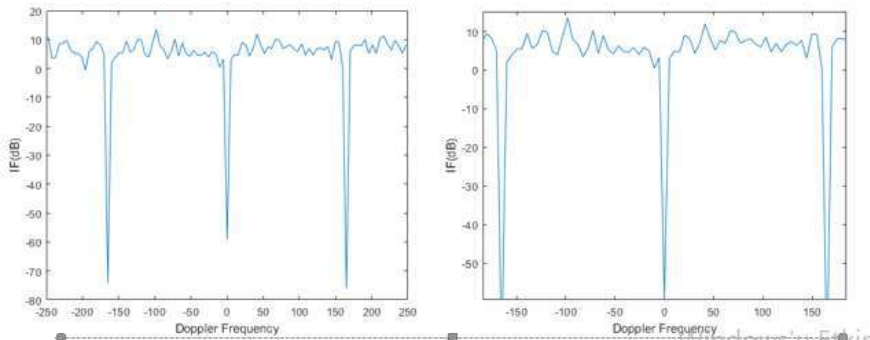


Fig. 14 IF of PBR system with CNR 50 and four receiver antennas. a) simulation results, b) zoomed version of the results.

The response of the system for 50 CNR values is shown in Figure 14.a and in Figure 14.b zoomed in between 15 dB and -58 dB. IF value not

changing much at 40 CNR. IF is the same as the other CNR values at 50 CNR. Differences are observed in target detection parts.

5.4 PBR system with three antennas

In this section, the improvement factor of the proposed three antenna PBR system is given for different CNR values. The response of the system for 30 CNR values is shown in Figure 15.a and in Figure 15.b zoomed in between 13 dB and -52 dB.

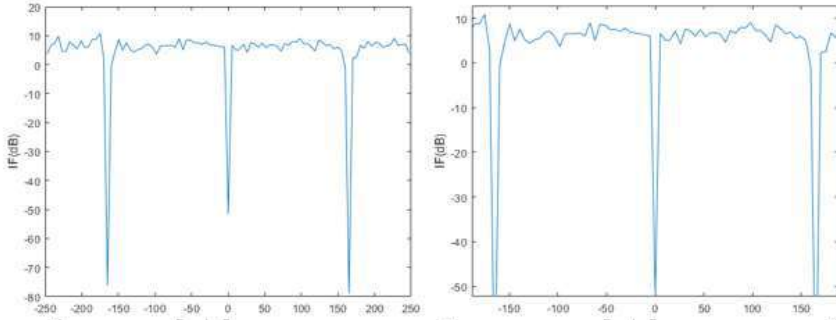


Fig. 15 IF of PBR system with CNR 30 and three receiver antennas. a) simulation results, b) zoomed version of the results.

The response of the system for 40 CNR values is shown in Figure 14.a and in Figure 14.b zoomed in between 12 dB and -57 dB.

The results obtained with different CNR values and antenna numbers show that the proposed system performance decreases at high clutter level. In terms of target detection and riot suppression, the effects are given in the outputs. The beamforming method used is more effective in terms of clutter suppression when the number of antennas increases.

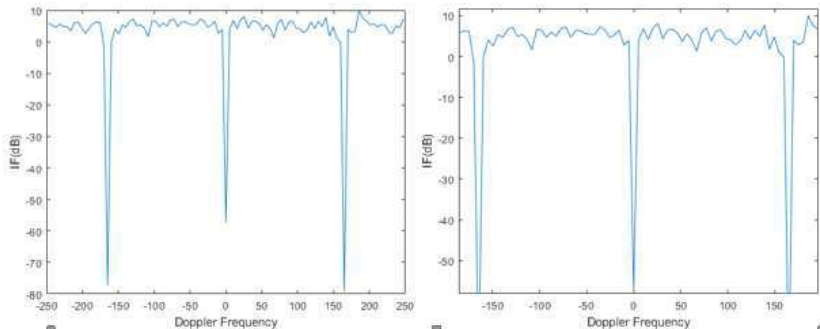


Fig. 16 IF of PBR system with CNR 40 and three receiver antennas. a) simulation results, b) zoomed version of the results.

It is seen that the target detection capability of the system, which is arranged using three antennas, has decreased. Especially in Figure 17, where the CNR value is high, the IF outputs show how much the target detection capability is compared to the five-antenna and four-antenna system. Correspondingly, the gain does not rise above 10 dB and shows an unstable response.

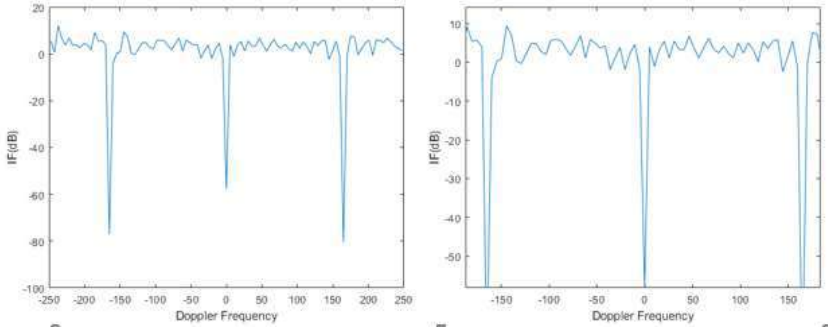


Fig. 17 IF of PBR system with CNR 50 and three receiver antennas. a) simulation results, b) zoomed version of the results.

6. Conclusion

In this study, the suitability of passive bistatic radar system with fixed receiver and transmitter circuits for clutter suppression and target detection has been analyzed. In this context, primarily the clutter signal, target signal and noise signal are modeled. The clutter and target signals are modeled by considering parameters such as scatterers, different angles of incidence, and distances between antennas. The noise signal is modeled using AWGN. The clutter signal, which affects the target detection performance of the passive radar, is suppressed by applying beamforming. A matched filter is used in the pulse compression stage. The methods used were tested for different CNR values and antenna numbers. Clutter is suppressed in the signal portions containing fixed targets where the Doppler frequency is 0 Hz. The parts containing the moving target, where the Doppler frequency is different from zero, are made suitable for target detection by obtaining gain.

Future works:

- Examining the situations that result from different broadcasts of different channels and affect the system performance.
- Testing of passive radar system on non-stationary platforms.
- Examining the effects of DSI (Direct Signal Interference), DPI (Direct Path Interference) and MPI (Multipath Interference).

- Increasing the range resolution by increasing the number of simultaneous channels used. Here, the increased complexity of processing should be taken into account.
- Increasing target detection capability or obtaining more precise results by using passive radar structure in a multistatic geometry.
- Examining the changes caused by the effects of different illuminators on the system.
- Modeling different landforms such as the sea and their effects on clutter suppression.

References

- [1] M. Malanowski, *Signal processing for passive bistatic radar*. Artech House, 2019.
- [2] M. Pola, P. Bezou, and J. Pidani, "Model Comparison of Bistatic Radar Clutter," 2013, pp. 182–185. doi: 10.1109/COMITE.2013.6545066.
- [3] D. W. O. Hagan and C. J. Baker, "Passive Bistatic Radar (PBR) Using FM Radio Illuminators of Opportunity," *2008 New Trends for Environmental Monitoring Using Passive Systems*, pp. 1–6, 2008, doi: 10.1109/PASSIVE.2008.4787000.
- [4] S. Bayat, M. M. Nayebi, and Y. Norouzi, "Target Detection by Passive Coherent FM Based Bistatic Radar," *2008 International Conference on Radar*, pp. 412–415, 2008, doi: 10.1109/RADAR.2008.4653957.
- [5] L. Bendjama and F. Mentouri, "Statistical Analysis and New Modeling of Real Clutter Signal in FM Radio-based Passive Radars," pp. 2–7, 2019.
- [6] K. Kulpa, B. Osi, D. Gromek, P. Samczy, M. Malanowski, and M. B., "Ground Clutter Stability Analyses in DAB based Passive Radar," pp. 2019–2022, 2021.
- [7] L. Rosenberg and D. J. Dowgiallo, "Passive Bistatic Sea Clutter Statistics From Spaceborne Illuminators," vol. 56, no. 5, pp. 3971–3984, 2020.
- [8] L. Rosenberg, S. Member, and V. Duk, "Land Clutter Statistics From an Airborne Passive Bistatic Radar," pp. 1–9, 2021.
- [9] H. Kuschel, "Approaching 80 Years of Passive Radar," pp. 213–217, 2013.
- [10] H. Griffiths, "Early History of Bistatic Radar," pp. 253–257, 2016.
- [11] C. J. B. Hugh D. Griffiths, - *An Introduction to Passive Radar-Artech House*. 2017.

- [12] H. Griffiths, “Klein Heidelberg – The First Modern Bistatic Radar System,” vol. 46, no. 4, pp. 1571–1588, 2010.
- [13] N. J. Willis and H. D. Griffiths, *Advances in Bistatic Radar*. Sci-Tech Publishing, 2007.
- [14] H. D. M. A. E. E. Griffiths and N. R. W. Long, “Television-based bistatic radar.”
- [15] A. Lauri, F. Colone, R. Cardinali, C. Bongioanni, and P. Lombardo, “Analysis and emulation of FM radio signals for passive radar,” *IEEE Aerospace Conference Proceedings*, pp. 1–10, 2007, doi: 10.1109/AERO.2007.353068.
- [16] A. S. Tasdelen and H. Koymen, “Range resolution improvement in passive coherent location radar systems using multiple FM radio channels,” *IET Seminar Digest*, vol. 2006, no. 11537, pp. 23–31, 2006, doi: 10.1049/ic:20060025.
- [17] S. Li, H. Yin, and Y. Huang, “Detection of Moving Targets in FM broadcast-based passive radar 1,” pp. 649–652, 2007.
- [18] P. Bezoušek and V. Schejbal, “Bistatic and Multistatic Radar Systems,” no. January, 2008.
- [19] S. Sistemi and I. Via, “DESIGN, DEVELOPMENT AND TEST ON REAL DATA OF AN FM BASED PROTOTYPICAL PASSIVE RADAR,” pp. 4–9, 2008.
- [20] R. A. S. A. Function, “FM-BASED PASSIVE BISTATIC RADAR AS A FUNCTION OF AVAILABLE BANDWIDTH,” pp. 6–13, 2008.
- [21] Z. Jiabing, H. Yi, T. Liang, H. Yi, and T. Liang, “Adaptive Beamforming Passive Radar Based on FM Radio Transmitter,” pp. 5–8.
- [22] K. E. Olsen and K. Woodbridge, “FM Based Passive Bistatic Radar Range Resolution Improvement”.
- [23] M. Malanowski and A. Detection, “Analysis of Bistatic Tracking Accuracy in Passive Radar,” no. 6, 2009.
- [24] M. Tofighi, “Pasif Bistatik Radarlarda Seyreklik Temelli Ters Evri , sim Kullanılarak Hedef Tespiti TARGET DETECTION USING SPARSITY BASED DECONVOLUTION IN PASSIVE BISTATIC RADARS,” pp. 0–3, 2015.
- [25] M. Zywek and M. Malanowski, “Real-Time Selection of FM Transmitter in Passive Bistatic Radar Based on Short-Term Bandwidth Analysis,” pp. 1–10, 2021.
- [26] M. Malanowski *et al.*, “Experimental results of the PaRaDe passive radar field trials,” 2012. doi: 10.1109/IRS.2012.6233290.
- [27] N. J. Willis, *Bistatic Radar*. Sci-Tech Publishing, 2005.
- [28] Mikhail. Cherniakov and Antonio. Moccia, *Bistatic radar : emerging technology*. John Wiley & Sons, 2008.
- [29] A. Eği̇tmen, “Pasif Radar Uygulamaları,” 2015.

[30] M. Malanowski, K. Kulpa, J. Kulpa, P. Samczynski, and J. Misiurewicz, "Analysis of detection range of FM-based passive radar," vol. 2013, no. December 2013, pp. 153–159, 2014, doi: 10.1049/iet-rsn.2013.0185.

[31] D. Park, G. Park, and H. Kim, "A Method for Eliminating False Detection Results in FM-radio-based Passive Bistatic Radar," *2020 International Conference on Electronics, Information, and Communication (ICEIC)*, pp. 1–3.

[32] G. Bournaka, A. Baruzzi, J. Heckenbach, and H. Kuschel, "Experimental validation of beamforming techniques for localization of moving target in passive radar," in *IEEE National Radar Conference - Proceedings*, Jun. 2015, vol. 2015-June, no. June, pp. 1710–1713. doi: 10.1109/RADAR.2015.7131274.

[33] J. C. Bancroft, "Introduction to matched filters," vol. 14, no. 1988, pp. 1–8, 2002.

[34] S. Wang, S. Song, and J. Huang, "LNCS 7202 - Measurement of Improvement Factor for Bistatic Radar," 2012.

CHAPTER II
RENEWABLE ENERGY POTENTIAL OF ISTANBUL

Dr. Haydar KEPEKÇİ*

*Nişantaşı University, Istanbul, Turkey,
haydar.kepekci@nisantasi.edu.tr, Orcid No:0000-0002-0037-8332

Abstract

The need for energy is increasing day by day with digitalization around the world. Obtaining the energy used from fossil sources causes great harm to both our health and the environment. The main reason for forest fires, air pollution, floods, and other natural disasters that have increased recently is greenhouse gases released into the atmosphere. What needs to be done to eliminate the threat of global warming is to turn to environmentally friendly renewable energy sources. In this study, the installed power and potential of renewable energy sources in Istanbul have been investigated. The example of Istanbul has been examined in terms of the use of renewable energy sources in energy production. As a result, it has been seen that the potential of wind energy is higher among renewable energy sources potential in Istanbul. In addition, it is seen that the share of renewable energy plants in the installed power in Istanbul is quite low. It has been concluded that this rate should be increased as soon as possible and it has been clearly stated in the study.

Keywords: Renewable energy, Energy production, Energy management

1. Introduction

With the effect of developing technology, rapidly increasing population, and digitalization, energy use is increasing day by day. Fossil fuels are mostly used during the production of demanded energy. This situation causes many environmental problems. As a result of the use of fossil fuels, toxic gases such as carbon dioxide, methane, and nitrous oxide are mixed into the air. These toxic gases cause permanent damage to living things breathing the air. This situation affects not only humans but also plants and animals (Kartal, 2021). One of the biggest harms of fossil fuels is that they directly contribute to global warming. The problem of global warming lies at the root of all-natural disasters in recent years (Chen and Geng, 2016). Increasing floods in Europe and

tsunamis in Southeast Asia can be given as examples of natural disasters caused by global warming. Based on the decision to fight against global warming within the scope of the Kyoto Protocol and the Paris Agreement, world states have turned to clean energy sources instead of fossil fuels (Khezri et al, 2021).

As a result of this decision taken to protect both the world and future generations, the installation of renewable energy power plants has accelerated. The main renewable energy sources used in Turkey are solar, wind, hydroelectric, geothermal, and biomass. Turkey's renewable energy potential is very high (Çapik et al., 2012). Due to its geographical location, Turkey is surrounded by seas on three sides and has a climate that can experience four seasons. Unfortunately, the use of renewable energy is far below the desired level, even though it has such a wide range of possibilities. The reason for this is that the necessary investments are not given priority. Turkey, which is completely dependent on foreign energy in terms of energy, should evaluate its own resources as soon as possible and start producing its own energy with its own means.

1.1. Solar energy

The source of solar energy is the sun. The hydrogen gas in the sun's structure turns into helium as a result of the fusion reaction. The energy released during this process is emitted by the sun. Electricity generation from solar energy is carried out through photovoltaic systems. Solar energy is not the same intensity at every hour of the day. It reaches its maximum level in the afternoon and gradually decreases in the evening hours. Therefore, storage systems are also integrated into solar energy systems (Kepekci, 2018).

1.2. Wind power

The source of wind energy is the sun. Wind energy is generated as the air moves from high pressure to low pressure. After solar energy, the most common type of renewable energy is wind energy. Energy is produced through turbines. Wind turbines are systems that convert kinetic energy into mechanical energy. The efficiency of the systems varies according to topographic conditions, wind speed, and turbine blade profiles. On average, system efficiencies are around 30% - 35% (Kepekci and Guven, 2019).

1.3. Geothermal energy

They are generally obtained from geothermal springs formed around active fault lines. 95% of geothermal fields in Turkey are used for heating and the remaining 5% is used for electricity generation. While

generating energy from geothermal sources, harmful chemicals such as hydrogen sulfide, ammonia, methane, and arsenic are released. The reinjection method is used to prevent these wastes from reaching the surface (Li et al., 2021). The yield of geothermal energy is not variable and approximately the same amount of energy is obtained every period of the year. The cost of geothermal energy is cheaper than other types of renewable energy. There is no geothermal power plant in Istanbul.

1.4. Biomass energy

The source of biomass energy is plant and animal products and domestic and industrial wastes. While the main source is plant products such as canola and hazelnut in rural areas, domestic wastes are used as the main source in urban areas (Kepekci, 2019).

1.5. Hydroelectric energy

The source of hydroelectric energy is water. It is obtained by converting the potential energy of water into kinetic energy. It is the energy released as a result of the movement of water down from a high place. The higher the water is dropped from a point, the higher the energy is obtained. The water flowing in the channel goes towards the turbines and makes them rotate. Turbines are connected to generators and convert mechanical energy into electrical energy. Changes in the flow of water affect the amount of energy produced. In order to prevent this, the water used in the power plants is stored using dams (Bulut and Muratoglu, 2019).

1.6. Hydrogen energy

The source of hydrogen energy is hydrogen. Hydrogen is one of the basic elements. It is a colorless, odorless, and non-toxic gas. It is not found alone in nature. It is mostly found in the structure of water. For this reason, scientists use water to obtain hydrogen energy. During this process, hydrogen is burned and water is released again. Since hydrogen can be obtained without wasting water, it is in the renewable energy class (Chi and Yu, 2018).

2. Renewable Energy Resources in Istanbul

Istanbul is located in the Çatalca-Kocaeli section of the Marmara region. It is located between 41 degrees 44 seconds north latitude and 28 degrees 58 minutes 34 seconds east longitude. It is surrounded by Tekirdağ from the west, Kocaeli from the east, the Black Sea from the north, and the Marmara Sea from the south. The province of Istanbul covers Adalar, Arnavutköy, Ataşehir, Avcılar, Bağcılar, Bahçelievler, Bakırköy, Başakşehir, Bayrampaşa, Beşiktaş, Beykoz, Beylikdüzü,

Beyoğlu, Büyükçekmece, Çatalca, Çekmeköy, Esenler, Esenyurt, Eyüp, Fatih, Gaziosmanpaşa, Güngören, Kadıköy, Kağıthane, Kartal, Küçükçekmece, Maltepe, Pendik, Sancaktepe, Sarıyer, Silivri, Sultanbeyli, Sultangazi, Şile, Şişli, Tuzla, Ümraniye, Üsküdar and Zeytinburnu districts (DB-City, 2021).

While the southern parts of Istanbul have characteristics closer to the Mediterranean climate, the northern parts have a Black Sea climate. Summers are hot and dry, while winters are mild and rainy. During the winter, the nighttime temperatures about 6 °C (Enerji Atlası, 2021). This city has 20 wind farms, 14 solar farms, and 5 biogas power plants. The installed capacities of these places are 432 MW, 10.2 MW and 72.61 MW, respectively (Enerji Atlası, 2021). The number of active energy plants in Istanbul is 39 and the installed power is 514.81 MW. The installed power of wind power plants ranks first among the power plants in Istanbul. Biogas plants are in second place and solar power plants are in third place.

3. Solar Power Plants in Istanbul

When Turkey's solar energy potential is examined, it is seen that Southeastern Anatolia, Mediterranean, and Eastern Anatolia Regions come to the fore. Considering the sunshine duration and global radiation values of Istanbul, it is seen that it has a potential below Turkey's average. It is seen from Fig. 1 that the total solar radiation values of Istanbul vary between 1400-1450 KWh/m²-year.

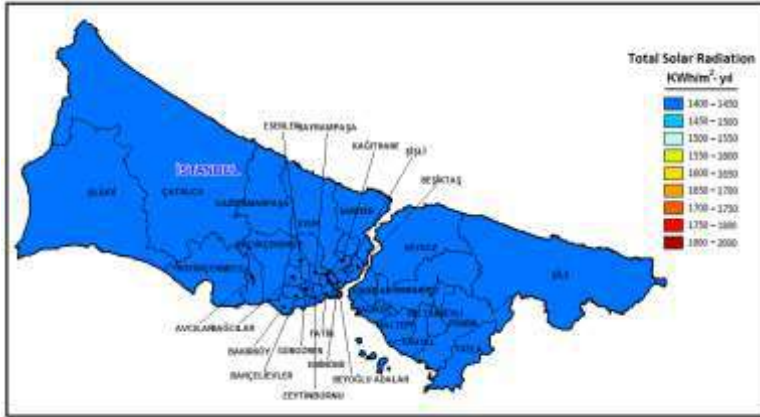


Fig. 1. Istanbul province solar energy potential (Enerji Bakanlığı, 2021)

It is known that all districts of Istanbul have close potential in terms of solar energy. Since Istanbul receives more sunlight, especially in

summer, electricity generation from solar energy is mostly done in summer. Excess energy produced can be stored and solar energy can be used in winter.

Table 1. Solar energy values of Istanbul province

| Months | Sunshine Duration (h) | Global Radiation Values (KWh/m ² -day) |
|-----------|-----------------------|---|
| January | 3.46 | 2.00 |
| February | 4.43 | 2.57 |
| March | 5.32 | 4.20 |
| April | 6.85 | 5.28 |
| May | 8.61 | 6.30 |
| June | 10.51 | 6.79 |
| July | 11.17 | 6.79 |
| August | 10.14 | 6.07 |
| September | 7.83 | 5.09 |
| October | 5.22 | 3.74 |
| November | 3.85 | 2.37 |
| December | 2.96 | 1.80 |

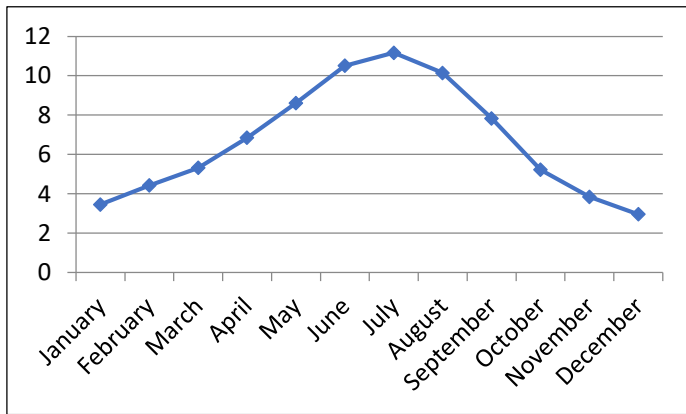


Fig. 2. Istanbul's sunshine duration (hours)

Looking at Table 1 and Fig. 2, it is seen that the highest value of sunshine duration in Istanbul is 11.17 hours in July (Enerji Bakanlığı, 2021).

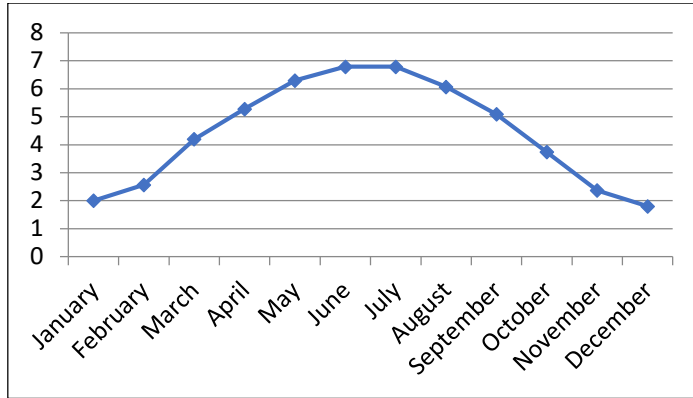


Fig. 3. Global radiation values in Istanbul (kWh/m²-day)

The global radiation values (kWh/m²-day) in Istanbul are given according to the months in Fig. 3. The highest global radiation value is in July (6.79 kWh/m²-day). A large area is required for the installation of solar power plants. This problem can be avoided by constructing power plants on unused and unproductive agricultural lands. Since Istanbul is the most populated city in Turkey, it is very difficult to find free space. However, regions with low urbanization rates can be evaluated. Solar energy is a sustainable energy source as it does not emit harmful emissions to the environment like fossil energy sources. With the widespread use of solar energy, the rate of CO₂ in the atmosphere can also be reduced (Kepekci, 2018). The financial incentives of the state are very important for the widespread use of solar energy. Turkey's December 2021 solar energy installed power is 848 MW. As of December 2021, Istanbul's solar installed power is 10 MW. In Table 2, the installed power of some solar power plants in Istanbul and their ratio in Turkey's total solar power installed power are given.

Table 2. Installed power of some solar power plants in Istanbul

| Solar Power Plants | Installed Power (MW) | Ratios in Turkey Solar Energy Installation Power (%) |
|---------------------------------------|----------------------|--|
| Yeditepe University Solar Power Plant | 1,00 MW | 0.117 |
| İkitelli Thermal Solar Power Plant | 0,50 MW | 0.058 |
| Technopark Istanbul Solar Power Plant | 0,46 MW | 0.054 |
| Özyeğin University Solar Power Plant | 0,35 MW | 0.041 |

| | | |
|--|----------|-------|
| Büyükçekmece Lake Floating Solar Power Plant | 0,24 MW | 0.028 |
| Samson Solar Power Plant | 0,17 MW | 0.020 |
| Aktaş Akıncı Textile Solar Power Plant | 0,10 MW | 0.011 |
| Private Asfa Halil Necati Primary School Solar Power Plant | 0,041 MW | 0.004 |
| Eyüp Municipality Solar Power Plant | 0,037 MW | 0.004 |
| Anel Business Center Solar Power Plant | 0,027 MW | 0.003 |
| IETT İkitelli Factory Solar Power Plant | 0,009 MW | 0.001 |
| Fronius Inverter Istanbul | 0,008 MW | 0.001 |
| Osman Muzaffer Tamer Solar Power Plant | 0,005 MW | 0.001 |
| Other unlicensed Solar Power Plant in Istanbul | 7,34 MW | 0.865 |

3.1. Technopark Istanbul solar power plant

Technopark Istanbul Solar Power Plant is located in the Sabiha Gökçen Airport area of the Pendik district of Istanbul. The picture of the relevant power plant is given in Fig. 4.



Fig. 4. Technopark Istanbul Solar Power Plant

It is Turkey's 1779th and Istanbul's 49th largest power plant. The facility is also Turkey's 402nd largest Solar Power Plant. Technopark Istanbul Solar Power Plant can meet all the electrical energy needs of 165 people in their daily life (such as housing, industry, subway

transportation, government offices, environmental lighting) with an average of 598,000 kilowatt-hours of electricity production. Technopark Istanbul Solar Power Plant produces electricity that can meet the electrical energy needs of 200 houses when only the residential electricity consumption is taken into account. If the electricity (598,000 kWh) produced by the Technopark Istanbul Solar Power Plant had been imported from abroad, approximately 100,410 TL would have been paid with the wholesale price. For this reason, Technopark Istanbul Solar Power Plant also contributes to the reduction of our dependence on foreign energy (Enerji Atlası, 2021).

3.2. Özyeğin University solar power plant

Özyeğin University Solar Power Plant is located in the Çekmeköy district of Istanbul. The power plant is Turkey's 1822 and Istanbul's 50th largest power plant with an installed power of 346.40 kW. The facility is also Turkey's 437th largest Solar Power Plant. The picture of the relevant power plant is given in Fig. 5.



Fig. 5. Özyeğin University Solar Power Plant

Özyeğin University Solar Power Plant, with an average of 505.744 kWh electricity generation, can meet all the electrical energy needs of 139 people in their daily lives (such as housing, industry, subway transportation, government offices, environmental lighting). Özyeğin University Solar Power Plant produces electricity that can meet the electrical energy needs of 169 residences when only residential electricity consumption is taken into account. If the electricity produced by Özyeğin University Solar Power Plant (505,744 kWh) had been imported from abroad, approximately 84,919 TL would have been paid at the wholesale price. For this reason, Özyeğin University's Solar Power Plant also contributes to reducing our dependence on foreign energy (Enerji Atlası, 2021).

3.3. Büyükçekmece Lake floating solar power plant

Büyükçekmece Lake Floating Solar Power Plant is located in Büyükçekmece district of Istanbul. It is Turkey's 1867 and Istanbul's 51st largest power plant. The facility is also Turkey's 471st largest Solar Power Plant. The picture of the relevant power plant is given in Fig. 6.



Fig. 6. Büyükçekmece Lake Floating Solar Power Plant

Büyükçekmece Lake Floating solar energy system can meet all the electrical energy needs of 96 people (such as housing, industry, subway transportation, government offices, environmental lighting) with an average of 350,000 kilowatt-hours of electricity production. Büyükçekmece Lake Floating SPP produces electricity that can meet the electrical energy needs of 117 residences when only residential electricity consumption is taken into account. If the electricity (350,000 kWh) produced by the Büyükçekmece Lake Floating Solar Power Plant had been imported from abroad, approximately 58,769 TL would have been paid at the wholesale price. For this reason, Büyükçekmece Lake Floating Solar Power Plant also contributes to the reduction of our dependence on foreign energy. The solar power plant built on Büyükçekmece Lake, which provides drinking water to Istanbul, is Turkey's first floating solar power plant (Enerji Atlası, 2021).

4. Wind Power Plants in Istanbul

When Turkey's wind potential is evaluated, it is seen that Aegean Region and Southern Marmara Region are more efficient in terms of wind energy compared to other regions (Turkmenler et al., 2015). In addition, for the Wind Power Plant (WPP) to be economical, the wind speed must be at least 7 m/s at 50 m altitude and the capacity factor must be at least 35% (Kepekci et al., 2021). There is no damage to the land where the wind turbines are located. Energy can be obtained from both agriculture and wind turbines in the same area. In recent years,

Northern European countries have started to install wind turbines on the seas due to insufficient space. Thus, they eliminated the need for land to establish a power plant. Wind turbines also have some disadvantages. An example of this is the noise they produce while working (Kepekci et al., 2021). Due to the noise, migratory birds change their trajectories and this causes ecological imbalance. Recently, studies have been carried out to optimize the shape of the tip region of the wind turbine blade in order to eliminate this problem (Kepekci et al., 2021)

The total installed power of the Wind Power Plants in Turkey is 9,559 MW. Istanbul, with its installed power of 432 MW, is in the 8th rank in the ranking of cities that obtain energy from wind energy in Turkey (Pinar et al., 2020) In Table 3, the installed power of some wind power plants in Istanbul and their ratios in Turkey's wind power installed power are given.

Table 3. Installed Powers of Some Wind Power Plants in Istanbul (Enerji Atlası, 2021)

| Wind Power Plants | Installed Power (MW) | Ratios in Turkey Wind Energy Installed Power (%) |
|-------------------------|----------------------|--|
| Çatalca Wind Farm | 93 | 0.972 |
| Silivri Wind Farm | 63 | 0.659 |
| Gaziosmanpaşa Wind Farm | 50 | 0.523 |
| Çanta Wind Farm | 48 | 0.502 |
| Tayakadın Wind Farm | 40 | 0.418 |
| Yamaçtepe Wind Farm | 30 | 0.313 |
| Şile Wind Farm | 26 | 0.271 |
| Kemerburgaz Wind Farm | 24 | 0.251 |
| Çataltepe Wind Farm | 10 | 0.104 |
| Küftepe Wind Farm | 10 | 0.104 |

4.1. Çatalca wind power plant

Çatalca Wind Power Plant, operated by Sanko Holding, is Turkey's 155th and Istanbul's 4th largest power plant with an installed power of 93 MW. The facility is also Turkey's 18th largest Wind Power Plant. The power plant has only been partially commissioned and when the production starts at full capacity, the installed power will be 100 MW.

30 Vestas wind turbines were used in the power plant. The image of the Çatalca wind farm is given in Fig. 7.



Fig. 7. Çatalca Wind Farm

Çatalca Wind Power Plant can meet all the electrical energy needs of 60,476 people in their daily life (such as housing, industry, subway transportation, government offices, environmental lighting) with an average of 219,648,454 kilowatt-hours of electricity production. When only residential electricity consumption is taken into account, Çatalca Wind Power Plant produces electricity that can meet the electrical energy needs of 73,535 houses.

Table 4. Annual electricity production table of Çatalca Wind Farm

| Year | Production (kWh) | Ratio to Provincial Consumption (%) | Ratio to Country Consumption (%) |
|-------------|-------------------------|--|---|
| 2016 | 191.411.980 | 0,40 | 0,07 |
| 2017 | 258.207.150 | 0,51 | 0,09 |
| 2018 | 292.853.970 | 0,56 | 0,10 |
| 2019 | 268.718.390 | 0,51 | 0,09 |
| 2020 | 288.565.000 | 0,55 | 0,09 |

Looking at Table 4, it is seen that the electricity produced by the Çatalca Wind Power Plant meets an average of 0.1% of the country's consumption. It is observed that as the amount of installed power in the country increases, the rate of meeting the consumption also increases. For this reason, the widespread use of renewable energy power plants is very important (Sanko, 2021).

4.2. Silivri wind power plant

Silivri Energy Inc. Operated by Silivri Wind Power Plant, it is Turkey's 202nd largest and Istanbul's 5th largest power plant with an installed power of 63 MW. The facility is also Turkey's 36th largest Wind Power

Plant. The power plant has only been partially commissioned and when the production starts at full capacity, the installed power will be 101 MW. 26 Nordex wind turbines have been used in the power plant. The image of the Silivri wind farm is given in Fig. 8.



Fig. 8. Silivri Wind Farm

With an average electricity production of 167,409,472 kilowatt-hours, Silivri Wind Power Plant can meet all the electrical energy needs of 46,093 people in their daily lives (such as housing, industry, subway transportation, government offices, environmental lighting).

Table 5. Annual electricity production table of Silivri Wind Farm

| Year | Production (kWh) | Ratio to Provincial Consumption (%) | Ratio to Country Consumption (%) |
|-------------|-------------------------|--|---|
| 2016 | 54.434.886 | 0,12 | 0,021 |
| 2017 | 170.053.573 | 0,37 | 0,06 |
| 2018 | 184.469.340 | 0,35 | 0,06 |
| 2019 | 206.958.080 | 0,40 | 0,07 |
| 2020 | 221.131.480 | 0,42 | 0,07 |

Looking at Table 5, it is seen that the country's consumption of electricity produced by Silivri Wind Power Plant is increasing every year on average. The main reason for this is thought to be the incentives given by the state (Gungor Elektrik, 2021).

4.3. Gaziosmanpaşa wind power plant

Öz-Yel Elektrik Üretim A.Ş. Operated by Gaziosmanpaşa Wind Power Plant, it is Turkey's 249th largest and Istanbul's 6th largest power plant with an installed power of 50 MW. The facility is also Turkey's 63rd largest Wind Power Plant. With an average of 77,942,340 kilowatt-hours of electricity production, Gaziosmanpaşa Wind Power Plant can meet all the electrical energy needs of 21,460 people in their daily lives

(such as housing, industry, subway transportation, government offices, environmental lighting). Considering only the residential electricity consumption, Gaziosmanpaşa WPP produces electricity that can meet the electrical energy needs of 26,094 houses (Çevre Bakanlığı, 2021).

5. Biogas Power Plants in Istanbul

Istanbul is the most crowded city in Turkey. Since the population density is high, the amount of garbage produced is higher than in other cities. One of the recycling methods is to get energy from wastes by burning them. Istanbul is very suitable for establishing such an energy facility. If appropriate programs are developed, the energy obtained by this method can make a significant contribution to economic development. In addition, the potential of converting wastes from sheep and goat farming activities, which are common in the western region of Istanbul, into energy can be evaluated. Most of the biogas energy in Istanbul is obtained from garbage. The total installed power of Biogas, Biomass, Waste Heat and Pyrolytic Oil Power Plants in Turkey is 1,184 MW. Istanbul, with its 72.61 MW installed power, is among the cities where biogas energy is obtained. In Table 6, the installed power of some biogas power plants in Istanbul and their ratios in Turkey's biogas energy installed power are given (Enerji Bakanlığı, 2021).

Table 6. Installed Powers of Some Biogas Power Plants in Istanbul

| Biogas Power Plants | Installed Power (MW) | Ratio in Turkey Biogas Energy Installed Power (%) |
|--|-----------------------------|--|
| Odayeri Landfill Gas Plant | 34 | 2,871 |
| İBB Biomass Power Plant | 20 | 1,689 |
| Kömürcüoda Landfill Biogas Power Plant | 14 | 1,18 |
| Hasdal Istanbul Biogas Power Plant | 4,02 | 0,34 |

5.1. Odayeri landfill gas power plant

Odayeri Landfill Gas Power Plant, operated by Ortadoğu Energy, is Turkey's 354th and Istanbul's 9th largest power plant with an installed power of 33.81 MW. The facility is also Turkey's largest Biogas Facility. The facility is also Turkey's largest Biogas Facility. The power plant has only been partially commissioned and when the production starts at full capacity, the installed power will be 37 MW. With an

average of 247,302,876 kilowatt-hours of electricity generation, the Landfill Gas Power Plant can meet all the electrical energy needs of 68,090 people in their daily lives (such as housing, industry, subway transportation, government offices, environmental lighting). Odayeri Landfill Gas Power Plant produces electricity that can meet the electrical energy needs of 82,793 residences when only residential electricity consumption is taken into account (Ortadoğu Enerji, 2021).

5.2. Istanbul Metropolitan Municipality waste incineration and energy production facility

IMM Waste Incineration and Energy Production Facility, operated by the Istanbul Metropolitan Municipality, is Turkey's 534th largest and Istanbul's 14th largest power plant with an installed power of 33.81 MW. The facility is also Turkey's 6th largest Biogas Facility. The power plant has only been partially commissioned and when it starts production at full capacity, the installed power will be 86 MW. IMM Biomass Power Plant can meet all the electrical energy needs of 55,066 people in their daily lives (such as housing, industry, subway transportation, government offices, environmental lighting) with an average of 200,000,000 kilowatt-hours of electricity production. IMM Biomass Power Plant produces electricity that can meet the electrical energy needs of 66,957 houses when only residential electricity consumption is taken into account (Istanbul Büyükşehir Belediyesi, 2021).

5.3. Kömürcüoda landfill biogas power plant

Operated by Ortadoğu Energy, Kömürcüoda Dumpster Biogas Power Plant is Turkey's 666th and Istanbul's 15th largest power plant with an installed power of 14.15 MW. The facility is also Turkey's 10th largest Biogas Facility. With an average of 91,464,277 kilowatt-hours of electricity production, Kömürcüoda Landfill Biogas Power Plant can meet all the electrical energy needs of 25,183 people in their daily life (such as housing, industry, subway transportation, government offices, environmental lighting). When only residential electricity consumption is taken into account, Kömürcüoda Dumpriy Biogas Power Plant produces electricity that can meet the electrical energy needs of 30,621 houses (Ortadoğu Enerji, 2021)

6. Conclusion

The use of fossil fuels in energy production causes environmental problems. Such fuels increase carbon emissions into the atmosphere and trigger global warming. Renewable energy sources, on the other hand, are environmentally friendly and sustainable, unlike fossil fuels.

According to Turkey's Solar Energy Potential Atlas (GEPA) in 2020, while Turkey's sunshine duration is 7.5 hours a day, the sunshine duration of Istanbul is 6.7 hours. From these data, it is understood that the solar energy potential of Istanbul is below the Turkey average. Installing solar energy systems in Istanbul and generating electricity from clean energy is one of the developments that will save the city from dependence on imported energy sources. The province of Istanbul gets the most sun in July. As a result of the researches, it has been calculated that the maximum solar energy power in July is 679 W/m². On the other hand, the month in which the least power can be obtained in December and it is 180 W/m². The solar energy produced in July is 3.8 times that produced in December. In this case, the energy produced in the summer months can be stored and used in the winter months. Because there is very little sunlight in winter. However, the existing solar energy system's installed power of Istanbul is 10 MW. This installed power should be increased by using the existing solar energy potential of Istanbul.

Istanbul has an installed wind power of 432 MW. The state can increase the installation of more wind power plants in the province by supporting it. Because wind energy does not create carbon emissions and waste in energy production. As the power plant increases employment in the region where it is established, agriculture and animal husbandry can be continued in the areas where the turbines are located. Among the renewable energy power plants in Istanbul, biogas power plants have an energy power of 72.61 MW. Necessary investments and incentives should be made for the use of other renewable energy sources such as biogas energy sources in energy production.

References

- Bulut, U., Muratoglu, G. Renewable energy in Turkey: Great potential, low but increasing utilization, and empirical analysis on renewable energy-growth nexus. *Energy Policy*, Vol.123 (2018), pp.240–250.
- Chen, W., Geng W. Fossil energy saving and CO₂ emissions reduction performance, and dynamic change in performance considering renewable energy input. *Energy*, Vol.120 (2016), pp.283-292.
- Chi, J., Yu, H. Water electrolysis based on renewable energy for hydrogen production. *Chinese Journal of Catalysis*, Vol.39 (2018), pp.390-394.
- Çapık, M., Yılmaz, A., Çavusoglu, I. Present situation and potential role of renewable energy in Turkey. *Renewable Energy*, Vol.46 (2012), pp.1-13.

- DB-City, Districts of Istanbul (online) available from <<https://tr.db-city.com/T%C3%BCrkiye--%C4%B0stanbul--%C4%B0stanbul>>, (accessed on 15 December, 2021).
- Enerji Atlası, Biogas Energy (online) available from <<https://www.enerjiatlası.com/biyogaz/>>, (accessed on 13 December, 2021).
- Enerji Atlası, Wind Energy (online) available from <<https://www.enerjiatlası.com/ruzgar-enerjisi-haritasi/istanbul>>, (accessed on 12 December, 2021).
- Enerji Atlası, Solar Energy (online) available from <<https://www.enerjiatlası.com/gunes-enerjisi-haritasi/istanbul>>, (accessed on 11 December, 2021).
- Enerji Bakanlığı, Solar Energy (online) available from <<https://gepa.enerji.gov.tr/MyCalculator/pages/34.aspx>>, (accessed on 11 December, 2021).
- Enerji Atlası, Technopark Power Plant (online) available from <<https://www.enerjiatlası.com/gunes/teknopark-istanbul-gunes-santrali.html>>, (accessed on 10 December, 2021).
- Enerji Atlası, Özyeğin Power Plant (online) available from <<https://www.enerjiatlası.com/gunes/ozyegin-universitesi-gunes-enerji-santrali.html>>, (accessed on 9 December, 2021) .
- Enerji Atlası, Büyükçekmece Power Plant (online) available from <<https://www.enerjiatlası.com/gunes/buyukcekmece-golu-yuzer-g%C3%BCnes-enerji-santrali.html>>, (accessed on 8 December, 2021).
- Güngör Elektrik, Silivri Power Plant (online) available from <<https://www.gungorelektrik.com/proje/silivri-ruzgar-enerji-santrali/>>, (accessed on 6 December, 2021).
- Istanbul Metropolitan Municipality, Istanbul's climate (online) available from <<https://www.iklim.istanbul/iklim/>>, (accessed on 14 December, 2021).
- Istanbul Metropolitan Municipality, Biogas Power Plant (online) available from <<https://atikyonetimi.ibb.istanbul/atik-yakma-ve-enerji-uretim-tesisi/>>, (accessed on 3 December, 2021).
- Kartal, M. The role of consumption of energy, fossil sources, nuclear energy, and renewable energy on environmental degradation in top-five carbon producing countries, *Renewable Energy*, Vol.184 (2021), pp.871-880.
- Khezri, M., Heshmati, A., Khodaei, M. Environmental implications of economic complexity and its role in determining how renewable energies affect CO2 emissions. *Applied Energy*, Vol.306 (2021), pp.1-12.

- Kepekci, H. Analysis and Design of Concentrated Solar Power Components. 4th International Conference of Advances in Mechanical Engineering (2018), pp.102-110.
- Kepekci, H. Bioenergy Potential for Energy Generation from Agriculture in Turkey. European International Journal of Science and Technology, Vol.8, No.3 (2019), pp.1-14.
- Kepekci, H., Guven, H. Review: Aeroacoustic Analysis in Wind Turbines. International Journal of Science, Environment and Technology, Vol.8, No.3 (2019), pp.454-471.
- Kepekci, H., Zafer, B., Guven, H., Korbahti, B. Aeroacoustics Investigation of a Wind Turbine for Different Blade Tip Shapes Using Computational Fluid Dynamics Software. Fresenius Environmental Bulletin, Vol.30, No.11 (2021), pp.12037-12047.
- Li, Y., Sun, R., Li, Y., Hu, B., Dong, J. An enhanced role understanding of geothermal energy on compressed air energy storage in aquifers considering the underground processes. Journal of Energy Storage, Vol.44 (2021), pp.1-17.
- Ministry of Environment, Environmental Reports (online), available from <<http://eced.csb.gov.tr/ced/jsp/ek1/10034>>, (accessed on 5 December, 2021).
- Ortadoğu Enerji, Kömürcüoda Power Plant (online) available from <<https://www.ortadoguenerjigrubu.com/projelerimiz-ve-santrallerimiz/proje-ve-lisans-haritasi/komurcuoda-santrali/>>, (accessed on 2 December, 2021).
- Ortadoğu Enerji, Wind Power Plant (online), available from <<https://www.ortadoguenerjigrubu.com/wp-content/uploads/2013/06/odayeri-tr.pdf>>, (accessed on 4 December, 2021).
- Pınar, A., Buldur, A., Tuncer, T. Examining the Distribution of Wind Power Plants in Turkey by means of Geographic Perspective. Eastern Geographical Review, Vol.25, No.43 (2020), pp.167-182.
- Sanko, Çatalca Power Plant (online) available from <<https://www.sanko.com.tr/tr/sektorel-enerji-catalca-ruzgar-santrali.aspx>>, (accessed on 7 December, 2021).
- Turkmenler, H., Sogukpinar, H., Bozkurt, I., Pala, M. Turkey's Wind Potential and Global Usage. International Journal of Engineering Applied Sciences, Vol.7, No.3 (2015), pp.26 - 32.

CHAPTER III

PRIORITIZING OF WASTEWATER-TO-HYDROGEN PRODUCTION PROCESSES USING DIFFERENT MCDM TECHNIQUES: COMPARISON AND SENSITIVITY ANALYSIS

Assoc. Prof. Elanur ADAR*

*Artvin Coruh University, Artvin, Turkey, e-mail:

aelanur@artvin.edu.tr / cm.elanur@gmail.com

Orcid No: 0000-0002-9609-0439

1. Introduction

Today, technology and industry are developing rapidly. The population is increasing day by day. According to the data of 2020, the world population is 7.8 billion. Increasing production-consumption and increasing population increase the demand for energy. As a result of increasing production and consumption, wastewater with various characteristics is formed. Discharging wastewater to the environment without treatment causes soil, air, groundwater/surface water pollution and adverse effects on living creatures.

The importance of preserving the environment and benefitting from the organic content of wastewater has been increasing day by day. It is estimated that 50% of the global energy demand will be met through renewable energy sources by the year 2050 (Lim et al., 2020). Biomass energy is among the various renewable energy sources (hydraulic, wind, solar). In comparison with other sources, biomass energy is an alternative that is not affected by weather conditions and has a continuous source of raw material (wastewater) (Lim et al., 2020). Particularly with the conscious use of water and the use of high production technologies (that cause less water consumption) in industries, it should be aimed to reduce the amount of wastewater produced. Afterwards, the management of the wastewater produced should be carried out in a sustainable manner. The organic materials and water (which constitutes most of wastewater) in wastewater should be recycled as hydrogen (H_2) and/or methane (CH_4) energy using appropriate processes. H_2 (120 MJ/kg) is 2.6 times higher than CH_4 and 2.75 times higher than hydrocarbon fuels (Koroglu, 2019). Additionally, the emergent CH_4 has a greenhouse effect if not converted into energy. On the other hand, H_2 is not a type of gas with a greenhouse effect (Barca et al., 2015). H_2 is an energy carrier that can be used in

various sectors including industry, transportation, heating and electricity (Xu et al., 2019a). H₂ is present in water, hydrocarbons and the compounds in biomass (Adar, 2018). 11.2% of water consists of H₂ (Onaran, 2016). The fact that H₂ is bound to other elements indicates the presence of a very large reserve in all parts of the world (Koroglu, 2019). 96% of H₂ is produced from fossil fuels through the steam-methane reforming process. Of this 96%, 48% is produced from natural gas, 30% from petroleum, and 18% from coal. The remaining 4% is produced from water and biomass (Sabankay, 2012; Xu et al., 2019a). H₂ gas is produced through water electrolysis, gasification, natural gas reforming, high-temperature water decomposition, photoelectrolysis and biological methods (Oncel, 2009). Water is the main product formed from the combustion of H₂. In other words, it is an energy source that does not cause pollution or damage the environment and human health (Sabankay, 2012). It is expected that H₂ will play a key role in the future of energy as an alternative to fossil-fuel-based energy sources.

Today, the vast majority of H₂ is produced from fossil fuels. In order to increase its production from biomass (e.g. wastewater), the sustainable management of wastewater should be prioritized. This way, environmental problems will be minimized as well. Hydrogen production from wastewater can be carried out through biological or thermal processes (Oncel, 2009), which can be listed as anaerobic biofilm reactors, microbial electrochemical methods, photobioreactors and hydrothermal gasification. These processes are newly-developing methods. Evaluating these processes in terms of different criteria is important for the selection of the most suitable process.

Making a decision based on different criteria among so many alternatives is a complex, conflicting and uncertain process. In such cases, researchers generally manage to make the most suitable decision using Multiple-Criteria Decision-Making (MCDM) techniques (Zavadskas et al., 2018; Abdullah et al., 2019). The prioritization of wastewater-to-hydrogen production processes is a decision-making problem that includes the selection and ranking of multiple alternatives in terms of multiple conflicting criteria. For this reason, the present study aims to prioritize wastewater-to-hydrogen production processes using the MCDM techniques Analytic Hierarchy Process (AHP) and Measurement Alternatives and Ranking According to Compromise Solution (MARCOS). AHP is among the most commonly used MCDM techniques (Rajak and Shaw, 2019). AHP is applied to both qualitative

and quantitative data, and it is one of the rare techniques that consider the consistency of decision-makers (Saaty, 1980). MARCOS, on the other hand, defines the relationship between alternatives and reference values (ideal and anti-ideal alternatives). It is a new-generation technique that considers a large number of criteria and alternatives (Stević et al., 2020). In environmental applications, namely wastewater management problems (location selection, process selection, etc.), many researchers (Goulart-Coelho et al., 2017; Abdullah et al., 2019; Adar and Delice, 2019) use MCDM methods and/or recommend their use. In the literature, there are studies on microalgae harvesting-drying processes (Tan et al., 2016) and location selection (Mohseni et al., 2016; Anggraini et al., 2018; Babazadeh et al., 2020); and hydrogen production processes (He and Ma, 2013; Ren et al., 2013; Xu et al., 2019a). In the study conducted by Xu et al. (2019a), thermochemical (coal gasification, biomass gasification, natural gas reforming, solar thermochemical, biomass-derived liquid reforming), electrolysis (grid, wind, solar), direct solar water splitting (photoelectrochemical) and biological (microbial biomass reforming, photobiological) H₂ production alternatives were discussed. In conclusion, the alternative with the highest priority was reported as alternative wind energy. Ren et al. (2013) prioritized pyrolysis, gasification, supercritical water gasification (SCWG) and fermentation processes for biomass-to-H₂ production using fuzzy Multi-actor Multi-criteria Decision Making. In the study, gasification was determined as the process with the highest priority in terms of environmental, cost and social criteria. When the studies in the literature are examined, it is observed that the studies are generally on different types of H₂ production technologies. Unlike the studies in the literature, in the present study, the selection and ranking of wastewater-to-hydrogen production processes are obtained for the first time.

The present study aims to prioritize the microbial fuel cells (MFC), supercritical water gasification (SCWG), dark fermentation (DF) and indirect photobioreactors (PBR), which can be used to generate H₂ energy from wastewater, in terms of technological, cost and environmental/social main criteria. In the prioritization, a decision was made between wastewater-to-hydrogen production processes by using the criteria weights obtained with AHP in the MARCOS method. The alternative rankings obtained with MARCOS were compared with the alternative rankings obtained through the new-generation MCDM technique, Combinative Distance-based Assessment (CODAS) and Technique for Order Preference by Similarity to an Ideal Solution

(TOPSIS), one of the commonly used techniques in the literature. Additionally, a sensitivity analysis was performed and the effects of the criteria on the alternative ranking were determined.

2. Materials and methods

2.1. Determination of decision-makers, alternatives and criteria

During the multiple-criteria decision-making process carried out to determine the most effective wastewater-to-hydrogen production alternative, the literature and expert opinion were referred to in the selection of the alternatives and criteria. The experts are environmental engineers and work in state universities. The pairwise comparison matrices were filled in by 5 academicians experienced in the field of the alternatives considered. There are a wide variety of hydrogen production technologies (electrolysis, solar energy, wind energy, hydraulic energy, natural gas reforming, high-temperature water decomposition, photoelectrolysis, etc.). These technologies are notable. However, the present study aims to discuss wastewater-to-hydrogen production processes. There are also gasification and pyrolysis processes. However, these are used not for wastewater but for solid wastes with high solid material content. Additionally, these technologies can be operated on a full scale, i.e., they are developed. For this reason, the following four processes were selected as alternatives.

Dark fermentation (A1)

DF is the most commonly used anaerobic biofilm reactor. It is a process where organic content is converted into H₂ by anaerobic bacteria or certain algae (Oncel, 2009). Carbohydrate-containing wastewater such as foods, whey, sugar, rice and wine are very suitable for this process. Metabolic reactions differ based on the substrate used. With acetate and butyrate substrates, 67% and 50% H₂ are obtained, respectively (Barca et al., 2015). The remaining content of the emergent gas is constituted by carbon dioxide, methane, carbon monoxide and hydrogen sulfur. For this reason, it is necessary to purify H₂ (Sabankay, 2012). In the DF process, the H₂ production rate ranges between 8.2-121 mmol/Lh (Sabankay, 2012). The main advantages of DF are that the system is simple, can be operated the whole day as it is operated in the dark, the decomposition takes place under anaerobic conditions (without the need for oxygen), and, therefore, the operating cost is lower (less energy consumption) (Oncel, 2009). The main disadvantages of DF are that the reaction time is long, additional

treatment is required to fulfill post-treatment discharge standards and the ambient presence of O₂ negatively affects the efficiency of H₂ production (Sabankay, 2012).

Photobioreactors (A2)

H₂ has been produced from green algae since 1942 (Koroglu, 2019). Photobioreactors are categorized into two as direct and indirect biophotolysis. Indirect photobioreactors (PBR) refer to nitrogen-fixing photoheterotrophic bacteria or cyanobacteria breaking down organic materials into H₂ using the nitrogenase enzyme or luminous energy. The H₂ production rate in PBR is 0.355 mmol/Lh. In this process, microalgae photosynthesize using CO₂ and produce glucose. In cyanobacteria, they produce acetic acid and H₂ by breaking down glucose. In addition to energy production, the main advantages of PBR are that it is an environmentally-friendly approach due to the consumption of CO₂ and the costs of the system (operating + investment) are low due to photosynthesis (Elcik, 2016). The main disadvantages of PBR are that the efficiency of H₂ production is low, the reaction time is long and it is affected by climatic conditions (Babazadeh et al., 2020).

Supercritical water gasification (A3)

SCWG, which was developed in the 1970s, is a hydrothermal gasification method and a thermal process. The SCWG process is operated at >374.15 °C and >22.12 MPa, which are the supercritical conditions of water. Compared to water under normal conditions, supercritical water has much fewer hydrogen bonds, lower dielectric constant, lower viscosity, higher diffusion coefficient and acidic behavior. Under supercritical conditions, organic materials have a high degree of solubility. This feature causes the environment to be homogeneous and ensures that there is no subsurface between the organic materials and water, eliminating mass transfer limitation. This causes the reaction time to be very fast (Xu et al., 2014). With SCWG, hazardous/non-hazardous wastewater with high concentrations can be gasified in a very short time period (within seconds) and with very high efficiency (>99%) without requiring dehydration (Yoshida et al., 2003). The gas composition in SCWG was reported as 40-60% H₂, 30-70% CO₂, 15-25% CH₄ and 5-30% CO, depending on operating conditions (Afif et al., 2011). It was also reported that more than 50% of the H₂ formed can originate from water (Kruse et al., 2003). The wastewater to be fed into the system must be pumpable (e.g. contain few solid

materials), have low inorganic content and have a water content of >60% (Chakinala, 2013). The main advantages of SCWG are that additional treatment is not required in either the gas product or the liquid product following the treatment and the number of solid products formed is low, pre-treatment dehydration is not required, and the reaction time is short, therefore requiring less space (Adar, 2018). The main disadvantages of SCWG are that corrosion/clogging problems may occur due to operating conditions (the inorganic content of the wastewater must be low), the risk level is high and operating costs are high (Adar, 2018). Today, laboratory and pilot-scale systems are available but have not yet been commercialized.

Microbial fuel cells (A4)

MFC, which has been used in the treatment of biodegradable wastewater since 1912, is the most commonly used microbial electrochemical process. MFC consists of anode, cathode and a proton exchange membrane separating these two parts (Cetinkaya, 2017). It is operated in low temperatures and anaerobic conditions. Operating the system under anaerobic and electrochemical conditions causes 20% less sludge formation compared to anaerobic digestion (Slate et al., 2019). Its development is currently close to commercialization. In an MFC process with a capacity of 54 m³/day (2.25 m³ volume, 10 cells), investment costs are €44850 and €43010, respectively, depending on whether platinum will be used as the cathode material. The annual sludge disposal and electricity consumption costs of this system are €1763 and €3155, respectively (Trapero et al., 2017). The main disadvantage of MFC is that it requires additional treatment since the wastewater quality generally does not meet discharge standards (Hou et al., 2016).

While MFC, DF and PBR are biological processes, SCWG is a thermal process. In MFC and DF, which are operated under anaerobic conditions, there is less sludge formation. Biological processes are operated within the pH range of 6-8, at a temperature of 20-40°C and at a long reaction time. In the SCWG process, higher efficiency is achieved in alkaline conditions. >40% H₂ can be produced in DF, MFC and SCWG. In PBR, on the other hand, H₂ production is lower. However, it is a technology that reduces CO₂. These processes have not yet been commercialized. Compared to the other processes, DF is the most economical alternative. Due to the electrode, membrane and electricity consumption in MFC and the high operating temperatures of SCWG, these alternatives are not economical.

In the selection of different treatment processes using MCDM techniques, mainly the technological, social, environmental and cost main criteria were selected (Qazi and Abushammala, 2020; Ren and Ren, 2020). When previous studies in the literature are examined, it is observed that these are the most commonly used criteria in the studies on the selection of wastewater treatment processes (Bottero et al., 2011; Ilangkumaran et al., 2013; Debnath et al., 2016; Yao et al., 2020). Additionally; operating cost, disposal efficiency, and technological development are the prioritized sub-criteria (Xu et al., 2019b; Padron-Paez et al., 2020). In the present study, various sub-criteria in line with the purpose of the study were determined in addition to the technological, cost and environmental/social main criteria. Table 1 shows the main- and sub-criteria.

Table 1 Main- and sub-criteria used in the evaluation of wastewater-to-hydrogen production processes.

| Main Criteria | Technological (T) | Cost (C) | Environmental/Social (E) |
|---------------|-------------------------------------|----------------------|-------------------------------|
| Sub-criteria | Development (T1) | Investment cost (C1) | Odor formation (E1) |
| | Ease of operation (T2) | Operating cost (C2) | Noise pollution (E2) |
| | Suitability for local climate (T3) | Land cost (C3) | Aesthetic pollution (E3) |
| | Treatment efficiency (T4) | | Solid waste generation (E4) |
| | H ₂ production rate (T5) | | Greenhouse gas formation (E5) |
| | Pre-treatment requirement (T6) | | Public acceptance (E6) |
| | Physical workload (T7) | | Potential of water reuse (E7) |
| | Shock load resistance (T8) | | Risk level (E8) |
| | Ease of operating conditions (T9) | | |
| | System lifetime (T10) | | |
| | Raw material variety (T11) | | |
| | Reaction time (T12) | | |

2.2. An integrated AHP&MARCOS model

The integrated AHP&MARCOS model consists of three steps. The first step is the determination of decision-makers, criteria and alternatives. The following step is the determination of criteria weights using AHP. In the final step, the four alternatives selected are ranked using the MARCOS technique. Additionally, the effects of criteria weights on the alternative ranking were determined through a sensitivity analysis. A comparative analysis was performed to

determine the validity of the AHP&MARCOS model. Using the weights calculated with AHP, changes in the alternative ranking depending on the technique used were examined through the TOPSIS and CODAS methods. Figure 1 shows the stages of the integrated method. The steps of AHP and MARCOS are summarized below.

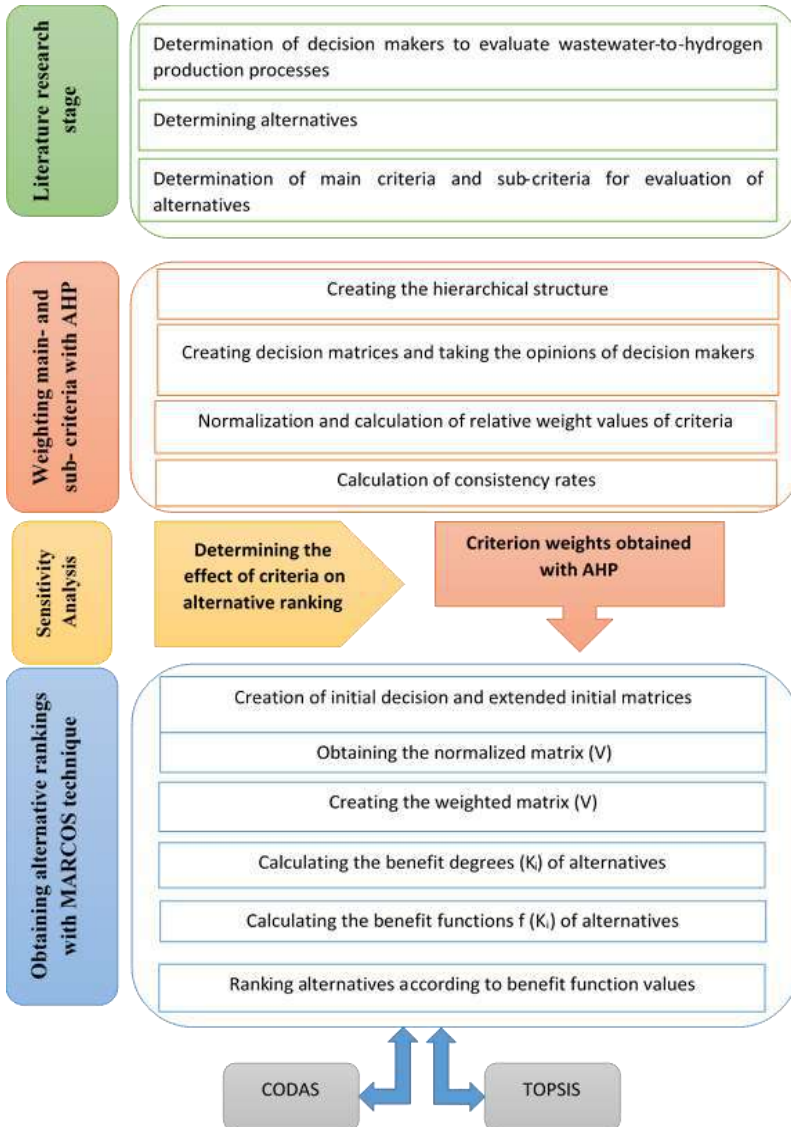


Fig. 1 Stages of the integrated AHP&MARCOS model

AHP (Analytic Hierarchy Process)

AHP, which was proposed by Saaty in 1980, is a very popular technique (Saaty, 1980; Rajak and Shaw, 2019). The main advantages of this technique are that it can be applied to qualitative and quantitative data, and that it converts a complex and multi-criteria problem/decision into a hierarchical structure. It is one of the rare techniques that consider the consistency of decision-makers (Adar and Delice, 2019). The steps of AHP are given below (Isiklar and Buyukozkan, 2007):

Step 1: Creation of the hierarchical structure:

The hierarchical structure consists of the alternatives and main- and sub-criteria used in the decision-making process for the specified goal.

Step 2: Creation of decision matrices:

Decision matrices (Equation 1) include the evaluations of each criterion regarding other criteria. Pairwise comparison matrices are developed between the criteria and the opinions of decision-makers are received. While stating their opinions, the decision-makers use the 1-9 comparison scale as shown in Table 2 (Saaty, 1980).

The pairwise comparison matrix A (Equation 1) to be created in the presence of n criteria has a size of nxn and consists of the elements $\{a_{ij}\}$ (Dağdeviren et al., 2009). In the decision-maker's comparison between criterion i and criterion j, a_{ij} ($i, j = 1, 2, \dots, n$) is the expression showing the rate in which criterion i is preferred over criterion j (Isiklar and Buyukozkan, 2007).

$$A = \begin{bmatrix} a_{11} & a_{12} & \cdots & a_{1n} \\ a_{21} & a_{22} & \cdots & a_{2n} \\ \vdots & \vdots & \ddots & \vdots \\ a_{n1} & a_{n2} & \cdots & a_{nn} \end{bmatrix} \quad a_{ii} = 1, \quad a_{ji} = 1/a_{ij}, \quad a_{ij} \neq 0 \quad (1)$$

Table 2 Saaty's 1-9 comparison scale (Saaty, 1980)

| Intensity of importance | Definition |
|--------------------------------|------------------------------|
| 1 | Equally important |
| 3 | Moderately more important |
| 5 | Strongly more important |
| 7 | Very strongly more important |
| 9 | Extremely more important |

Step 3: Normalization and the determination of relative weights (eigenvector):

First, the comparison matrix is normalized. Each element (a_{ij}) in the pairwise comparison matrix (A) is normalized by being divided by its own column sum based on Equation (2).

$$x'_{ij} = \frac{x_{ij}}{\sum_{i=1}^n x_{ij}} \quad (2)$$

After the decision matrices are normalized, the eigenvalues that will give the relative weights of the criteria are calculated. With the right eigenvector (w) corresponding to the maximum eigenvalue (λ_{\max}), the relative weights are displayed as in Equation 3:

$$Aw = \lambda_{\max} w \quad (3)$$

If all of the pairwise comparisons are consistent, the matrix A has rank 1 and $\lambda_{\max} = n$. In this case, the weights are obtained by the normalization of any of the rows or columns of the A matrix. These calculations are performed for the main- and sub-criteria in the hierarchy. The relative priorities of the sub-criteria are determined by multiplying the local weights of the sub-criteria by the global weights of the main criteria. Relative priorities indicate the level at which the criteria contribute to the realization of the goal. With this evaluation process, the perspectives of different stakeholders are integrated (Wang and Yang, 2007).

Step 4: Calculation of the consistency ratio (CR):

The consistency of the judgments obtained as a result of the pairwise comparisons performed between the criteria is checked. The consistency of an A matrix created with the judgments of the decision-maker is tested through the calculation of the "Consistency Index (CI)" coefficient given in Equation (4).

$$CI = (\lambda_{\max} - n) / (n - 1) \quad (4)$$

In order to check consistency, it is also necessary for the "Random Index (RI)" value to be known. Table 3 shows the RI values corresponding to each matrix size n. The RI value can be calculated for matrices with a maximum size of 15 (Saaty and Tran, 2007).

Table 3 Random index according to the matrix size (Saaty and Tran, 2007)

| | | | | | | | | |
|----------|----------|-----------|-----------|-----------|-----------|-----------|-----------|----------|
| n | 1 | 2 | 3 | 4 | 5 | 6 | 7 | 8 |
| RI | 0.00 | 0.00 | 0.58 | 0.90 | 1.12 | 1.24 | 1.32 | 1.41 |
| n | 9 | 10 | 11 | 12 | 13 | 14 | 15 | |
| RI | 1.45 | 1.49 | 1.51 | 1.53 | 1.56 | 1.57 | 1.59 | |

After the CI and RI ratios are determined, the CR value is calculated using Equation (5).

$$CR = CI/RI \quad (5)$$

In order for the matrix to be consistent, the CR value must be less than 0.1. If the CR value is greater than 0.1, the matrix is regarded as inconsistent and the pairwise comparison matrix is either reviewed or disregarded in the calculation (Saaty, 1980).

MARCOS (Measurement Alternatives and Ranking According to Compromise Solution)

The MARCOS technique proposed by Stević et al. (2020) is a new-generation, multi-criteria decision-making technique. MARCOS defines the relationship between alternatives and reference values (ideal and anti-ideal alternatives). Based on the relationships defined, the benefit functions of the alternatives are determined and an agreement ranking is made in accordance with ideal and anti-ideal solutions. Decision preferences are defined based on benefit functions. Benefit functions represent the position of the alternative in terms of an ideal or anti-ideal solution. The best alternative is the one closest to the ideal and, at the same time, the furthest from the anti-ideal reference point. The main advantages of this technique are: the evaluation of the anti-ideal and ideal solution at the beginning of the formation of an initial matrix, closer determination of the benefit degree regarding both solutions, definition of a new benefit function to determine the benefit, and the possibility to consider a large number of criteria and alternatives while maintaining the stability of the method. Additionally, it is a technique that regards benefit and cost criteria during the calculation.

There are a limited number of studies on this technique (Stević et al., 2020; Stević and Brković, 2020), which was proposed in 2020. There are previous studies on the selection of sustainable suppliers in healthcare sectors using the MARCOS technique (Stević et al., 2020) and the evaluation of human resources in a transportation company with the FUCOM-MARCOS approach (Stević and Brković, 2020).

The MARCOS technique consists of 6 main steps:

Step 1: Formation of the origin decision matrix:

In a decision-making situation with an n number of criteria and m number of alternatives, decision-makers are selected to evaluate alternatives based on criteria. In cases where there is more than one decision-maker, the expert evaluation matrices are combined. Decision-makers use the 1-9 comparison scale as shown in Table 1.

Step 2: Formation of an extended initial matrix:

In this step, the extension of the initial matrix is performed by defining the ideal (AI) and anti-ideal (AAI) solution (Equation 6).

$$X = \begin{matrix} & C_1 & C_2 & \cdots & C_n \\ \begin{matrix} AAI \\ A_1 \\ A_2 \\ \vdots \\ A_m \\ AI \end{matrix} & \begin{bmatrix} x_{aa1} & x_{aa2} & \cdots & x_{aan} \\ x_{11} & x_{12} & \cdots & x_{1n} \\ x_{21} & x_{22} & \cdots & x_{2n} \\ \vdots & \vdots & \ddots & \vdots \\ x_{m1} & x_{m2} & \cdots & x_{mn} \\ x_{ai1} & x_{ai2} & \cdots & x_{ain} \end{bmatrix} \end{matrix} \quad (i=1,\dots,m, \quad j=1,\dots,n) \quad (6)$$

While the anti-ideal solution (AAI) is the least desirable alternative, the ideal solution (AI) represents the alternative with the best features. Depending on the properties of the criteria, AAI and AI are obtained with Equations 7 and 8:

$$\begin{aligned} AAI &= \min_i x_{ij} \quad \text{if } j \in B \quad \text{and} \quad \max_i x_{ij} \quad \text{if } j \in C \\ AI &= \max_i x_{ij} \quad \text{if } j \in B \quad \text{and} \quad \min_i x_{ij} \quad \text{if } j \in C \end{aligned} \quad (7-8)$$

Here, B shows the benefit-oriented criteria while C represents the cost-oriented criteria.

Step 3: Normalization of the extended initial matrix (X):

The elements of the normalized matrix N (n_{ij}) are obtained using Equations 9 and 10.

$$n_{ij} = \frac{x_{ai}}{x_{ij}} \quad \text{if } j \in C$$

$$n_{ij} = \frac{x_{ij}}{x_{ai}} \quad \text{if } j \in B$$
(9-10)

Here, x_{ij} and x_{ai} represent the elements of matrix X.

Step 4: Determination of the weighted matrix (V):

The weighted matrix (V) is obtained through the multiplication of normalized matrix elements by criteria weights (w_j) (Equation 11).

$$v_{ij} = n_{ij} \times w_j$$
(11)

Step 5: Calculation of the benefit degree (K_i) of the alternatives:

The benefit degrees of the alternatives are calculated in accordance with the anti-ideal and ideal solutions using Equations 12 and 13.

$$K_i^- = \frac{S_i}{S_{aai}}$$

$$K_i^+ = \frac{S_i}{S_{ai}}$$
(12-13)

Here, S_i ($i = 1, \dots, m$) represents the sum of the weighted matrix (V) elements (Equations 14).

$$S_i = \sum_{j=1}^n v_{ij}$$
(14)

Step 6: Determination of the benefit functions of $f(K_i)$ alternatives:

The benefit function is the compromise value of the alternative observed in relation to the ideal and anti-ideal solutions. Benefit functions of the alternatives are determined using Equation 15.

$$f(K_i) = \frac{K_i^+ + K_i^-}{1 + \frac{1 - f(K_i^+)}{f(K_i^+)} + \frac{1 - f(K_i^-)}{f(K_i^-)}} \quad (15)$$

Here, $f(K_i^+)$ shows the benefit function based on the ideal solution while $f(K_i^-)$ shows the one based on the anti-ideal solution. These functions are calculated using Equations 16 and 17.

$$f(K_i^-) = \frac{K_i^+}{K_i^+ + K_i^-} \quad (16-17)$$

$$f(K_i^+) = \frac{K_i^-}{K_i^+ + K_i^-}$$

Step 7: Ranking of the alternatives based on their benefit function values:

A ranking is made from the alternative with a high benefit function value to the alternative with a low benefit function value and ultimately, the best alternative is selected.

3. Results

3.1. Determination of criteria weights using the AHP technique

Wastewater-to-hydrogen production processes were evaluated by the decision-makers in terms of the main criteria of technological, cost and environmental/social and twenty-three sub-criteria (T_1 - T_{12} , C_1 - C_3 , and E_1 - E_8). As a result of the calculations, the local and global weight values were determined. In the local weight evaluation, the sub-criteria in each main criterion are weighted over 1 and in the global weight evaluation, all sub-criteria are weighted over 1. The weight ranking of the main criteria in descending order is technological (63.37%), cost (26.65%), and environmental/social (9.98%) (Table 4). High weight values indicate that a criterion is prioritized, in other words, of great importance in the evaluation of H_2 production processes. The most important reason why the technological criterion has the highest weight value is likely that it includes sub-criteria related to both H_2 production (purpose of the study) and treatment efficiency. When the local weight values are examined, it is observed that the top three most prioritized criteria are development (T_1 -23.81%), H_2 production rate (T_5 -17.32%) and treatment efficiency (T_4 -14.35%) from the technological main criterion, operating cost (C_2 -68.96%), investment cost (C_1 -23.77%) and

land cost (C₃-7.27%) from the cost main criterion, and risk level (E₈-33.61%), waste recycling potential (E₇-25.72%) and greenhouse gas formation (E₅-12.47%) from the environmental/social main criterion.

Table 4 Local and global weights of main- and sub-criteria based on AHP

| Main Criteria | Main Criteria Weights | Sub-Criteria | Local Weights | Global Weights | Ranking |
|----------------------|-----------------------|----------------------|---------------|----------------|----------|
| T | 0.6337 | <i>T₁</i> | 0.2381 | 0.1509 | 2 |
| | | T ₂ | 0.0553 | 0.0351 | 9 |
| | | T ₃ | 0.0145 | 0.0092 | 19 |
| | | T ₄ | 0.1435 | 0.0909 | 4 |
| | | <i>T₅</i> | 0.1732 | 0.1098 | 3 |
| | | T ₆ | 0.0494 | 0.0313 | 11 |
| | | T ₇ | 0.0158 | 0.0100 | 18 |
| | | T ₈ | 0.1087 | 0.0689 | 5 |
| | | T ₉ | 0.0733 | 0.0465 | 7 |
| | | T ₁₀ | 0.0310 | 0.0196 | 13 |
| | | T ₁₁ | 0.0265 | 0.0168 | 15 |
| | | T ₁₂ | 0.0708 | 0.0448 | 8 |
| | | C | 0.2665 | C ₁ | 0.2377 |
| <i>C₂</i> | 0.6896 | | | 0.1838 | 1 |
| C ₃ | 0.0727 | | | 0.0194 | 14 |
| E | 0.0998 | E ₁ | 0.0621 | 0.0062 | 20 |
| | | E ₂ | 0.0491 | 0.0049 | 21 |
| | | E ₃ | 0.0271 | 0.0027 | 23 |
| | | E ₄ | 0.1031 | 0.0103 | 17 |
| | | E ₅ | 0.1247 | 0.0124 | 16 |
| | | E ₆ | 0.0406 | 0.0040 | 22 |
| | | E ₇ | 0.2572 | 0.0257 | 12 |
| | | E ₈ | 0.3361 | 0.0335 | 10 |

The alternatives were evaluated through pairwise comparison in terms of all of the criteria. The wastewater-to-hydrogen processes were weighted with the MARCOS technique using the weights of the main- and sub-criteria determined with the AHP technique. Table 5 shows the

weight values obtained as a result of the MARCOS calculations. No major difference was observed between the alternative weight values. The priority order of the alternatives is DF>SCWG>MFC>PBR, respectively. The weight values of MFC and PBR were obtained very close to each other.

Table 5 Priority order of wastewater-to-hydrogen production processes based on MARCOS

| | S_i | K_i^- | K_i^+ | fK^- | fK^+ | fK_i | Ranking |
|-------------|--------|---------|---------|--------|--------|--------|---------|
| AAI | 0.6228 | 1 | - | - | - | - | |
| DF | 0.7266 | 1.1666 | 1.0082 | 0.4636 | 0.5364 | 0.7198 | 1 |
| PBR | 0.5704 | 0.9158 | 0.7914 | 0.4636 | 0.5364 | 0.5650 | 4 |
| SCWG | 0.6728 | 1.0802 | 0.9335 | 0.4636 | 0.5364 | 0.6665 | 2 |
| MFC | 0.5836 | 0.9370 | 0.8097 | 0.4636 | 0.5364 | 0.5781 | 3 |
| AI | 0.7207 | 1.1572 | 1 | | | | |

3.2. Sensitivity analysis

In order to determine the critical criterion/criteria, i.e., to observe the effects of the main criteria on the alternative ranking, a sensitivity analysis is performed (Wang et al., 2020). 4 scenarios were developed for the sensitivity analysis. These scenarios are as follows:

- Scenario 1: The main criteria weights obtained as a result of the calculation ($T=0.63$, $C=0.27$, $E=0.10$)
- Scenario 2: The technological criterion has the highest weight value while the weights of the other main criteria are equal ($T= 0.50$, $C=E=0.25$).
- Scenario 3: The cost criterion has the highest weight value while the weights of the other main criteria are equal ($C= 0.50$, $T=E=0.25$).
- Scenario 4: The environmental/social criterion has the highest weight value while the weights of the other main criteria are equal ($E= 0.50$, $T=C=0.25$).

Figure 2 shows the changes in the alternative ranking based on these scenarios.

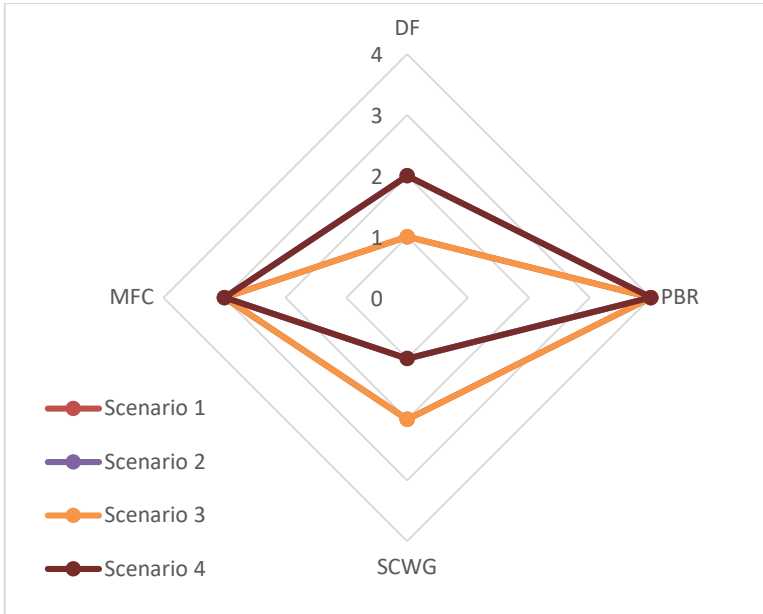


Fig. 2 Alternative ranking according to sensitivity analysis

In the sensitivity analysis, the ranking in Scenario 1 (calculated weights) and Scenario 3 ($C=0.50$, others are equal) was obtained as $DF > SCWG > MFC > PBR$ while the ranking in Scenario 2 ($T=0.50$, others are equal) and Scenario 4 ($E=0.50$, others are equal) was obtained as $SCWG > DF > MFC > PBR$. This means that in the scenarios, only the order of DF and SCWG changed. The fact that no significant change occurred in the ranking shows the reliability of the results (Dong et al., 2014). While DF is the alternative with the highest priority in terms of cost, SCWG is the most important alternative in terms of environmental/social criteria. The change in the ranking of DF and SCWG shows that cost in particular is an important criterion.

3.3. Comparison analysis

One of the most important disadvantages of MCDM methods is that the ranking may differ depending on the technique used. Due to this disadvantage, in the present study, a comparison analysis was performed using TOPSIS and CODAS techniques in addition to MARCOS. While DF was obtained as the top-priority alternative in all three techniques, certain changes occurred in the ranking of the other alternatives (Figure 3).

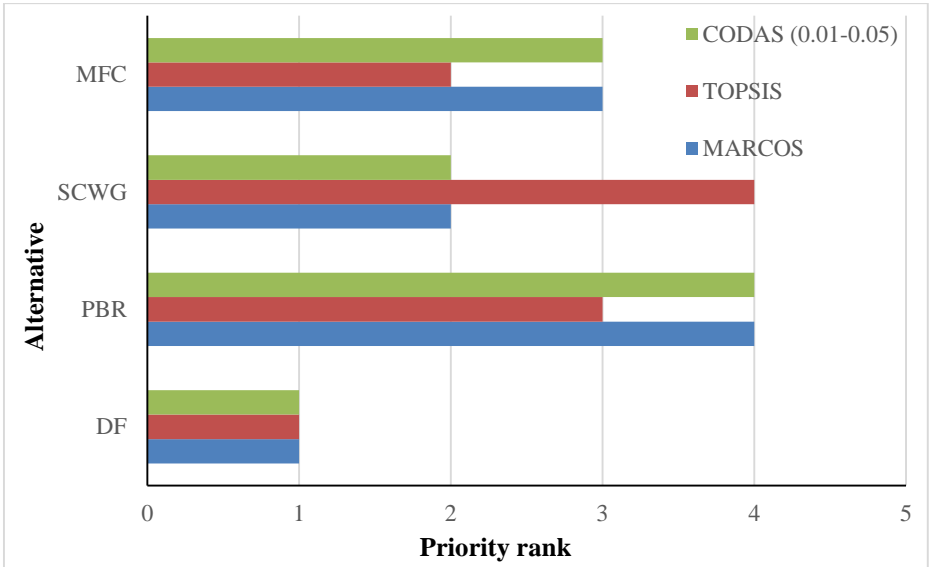


Fig. 3 Comparison analysis of wastewater-to-hydrogen production processes

4. Discussion

As a result of the calculation of the main technological, cost and environmental/social criteria used in technology selection (Tan et al., 2016; Zavadskas et al., 2017; Xu et al., 2019b; Ren and Ren, 2020; Qazi and Abushammala, 2020; Shahnazari et al., 2020), the weight of the technological criterion was obtained 2.4 times higher than the cost criterion and 6.4 times higher than the environmental/social criterion. When all of the sub-criteria are considered, it is observed that operating cost has the highest priority. The cost criterion was preferred as the top-priority criterion in some studies (Xu et al., 2019b; Ren and Ren, 2020) while others preferred the technological criterion (Acar et al., 2018). There are also studies where the environmental criterion was selected as the top-priority criterion (Shahnazari et al., 2020). Criteria such as environmental/social and political criteria are also important, however, it was concluded that there are more important criteria in technological and cost technology selection. The most important reasons behind the change in the priority of technological and cost criteria are the alternatives considered, other criteria, the sub-criteria determined for each main criterion and the difference in the opinions of the decision-makers.

DF is a near-developed technology and an alternative with high H₂ production, low risk and low cost. The most important disadvantages of DF are that the reaction time is long due to decomposition by microorganisms and that treatment efficiency is not high enough to meet discharge standards. SCWG, which generally had the second-highest priority in the calculations, has high H₂ production, short reaction time and meets discharge standards. The most important disadvantages of SCWG are that its operating conditions are extreme (high temperature, high pressure), high risk level, and the presence of operational problems (mainly clogging and corrosion). The most important disadvantages of MFC, which generally had the third-highest priority in the calculations, are that its reaction time is long and operating cost is high. Uctug and Fahrioglu (2018) reported that MFC is generally ideal for small-scale applications.

The most important advantage of PBR, which ranks last in terms of priority, is that it enables the reduction of global warming through CO₂ fixation from industrial emissions (cement, coal, etc.) (Xu et al., 2019a). Additionally, the fact that microalgae grow in different aquatic environments (salt, fresh, brackish and wastewater) and have the ability of rapid growth (a few days), and that it is a significantly developed technology can be listed as other advantages (Xu et al., 2019a). The possible reasons behind the fact that PBR was not determined as the top-priority technology in the present study are low H₂ production algae biomass harvest constituting 20-30% of the cost, and low treatment efficiency (Tan et al., 2016, Xu et al., 2019a). In PBR, wastewater treatment is carried out by the use of pollutants in wastewater (nitrogen, phosphorus, certain heavy metals, inorganics and organics) as nutrients (Mohseni et al., 2016). If the nutrients are not sufficient, necessary nutrients are provided for the algae with materials such as synthetic fertilizers (Anggraini et al., 2018).

With AHP, which is one of the most widely-used MCDM techniques, various H₂ production processes (natural gas reforming, coal gasification, biomass gasification, water electrolysis, thermochemical production-solar, nuclear, H₂O, heat-, photo-electrochemical, biological production-photolysis, dark fermentation, photosynthetic bacterial, microbial, electrolysis cell) were evaluated for the years 2012 and 2040 based on four criteria. Natural gas reforming and water electrolysis were determined as prioritized alternatives for the years 2012 and 2040, respectively. In terms of efficiency, natural gas reforming (65-80%), dark fermentation (60-80%), microbial

electrolysis cell/microbial fuel cell (78%) and water electrolysis (30-70%) were determined as the top-priority alternatives. At the same time, among the methods that provide wastewater treatment (DF and MFC), DF was determined as having a higher priority (Chung et al., 2014). Liu et al. (2020) evaluated alternatives of energy production in treatment sludge (incineration, fuel cells, gas engine and microbial fuel cells) using the Dempster-Shafer and fuzzy best-worst methods. As a result of the calculation, incineration was determined as the alternative with the highest priority while MFC had the lowest priority. Nevertheless, it was stated that MFC is a technology that can promote sustainable development for wastewater treatment and electricity production in the future (Liu et al., 2020).

Current treatment systems are not sustainable as they consume high amounts of energy and emit greenhouse gas. Wastewater treatment facilities account for approximately 3-5% of the global energy consumption. In current treatment facilities, energy demand will increase as the infrastructure ages and discharge standards get stricter (Nguyen et al., 2020). For this reason, producing energy while treating wastewater with organic and water content should be determined as a new target. This way, a sustainable form of wastewater management can be established. In other words, producing H₂ from wastewater minimizes the consumption of fossil-based fuels, reduces energy costs and minimizes climate change.

Selecting the most suitable alternative among many options based on various criteria is a difficult process due to the presence of a large number of verbal judgments that include great subjectivity and uncertainty. MCDM techniques are used to facilitate technology selection. Prioritization of different alternatives based on various criteria using MCDM techniques may guide researchers, decision-makers in wastewater treatment sectors, politicians, etc. (Padron-Paez et al., 2020). Wastewater treatment process selection should not be carried out merely in terms of efficiency and cost. These two criteria are very important, however, considering different criteria optimizes the decision.

The results obtained from the present study indicate that further research and development efforts are necessary to develop the DF and SCWG technologies on a full scale and minimize their disadvantages.

5. Conclusion

In the present study, the selection of potential alternatives that can be used for wastewater-to-hydrogen production (microbial fuel cells, dark fermentation, supercritical water gasification, photobioreactors) was carried out based on technological, cost and environmental/social criteria. The AHP, MARCOS, TOPSIS and CODAS techniques were used for the decision-making process. A sensitivity analysis was performed to observe the effects of the criteria.

As a result, with the AHP technique, the top-priority main criterion was determined as technological while the top-priority sub-criteria were determined as operating cost, development and H₂ production rate. As a result of the MARCOS, TOPSIS and CODAS calculations, DF and SCWG were preferred as the top-priority alternatives. As a consequence of the sensitivity analysis, it was determined that the technological and cost criteria were significant in technology selection. DF is economical and has a high H₂ production rate. However, it is necessary to reduce its reaction time in order to meet discharge standards and improve treatment efficiency. In SCWG, on the other hand, it is necessary to reduce the operating costs and risk level. Further research is needed to minimize these disadvantages.

Future studies can be conducted to observe the effects of different MCDM techniques, main- and sub-criteria on the selection of wastewater-to-hydrogen production technologies.

References

- Abdullah, L., Zulkifli, N., Liao, H., Herrera-Viedma, E., Al-Barakati, A., (2019), An interval-valued intuitionistic fuzzy DEMATEL method combined with Choquet integral for sustainable solid waste management, *Engineering Applications of Artificial Intelligence*, 82, 207-215.
- Acar, C., Beskese, A., Temur, G.T., (2018), Sustainability analysis of different hydrogen production options using hesitant fuzzy AHP, *International Journal of Hydrogen Energy*, 43(39), 18059-18076.
- Adar, E., (2018), Supercritical Gasification of Wastewater Treatment Plant Sludge for Energy Production, Dissertation, Yildiz Technical University, Istanbul, Turkey.

- Adar, T., Delice, E.K., (2019), New integrated approaches based on MC-HFLTS for healthcare waste treatment technology selection, *Journal of Enterprise Information Management*, 32(4), 688-711. <https://doi.org/10.1108/JEIM-10-2018-0235>
- Afif, E., Azadi, P., Farnood, R., (2011), Catalytic hydrothermal gasification of activated sludge, *Applied Catalysis B: Environmental*, 105, 136-143.
- Angraini, R.C.P.K., Sasongko, N.A., Kuntjoro, Y.D., (2018), Preliminary study on the location selection of microalgae cultivation in Nusa Tenggara region as a potential feedstock for bioavtur, *In E3S Web of Conferences*, EDP Sciences.
- Babazadeh, R., Khalili, M., Toloo, M., (2020), A data envelopment analysis method for location optimization of microalgae cultivation: A case study, *Waste and Biomass Valorization*, 11(1), 173-186.
- Barca, C., Soric, A., Ranava, D., Giudici-Ortoni, M.T., Ferrasse, J.H., (2015), Anaerobic biofilm reactors for dark fermentative hydrogen production from wastewater: A review, *Bioresource Technology*, 185, 386-398.
- Bottero, M., Comino, E., Riggio, V., (2011), Application of the analytic hierarchy process and the analytic network process for the assessment of different wastewater treatment systems, *Environmental Modelling & Software*, 26(10), 1211-1224. <https://doi.org/10.1016/j.envsoft.2011.04.002>
- Cetinkaya, A., (2017), Treatment of Industrial Wastewaters by Low-Cost and High-Efficiency Microbial Fuel Cell and Electricity Energy Production, Dissertation, Yildiz Technical University, Istanbul, Turkey.
- Chakinala, A.G., (2013), Supercritical Water Gasification of Biomass: An Experimental Study of Model Compounds and Potential Biomass Feeds, Dissertation, Twente University, Netherlands.
- Chung, Y., Hong, S., Kim, J., (2014), Which of the technologies for producing hydrogen is the most prospective in Korea?: Evaluating the competitive priority of those in near-, mid-, and long-term, *Energy Policy*, 65, 115-125.

- Dagdeviren, M., Yavuz, S., Kilinc, N., (2009), Weapon selection using the AHP and TOPSIS methods under fuzzy environment, *Expert Systems with Applications*, 36(4), 8143-8151. <https://doi.org/10.1016/j.eswa.2008.10.016>.
- Debnath, A., Majumder, M., Pal, M., (2016), Potential of fuzzy-ELECTRE MCDM in evaluation of cyanobacterial toxins removal methods, *Arabian Journal for Science and Engineering*, 41(10), 3931-3944. <https://doi.org/10.1007/s13369-016-2032-7>
- Dong, J., Chi, Y., Zou, D., Fu, C., Huang, Q., Ni, M., (2014), Energy–environment–economy assessment of waste management systems from a life cycle perspective: Model development and case study, *Applied Energy*, 114, 400-408. <https://doi.org/10.1016/j.apenergy.2013.09.037>
- Elcik, H., (2016), Application of Membrane Processes in Microalgae Harvesting and Optimisation of Operational Conditions, Dissertation, Yildiz Technical University, Istanbul, Turkey.
- Goulart-Coelho, L.M., Lange, L.C., Coelho, H.M., (2017), Multi-criteria decision making to support waste management: A critical review of current practices and methods, *Waste Management & Research*, 35(1), 3-28.
- He, Y.J., Ma, Z.F., (2013), Robust optimal operation of two-chamber microbial fuel cell system under uncertainty: A stochastic simulation based multi-objective genetic algorithm approach, *Fuel Cells*, 13(3), 321-335.
- Hou, D., Lu, L., Ren, Z.J., (2016), Microbial fuel cells and osmotic membrane bioreactors have mutual benefits for wastewater treatment and energy production, *Water Research*, 98, 183-189.
- Ilangkumaran, M., Sasirekha, V., Anojkumar, L., Sakthivel, G., Raja, M.B., Raj, T.R.S. ... ,Kumar, S.P., (2013), Optimization of wastewater treatment technology selection using hybrid MCDM, *Management of Environmental Quality: An International Journal*, 24 (5), 619-641.
- Isiklar, G., Buyukozkan, G., (2007), Using a multi-criteria decision making approach to evaluate mobile phone alternatives, *Computer Standards & Interfaces*, 29(2), 265-274. <https://doi.org/10.1016/j.csi.2006.05.002>

- Koroglu, E., (2019), Hydrogen Production and Evaluation Using Biological Processes from Food Industry Wastewater, Dissertation, Yildiz Technical University, Istanbul, Turkey.
- Kruse, A., Henningsen, T., Sinag, A., Pfeiffer, J., (2003), Biomass gasification in supercritical water: Influence of the dry matter content and the formation of phenols, *Industrial & Engineering Chemistry Research*, 42, 3711-3717.
- Lim, J.Y., How, B.S., Rhee, G., Hwangbo, S., Yoo, C.K., (2020), Transitioning of localized renewable energy system towards sustainable hydrogen development planning: P-graph approach, *Applied Energy*, 263, 114635.
- Liu, Y., Ren, J., Man, Y., Lin, R., Lee, C.K., Ji, P., (2020), Prioritization of sludge-to-energy technologies under multi-data condition based on multi-criteria decision-making analysis, *Journal of Cleaner Production*, 273, 123082.
- Mohseni, S., Pishvae, M.S., Sahebi, H., (2016), Robust design and planning of microalgae biomass-to-biodiesel supply chain: A case study in Iran, *Energy*, 111, 736-755.
- Nguyen, H.T., Safder, U., Nguyen, X.N., Yoo, C., (2020), Multi-objective decision-making and optimal sizing of a hybrid renewable energy system to meet the dynamic energy demands of a wastewater treatment plant, *Energy*, 191, 116570.
- Onaran, G., (2016), Hydrogen Production from Waste Paper Towel by Dark Fermentation, Dissertation, Pamukkale University, Denizli, Turkey.
- Oncel, S.S., (2009), Biohydrogen Production and Usage in Fuel Cells, Dissertation, Ege University, Izmir, Turkey.
- Padrón-Páez, J.I., Almaraz, S.D.L., Román-Martínez, A., (2020), Sustainable wastewater treatment plants design through multiobjective optimization, *Computers & Chemical Engineering*, 140, 106850.
- Qazi, W.A., Abushammala, M.F., (2020), Multi-Criteria Decision Analysis of Waste-to-Energy Technologies, In *Waste-to-Energy*, Academic Press, 265-316.

- Rajak, M., Shaw, K., (2019), Evaluation and selection of mobile health (mHealth) applications using AHP and fuzzy TOPSIS, *Technology in Society*, 59, 101186. <https://doi.org/10.1016/j.techsoc.2019.101186>.
- Ren, J., Ren, X., (2020), Sustainability Prioritization of Sludge-to-Energy Technologies Based on An Improved DS/AHP Method, In *Waste-to-Energy*, Academic Press, 317-343.
- Ren, J., Fedele, A., Mason, M., Manzardo, A., Scipioni, A., (2013), Fuzzy multi-actor multi-criteria decision making for sustainability assessment of biomass-based technologies for hydrogen production, *International Journal of Hydrogen Energy*, 38(22), 9111-9120.
- Saaty, T.L., Tran, L.T., (2007), On the invalidity of fuzzifying numerical judgments in the Analytic Hierarchy Process, *Mathematical and Computer Modelling*, 46(7-8), 962-975.
- Saaty, T.L., (1980), *The Analytic Hierarchy Process*, New York McGraw-Hill.
- Sabankay, M., (2012), Scale-up for Biohydrogen Production in Photobioreactors, Dissertation, Ege University, Izmir, Turkey.
- Shahnazari, A., Rafiee, M., Rohani, A., Nagar, B.B., Ebrahimini, M.A., Aghkhani, M.H., (2020), Identification of effective factors to select energy recovery technologies from municipal solid waste using multi-criteria decision making (MCDM): A review of thermochemical technologies, *Sustainable Energy Technologies and Assessments*, 40, 100737.
- Slate, A.J., Whitehead, K.A., Brownson, D.A., Banks, C.E., (2019), Microbial fuel cells: An overview of current technology, *Renewable and Sustainable Energy Reviews*, 101, 60-81.
- Stević, Ž., Brković, N., (2020), A novel integrated FUCOM-MARCOS model for evaluation of human resources in a transport company, *Logistics*, 4(1), 4.
- Stević, Ž., Pamučar, D., Puška, A., Chatterjee, P., (2020), Sustainable supplier selection in healthcare industries using a new MCDM method: Measurement of alternatives and ranking according to Compromise solution (MARCOS), *Computers & Industrial Engineering*, 140, 106231.

- Tan, J., Low, K.Y., Sulaiman, N.M.N., Tan, R.R., Promentilla, M.A.B., (2016), Fuzzy analytic hierarchy process (FAHP) for multi-criteria selection of microalgae harvesting and drying processes, *Clean Technologies and Environmental Policy*, 18(7), 2049-2063.
- Trapero, J.R., Horcajada, L., Linares, J.J., Lobato, J., (2017), Is microbial fuel cell technology ready? An economic answer towards industrial commercialization, *Applied Energy*, 185, 698-707.
- Uctug, F.G., Fahrioglu, M., (2018), Multi-criteria decision making-based comparison of fuel cell types for distributed generation applications, *16th International Conference on Clean Energy (ICCE)*, Famagusta, N. Cyprus, <https://icce2018.emu.edu.tr/>
- Wang, J.J., Yang, D.L., (2007), Using a hybrid multi-criteria decision aid method for information systems outsourcing, *Computers & Operations Research*, 34(12), 3691-3700.
- Wang, Y., Xu, L., Solangi, Y.A., (2020), Strategic renewable energy resources selection for Pakistan: Based on SWOT-Fuzzy AHP approach, *Sustainable Cities and Society*, 52, 101861. <https://doi.org/10.1016/j.scs.2019.101861>.
- Xu, D., Wang, S., Huang, C., Tang, X., Guo, Y., (2014), Transpiring wall reactor in supercritical water oxidation, *Chemical Engineering Research and Design*, 92, 2626-2639.
- Xu, L., Wang, Y., Shah, S.A.A., Zameer, H., Solangi, Y.A., Walasai, G.D., Siyal, Z.A., (2019a), Economic viability and environmental efficiency analysis of hydrogen production processes for the decarbonization of energy systems, *Processes*, 7(8), 494.
- Xu, L., Shah, S.A.A., Zameer, H., Solangi, Y.A., (2019b), Evaluating renewable energy sources for implementing the hydrogen economy in Pakistan: A two-stage fuzzy MCDM approach, *Environmental Science and Pollution Research*, 26(32), 33202-33215.
- Yao, L., Xu, Z., Lv, C., Hashim, M., (2020), Incomplete interval type-2 fuzzy preference relations based on a multi-criteria group decision-making model for the evaluation of wastewater

treatment technologies, *Measurement*, 151, 107137.
<https://doi.org/10.1016/j.measurement.2019.107137>

Yoshida, Y., Dowaki, K., Matsumura, Y., Matsuhashi, R., Li, D., Ishitani, H., Komiyama, H., (2003), Comprehensive comparison of efficiency and CO₂ emissions between biomass energy conversion technologies—position of supercritical water gasification in biomass technologies, *Biomass and Bioenergy*, 25, 257-272.

Zavadskas, E.K., Cavallaro, F., Podvezko, V., Ubarte, I., Kaklauskas, A., (2017), MCDM assessment of a healthy and safe built environment according to sustainable development principles: A practical neighborhood approach in Vilnius, *Sustainability*, 9(5), 702.

Zavadskas, E.K., Kaklauskas, A., Kalibatas, D., Turskis, Z., Krutinis, M., Bartkienė, L., (2018), Applying the TOPSIS-F method to assess air pollution in Vilnius, *Environmental Engineering & Management Journal*, 17 (9), 2041-2050.

CHAPTER IV

CHARACTERIZATION OF PERLITE AND EXPANDED PERLITE-BASED GEOPOLYMERS WITH DIFFERENT ANALYSIS TECHNIQUES

Assoc. Prof. Dr. Ceyda BİLGİÇ

Eskişehir Osmangazi University, Eskişehir, Turkey
e-mail: cbilgic@ogu.edu.tr, Orcid No: 0000-0002-9572-3863

Asst. Prof. Dr. Şafak BİLGİÇ

Eskişehir Osmangazi University, Eskişehir, Turkey
e-mail: safakb@ogu.edu.tr, Orcid No: 0000-0002-9336-7762

1. Introduction

Living necessities, global megatrends, environmental limitations, together with humanistic concerns, have jointly promoted researchers to develop carbon neutrality technologies to satisfy humans' energy and environment requirements nowadays. According to the reports from the International Energy Agency, buildings are responsible for over 1/3 of global final energy consumption and nearly 40% of total direct and indirect CO₂ emissions. Therefore, developing building energy conservation technology is critical to carbon neutrality (Xu et al., 2017:91). China also has taken a series of measures to cut down energy consumption and declared to strive for "Peak carbon dioxide emissions" in 2030 and "Carbon neutrality" in 2060 (Gong et al., 2021). Above all, thermal insulation materials play a vital role in energy saving for buildings (Li and Shui, 2015:326). Using thermal insulation materials, including organic (expanded polystyrene, extruded polystyrene, polyurethane, etc.) and inorganic type (glass wool, rock wool, expanded perlite, etc.), is the most effective way for building energy saving at present (Kumar et al., 2020:1) Organic thermal insulation materials have low thermal conductivity, but they are very easy to burn and release harmful smoke (Wi et al., 2021:1). Traditional inorganic thermal insulation materials are incombustible, but their thermal conductivity is relatively high and their fabrication is high in energy consumption (Abu-Jdayil et al., 2019:709). Therefore, it is of great necessity to develop new inorganic thermal insulation materials with low-cost and energy-saving methods.

Perlite is derived from volcanic sources and after size reduction and heating to render it porous via the escape of water, it is used as a water-absorbent in agricultural applications. Waste perlite arises in the manufacturing process as unwanted particle size ranges or material that has not become adequately porous. Perlite is X-ray amorphous and has the basic composition of around 80 wt% SiO₂, 15 wt% Al₂O₃, and a few wt% of alkali. As a candidate reactive waste aluminosilicate, we have explored the possible use of this material as a useful constituent of geopolymers for construction material or immobilization of hazardous/radioactive waste. Work has been carried out on the addition of waste perlite to Portland cement, but the perlite imparted only a minor contribution to the strength (Davidovits, 2005:9).

Perlite is an amorphous aluminosilicate volcanic glass taht, upon rapid controlled heating, expands into a foam material of low bulk density. Perlite deposits are normally exploited using low-cost open-pit mining methods followed by in-situ milling and screening. Greece and Turkey are the world's leading perlite producers, with annual production in 2015 of 700,000 tons and 1,100,000 tons, respectively, while in Europe the annual production of perlite was estimated at about 1,935,000 tons in 2015 (Gambogi, 2016).

Porous geopolymers can be applied as prospective inorganic thermal insulation materials, which are mainly composed of corner-sharing [AlO₄] and [SiO₄] tetrahedron networks. They are considered as green building materials, owing to their low cost, green process in production and excellent fire-proof ability (Farhan et al., 2020). Porous geopolymers are usually prepared through alkali-activated reaction and chemical and/or physical foaming, with aluminosilicates (fly ash, kaolinite, waste glass, etc.) as the main raw material (Bai and Colombo, 2018:16103). Perlite mainly composed of SiO₂, Al₂O₃, Na₂O, K₂O, and H₂O is a kind of important no-metallic ore resource, which can be used for producing expanded perlite mineral materials. On the one hand, the expanded perlite as lightweight aggregate plays an important role in thermal insulation (Pasupathy et al., 2020:120713; Pasupathy et al., 2021:121850; Pichor et al., 2019:1; Ramakrishnan et al., 2021:102756.). On the other hand, the expanded perlite industry will bring a great deal of perlite tailings or thin powders that can't be produced for expanded perlite. Therefore, many researchers have suggested that perlite could serve as aluminosilicates in geopolymer or porous geopolymer production (Erdoğan, 2015:1; Vaou and Panias, 2010:1146).

Civil engineers and architects frequently use the word “sustainability” to characterize various activities’ positive and negative effects on the

Planet, just like in many other fields. When it comes to civil engineering materials, apart from indispensable service performance, their adverse impacts imposed on the ecosystem should be minimized (Wiyono and Hardjito, 2015:747; Temuujin et al., 2011:1399). Geopolymer cements are defined as sustainable materials due to reduced pollution, money-saving and eco-friendliness, as well as outstanding performance as outlined earlier. The sustainability of geopolymer cement is intensively related to their constituent materials and manufacture. Geopolymer cement can be synthesized by reusing and recycling solid wastes and industrial byproducts such as fly ash, slag and tailings (Lv et al., 2019:441). The preparation of geopolymer cement relies on the alkali-activation and the subsequent polycondensation without any extra inputs (Duxson et al., 2007:1590; Balaguru et al., 2008). Furthermore, geopolymer cements' durability could be greatly extended by means of the strong spatial molecular structure in terms of stable $\text{SiO}_4\text{-AlO}_4$ tetrahedron unit as well as the formed 3D networks (Duan et al., 2015:125; Rickard et al., 2016:33). Because its microstructure is finer and the gel structure is stronger than that of other materials, geopolymer cement possesses excellent durability (Wang et al., 2019:1; Duan et al., 2015:125; Rickard et al., 2016:33). In a word, the improved long-term performance and reduced environmental impacts make geopolymer cement a class of admirable construction materials for future buildings and other structures.

Geopolymer cements have been utilized as a protective enclosure for concrete structures (Zhang et al., 2010:7; Balaguru et al., 2008; Zhang et al., 2010:7; Zhang et al., 2012:57), transportation infrastructures (Papakonstantinou and Balaguru, 2007:3; Balaguru, 2002), steel and other metal structures (Janaki and Selvaraj, 2017:13; Ma and Ye, 2015:82; Ma et al., 2012:4568; Davidovits, 1994:91), wood structures and products (Papakonstantinou and Balaguru, 2007:3; Wang et al., 2019:1; Davidovits, 2008:145; Salwa et al., 2013:246), as well as decorative surface layers of buildings and other structures (Pan et al., 2017:578; Zhang et al., 2010:7). As far as concrete structures are concerned, the direct application of geopolymer cement is sealing the exposed surface of the concrete. An alternative usage is preventing the reinforcing bar from corrosion. Kriven et al., painted the surfaces of steel bars with metakaolin-based geopolymer cements (Kriven et al., 2008:373). The steel bars were embedded in mortar prism specimens. After a period of curing, the specimens were subjected to accelerated corrosion immersed in a 3.5% NaCl solution. The results indicated that the geopolymer cements improved anti-corrosion of the reinforcing bars. Incidentally, Rostami et al., brushed fly ash-based geopolymer cements

on steel bars buried in a concrete prism and found that the corrosive rate of the steel was significantly reduced (Rostami et al., 2015:136).

2. Pretreatments applied to prepare the perlite and expanded perlite geopolymer cement

In order to prepare the geopolymer cement product with a fair surface protection function, the synergy of powder precursor together with alkali-activator requires to be fully taken into account. Some precursors perform more efficiently with a specific class of activators than others in the difference in oxide compositions and kinetics of chemistry. For instance, in contrast with other activators, the ground granulated blast-furnace slag precursor can be fully activated by Na_2SiO_3 solution, provided that the mixture proportion is properly designed (Cheah et al., 2019:558).

The applications of geopolymer-based materials are determined by their molecule structures in terms of the atomic (or molar) ratio of Si and Al in the formed polysialate (Wang et al., 2019:1). A relatively low Si to Al molar ratio is favorable to most of applications in the construction engineering field (Phoo-ngernkham et al., 2015:1). Therefore, a proper overall Si/Al ratio must be considered and determined in the mixture proportioning of geopolymer cements. On the other hand, due to water glass is often cheaper than NaOH and the precursors are comparably cheaper than the alkaline compounds, economical cost should be emphasized in formulating and proportioning geopolymer cements (Wang et al., 2019:1; Hu et al., 2008:239; Li et al., 2019:34). In addition, keeping an eye on environmental impacts is also essential. A series of basic information of mixture formulations of geopolymer cements was reported in previous publications.

It was concluded that the mass ratio of Na_2SiO_3 solution to NaOH solution (SS/SH) performed a remarkable effect on geopolymer cements' properties. Nevertheless, different authors (Hadi et al., 2019:301; Biondi et al., 2019:1; Fernández-Jiménez and Palomo, 2005:1984), proposed different optimum SS/SH ratios, which may result from varying compositions of the alkali-activator and the precursor used in their research, as well as different mass ratios of both components. As an alternative, the SS/SH ratio of the activator solution can also be expressed by the total molar ratio of $\text{SiO}_2/\text{Na}_2\text{O}$, i.e., overall modulus other than the modulus of commercially available water glass to be used. It is should be noticed that these studies exploring the optimized mixture proportion of geopolymer cements were based on the strength properties alone (Habert et al., 2011:1229; Duan et al., 2016:115; Hassan et al., 2019:704; Chindaprasirt et al., 2018:1; Nath and Sarker, 2014:163; Morsy et al., 2014:4333). However, the properties of a fresh mixture such as setting

behavior and workability must also be considered to make sure that it can work on site properly.

Ohno and Li (Ohno and Li, 2018:73) proposed a new mixture design method of engineered geopolymer composites that combine three correlative approaches, i.e., design of experiment, micro-mechanical modeling, and material sustainability indices. The mixture design of an initial version of geopolymer was optimized to achieve improved mechanical properties and durability, and enhance the sustainability of material concurrently. The authors believe that the integrated methodology can also be applied to the mixture proportioning of geopolymer cements by some modifications. In shorts, the mixture design of geopolymer cements, basically consists of three dependent parts, i.e., the precursor components, the activator components as well as the additives and/or fillers. All the procedures of geopolymer cements mixture proportioning are intensively related to their performance and practical applications.

The preparation of geopolymer cements often consists of four steps. The first step is formulating and preparing activator solutions (Elyamany et al., 2018:974). Specific alkaline compounds were blended and dissolved in mixing water to compound the alkali-activator with the prescribed molarity. The desired molarity of NaOH/KOH can vary in the range of 8-16 mol/L (Ng et al., 2018:550; Pacheco-Torgal et al., 2008:1939). However, 8 mol/L is adequate for most of the potential applications (Janaki et al., 2017:13). The activator solution was often required to cool down and stabilize for at least 24 h before further mixing with precursors (or binders) (Zhang et al., 2010:6; Lv et al., 2019:441; Alanazi et al., 2016:75; Kupaei et al., 2013:490; Ma et al., 2019:188), though there exist exceptions to this rule: the precursor is added to the prepared solution immediately after the dissolution of alkaline compounds (Ma et al., 2019:188). Secondly, the precursor powders, including possible fine aggregates and solid additives and/or fillers, are fully mixed to ensure uniformity using a mechanical mixer. In the third step, the formulated alkaline solution is fully mixed with various liquid chemical additives (e.g., superplasticizer, water reducing agent and retarder). At this point, the liquid and solid components of two-part geopolymer cements are prepared. Finally, the solid part is added to the liquid one and then the stirring process is conducted to obtain the fresh geopolymer cement mixture. In the above-mentioned procedures, the mixers used and mixing times are different from one author to another (Balaguru, 2002; Phoo-ngernkham et al., 2015:482; Kumar et al., 2012:511; Hu et al., 2008:239).

In order to simplify the preparation and ease of use, Ma et al., proposed single-component geopolymer cement analogous to common Portland cement by just adding the prescribed mixing water (Ma et al., 2019:188). In other words, the precursors and solid activators are ready-mixed to form the one-part powder geopolymer cements. When the geopolymer cements are used, the precursor parts can be activated by the activators with the help of a quantity of water. This would mean that frequent operation and usage of harmful and corrosive alkaline solutions in sites can be avoided.

On the curing regime of geopolymer cements, it is known that the geopolymerization at ambient temperature is slow. Higher temperature around 40 to 75 °C is beneficial to the evolution of reaction products (Aliabdo et al., 2016:694). The heat curing process is, however, often impossible to achieve in coating applications (Hadi et al., 2019:301). The use of geopolymer cements cured at ambient temperature and stored in harsh conditions is a challenging task. The geopolymer cement, that can take effects at ambient conditions are desirable specifications. (Hadi et al., 2019:301; Aliabdo et al., 2016:694).

According to Zhang et al., apart from all the above reviewed basic properties, specific properties for geopolymer cements potentially applied in marine structures are required as follows: (a) low water permeability, (b) high anti-corrosion and (c) good volume stability. (Zhang et al., 2010:1). In a Chinese technical specification on anti-corrosive coatings for concrete bridge structure, a set of systematic indicators evaluating the properties and performance of protective coatings was set up. The indicators mainly include water/saline water resistance, alkaline resistance, resistance to corrosive chemicals, chloride ion penetration resistance, adhesive strength and weatherability in terms of exposed environment and design lifetime. Resistances to thermal cycle, freeze-thaw cycle, humidity and UV radiation is of great importance in steel structure applications of geopolymer cements (Jiang et al., 2020:1). Therefore, as a relatively new member in the family of protective coatings, the specific properties of geopolymer cements have to comply with the relevant mandatory standards and technical specifications in terms of practical applications. It is essential that we develop exclusive technical provisions of geopolymer cements other than referring to other standards and specifications.

Geopolymer-based materials along with geopolymer cement possess intrinsic and excellent fire/thermal/elevated temperature resistance. They possess attributes of inorganic materials and are not inclined to burn as most of organic polymers. They are non-combustible, non-toxic, and

require only a lower manufacturing temperature other than commonly-used ceramic materials (Lahoti et al., 2019:514). According to building standards, the duration of fire resistance of geopolymer cement is adequate (Ding et al., 2019:611). Desirable fire resistance and resistance to chemical corrosion lead to geopolymer cement a typical of ideal coating materials used in steel and wood structures, especially in outdoor and severe conditions (Aguirre-Guerrero et al., 2017:437; Kaloari and Haris, 2016:79; Shill et al., 2020: 117886).

Surface abrasion resistance is one of the vital indicators to characterize the performance of geopolymer cement under repetitive traffic loadings. Lau et al., suggested that the pure fly ash-based geopolymer cement with a liquid/solid ratio of 0.60 provides the utmost abrasion resistance in all nine mixtures with four variables. (Lau et al., 2019:635). Yan et al., indicated that sepiolite can enhance the resistance to abrasion (Yan, et al., 2017:1052).

Due to water is a prerequisite for various deteriorations and damages of civil structures, waterproofness is of great importance to the coating materials, and geopolymer cements are no exception (Aguirre-Guerrero et al., 2017:437; Liang et al., 2019:603; Zhu et al., 2019:394). The waterproofness of geopolymer cement can not only be enhanced from microstructure densification and pore refinement, but also from surface modification. For example, Duan et al., developed a novel geopolymer with a hydrophobic surface by the addition of low-cost fatty acid as a modifier. (Duan et al., 2016:172). The contact angle of the geopolymer paste increased from 36° of the control mixture to 132° of the modified one. However, limited data related to the waterproofness of geopolymer cement can be collected, systematic studies are strongly required.

Besides, the efflorescence is also a severe issue to geopolymer cement, particularly applied in drying and wetting cycle conditions, however, with relatively little attention. This is associated with this type of novel materials that are still being researched in laboratories. The malady not only affects the aesthetics of the geopolymer cement layer but also undermines their performance seriously (Wang et al., 2020: 118852). Efflorescence of geopolymer cement is the result of incomplete consumption of alkali-activator that results in the formation of sodium carbonate (Na_2CO_3) in the pores of bulk geopolymer or on the surface of thin geopolymer cement layer (Xue et al., 2018 :43). This can also be ascribed to the presence of water which weakens the bond of Na in geopolymer cement (Hou et al., 2009:711).

3. The morphology and microstructure variations

3.1. Chemical composition

The chemical composition of the sample is analyzed by X-ray fluorescence spectrometry (XRF). The results of X-ray fluorescence analysis of perlite heated in air at 1000°C for 3 hours are as follows: (elemental wt%; rest oxygen): Na (1.9); Mg(0.3); Al (6.9); Si (33.6); S(1,1); K(5,1); Ca(0.9); Fe(1.0). Elements having abundances of < 0.1% were ignored. From the chemical composition of the perlite, it has been seen that the Na, Al and Ca contents are different, higher Na content and lower Al, Ca and Mg contents are harmful to the long-term stability of the porous perlite geopolymer. In addition, it was observed that the aging process performed in the production of geopolymers did not make an obvious variation in the chemical composition (Erdoğan, 2015:1).

Fourier transform infrared (FTIR) spectroscopy measurements were carried out in the 500-4000 cm^{-1} spectral region by mixing 10% of the KBr amount with the sample. FTIR spectra of calcined perlite prepared by heating at 300 °C and 1000 °C; it shows an enlargement of the spectra from the region between 4000 and 1000 cm^{-1} . The region 500 cm^{-1} to 1500 cm^{-1} is characterized by the presence of the main absorption structures, an intense band at about 1030 cm^{-1} with a second intense peak at about 1135 cm^{-1} . These two peaks are respectively attributed to Si–O–Si and Si–O–R asymmetric stretching where R can be Al or Si. A further group of three peaks of medium intensity is present at lower wavelengths: (787 cm^{-1}), (730 cm^{-1}) and (575 cm^{-1}). This group remains unaltered in shape, position and intensity with the annealing. Peaks are attributed to symmetric stretching of Si–O–Si (787 cm^{-1}), the peak of bending of Si–O–Al (730 cm^{-1}), and the peak of symmetrical stretching of Si–O–R (575 cm^{-1}).

The change of intense peaks at 1000-1200 cm^{-1} with increasing calcination temperature is an interesting feature. This is due to the rearrangement of Si–O–R, as the interstitial water is progressively evolved, with the annealing producing a better ordering of the chains. It may also be caused by changes associated with the decreasing amorphous silica fraction as the calcination temperature increases. The main fused silica IR peak (with the fusion of the intense peak at 1030 cm^{-1} and a second intense peak at 1135 cm^{-1}) is expected to be at 1126 cm^{-1} (Sakkas et al., 2015:259).

Al–OH and Si–OH bending and stretching bands, expected in the range 955- 830 cm^{-1} , are not observed. A decrease of the shoulder at 915 cm^{-1} with the increase of the annealing temperature should be expected

with the formation of Al–OH and Si–OH groups (Sakkas et al., 2015:259). This confirms an increase of the ordering with the annealing temperature, imparting strength to the Si–O in-plane vibrations. (Sakkas et al., 2014:148). The composite peak is not affected by the annealing and could be tentatively attributed to Si–H and Al–H stretching bands.

The FT-IR spectra obtained during the aging of perlite-based geopolymers show that there are almost no obvious differences in geopolymers before aging. The broadband at 3432 cm^{-1} is assigned to the O–H stretching vibrations of Si–OH and water (Hooshmand et al., 2004:635). The band at 1638 cm^{-1} corresponded to the H–O–H bending vibration and indicates the presence of water in the sample (Gotić et al., 1994 :2474). The broadband between 968 and 1066 cm^{-1} is owned to the Si–O–T (T = Al, Si) asymmetric stretching vibration (Puligilla and Mondal, 2015:39). The band at 780 cm^{-1} could be assigned to Si–O–Al symmetric stretching vibration. The band at 470 cm^{-1} is owned to Si–O bending vibration (Rattanasak et al., 2010 :654).

Compared with samples without aging (day 0), the absorption band at 3619 cm^{-1} assigned to OH stretching vibration, gets stronger and shifts towards high wavenumber, which indicates more water in the pore and stronger interaction between water and the silanol (Si–OH) and aluminol (Al–OH) in gel framework (Naghsh and Shams, 2017:238). The 868 , 1459 and 1510 cm^{-1} bands are owned to C–O asymmetric and symmetric stretching vibration of Na_2CO_3 , which become stronger with aging (Catauro et al., 2017:1919; Baykara et al., 2017:1). This phenomenon is in accordance with XRD analysis and indicates that porous perlite geopolymers experience carbonation during aging, i.e., Na^+ in pores of geopolymer reacts with CO_2 and H_2O in the air to form $\text{Na}_2\text{CO}_3\cdot\text{H}_2\text{O}$. The band assigned to Si–O–T (Si, Al) between 968 and 1066 cm^{-1} shifts towards 1044 cm^{-1} , which indicates the further polymerization in geopolymer or the reaction of unreacted raw materials.

3.2. Phase composition

Aluminosilicate inorganic polymers are called X-ray amorphous when they form a hump with a center of approximately $27\text{--}29^\circ$ at 2θ in XRD models (Duxson et al., 2007:2917). XRD patterns for raw and calcined perlite; the main mineral component of the raw material shows the presence of a broad peak of amorphous structures originating from diffuse scattering is visible between 15° and 40° at 2θ . After 1 day of aging, $\text{Na}_2\text{CO}_3\cdot\text{H}_2\text{O}$ started to appear and kept increasing with aging time. The results indicate that the porous perlite geopolymer undergoes deeper and deeper carbonation during aging.

In order to obtain perlite-based geopolymer cement, geopolymers showed that the perlite had a high water demand so it was not surprising that setting by curing by conventional methods in sealed systems at ~ 60 °C led to soft materials with several percent of excess water. Although this could be removed by evaporation, the products were quite soft and could be readily deformed by hand. However, by further drying up to 4 days a material resulted that could be handled without breaking. XRD analysis of geopolymers shows mainly the presence of crystalline zeolite, with sharp peaks between 20° and 40° at 2θ. The strongest of the crystalline peaks however was only a factor of 2-3 times greater than the height of the broad peak. The formation of the zeolite phase is characteristic of the nominally reacted material having a Si/Al molar ratio of around 1, rather than the value of 2 expected if all the perlite took part in the reaction. (Barbosa and MacKenzie, 2003:319; Davidovits, 1994:131).

In the SEM image of the perlite-based geopolymer, the solid phase was clearly unreacted coarse perlite plus fine perlite surrounded by a Na-rich phase on the rims of the pores, probably derived from the original NaOH solution forming an alkaline pore water which had subsequently dried. No clear evidence of the zeolite evidenced in XRD was visible in SEM so it was assumed that the zeolite grain size was very fine.

SEM examinations of perlite-based geopolymers were investigated, which also made using stronger (~ 5 Mol/L) alkali solution to induce more reaction by increasing the Si/Al molar ratio (Davidovits, 2005:9). Na aluminosilicate phases corresponding to the main phase were observed. This result is also consistent with the XRD patterns and the porosity of the obtained geopolymers was quite high (~30%).

4. Conclusions

From a holistic viewpoint, the properties of geopolymer cement in the civil engineering field can be systemically outlined. The applications of geopolymer cements are intensively related with their properties and performance, meanwhile, the latter is essentially determined by microstructures as well as constituent materials and mixture proportions of geopolymer cements. On the other hand, the performance of the protected structures by the geopolymer cement layer is of vital importance. The topic along with the microstructures and mechanisms of geopolymer cement will be further reviewed.

References

- Abu-Jdayil, B., Mourad, A. H., Hittini, W., Hassan, M., Hameedi, S. (2019). Traditional, state-of-the-art and renewable thermal building insulation materials: An overview. *Construction and Building Materials*, 214, 709-735.
- Aguirre-Guerrero, A. M., Robayo-Salazar, R. A., de Gutiérrez, R. M. (2017). A novel geopolymer application: Coatings to protect reinforced concrete against corrosion. *Applied Clay Science*, 135, 437-446.
- Alanazi, H., Yang, M., Zhang, D., Gao, Z. J. (2016). Bond strength of PCC pavement repairs using metakaolin-based geopolymer mortar. *Cement and Concrete Composites*, 65, 75-82.
- Aliabdo, A., Abd Elmoaty, M.A., Salem, H. A. (2016). Effect of water addition, plasticizer and alkaline solution constitution on fly ash based geopolymer concrete performance. *Construction and Building Materials*, 121, 694-703.
- Bai, C., Colombo, P. (2018). Processing, properties and applications of highly porous geopolymers: A review. *Ceramics International*, 44(14), 16103-16118.
- Balaguru, P.N., (2002) Geopolymer for Protecting Coating of Transportation Infrastructures, Center for Advanced Infrastructure and Transportation (CAIT), Civil & Environmental Engineering, Rutgers State University, Piscataway.
- Balaguru, P. N., Nazier, M., Arafa, M. D., Sasor, M. R. (2008). *Field implementation of geopolymer coatings*, New Jersey Department of Transportation, Final report, No. 94 RU951.
- Barbosa, V. F.F., MacKenzie, K. J.D. (2003). Thermal behaviour of inorganic geopolymers and composites derived from sodium polysialate. *Materials research bulletin*, 38(2), 319-331.
- Baykara, H., Cornejo, M. H., Murillo, R., Gavilanes, A., Paredes, C., Elsen, J. (2017). Preparation, characterization and reaction kinetics of green cement: Ecuadorian natural mordenite-based geopolymers. *Materials and Structures*, 50(3), 1-12.
- Biondi, L., Perry, M., Vlachakis, C., Wu, Z., Hamilton, A., McAlorum, J. (2019). Ambient cured fly ash geopolymer coatings for concrete. *Materials*, 12(6), 923.
- Catauro, M., Bollino, F., Cattaneo, A. S., Mustarelli, P. (2017). $\text{Al}_2\text{O}_3 \cdot 2\text{SiO}_2$ powders synthesized via sol-gel as pure raw material in

- geopolymer preparation. *Journal of the American Ceramic Society*, 100(5), 1919-1927.
- Cheah, C. B., Tan, L. E., Ramli, M. (2019). The engineering properties and microstructure of sodium carbonate activated fly ash/slag blended mortars with silica fume. *Composites Part B: Engineering*, 160, 558-572.
- Chindaprasirt, P., Phoo-ngernkham, T., Hanjitsuwan, S., Horpibulsuk, S., Poowancum, A., Injorhor, B. (2018). Effect of calcium-rich compounds on setting time and strength development of alkali-activated fly ash cured at ambient temperature. *Case Studies in Construction Materials*, 9, e00198.
- Davidovits, J. (1994). Geopolymers: man-made rock geosynthesis and the resulting development of very early high strength cement. *Journal of Materials Education*, 16(2-3), 91-139.
- Davidovits, J. (1994) Properties of geopolymer cements, In: Proceedings of the first international conference on alkaline cements and concretes, Kiev, Ukraine, 131–149.
- Davidovits, J. (2005, June). Geopolymer chemistry and sustainable development. The poly (sialate) terminology: a very useful and simple model for the promotion and understanding of green-chemistry. In *Proceedings of the world congress Geopolymer*, Saint Quentin, France, 28, 9-15.
- Davidovits, J. (2008) “ Geopolymer Chemistry and Applications”, 2nd edition., Ch. 8, Geopolymer Institute, Saint-Quentin, France, pp. 145-192.
- Ding, R., Chen, S., Lv, J., Zhang, W., Zhao, X. D., Liu, J., Li, W. H. (2019). Study on graphene modified organic anti-corrosion coatings: A comprehensive review. *Journal of Alloys and Compounds*, 80625(10), 611-635.
- Duan, P., Yan, C., Zhou, W., Luo, W., Shen, C. (2015). An investigation of the microstructure and durability of a fluidized bed fly ash–metakaolin geopolymer after heat and acid exposure. *Materials & Design*, 74, 125-137.
- Duan, P., Yan, C., Luo, W., Zhou, W. (2016). A novel surface waterproof geopolymer derived from metakaolin by hydrophobic modification. *Materials Letters*, 164(2), 172-175.
- Duan, P., Yan, C., Luo, W., Zhou, W. (2016). Effects of adding nano-TiO₂ on compressive strength, drying shrinkage, carbonation and microstructure of fluidized bed fly ash based geopolymer

- paste. *Construction and Building Materials*, 106, 115-125.
- Duxson P., Provis J.L., Lukey G.C., van Deventer J. S. J. (2007) “The Role of Inorganic Polymer Technology in the Development of 'Green Concrete'”, *Cement and Concrete Research*, 37(12), 1590-1597.
- Duxson, P., Fernández-Jiménez, A., Provis, J.L., Lukey, G.C., Palomo, A., van Deventer, J. S. J. (2007) “Geopolymer Technology: the Current State of the Art”, *Journal of Materials Science*, 42(9), 2917-2933.
- Elyamany, H. E., Abd Elmoaty, M., Elshaboury, A. M. (2018). Setting time and 7-day strength of geopolymer mortar with various binders. *Construction and Building Materials*, 187, 974-983.
- Erdoğan, S. T. (2015). Properties of ground perlite geopolymer mortars. *Journal of Materials in Civil Engineering*, 27(7), 04014210, 1-17.
- Farhan, K. Z., Johari, M. A. M., Demirboğa, R. (2020). Assessment of important parameters involved in the synthesis of geopolymer composites: A review. *Construction and Building Materials*, 264, 120276.
- Fernández-Jiménez, A., Palomo, A. (2005). Composition and microstructure of alkali activated fly ash binder: Effect of the activator. *Cement and concrete research*, 35(10), 1984-1992.
- Gambogi, J. (2016). US Geological Survey, Mineral Commodity Summaries, January 2016.
- Gong, W., Fan, Z., Xu, Y. (2021). Drivers of the Peaking and Decoupling Between CO₂ Emissions and Economic Growth Around 2030 in China.
- Gotić, M., Popović, S., Ljubešić, N., Musić, S. (1994). Structural properties of precipitates formed by hydrolysis of Fe³⁺ ions in aqueous solutions containing NO₃⁻ and Cl⁻ ions. *Journal of materials science*, 29(9), 2474-2480.
- Habert, G., De Lacaillerie, J. D. E., Roussel, N. (2011). An environmental evaluation of geopolymer based concrete production: reviewing current research trends. *Journal of cleaner production*, 19(11), 1229-1238.
- Hadi, M. N., Zhang, H., Parkinson, S. (2019). Optimum mix design of geopolymer pastes and concretes cured in ambient condition based on compressive strength, setting time and workability. *Journal of*

Building engineering, 23, 301-313.

- Hassan, A., Arif, M., Shariq, M. (2019). Use of geopolymer concrete for a cleaner and sustainable environment—A review of mechanical properties and microstructure. *Journal of cleaner production*, 223, 704-728.
- Hooshmand, T., van Noort, R., Keshvad, A. (2004). Storage effect of a pre-activated silane on the resin to ceramic bond. *Dental Materials*, 20(7), 635-642.
- Hou, Y., Wang, D., Zhou, W., Lu, H., & Wang, L. (2009). Effect of activator and curing mode on fly ash-based geopolymers. *Journal of Wuhan University of Technology-Mater. Sci. Ed.*, 24(5), 711-715.
- Hu, S., Wang, H., Zhang, G., Ding, Q. (2008). Bonding and abrasion resistance of geopolymeric repair material made with steel slag. *Cement and concrete composites*, 30(3), 239-244.
- Janaki, P., Selvaraj, R. (2017). Experimental study on mechanical properties of geopolymer coatings for corrosion protection of steel. *Advances in Natural and Applied Sciences*, 11(4), 13-20.
- Jiang, C., Wang, A., Bao, X., Ni, T., Ling, J. (2020). A review on geopolymer in potential coating application: Materials, preparation and basic properties. *Journal of Building Engineering*, 101734, (1-16).
- Kaloari, R. M., Haris, A. (2016). Synthesis of geopolymer paste as coating material based on kaolinite and rice husk ash. In *Materials Science Forum*, 841, 79-82, Trans Tech Publications Ltd.
- Kriven, W. M., Gordon, M., Ervin, B. L., Reis, H. (2008). Corrosion protection assessment of concrete reinforcing bars with a geopolymer coating. *Developments in Porous, Biological and Geopolymer Ceramics*, Ceramics Engineering Science Process, 28 (9) (2009) 373-381.
- Kumar, S., Sahoo, D. P., Nath, S. K., Alex, T. C., Kumar, R. (2012). From grey waste to green geopolymer. *Science and Culture*, 78(11-12), 511-516.
- Kumar, D., Alam, M., Zou, P. X., Sanjayan, J. G., Memon, R. A. (2020). Comparative analysis of building insulation material properties and performance. *Renewable and Sustainable Energy Reviews*, 131, 110038, 1-22.
- Kupaei, R. H., Alengaram, U. J., Jumaat, M. Z. B., Nikraz, H. (2013).

- Mix design for fly ash based oil palm shell geopolymer lightweight concrete. *Construction and Building Materials*, 43, 490-496.
- Lahoti, M., Tan, K. H., Yang, E. H. (2019). A critical review of geopolymer properties for structural fire-resistance applications. *Construction and Building Materials*, 221, 514-526.
- Lau, C. K., Lee, H., Vimonsatit, V., Huen, W. Y., Chindaprasirt, P. (2019). Abrasion resistance behaviour of fly ash based geopolymer using nanoindentation and artificial neural network. *Construction and Building Materials*, 212, 635-644.
- Li, J., Shui, B. (2015). A comprehensive analysis of building energy efficiency policies in China: status quo and development perspective. *Journal of Cleaner Production*, 90, 326-344.
- Li, N., Shi, C., Zhang, Z. (2019). Understanding the roles of activators towards setting and hardening control of alkali-activated slag cement. *Composites Part B: Engineering*, 171, 34-45.
- Liang, G., Zhu, H., Zhang, Z., Wu, Q., Du, J. (2019). Investigation of the waterproof property of alkali-activated metakaolin geopolymer added with rice husk ash. *Journal of Cleaner Production*, 230, 603-612.
- Lv, X., Wang, K., He, Y., Cui, X. (2019). A green drying powder inorganic coating based on geopolymer technology. *Construction and Building Materials*, 214(7), 441-448.
- Ma, C., Zhao, B., Guo, S., Long, G., Xie, Y. (2019). Properties and characterization of green one-part geopolymer activated by composite activators. *Journal of Cleaner Production*, 220, 188-199.
- Ma, Y., Ye, G. (2015). The shrinkage of alkali activated fly ash. *Cement and Concrete Research*, 68, 75-82.
- Ma, Y., Hu, J., Ye, G. (2012). The effect of activating solution on the mechanical strength, reaction rate, mineralogy, and microstructure of alkali-activated fly ash. *Journal of Materials Science*, 47(11), 4568-4578.
- Morsy, M. S., Alsayed, S. H., Al-Salloum, Y., Almusallam, T. (2014). Effect of sodium silicate to sodium hydroxide ratios on strength and microstructure of fly ash geopolymer binder. *Arabian journal for science and engineering*, 39(6), 4333-4339.
- Naghsh, M., Shams, K. (2017). Synthesis of a kaolin-based geopolymer using a novel fusion method and its application in effective water

- softening. *Applied Clay Science*, 146, 238-245.
- Nath, P., Sarker, P. K. (2014). Effect of GGBFS on setting, workability and early strength properties of fly ash geopolymer concrete cured in ambient condition. *Construction and Building materials*, 66, 163-171.
- Ng, C., Alengaram, U. J., Wong, L. S., Mo, K. H., Jumaat, M. Z., Ramesh, S. (2018). A review on microstructural study and compressive strength of geopolymer mortar, paste and concrete. *Construction and Building Materials*, 186, 550-576.
- Ohno, M., Li, V. C. (2018). An integrated design method of Engineered Geopolymer Composite. *Cement and Concrete Composites*, 88, 73-85.
- Pacheco-Torgal, F., Castro-Gomes, J. P., Jalali, S. (2008). Investigations on mix design of tungsten mine waste geopolymeric binder. *Construction and Building Materials*, 22(9), 1939-1949.
- Pan, X., Shi, Z., Shi, C., Ling, T. C., Li, N. (2017). A review on concrete surface treatment Part I: Types and mechanisms. *Construction and Building Materials*, 132, 578-590.
- Papakonstantinou, C. G., Balaguru, P. N. (2007, June). Geopolymer protective coatings for concrete. In *Proceedings of the International Sampe Symposium Exhibition, Baltimore, MD, USA*, 52, (pp. 3-7).
- Pasupathy, K., Ramakrishnan, S., Sanjayan, J. (2020). Enhancing the mechanical and thermal properties of aerated geopolymer concrete using porous lightweight aggregates. *Construction and Building Materials*, 264, 120713.
- Pasupathy, K., Ramakrishnan, S., Sanjayan, J. (2021). Influence of recycled concrete aggregate on the foam stability of aerated geopolymer concrete. *Construction and Building Materials*, 271, 121850.
- Pichor, W., Kaminski, A., Szoldra, P., Frac, M. (2019). Lightweight cement mortars with granulated foam glass and waste perlite addition. *Advances in Civil Engineering*, 2019, 1-9.
- Phoo-ngernkham, T., Sata, V., Hanjitsuwan, S., Ridtirud, C., Hatanaka, S., Chindaprasirt, P. (2015). High calcium fly ash geopolymer mortar containing Portland cement for use as repair material. *Construction and building materials*, 98, 482-488.
- Puligilla, S., Mondal, P. (2015). Co-existence of aluminosilicate and

- calcium silicate gel characterized through selective dissolution and FTIR spectral subtraction. *Cement and Concrete Research*, 70, 39-49.
- Ramakrishnan, S., Pasupathy, K., Sanjayan, J. (2021). Synthesis and properties of thermally enhanced aerated geopolymer concrete using form-stable phase change composite. *Journal of Building Engineering*, 102756.
- Rattanasak, U., Chindaprasirt, P., Suwanvitaya, P. (2010). Development of high volume rice husk ash alumino silicate composites. *International Journal of Minerals, Metallurgy, and Materials*, 17(5), 654-659.
- Rickard, W. D., Gluth, G. J., Pistol, K. (2016). In-situ thermo-mechanical testing of fly ash geopolymer concretes made with quartz and expanded clay aggregates. *Cement and concrete research*, 80, 33-43.
- Rostami, H., Tovia, F., Masoodi, R., Bahadory, M. (2015). Reduction of corrosion of reinforcing steel in concrete using alkali ash material. *The Journal of Solid Waste Technology and Management*, 41(2), 136-145.
- Sakkas, K., Nomikos, P., Sofianos, A., Panias, D. (2015). Sodium-based fire resistant geopolymer for passive fire protection. *Fire and Materials*, 39(3), 259-270.
- Sakkas, K., Panias, D., Nomikos, P. P., Sofianos, A. I. (2014). Potassium based geopolymer for passive fire protection of concrete tunnels linings. *Tunnelling and underground space technology*, 43, 148-156.
- Salwa, M. S., Al Bakri, A. M., Kamarudin, H., Ruzaidi, C. M., Binhussain, M., Zaliha, S. S. (2013). Review on current geopolymer as a coating material. *Australian Journal of Basic and Applied Sciences*, 7(5), 246-257.
- Shill, S. K., Al-Deen, S., Ashraf, M., Hutchison, W. (2020). Resistance of fly ash based geopolymer mortar to both chemicals and high thermal cycles simultaneously. *Construction and Building Materials*, 239, 117886.
- Temuujin, J., Rickard, W., Lee, M., van Riessen, A. (2011). Preparation and thermal properties of fire resistant metakaolin-based geopolymer-type coatings. *Journal of non-crystalline solids*, 357(5), 1399-1404.
- Wang, Y. S., Alrefaei, Y., Dai, J. G. (2019). Silico-aluminophosphate and

- alkali-aluminosilicate geopolymers: A comparative review. *Frontiers in Materials*, 6, 106 (1-17).
- Wang, Y., Liu, X., Zhang, W., Li, Z., Zhang, Y., Li, Y., Ren, Y. (2020). Effects of Si/Al ratio on the efflorescence and properties of fly ash based geopolymer. *Journal of Cleaner Production*, 244, 118852.
- Wi, S., Park, J. H., Kim, Y. U., Kim, S. (2021). Evaluation of environmental impact on the formaldehyde emission and flame-retardant performance of thermal insulation materials. *Journal of Hazardous Materials*, 402, 123463.
- Vaou, V., Papias, D. (2010). Thermal insulating foamy geopolymers from perlite. *Minerals Engineering*, 23(14), 1146-1151.
- Wiyono, D., Hardjito, D. (2015). Improving the durability of pozzolan concrete using alkaline solution and geopolymer coating. *Procedia Engineering*, 125, 747-753.
- Xu, X., Sun, S., Liu, W., García, E. H., He, L., Cai, Q., Zhu, J. (2017). The cooling and energy saving effect of landscape design parameters of urban park in summer: A case of Beijing, China. *Energy and Buildings*, 149, 91-100.
- Xue, X., Liu, Y. L., Dai, J. G., Poon, C. S., Zhang, W. D., Zhang, P. (2018). Inhibiting efflorescence formation on fly ash-based geopolymer via silane surface modification. *Cement and Concrete Composites*, 94, 43-52.
- Yan, B., Duan, P., & Ren, D. (2017). Mechanical strength, surface abrasion resistance and microstructure of fly ash-metakaolin-sepiolite geopolymer composites. *Ceramics International*, 43(1), 1052-1060.
- Zhang, Z., Yao, X., Zhu, H. (2010). Potential application of geopolymers as protection coatings for marine concrete: I. Basic properties, *Applied Clay Science*, 49(1-2), (2010) 1-6.
- Zhang, Z., Yao, X., Zhu, H. (2010). Potential application of geopolymers as protection coatings for marine concrete: II. Microstructure and anticorrosion mechanism. *Applied Clay Science*, 49(1-2), 7-12.
- Zhang, Z., Yao, X., Wang, H. (2012). Potential application of geopolymers as protection coatings for marine concrete III. Field experiment. *Applied Clay Science*, 67-68, 57-60.
- Zhu, H., Liang, G., Xu, J., Wu, Q., Zhai, M. (2019). Influence of rice husk ash on the waterproof properties of ultrafine fly ash based geopolymer. *Construction and Building Materials*, 208, 394-401.

CHAPTER V

USING OF SUPERHYDROPHOBICITY, SELF-CLEANING, LOW ADHESION, AND DRAG REDUCTION PROPERTIES IN GREEN ENGINEERING APPLICATIONS

Assoc. Prof. Dr. Ceyda BİLGİÇ

Eskişehir Osmangazi University, Eskişehir, Turkey
e-mail: cbilgic@ogu.edu.tr, Orcid No: 0000-0002-9572-3863

Asst. Prof. Dr. Şafak BİLGİÇ

Eskişehir Osmangazi University, Eskişehir, Turkey
e-mail: safakb@ogu.edu.tr, Orcid No: 0000-0002-9336-7762

1. Introduction

Biomimetics allows one to mimic biology or nature to develop materials and devices of commercial interest by engineers. Properties of biological materials and surfaces result from a complex interplay between surface morphology and physical and chemical properties. Hierarchical structures with dimensions of features ranging from the macroscale to the nanoscale are extremely common in nature to provide properties of interest. There are a large number of objects including bacteria, plants, land and aquatic animals, and seashells, with properties of commercial interest.

Nature has gone through evolution over the 3.8 Gyr since life is estimated to have appeared on the Earth (Gordon, 1976). Nature has evolved objects with high performance using commonly found materials. These function on the macroscale to the nanoscale. The understanding of the functions provided by objects and processes found in nature can guide us to imitate and produce nanomaterials, nanodevices, and processes (Bhushan, 2009:1445).

It is well known that the leaves of many plants such as lotus leaves show particular characteristics like water-repelling, easily rolling off the surface and antifouling even though the leaves are covered by dirty water or dust. The rainwater can smoothly roll off the lotus leaves without any pinning (Feng et al., 2002:1857; Barthlott and Neinhuis, 1997:1; Neinhuis and Barthlott, 1997:667; Yan et al., 2011:80; Zhang et al., 2012:11217; Koch et al., 2009a:137). If the features of lotus leaves can be

functionalized on various metal surfaces or substrates, it can be useful and helpful in many applications for energy saving. For example, it can reduce the friction of liquid flow, avoid fouling and enhance the heat transfer performance.

The wettability of solid surfaces attracts much attention both in research and practical applications. Studies conducted on the superhydrophobic surfaces have grown dramatically since 2004 and several review articles have been published about different aspects of superhydrophobic surfaces (Chu and Seeger, 2014:2784; Ragesh et al., 2014:14773; Bagheri et al., 2018:1134; Shin et al., 2016:1; Simpson et al., 2015:1; Su et al., 2016:1727; Tam et al., 2016:1). Basically, superhydrophobic surfaces are described by static contact angles higher than 150° and sliding angles less than 10° . It is well known that the wettability of a solid surface is a function of two primary factors including surface roughness and surface chemistry. The chemical composition of the surface determines the surface energy, which has a great effect on its wettability. However, only changing the surface chemistry cannot determine the superhydrophobic state, and these two factors must exist simultaneously (Woodward et al., 2000:2957).

Recently, superhydrophobic surfaces have attracted significant attention since it is highly desirable in many important applications; for example, since the surface is more wettable to water than to oil, it can be used as a detergent-free cleaning surface where water can easily replace the oil contaminants and push the oils away. The superhydrophobic surfaces can reduce the consumption of detergents that are made from petroleum. Therefore, it can save energy and protect the environment from detergent-related pollution, which are current environmental challenges. It can also be used as an anti-fogging surface, which is crucial for eyeglasses, camera lenses, automobiles, and medical instruments such as infrared microscopes (Howarter and Youngblood, 2007; Howarter and Youngblood, 2008).

Exemplifies the importance towards for potential applications of superhydrophobic surfaces have many industries, in particular in energy-related fields, which has been summarized in figure 1. superhydrophobic surfaces are becoming an integral part of our daily life because of their utility in various applications such as windows, solar panels, cement, paints, etc. Furthermore, different natural organisms exhibiting superhydrophobic behavior have been analyzed and the fundamentals of superhydrophobic surface attribute such as water contact angle, surface energy, contact angle hysteresis, etc. The fabrications and characterization of the superhydrophobic surfaces are introduced. Then,

the characteristics, such as wettability, anti-frosting and anti-icing, lower ice adhesion strength, are described, and many energy-related applications of superhydrophobic surfaces are discussed as well.

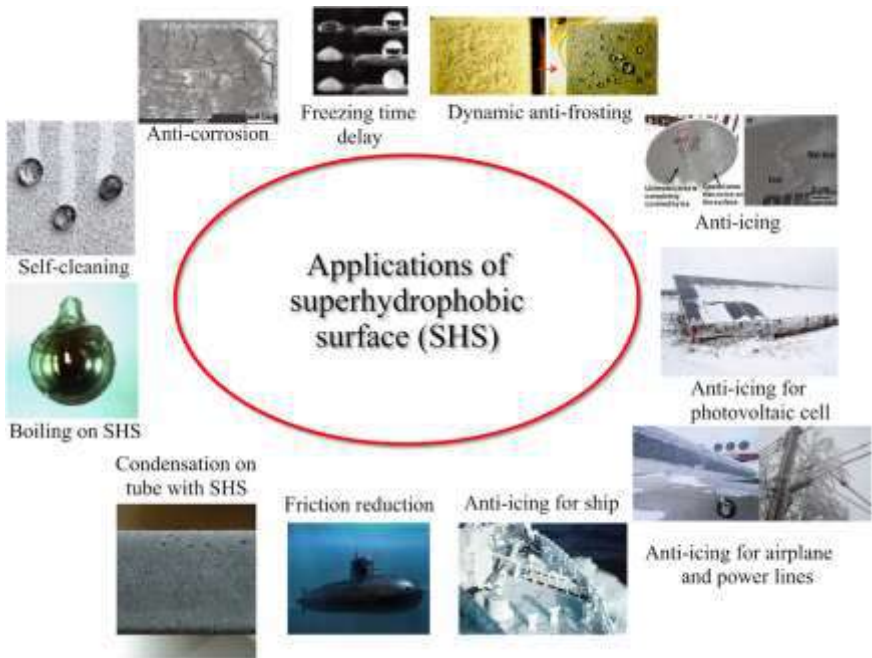


Figure 1. The applications of superhydrophobic surfaces (Zhang and Lv, 2015:1068).

Numerical models which provide relationships between roughness and contact angle and contact angle hysteresis as well as the Cassie–Baxter and Wenzel regime transition are discussed. To further examine the effect of meniscus force and real area of contact, scale dependence is considered with the use of Atomic Force Microscopy (AFM) tips of various radii. To investigate how the effects of droplet size and impact velocity influence the transition, evaporation and bouncing studies are conducted on silicon surfaces patterned with pillars of two different diameters and heights and with varying pitch values and deposited with a hydrophobic coating. In order to generate submicron droplets, an atomic force microscopy-based technique using a modified nanoscale dispensing probe is presented. An Environment Scanning Electron Microscopy (ESEM) study on the wetting behavior for a microdroplet with about 20

μm radius on the micropatterned Si surfaces is presented. For the durability of the various fabricated surfaces, the loss of superhydrophobicity, as well as wear and friction, is investigated.

This article has focused on surfaces with superhydrophobicity, self-cleaning, low adhesion, and drag reduction, such as Lotus leaf and sharkskin. The development of superhydrophobic and self-cleaning surfaces is important for basic research as well as various applications, including self-cleaning windows, exterior paints for buildings, navigation ships, textiles, solar panels, and applications requiring anti-fouling and a reduction in fluid flow, e.g., in micro/nanochannels. These surfaces can also be used in energy conversion and conservation.

2. The Cassie–Baxter and Wenzel wetting regime transition

Since superhydrophobicity requires a stable composite interface, it is important to understand the destabilization mechanisms for the Cassie–Baxter and Wenzel wetting transition. Based on Nosonovsky and Bhushan (Nosonovsky and Bhushan, 2008; Nosonovsky and Bhushan, 2008a:1525), it is known from experimental observations that the transition from the Cassie–Baxter to Wenzel regime can be an irreversible event. Whereas such a transition can be induced, for example, by applying pressure or force to the droplet (Jung and Bhushan, 2008:6262; Nosonovsky and Bhushan, 2008), electric voltage (Krupenkin et al., 2004:3824; Bahadur and Garimella 2007:4918), light for a photocatalytic texture (Feng et al., 2004:62), and vibration (Bormashenko et al., 2007a:6501), the opposite transition is never observed. Several approaches have been proposed for investigation of the transition between the Cassie–Baxter and Wenzel regimes, referred to as “the Cassie–Wenzel transition.” It has been suggested that the transition takes place when the net surface energy of the Wenzel regime becomes equal to that of the Cassie–Baxter regime, or, in other words, when the contact angle predicted by the Cassie–Baxter equation is equal to that predicted by the Wenzel equation. Lafuma and Quere (Lafuma and Quere, 2003:457) noticed that in certain cases the transition does not occur even when it is energetically profitable, and considered such a Cassie–Baxter state metastable. Extrand (Extrand, 2003:3793) suggested that the weight of the droplet is responsible for the transition and proposed the contact line density model, according to which the transition takes place when the weight exceeds the surface tension force at the triple line. Patankar (Patanekar, 2004:7097) suggested that which of the two states is realized may depend upon how the droplet was formed, that is upon the history of the system. Quéré (Quéré, 2005:2495) also suggested that the droplet curvature (which depends upon the pressure difference between the inside

and the outside of the droplet) governs the transition. Nosonovsky and Bhushan (Nosonovsky and Bhushan, 2006:231) suggested that the transition is a dynamic process of destabilization and identified possible destabilizing factors. It has been also suggested that the curvature of multiscale roughness defines the stability of the Cassie–Baxter wetting regime ([Nosonovsky, 2007a:3157; Nosonovsky, 2007b; Nosonovsky and Bhushan, 2007a:162; Nosonovsky and Bhushan, 2007b:382; Nosonovsky and Bhushan, 2007c:969; Nosonovsky and Bhushan, 2008a:1525; Nosonovsky and Bhushan, 2008b:1181; Nosonovsky and Bhushan, 2008c; Nosonovsky and Bhushan, 2008d) and that the transition is a stochastic gradual process (Nosonovsky and Bhushan, 2005:535; Ishino and Okumura, 2006:464; Bormashenko et al., 2007b:4378; Bormashenko et al., 2007a:6501). Numerous experimental results support many of these approaches, however, it is not clear which particular mechanism prevails.

To summarize, the contact angle hysteresis and Cassie–Baxter and Wenzel transition cannot be determined from the macroscale equations and are governed by micro- and nanoscale phenomena (Nosonovsky and Bhushan, 2008e; Nosonovsky and Bhushan, 2008a:1525).

3. Lotus effect surfaces in nature

Many biological surfaces are known to be superhydrophobic and self-cleaning. In this section, we will discuss various plant leaves, their roughness and wax coatings in relation to their hydrophobic/ hydrophilic and self-cleaning properties.

The hydrophobic and water-repellent abilities of many plant leaves have been known for a long time. Scanning electron microscope (SEM) studies since the 1970s have revealed that the hydrophobicity of the leaf surface is related to its microstructure. The outer cells covering a plant, especially the leaf, are called epidermis cells. The epidermis in all plant surfaces is covered by a thin extracellular membrane, called the cuticle. The plant cuticle is a composite material mainly built up of a cutin network and hydrophobic waxes (Barthlott and Neinhuis, 1997:1; Koch et al., 2008:1943; Koch et al., 2009a:137). The chemical structure of the epicuticular waxes has been studied extensively by plant scientists and lipid chemists in recent decades (Baker, 1982:139; Jetter et al., 2006:145). The epicuticular waxes can be either thin with a 2-D structure or thick with a 3-D structure or a combination thereof. It is believed that waxes diffuse through the cuticle via a lipidic pathway (Koch et al., 2009b:1673). After diffusion of the wax, the tubular wax morphologies grow by crystallization or self-assembly. The plants are able to repair the wax layer by self-assembly.

The hydrophobicity of the leaves is related to another important effect, the ability to remain clean after being immersed in dirty water, known as self-cleaning. This ability is best known for the Lotus (*Nelumbo nucifera*) leaf that is considered by some Asian cultures as “sacred” due to its purity. Not surprisingly, the ability of Lotus-like surfaces for self-cleaning and water-repellency was dubbed the “Lotus effect.” As far as the biological implications of the Lotus effect, self-cleaning plays an important role in the defense against pathogens binding to the leaf surface. Many spores and conidia of pathogenic organisms –most fungi – require water for germination and can infect leaves only in the presence of water.

Neinhuis and Barthlott (Neinhuis and Barthlott, 1997:667) systematically studied surfaces and wetting properties of about 200 water-repellent plants (for a comprehensive review, see (Koch et al., 2008:1943; Koch et al., 2009:137). Among the epidermal relief features are the papillose epidermal cells either with every epidermal cell forming a single papilla or cells being divided into papillae. The scale of the epidermal relief ranged from 5 μm in multipapillate cells to 100 μm in large epidermal cells. Some cells also are convex (rather than having real papillae) and/or had hairs (trichomes). Neinhuis and Barthlott (Neinhuis and Barthlott, 1997:667) also found various types and shapes of wax crystals at the surface. Also see Koch et al. (Koch et al., 2008:1943; Koch et al., 2009:137). Interestingly, the hairy surfaces with a thin film of wax exhibited water-repellency for short periods (minutes), after which water penetrated between the hairs, whereas hairs with a thick film led to strong water-repellency. The wax crystal creates nanoroughness, in addition to the microroughness created by the papillae. Apparently, roughness plays the dominant role in the Lotus effect.

The SEM study reveals that the Lotus leaf surface is covered by “bumps,” more exactly called papillae (papillose epidermal cells), which, in turn, are covered by an additional layer of epicuticular waxes (Barthlott and Neinhuis, 1997:1). The wax is present in crystalline tubules, composed of a mixture of long-chain aliphatic compounds, principally nonacosanol and nonacosanediols (Koch et al., 2006:2571; Koch et al., 2008:1943; Koch et al., 2009:137). The wax is hydrophobic with a water contact angle of about 95–110°, whereas the papillae provide the tool to magnify the contact angle based on the Wenzel model, discussed in the preceding section. The experimental value of the static water contact angle with the Lotus leaf was reported about the 164° (Bhushan et al., 2009:1631; Koch et al., 2009c:1386).

3.2. Characterization of superhydrophobic and hydrophilic surfaces

In order to understand the mechanisms of hydrophobicity in plant leaves, a comprehensive comparative study of superhydrophobic and hydrophilic leaf surfaces and their properties was carried out by Bhushan and Jung (Bhushan and Jung, 2006:2758) and Burton and Bhushan (Burton and Bhushan, 2006:709).

3.2.1. SEM micrographs

The SEM micrographs of two superhydrophobic leaves –Lotus (*Nelumbo nucifera*) and elephant ear or taro plant (*Colocasia esculenta*), referred to as Lotus and Colocasia, respectively –and two hydrophilic leaves –beech (*Fagus sylvatica*) and Magnolia (*Magnolia grandiflora*), referred to as Fagus and Magnolia, respectively (Bhushan and Jung, 2006:2758). Lotus and Colocasia are characterized by papillose epidermal cells responsible for the creation of papillae or microbumps on the surfaces, and an additional layer of 3-D epicuticular waxes which are a mixture of very long chain fatty acids molecules (compounds with chains >20 carbon atoms) and create nanostructure on the entire surface. Fagus and Magnolia are characterized by rather flat tabular cells with a thin wax film with a 2-D structure (Barthlott and Neinhuis, 1997:1). The leaves are not self-cleaning, and contaminant particles from ambient are accumulated, which makes them hydrophilic.

3.2.2. Contact angle measurements

The contact angles for the superhydrophobic and hydrophilic leaves before and after applying acetone. The acetone was applied in order to remove any wax present on the surface. As a result, for the superhydrophobic leaves, the contact angle dramatically reduced, whereas for the hydrophilic leaves, the contact angle was almost unchanged. It is known that there is a 2-D very thin wax layer on the hydrophilic leaves, which introduces little roughness. In contrast, superhydrophobic leaves are known to have a thin 3-D wax layer on their surface consisting of nano scale roughness over micro roughness created by the papillae, which results in a hierarchical roughness. The combination of this wax and the roughness of the leaf creates a superhydrophobic surface.

3.2.3. Surface characterization using an optical profiler

The use of an optical profiler allows measurements to be made on fresh leaves which have a large P–V distance. Three different surface height maps for superhydrophobic and hydrophilic leaves (Bhushan and

Jung, 2006:2758). A 3-D map and a flat map along with a 2-D profile in a given location of the flat 3-D map are shown. A scan size of 60 μm x 50 μm was used to obtain a sufficient amount of bumps to characterize the surface but also to maintain enough resolution to get an accurate measurement.

The structures found with the optical profiler correlate well with the SEM images. The bumps on the Lotus leaf are distributed on the entire surface, but the Colocasia leaf shows a very different structure to that of the Lotus. The surface structure for Colocasia not only has bumps similar to Lotus, but also surrounding each bump is a ridge that keeps the bumps separated. With these ridges, the bumps have a hexagonal (honeycomb) packing geometry that allows for the maximum number of bumps in a given area. The bumps of Lotus and both bumps and ridges of Colocasia contribute to the superhydrophobic nature since they both increase the R_f factor and result in air pockets between the droplet of water and the surface. In Fagus and Magnolia height maps, short bumps can be seen on the surface. This means that with decreased bump height, the probability of air pocket formation decreases, and bumps have a less beneficial effect on the contact angle (Bhushan and Jung, 2006:2758; (Burton and Bhushan, 2006:709).

Using these optical surface height maps, different statistical parameters of bumps and ridges can be found to characterize the surface: P–V height, mid-width, and peak radius (Bhushan, 1999; Bhushan, 2002). Comparing the superhydrophobic and hydrophilic leaves, it can be seen that the P–V height for bumps of Lotus and Colocasia is much taller than that for the bumps of Fagus and Magnolia. The peak radius for the bumps of Lotus and Colocasia is also smaller than that for the bumps of Fagus and Magnolia. However, the values of mid-width for the bumps of the four leaves are similar.

3.2.4. Surface characterization, adhesion, and friction using an AFM

3.2.4.1. Comparison of two AFM measurement techniques

To measure topographic images of the leaf surfaces, both the contact and tapping modes were first used (Bhushan and Jung, 2006:2758). Surface height maps of dried Lotus were obtained using the two techniques. In the contact mode, local height variation for Lotus leaf was observed in 50 μm scan size. However, little height variation was obtained in a 2 μm scan even at loads as low as 2 nN. This could be due to the substantial frictional force generated as the probe scanned over the sample. The frictional force can damage the sample. The tapping mode

technique allows high-resolution topographic imaging of sample surfaces that are easily damaged, loosely held to their substrate, or difficult to image by other AFM techniques (Bhushan, 1999; Bhushan, 2002). With the tapping mode technique, the soft and fragile leaves can be imaged successfully. Therefore tapping mode technique was used to examine the surface roughness of the superhydrophobic and hydrophilic leaves using an AFM.

3.2.4.2. Surface characterization

The AFM has a Z-range on the order of 7 μm , and cannot be conventionally used for measurements because of the high P–V distances of a Lotus leaf. Burton and Bhushan (Burton and Bhushan, 2006:709) developed a new method to fully determine the bump profiles. In order to compensate for the large P–V distance, two scans were made for each height: one measurement that scans the tops of the bumps and another measurement that scans the bottom or valleys of the bumps. The total height of the bumps is embedded within the two scans. The 50 μm surface height maps were obtained using this method (Bhushan and Jung, 2006:2758). The 2-D profiles in the right side column take the profiles from the top scan and the bottom scan for each scan size and splice them together to get the total profile of the leaf. The 2 μm surface height maps for both fresh and dried Lotus. This scan area was selected on the top of a microbump obtained in the 50 μm surface height map. It can be seen that nanobumps are randomly and densely distributed on the entire surface of Lotus.

Bhushan and Jung (Bhushan and Jung, 2006:2758) also measured the surface height maps for the hydrophilic leaves in both 50 μm and 2 μm scan sizes. For *Fagus* and *Magnolia*, microbumps were found on the surface, and the P–V distance of these leaves is lower than that of Lotus and *Colocasia*. It can be seen in the 2 μm surface height maps that nanobumps selected on the peak of the microbump have an extremely low P–V distance.

3.2.4.3. Adhesive force and friction

Adhesive force and coefficient of friction of superhydrophobic and hydrophilic leaves using AFM (Bhushan and Jung, 2006:2758). For each type of leaf, adhesive force measurements were made for both fresh and dried leaves using a 15 μm radius tip. It is found that the dried leaves had a lower adhesive force than the fresh leaves. Adhesive force arises from several sources in changing the presence of a thin liquid film, such as an adsorbed water layer that causes meniscus bridges to build up around the contacting and near-contacting bumps as a result of surface energy effects

(Bhushan, 1999; Bhushan, 2002). When the leaves are fresh there is moisture within the plant material that causes the leaf to be soft, and when the tip comes into contact with the leaf sample, the sample will deform, and a larger real area of contact between the tip and sample will occur, and the adhesive force will increase. After the leaf has dried, the moisture that was in the plant material is gone, and there is not as much deformation of the leaf when the tip comes into contact with the leaf sample. Hence, the adhesive force is decreased because the real area of contact has decreased.

The adhesive force of *Fagus* and *Magnolia* is higher than that of *Lotus* and *Colocasia*. The reason is that the real area of contact between the tip and leaf surface is expected to be higher in hydrophilic leaves than in superhydrophobic leaves. In addition, the *Fagus* and *Magnolia* are hydrophilic and have a high affinity to water. The combination of the high real area of contact and affinity to water are responsible for higher meniscus forces (Bhushan, 1999; Bhushan, 2002). The coefficient of friction was only measured on a dried plant surface with the same sliding velocity (10 $\mu\text{m/s}$) in different scan sizes rather than including the fresh surface because the $P-V$ was too large to scan back and forth with the AFM to obtain friction force. As expected, the coefficient of friction for superhydrophobic leaves is lower than that for hydrophilic leaves due to the real area of contact between the tip and leaf sample, similar to the adhesive force results. When the scan size from microscale to nanoscale decreases, the coefficient of friction also decreases in each leaf. The reason for such dependence is the scale dependent nature of the roughness of the leaf surface. AFM topography images and 2-D profiles of the surfaces for different scan sizes. The scan size dependence of the coefficient of friction has been reported previously (Poon and Bhushan, 1995:76; Koinkar and Bhushan, 1997:2472; Tambe and Bhushan, 2004:1561).

4. Conclusions

Advanced engineering materials are used extensively in every field today. The theoretical mechanisms of wetting of rough surfaces and characterization of natural and artificial surfaces with superhydrophobicity, self-cleaning, low adhesion, and drag reduction have been presented. Theoretical approaches have been presented to understand these phenomena such as the transition between the Wenzel and Cassie–Baxter wetting regimes, contact angle hysteresis, the role of hierarchical roughness, and the possibility of the creation of reversible hydrophobicity. Based on learning from the theoretical background, various leaf surfaces on the micro-and nanoscale have been characterized

and attempts are made to separate out the effects of the micro and nanobumps and the wax on the hydrophobicity. The next logical step in realizing superhydrophobic surfaces is to design surfaces based on the understanding of the leaves. Artificial superhydrophobic surfaces have been fabricated using various fabrication techniques. The influence of micro, nano and hierarchical structures on superhydrophobicity have been discussed by the investigation of static contact angle, contact angle hysteresis, evaporation, bouncing and vibration of a water droplet, and propensity of air pocket formation. In addition, their influence on adhesive force as well as efficiency of self-cleaning have been discussed. The models for the transition from Cassie–Baxter regime to Wenzel regime have been presented. Furthermore, the durability of the various fabricated surfaces has been discussed by the investigation of the loss of superhydrophobicity as well as wear and friction.

This article provides a useful guide for the development of biomimetic artificial surfaces. Hierarchical structures are typical for surfaces with superhydrophobic, self-cleaning, low adhesion and drag reduction in nature. The flexible and low-cost technique demonstrates that hierarchical surfaces can be produced in the laboratory for further investigations of the properties of hierarchically structured materials. A proper control of roughness constitutes the main challenge in producing a reliable hierarchical surface and furthermore the mechanisms that trigger the Cassie–Baxter and Wenzel regime transitions still remain to be further investigated. Such applications are of positive significance for energy saving and performance improvement. Although superhydrophobic surfaces have been subjected to intensive investigations, it is apparent that further investigations are still necessary for both fundamental and applicational aspects.

References

- Bagheri H, Aliofkhazraei M, Forooshani HM, Rouhaghdam AS, Facile fabrication of uniform hierarchical structured (UHS) nanocomposite surface with high water repellency and selfcleaning properties. *Appl. Surf. Sci.*, 2018; 436:1134-1146.
- Bahadur V, Garimella SV. Electrowetting-based control of static droplet states on rough surfaces. *Langmuir* 2007;23:4918-4924.
- Baker EA. Chemistry and morphology of plant epicuticular waxes. In: Cutler DF, Alvin KL, Price CE, editors. *The plant cuticle*. London: Academic Press; 1982. p. 139-165.

- Barthlott W, Neinhuis C. Purity of the sacred lotus, or escape from contamination in biological surfaces. *Planta* 1997;202:1-8.
- Bhushan B. Principles and applications of tribology. New York: Wiley; 1999.
- Bhushan B. Introduction to tribology. New York: Wiley; 2002.
- Bhushan B. Biomimetics: lessons from nature – an overview. *Phil Trans R Soc A* 2009;367:1445-1486.
- Bhushan B, Jung YC. Micro and nanoscale characterization of hydrophobic and hydrophilic leaf surface. *Nanotechnology* 2006;17:2758-2772.
- Bhushan B, Jung YC, Koch K. Micro-, nano- and hierarchical structures for superhydrophobicity, self-cleaning and low adhesion. *Phil Trans R Soc A* 2009;367:1631-1672.
- Bormashenko E, Pogreb R, Whyman G, Erlich M. Cassie–Wenzel wetting transition in vibrated drops deposited on the rough surfaces: is dynamic Cassie–Wenzel transition 2D or 1D affair? *Langmuir* 2007a;23:6501-6503.
- Bormashenko E, Bormashenko Y, Stein T, Whyman G, Pogreb R, Barkay Z. Environmental scanning electron microscope study of the fine structure of the triple line and Cassie–Wenzel wetting transition for sessile drops deposited on rough polymer substrates. *Langmuir* 2007b;23:4378-4382.
- Burton Z, Bhushan B. Surface characterization and adhesion and friction properties of hydrophobic leaf surfaces. *Ultramicroscopy* 2006;106:709-719.
- Chu, Z, Seeger, S, Superamphiphobic surfaces. *Chem. Soc. Rev.* 2014; 43 (8):2784-2798.
- Extrand CW. Contact angle hysteresis on surfaces with chemically heterogeneous islands. *Langmuir* 2003;19:3793-3796.
- Feng, L., Li, S., Li, Y., Li, H., Zhang, L., Zhai, J., Song, Y., Liu, B., Jiang, L., Zhu, D., Super-hydrophobic surfaces: from natural to artificial, *Advanced Materials*, 2002;14:1857-1860.
- Feng XJ, Feng L, Jin MH, Zhai J, Jiang L, Zhu DB. Reversible super-hydrophobicity to super-hydrophilicity transition of aligned ZnO nanorod films. *J Am Chem Soc*, 2004;126:62-63.
- Gordon JE. The new science of strong materials, or why you don't fall through the floor. 2nd ed. London, UK: Pelican–Penguin; 1976.

- Jung YC, Bhushan B. Dynamic effects of bouncing water droplets on superhydrophobic surfaces. *Langmuir* 2008;24:6262-6269.
- Ishino C, Okumura K. Nucleation scenarios for wetting transition on textured surfaces: the effect of contact angle hysteresis. *Europhys Lett* 2006;76:464-470.
- Jetter R, Kunst L, Samuels AL. Composition of plant cuticular waxes. In: Riederer M, Müller C, editors. *Biology of the plant cuticle*. Oxford: Blackwell Publishing; 2006. p. 145-181.
- Koch K, Dommissie A, Barthlott W. Chemistry and crystal growth of plant wax tubules of *Lotus (Nelumbo nucifera)* and *Nasturtium (Tropaeolum majus)* leaves on technical substrates. *Crystal Growth Des* 2006;6:2571-2578.
- Koch K, Bhushan B, Barthlott W. Diversity of structure, morphology, and wetting of plant surfaces. *Soft Matter* 2008;4:1943-1963.
- Koch K, Bhushan B, Barthlott W. Multifunctional surface structures of plants: an inspiration for biomimetics. *Prog Mater Sci* 2009a;54:137-178.
- Koch K, Bhushan B, Eniskat H-J, Barthlott W. Self-healing of voids in the wax coating on plant surfaces. *Philos Trans R Soc A* 2009b;367:1673-1688.
- Koch K, Bhushan B, Jung YC, Barthlott W. Fabrication of artificial lotus leaves and significance of hierarchical structure for superhydrophobicity and low adhesion. *Soft Matter* 2009c;5:1386-1393.
- Koinkar VN, Bhushan B. Effect of scan size and surface roughness on microscale friction measurements. *J Appl Phys* 1997;81:2472-2479.
- Krupenkin TN, Taylor JA, Schneider TM, Yang S. From rolling ball to complete wetting: the dynamic tuning of liquids on nanostructured surfaces. *Langmuir* 2004;20:3824-3827.
- Lafuma A, Quere D. Superhydrophobic states. *Nat Mater* 2003;2:457-460.
- Neinhuis C, Barthlott W. Characterization and distribution of water-repellent, self-cleaning plant surfaces. *Ann Bot* 1997;79:667-677.
- Nosonovsky M. Multiscale roughness and stability of superhydrophobic biomimetic interfaces. *Langmuir* 2007a;23:3157-161.
- Nosonovsky M. On the range of applicability of the Wenzel and Cassie equations. *Langmuir* 2007b;23:9919-9920.

- Nosonovsky M, Bhushan B. Roughness optimization for biomimetic superhydrophobic surfaces. *Microsyst Technol* 2005;11:535-549.
- Nosonovsky M, Bhushan B. Wetting of rough three-dimensional superhydrophobic surfaces. *Microsyst Technol* 2006;12:273-281.
- Nosonovsky M, Bhushan B. Multiscale friction mechanisms and hierarchical surfaces in nano- and bio-tribology. *Mater Sci Eng R* 2007a;58:162-193.
- Nosonovsky M, Bhushan B. Hierarchical roughness makes superhydrophobic surfaces stable. *Microelectron Eng* 2007b;84:382-386.
- Nosonovsky M, Bhushan B. Hierarchical roughness optimization for biomimetic superhydrophobic surfaces. *Ultramicroscopy* 2007c; 107:969-979.
- Nosonovsky M, Bhushan B. Multiscale dissipative mechanisms and hierarchical surfaces: friction, superhydrophobicity, and biomimetics. Heidelberg, Germany: Springer-Verlag; 2008.
- Nosonovsky M, Bhushan B. Patterned non-adhesive surfaces: superhydrophobicity and wetting regime transitions. *Langmuir* 2008a; 24:1525-1533.
- Nosonovsky M, Bhushan B. Capillary effects and instabilities in nanocontacts. *Ultramicroscopy* 2008b; 108:1181-1185.
- Nosonovsky M, Bhushan B. Roughness-induced superhydrophobicity: a way to design non-adhesive surfaces. *J Phys: Condens Matter* 2008c; 20:225009.
- Nosonovsky M, Bhushan B. Biologically-inspired surfaces: broadening the scope of roughness. *Adv Func Mater* 2008d; 18:843-855.
- Nosonovsky M, Bhushan B. Energy transitions in superhydrophobicity: low adhesion, easy flow and bouncing. *J Phys: Condens Matter* 2008e; 20:395005.
- Patankar NA. Transition between superhydrophobic states on rough surfaces. *Langmuir* 2004; 20:7097-7102.
- Poon CY, Bhushan B. Comparison of surface roughness measurements by stylus profiler, AFM and non-contact optical profiler. *Wear* 1995; 190:76-88.
- Quére D. Non-sticking drops. *Rep Prog Phys* 2005; 68:2495-2535.

- Ragesh P, Anand Ganesh V, Nair SV, Nair AS, A review on 'self-cleaning and multifunctional materials'. *J. Mater. Chem. A*, 2014; (36), 14773-14797.
- Shin, S., Seo, J., Han, H., Kang, S., Kim, H., Lee, T. Bio-inspired extreme wetting surfaces for biomedical applications. *Materials*, 2016; 9(2):116, 1-26.
- Simpson, J. T., Hunter, S. R., Aytug, T. Superhydrophobic materials and coatings: a review. *Reports on Progress in Physics*, 2015;78(8), 086501: 1-14.
- Su, B., Tian, Y., Jiang, L., Bioinspired interfaces with superwettability: from materials to chemistry. *J. Am. Chem. Soc.*, 2016; 138 (6):1727-1748.
- Tam, J., Palumbo, G., Erb, U, Recent advances in superhydrophobic electrodeposits, *Materials*, 2016; 9 (3), 151:1-27.
- Tambe NS, Bhushan B. Scale dependence of micro/nano-friction and adhesion of MEMS/NEMS materials, coatings and lubricants. *Nanotechnology* 2004; 15:1561-1570.
- Woodward, J., Gwin, H., Schwartz, D., Contact angles on surfaces with mesoscopic chemical heterogeneity. *Langmuir*, 2000; 16 (6):2957-2961.
- Yan YY, Gao N, Barthlott W. Mimicking natural superhydrophobic surfaces and grasping the wetting process: a review on recent progress in preparing superhydrophobic surfaces. *Advances in Colloid and Interface Science*, 2011;169(2):80-105.
- Zhang, Y.L., Xia, H., Kim E., Sun, H.B., Recent developments in superhydrophobic surfaces with unique structural and functional properties, *Soft Matter*, 2012; 8:11217-11231.
- Zhang, P., Lv, F.Y., A review of the recent advances in superhydrophobic surfaces and the emerging energy-related applications, *Energy*, 2015; 82:1068-1087.

CHAPTER VI

PHYSICOCHEMICAL, MICROBIOLOGICAL AND ECOTOXICOLOGICAL CHARACTERIZATION OF HOSPITAL WASTEWATER

Prof. Dr. Mahir İNCE*, Res. Asst. Handenur YAŞAR**, Res. Asst. Yasin Abdullah USLU*** and Prof. Dr. Elif İNCE****

*Gebze Technical University, Kocaeli, Turkey, e-mail:
mahirince@gtu.edu.tr

Orcid No: 0000-0003-1193-7432

**Gebze Technical University, Kocaeli, Turkey, e-mail:
hnuryasar@gtu.edu.tr

Orcid No: 0000-0003-2829-9166

***Gebze Technical University, Kocaeli, Turkey, e-mail:
yuslu@gtu.edu.tr

Orcid No: 0000-0003-0496-8142

****Gebze Technical University, Kocaeli, Turkey, e-mail:
e.senturk@gtu.edu.tr

Orcid No: 0000-0002-0106-4677

1. Introduction

In the last 20 years, hospital wastewaters (HWWs), causing different problems in various countries of the world, have attracted great attention. Although HWW is very similar to domestic wastewater in respect to chemical oxygen demand (COD) and biochemical oxygen demand (BOD), conventional pollutants, it is a more specific wastewater group. Scientists compared HWW to urban wastewater and proved that they have really qualitatively and quantitatively different characteristics (Altin, Altin, & Degirmenci, 2003; Pauwels & Verstraete, 2006; Verlicchi, Galletti, Petrovic, & BarcelÓ, 2010). HWW originates from different units including patient wards, surgical units, laboratories, clinical units, intensive care units, laundries and has a highly variable composition, depending on the related activities. Therefore, HWW, unlike urban wastewater, consists of a large number of permanent chemical compounds and mixtures of organic substances, including pharmaceuticals, radionuclides, detergents, antibiotics, antiseptics, surfactants, solvents, medical drugs, heavy metals, radioactive substances and microorganisms. Some of these compounds are non-metabolized drugs that are excreted by patients and, although they detected in HWW, the wastewater sent to the

sewer network without pre-treatment. Also, in HWW, conventional pollutants are generally higher than urban wastewater (Verlicchi et al., 2010). In HWW, BOD₅, COD and TSS concentrations are observed to extent 2-3 times higher than urban wastewater (Altin et al., 2003; Chiang, Tsai, Lin, Huo, & Lo, 2003; Gautam, Kumar, & Sabumon, 2007; Pauwels & Verstraete, 2006). One of the most important problems that arise from HWW is that they contain pathogens such as bacteria, viruses and helminths. Microbiologically, HWW have a lower load than domestic wastewater as they contain powerful disinfectants. The microbiological hazard is the presence of antibiotics resistant bacteria and hospital-specific species. Although the similarity of HWW to urban wastewater is known, it should be evaluated and controlled in terms of ecotoxicology. In the HWW characterization studies conducted in the literature, certain parameters were generally examined. In most studies, either physicochemical parameters or microbiological parameters were analysed or ecotoxicological tests were performed. Therefore, the aim of this study is to compare the results obtained in this research with the existing others in the literature by characterizing the HWW taken from a research hospital in terms of physicochemical, microbiological and ecotoxicology.

2. Experimental methods

In the period covering the spring and summer months of 2016, the HWW supplied from a research hospital was used for the characterization study. In 2016, a monthly average of 2688 patients were operated on in this hospital, 2786 inpatients were served, and an average of 36538 patients had an outpatient examination. In this study, the HWW used was supplied from the building connection channel before giving it to the main/urban sewage channel. Since the HWW changes both during daytime and day to day, it would be a problem in the explicating of the results obtained. Hence daily composite samples were obtained from the wastewater channel by the automatic sampler within 2 hour periods in this study. These daily composite samples were collected in the cold room and at the end of a week, the daily composite samples were mixed at the same ratio and weekly composite wastewater was obtained. The parameters and methods analysed within the scope of the study listed in Table 1.

Seven different bacterial species were analysed to determine the bacterial population in the HWW by using membrane filter method. In these analyses performed within the first 6 hours (Clescerl, Green, & Eaton, 1998), were also made for weekly composite samples for control purposes. In the analysis, sterile isotonic solution (0.9 M NaCl) was used in dilutions so that the cells do not disintegrate due to osmotic difference. The colonies formed were counted with a colony counter.

Table 1 Parameters and methods analysed in HWW

| Parameters | Methods |
|-------------------------------------|--|
| Physicochemical Properties | |
| TOC (Total Organic Carbon) | HACH IL 550 TOC-TN |
| COD (Chemical Oxygen Demand) | APHA (2005) 5220-D |
| TSS (Total Suspended Solids) | APHA (2005) 2540 – D |
| BOD (Biochemical Oxygen Demand) | APHA (2005)-5210 B |
| Absorbable Organic Halogens (AOX) | AOX Cell Test (photometric, merck) |
| Cl ⁻ (chloride) | APHA (2005) 4500-Cl ⁻ |
| TKN (Total Kjeldahl Nitrogen) | APHA (2005) 4500-N _{org} - B |
| NH ₃ -N | APHA (2005) 4500-NH ₃ - B |
| Orthophosphate | APHA (2005) 4500-P - G |
| Detergents | APHA (2005) 5540 |
| Phenol | GC-FID (Agilent Technologies 6890N) |
| Glutaraldehyde (GA) | (Boratynski & Zal, 1990) |
| Microbiological Properties | |
| <i>Total Coliform</i> | Sartorius SM 14053-050N |
| <i>Enterococci</i> | Sartorius SM 14051-050N |
| <i>Staphylococci</i> | Sartorius SM 14074-050N |
| <i>Salmonella</i> | Sartorius SM 14057-050N |
| <i>Shigella</i> | APHA-(2005) 9260 –E |
| <i>Staphylococcus aureus</i> | APHA-(2005) 9213 –F |
| Ecotoxicological Properties | |
| <i>Daphnia magna</i> | Daphtox Kit |
| <i>P. Subcapitata</i> | AlgalToxkit F |
| <i>Mutagenicity</i> | MUTA-Chromo Plate Test Kit (Ames Test) |
| <i>Genotoxicity</i> | SOS Chromo Plate Test Kit |
| <i>Toxicity (Acute and Chronic)</i> | TOXI Chromo Test Kit |

Daphnia magna: Samples were prepared by making dilutions (control sample and five different concentrations). Samples of a certain volume (10 mL) were filled into the multi-compartment measuring cup with different cells from each concentration. They were transferred to all cells with 5 daphnia and kept in the dark at 20-22°C for 48 hours. At the end of 24 hours and 48 hours, calculations were made separately for the cells

numbered as 1, 2, 3 and 4 of dead and immobile daphnia in each concentration.

P. Subcapitata: Algae growth culture was prepared and pH was adjusted to 8.1. A calibration was performed between the algae cell and OD with different amounts of algae dilutions. Samples were prepared at different dilution ratios in 200 mL volumetric flask. 1 mL of stock was added to each flask. The samples were taken into the test cells and incubated for 72 hours at $23\pm 2^{\circ}\text{C}$ under 1000 lux light. Algae cell values were measured in the samples at the end of 24, 48 and 72 hours. It was determined whether there was inhibition of cell growth.

Mutagenicity test (Ames test): Before starting the test, in aseptic conditions, the dry bacterium bottle was poured into the nutrient development bottle, mixed, closed, and incubated at 37°C for 16-18 hours. The reaction mixture solution was added to the samples. Subsequently, certain volumes of mixture solution and sterile and filtered samples were added to each sterile measuring tube. Pre-prepared and incubated $5\ \mu\text{L}$ of *S. typhimurium* was added to each tube. Each sample was taken into a reagent boat and $200\ \mu\text{L}$ of the mixture was placed in cells and incubated for 3-5 days at 37°C .

SOS Chromotest Method: It was used to determine the genotoxic characteristics of the HWW. The basis of the test is to stimulate the SOS response in damaged DNA in *E. coli*. Each toxicity test was carried out simultaneously in the same sample to compare the tests performed to determine the toxic properties of the HWW.

3. Result and discussion

Physicochemical characterization: The analysis of the physicochemical parameters made in 24 composite samples (one for each week) in HWW characterization are presented in Table 2.

In this study, it was determined that the COD concentration ranged from 201.3 to 396.2 mg/L. The COD value given in the study is one of the highest COD values in the literature for HWW. A group of researchers reported that COD value was high (1350 mg/L) in Thailand (Chiang et al., 2003). However, there are many studies reporting low COD concentrations in HWW (Altin et al., 2003; Escolà Casas et al., 2015). Amouei et al. (2015) studied the characterization of wastewater from four different hospitals in the same city, and they reported that the COD concentration ranged from 379 mg/L to 1187 mg/L (Amouei et al., 2015).

Table 2 Minimum, maximum and average values of physicochemical parameters

| Parameters | Unit | Minimum Value | Maximum Value | Average |
|-------------------------|-------------|----------------------|----------------------|----------------|
| COD | mg/L | 201.3 | 396.2 | 286.7 |
| BOD | mg/L | 125 | 280 | 184.3 |
| TOC | mg/L | 163.02 | 176.10 | 166.85 |
| TKN | mg/L | 32.8 | 52.5 | 43.0 |
| NH₃-N | mg/L | 23.6 | 37.4 | 30.9 |
| pH | - | 7.11 | 8.11 | 7.7 |
| TSS | mg/L | 152.04 | 188.10 | 167.80 |
| AOX | mg/L | 1.03 | 1.52 | 1.43 |
| Cl⁻ | mg/L | 68.01 | 75.03 | 71.42 |
| Orthophosphate | mg/L | 0.59 | 1.43 | 1.00 |
| Detergent | mg/L | 1.59 | 4.08 | 2.51 |
| Phenol | mg/L | 0.40 | 0.84 | 0.67 |
| GA | mg/L | 2.03 | 5.73 | 3.62 |

The BOD₅ concentration, in this study, was between 125 and 280 mg/L. It is reported that the BOD₅ value was 410 mg/L for HWW in Thailand (Chiang et al., 2003). There is also a study in the literature reporting that the concentration of BOD₅ in HWW was very low (40 mg/L) (Ekhaïse & Omavwoya, 2008). In most of the studies in the literature, TOC measurement was not performed. It was measured the TOC concentration in a hospital wastewater as maximum 350 mg/L in 2001 and 3095 mg/L in 2002 (E. Emmanuel, Perrodin, Keck, Blanchard, & Vermande, 2005). In our study, TOC concentration was measured as maximum 176.1 mg/L. Average TKN and ammonia concentrations in HWW, in this study, were measured as 43.0 mg/L and 30.9 mg/L, respectively. It is reported that the concentration of TKN in four different HWW was 18.5±8, 16±6.5, 13.5±4, 11.8±3.7 mg/L, but not measure ammonia (Amouei et al., 2015). It is only measured ammonia which was reported to be 54±16 mg/L in another study (Escolà Casas et al., 2015). In this study, pH values measured in HWW are also compatible with the literature and ranged from 7.11 to 8.11. When the studies conducted with HWW were evaluated, it was observed that it varied

between 7.7 and 8.1. The average pH values measured in different hospitals in Iran were averagely 6.9 and its the lowest and the highest values were given as 5.6 and 7.8, respectively. Considering studies in the literature, it can be stated that pH of HWW wastewater is similar to one of the domestic wastewater. In studies conducted with HWW, TSS concentrations appear to vary from hospital to hospital, seasons, months and days. It is known that these values are higher especially in rainy seasons. In a study, the concentration of TSS was reported to be 150 mg/L (Altin et al., 2003). In another study, TSS concentration in HWW was measured as 220 mg/L (E. Emmanuel et al., 2005). Considering the TSS concentration values in different studies, it can be seen that the TSS concentration changes on a wide scale and the TSS value obtained in this study also takes place in this scale (Table 2). The change of AOX concentration in HWW was also followed, with minimum and maximum concentrations of 1.03 mg/L and 1.52 mg/L, respectively, very close to each other. In a study conducted in Germany, AOX concentration was determined between 0.13-0.94 mg/L in samples taken from the discharge point to the sewage system. When the values in the literature and the AOX results in this study are compared, the concentration values we obtained remain within the value range in the literature (Table 2). The chloride concentration in HWW ranges from approximately 68 mg/L to 76 mg/L with an average value of 71.42 mg/L. It was reported that the chloride concentration range of HWW is 65-360 mg/L and an average of 200 mg/L (Verlicchi et al., 2010). However, in a study, the chloride concentration in hospital water was found to be minimum 1603.8 mg Cl⁻/L (Mir-Tutusaus, Sarrà, & Caminal, 2016). It was also reported in this study that the minimum chlorine concentration was measured as 47 mg/L. When comparing the results obtained in the literature, it is thought that chlorine can be used by different ratio as more or less preferred in some hospitals as a disinfection agent in resulting such various values. In this study, the average orthophosphate concentration determined in HWW was 1 mg/L. Prayitno et al. (2013) examined the wastewater of three different hospitals, and detected that the orthophosphate concentration in hospitals was measured as 6.25, 3.52 and 2.31 mg/L (Prayitno, Yanuwadi, & Laksmo, 2013). In this study, the average concentration of detergent in HWW was measured 2.51 mg/L. Kümmerer et al. (1997) determined the amount of surfactant in hospital water to be 6 mg BAC/L (Kümmerer, Steger-Hartmann, & Meyer, 1997). Verlicchi et al. (2010) reported in their review study that the average concentration of detergent in HWW was 4.5 mg/L and varied between 3 mg/L and 7.2 mg/L (Verlicchi et al., 2010). In this study, phenol measurement was also made in HWW and the average phenol concentration was determined as 0.67 mg/L. In the determination of phenol in wastewater from three different hospitals in Indonesia, the phenol

concentration was measured quite low (0.01-0.04 mg/L) (Prayitno et al., 2013). GA concentration in HWW was determined as 3.62 mg/L in this study. It was reported that the GA concentration in HWW was quite variable in different timeframes and the maximum value was measured as 3.9 $\mu\text{g/L}$ (Boillot et al., 2008).

Microbiological characterization: Bacterial flora concentration in HWW ranges from 2.4×10^3 to 3×10^5 per 100 mL. These concentration ranges are generally lower than the $10^8/100$ mL concentration given for domestic wastewater. The reason of this may be due to the presence of disinfectants and antibiotics in the HWW. *Total Coliform*, *Enterococci*, *Staphylococci*, *Salmonella*, *Shigella* and *Staphylococcus aureus* counts were performed in the wastewater samples taken within the scope of the study (Figure 1). In addition, the distribution of bacterial species was determined by making a total bacteria count and also dominant species were identified.

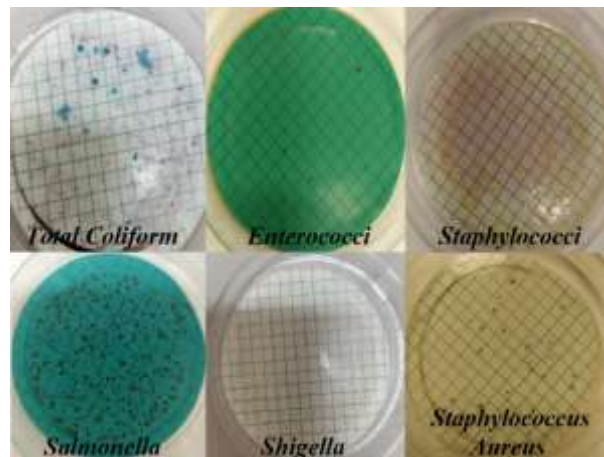


Fig. 1 Examples of samples with bacterial count

Total coliform population in HWW was measured in the range of 2.7×10^5 - 1.52×10^6 /100 mL. In addition, the most dominant type was found to be total coliform. In the study conducted in 2008 in Nigeria, it was reported that there was 1.8×10^3 MPN/100 mL Total coliform in HWW (Ekhaise & Omavwoya, 2008). In the characterization study conducted, in four different hospitals, the total coliform amount for each HWW was 1.8×10^9 MPN/100 mL, 3.5×10^8 MPN/100 mL, 4.2×10^6 MPN/100 mL and 2.4×10^8 MPN/100 mL (Amouei et al., 2015). In this study, *Enterococci*, which is known to resist antibiotics in HWW, was found to be between $3.5 \times 10^3/100$ mL and $1.8 \times 10^4/100$ mL. A group of researcher made Enterococci measurements in two different HWW and reported that they

were 1.5×10^3 MPN/100 mL and 8.6×10^4 MPN/100 mL (Fekadu & Getachewu, 2015). In this study, *Staphylococci* was determined between $1.5 \times 10^4/100$ mL and $5.7 \times 10^4/100$ mL in HWW. It is determined that *Staphylococci* are the second dominant species among bacteria after total coliform. In the study conducted in two different HWW, *Staphylococci* amount was reported as 2.0×10^3 cfu/mL for both HWW (Fekadu & Getachewu, 2015). In this study, *Salmonella* type was observed to be $1.6 \times 10^3/100$ mL and $6 \times 10^3/100$ mL in HWW. In a study carried out in China in 1998, it was reported that there was 2.2×10^5 cfu/100 mL *Salmonella* in HWW (Tsai & Lin, 1999). Fekadu et al. (2015) reported that the amount of *Shigella* in a HWW was 5/100 mL. Also in our study, $2.1 \times 10^2/100$ mL and $8 \times 10^2 /100$ mL *Staphylococcus aureus* were counted in HWW. Ekhaise and Omavwoya used wastewater from a training hospital in their study. They performed microbiological analyses in wastewater samples taken from different points, but in some points they did not give a numerical value even though they detected *Staphylococcus aureus* (Ekhaise & Omavwoya, 2008).

Ecotoxicological characterization: Considering all the experiments, done with Algal Toxkit F test for the detection of acute toxicity, algae cell growth curves in dilute wastewater showed that cell growth was slower in the next timeframe between 24-48 hours. The reason of this was because the cells first show that they are sensitive to the substances in the wastewater and then get used to the environment. In the study, toxic effect was clearly observed in some samples. In concentrate ones of these samples (dilution was done less), it was observed that cells tend to decrease rather than growth, especially between 24-48 hours. The most important factors in the toxicity study are the **dose** and the **contact time**. Especially considering the first 48-hour period, the toxic effect seems more clearly. Likewise, low and/or significant toxicity was found in the majority of the samples with low dilution rate. *Daphnia magna* toxicity test was also conducted for the HWW. As a result of the measurements made in the samples, the number of dead *Daphnia magna* was 1 in dilutions of 1/16 generally. In other dilution rates, deaths occurred in each sample. Also, after 48 hours, the number of dead *Daphnia magna* was higher. In general, the mortality rate in diluted HWW samples remains below 50%, while in raw wastewater this rate is above 50%. For this reason, dilute wastewater is not acute toxic, but HWW is acute toxic because it has a mortality rate of 50% and above. In addition, *Daphnia magna* test was performed in HWW taken daily. As a result of this study, it was observed that HWW did not show any acute toxic properties (mortality rate <50% or mortality rate = 0) on some days, and acute toxicity (mortality rate > 50%) on some days. Emmanuel et al., (2002) conducted an ecotoxic test of HWW with *Daphnia*

magna. They reported that the wastewater of the hospital had a very high toxicity ($116.8 \text{ equitox/m}^3$) (Evens Emmanuel, Perrodin, Keck, Blanchard, & Vermande, 2002). MUTA-Chroma Plate Test Kit (Ames Test): The method was used to determine the mutagenicity of HWW. In the study, samples were taken from the weekly wastewater and also from the composite sample prepared from these waters. It was decided whether the sample shows mutagenic properties and/or is slightly mutagenic, mutagenic or strongly mutagenic in accordance with the values corresponding to the positive cell numbers obtained in the mutagenicity analysis. In the study, 7 positive cells were detected for the background on the 5th day in the samples. Looking at the positive cell numbers on the 5th day in the samples, 24 and 61 positive cells were determined on Wednesday and Thursday, respectively. These values indicate that the wastewater sample from Wednesday was mutagenic and the sample from Thursday was strong mutagenic. No positive cells were detected in Saturday, Sunday and Monday samples. Therefore, it was concluded that the wastewater of these days does not show mutagenic properties. The positive cell count for Tuesday was found to be 3, indicating that today's wastewater was very slightly mutagenic. In the composite sample obtained by mixing all the days with the same volume, the number of positive cells was 10 on the 5th day. This showed that the obtained composite sample was also slightly mutagenic. In the studies carried out for the other weeks, composite samples were taken as basis and were done once a week. According to obtained results, the composite samples showed mild mutagenic properties. Hartmann et al., (1999) reported that HWW is mutagenic and can be completely eliminated by selecting the appropriate treatment method (Hartmann et al., 1999). Mutagenicity analysis of HWW was also carried out in the study made from the sewage of three large hospitals in India. TA 98, TA 100 and TA 102 strains were used in the study and it was reported that especially untreated HWW was very strong mutagenic (Gupta, Daigle, Mojica, & Hurley, 2009).

4. Conclusion

Differences in diagnosis, treatment and other services in hospitals and/or effects such as number of patients or bed capacity directly affect the HWW character. For this reason, it is common to find different values in studies with different HWW. As a result of the characterization study conducted in this study, it was determined that the HWW contains macropollutants such as 286.7 mg COD/L, 184.3 mg BOD/L, 166.85 mg TOC/L and 43.0 mg TKN/L. Some species were performed in wastewater and it was determined that the most dominant species was total coliform. Microbiological analyses showed that HWW was not microbiologically stable. In hourly studies with HWW, quite different results were also

showed that the microbiological character of the HWW changes according to the medical activity, scope and patient density of the hospital. *Daphnia magna* and toxicity tests, Ames test method, SOS Chromotest Method were used to determine the toxicity of the HWW, and it was observed that the toxicity of the HWW was slightly mutagenic and increased by decreasing the rate of dilution. The results show that the HWW should be pre-treated before it can be given to the sewer system.

5. Acknowledgement

This study was supported by The Scientific and Technological Research Council of Turkey [115Y277]

References

- Altin, A., Altin, S., & Degirmenci, M. (2003). Characteristics and treatability of hospital (medical) wastewaters. *Fresenius Environmental Bulletin*, 12(9), 1098–1108.
- Amouei, A., Asgharnia, H., Fallah, H., Faraji, H., Barari, R., & Naghipour, D. (2015). Characteristics of Effluent Wastewater in Hospitals of Babol University of Medical Sciences, Babol, Iran. *Health Scope*, 4(2), 4–7. Retrieved from <https://doi.org/10.17795/jhealthscope-23222>
- Boillot, C., Bazin, C., Tissot-Guerraz, F., Droguet, J., Perraud, M., Cetre, J. C., ... Perrodin, Y. (2008). Daily physicochemical, microbiological and ecotoxicological fluctuations of a hospital effluent according to technical and care activities. *Science of the Total Environment*, 403(1–3), 113–129. Retrieved from <https://doi.org/10.1016/j.scitotenv.2008.04.037>
- Boratyński, J., & Zal, T. (1990). Colorimetric micromethods for glutaraldehyde determination by means of phenol and sulfuric acid or phenol and perchloric acid. *Analytical Biochemistry*, 184(2), 259–262. Retrieved from [https://doi.org/10.1016/0003-2697\(90\)90677-2](https://doi.org/10.1016/0003-2697(90)90677-2)
- Chiang, C. F., Tsai, C. T., Lin, S. T., Huo, C. P., & Lo, K. V. (2003). Disinfection of Hospital Wastewater by Continuous Ozonation. *Journal of Environmental Science and Health - Part A Toxic/Hazardous Substances and Environmental Engineering*, 38(12), 2895–2908. Retrieved from <https://doi.org/10.1081/ESE-120025839>
- Clescerl, L. S., Green, A. E., & Eaton, A. D. (1998). *Standard Methods for the Examination of Water and Wastewater* (20th ed.). Washington

DC: American Public Health Association.

- Ekhaise, F. O., & Omavwoya, B. P. (2008). Influence of Hospital Wastewater Discharged from University of Benin Teaching Hospital (UBTH), Benin City on its Receiving Environment. *American-Eurasian Journal of Agricultural & Environmental Sciences*, 4(4), 484–488.
- Emmanuel, E., Perrodin, Y., Keck, G., Blanchard, J. M., & Vermande, P. (2005). Ecotoxicological risk assessment of hospital wastewater: A proposed framework for raw effluents discharging into urban sewer network. *Journal of Hazardous Materials*, 117(1), 1–11. Retrieved from <https://doi.org/10.1016/j.jhazmat.2004.08.032>
- Emmanuel, Evens, Perrodin, Y., Keck, G., Blanchard, J.-M., & Vermande, P. (2002). Effects of Hospital Wastewater on Aquatic Ecosystem. *XXVIII Congreso Interamericano de Ingeniería Sanitaria y Ambiental Cancún, México, 27 Al 31 de Octubre, 2002*, (October), 7.
- Escolà Casas, M., Chhetri, R. K., Ooi, G., Hansen, K. M. S., Litty, K., Christensson, M., ... Bester, K. (2015). Biodegradation of pharmaceuticals in hospital wastewater by a hybrid biofilm and activated sludge system (Hybas). *Science of the Total Environment*, 530–531, 383–392. Retrieved from <https://doi.org/10.1016/j.scitotenv.2015.05.099>
- Fekadu, S., & Getachewu, B. (2015). Microbiological Assessment of Indoor Air of Teaching Hospital Wards: A case of Jimma University Specialized Hospital. *Ethiopian Journal of Health Sciences*, 25(2), 117–122. Retrieved from <https://doi.org/10.4314/ejhs.v25i2.3>
- Gautam, A. K., Kumar, S., & Sabumon, P. C. (2007). Preliminary study of physico-chemical treatment options for hospital wastewater. *Journal of Environmental Management*, 83(3), 298–306. Retrieved from <https://doi.org/10.1016/j.jenvman.2006.03.009>
- Gupta, A., Daigle, S., Mojica, J., & Hurley, R. W. (2009). Patient perception of pain care in hospitals in the United States. *Journal of Pain Research*, 2, 157–164. Retrieved from <https://doi.org/10.2147/jpr.s7903>
- Hartmann, A., Golet, E. M., Gartiser, S., Alder, A. C., Koller, T., & Widmer, R. M. (1999). Primary DNA damage but not mutagenicity correlates with ciprofloxacin concentrations in german hospital wastewaters. *Archives of Environmental Contamination and Toxicology*, 36(2), 115–119. Retrieved from <https://doi.org/10.1007/s002449900449>

- Kümmerer, K., Steger-Hartmann, T., & Meyer, M. (1997). Biodegradability of the anti-tumour agent ifosfamide and its occurrence in hospital effluents and communal sewage. *Water Research*, 31(11), 2705–2710. Retrieved from [https://doi.org/10.1016/S0043-1354\(97\)00121-8](https://doi.org/10.1016/S0043-1354(97)00121-8)
- Mir-Tutusaus, J. A., Sarrà, M., & Caminal, G. (2016). Continuous treatment of non-sterile hospital wastewater by *Trametes versicolor*: How to increase fungal viability by means of operational strategies and pretreatments. *Journal of Hazardous Materials*, 318, 561–570. Retrieved from <https://doi.org/10.1016/j.jhazmat.2016.07.036>
- Pauwels, B., & Verstraete, W. (2006). The treatment of hospital wastewater: An appraisal. *Journal of Water and Health*, 4(4), 405–416. Retrieved from <https://doi.org/10.2166/wh.2006.025>
- Prayitno, K. Z., Yanuwadi, B., & Laksmono, R. W. (2013). Study of Hospital Wastewater Characteristic in Malang City. *Research Inveny: International Journal Of Engineering And Science*, 2(2), 2278–4721.
- Tsai, C. T., & Lin, S. T. (1999). Disinfection of hospital waste sludge using hypochlorite and chlorine dioxide. *Journal of Applied Microbiology*, 86(5), 827–833. Retrieved from <https://doi.org/10.1046/j.1365-2672.1999.00732.x>
- Verlicchi, P., Galletti, A., Petrovic, M., & BarcelÓ, D. (2010). Hospital effluents as a source of emerging pollutants: An overview of micropollutants and sustainable treatment options. *Journal of Hydrology*, 389(3–4), 416–428. Retrieved from <https://doi.org/10.1016/j.jhydrol.2010.06.005>

CHAPTER VII

THE EFFECT OF TEMPERATURE AND Al CONTENT ON THE THERMO-ELECTRICAL, MICROSTRUCTURE AND MECHANICAL PROPERTIES OF Sn-Al ALLOYS

Prof. Dr. Fatma MEYDANERİ TEZEL* and Prof. Dr. Buket SAATÇI**

*Department of Metallurgy and Materials Engineering, Faculty of Engineering, Karabük University, 78050, Karabük, Turkey,
E-mail: fatmameydaneri@karabuk.edu.tr,
ORCID ID: 0000-0003-1546-875X

**Department of Physics, Faculty of Sciences, Erciyes University, 38039, Kayseri, Turkey, E-mail: bayender@erciyes.edu.tr,
ORCID ID: 0000-0002-1351-5279

1. Introduction

Al-Sn alloys have high corrosion resistance, thermal conductivity*, and abrasion resistance. They are also environmentally friendly (Pb-free), cheap, economical, and suitable for the production of bearing materials. These alloys are extensively used in engineering applications. Thanks to their high load carrying capacity, low density, lightweight, excellent castability, wear resistance, fatigue resistance, and sliding properties, they are widely used for sliding bearing applications in gas turbines, automobile industries, aircraft, and aerospace industries. Al-Sn is an immiscible binary alloy system. Sn has a solid solubility in Al below 0.09 wt.% at room temperature; it is dissoluble in Al. The melting temperature of Al is 933 K (660 °C), which is almost three times higher than that of Sn. The density of Sn is 7.28 gr/cm³, which is about three times higher than Al. The immiscibility of the Al-Sn system, the huge difference between their melting temperatures, and the density difference between Al and Sn cause coarse grains and segregation in Al-Sn alloys. The insoluble Sn phase causes the segregation of Al-Sn alloy. The width of the Al-Sn alloy's Mushy zone increases with the increase of Sn content. Because of the soft content (6-40%), tin is distributed in the Al matrix in the reticular structure through the edges of Al grains at a different phase

* Only the thermal conductivity part of the our working was published in *Fluid Phase Equilibria*, 298 (2010) 97-105, and referenced in the chapter.

(Nassar et al.,2015; O'sorio et al.,2006; Cruz et al.,2010; Kim et al.,2015; Liu et al.,2009; Cruz et al.,2008; Liu et al.,2008).

The materials' thermal and electrical properties provide information about the stability of phases, driving forces of chemical reactions, diffusion processes, the development of electronic materials, and interconnection technologies, especially in modern industry and microelectronics. Furthermore, in most cases, high-level mechanical properties are required for industrial applications. The hardness and strength of these alloys mainly depend on their microstructure. Thus, many micromechanical investigations have been performed to evaluate their performance. Hence, this study aims to analyze the some mechanical, thermal and electrical properties of Sn-(x) wt. % Al (x= 0.5, 2.2, 25, 50, 75) alloys, lacking in the literature, using experimental and theoretical calculations.

2. Experimental procedure

This study was performed in three steps. Sn and Al amounts in the compounds were calculated in the first step versus the Sn-Al binary phase diagram. They were melted in a graphite crucible in the vacuum melting furnace, and the melted alloys were cast into specially designed graphite mold placed in the hot casting furnace. They were solidified directionally, from bottom to top. Thermal conductivity coefficients of these alloys (Sn-(x) wt. % Al (x= 0.5, 2.2, 25, 50, 75)) were measured using the radial heat flow apparatus. The experimental system and specially designed graphite mold were detailed in the literature (Meydaneri et al.,2010). The variations of electrical conductivity and resistivity with temperature and composition were determined from the Wiedemann-Franz-Lorenz law and Smith-Palmer equation using thermal conductivities and the Lorenz coefficient. In the second step, the fusion enthalpies (ΔH) and change of the specific heat capacities (ΔC_p) were determined. In the third step, surface morphologies, compositions, grain sizes, tensile strength, and microhardness properties of the alloys were investigated.

2.1 Measurement of the thermal conductivity

Different methods are used to determine the thermal conductivity of materials experimentally (Touloukian et. al.,1970; Callendar& Nicolson, 1897; Niven, 1905; Powell, 1939; McElroy& Moore, 1969; Gündüz& Hunt, 1985; Saatçi et al., 2006; Meydaneri et al., 2011; Meydaneri et al., 2010). The radial heat flow method is a well-known process for obtaining the thermal conductivity of solids. In this method, a sample in the form of

a right circular cylinder with a coaxial central hole, which contains either a heater or a heat sink, is used. Radial heat flow was preferred in this study, considering the symmetrical characteristics of Sn-(x) wt. % Al (x= 0.5, 2.2, 25, 50, 75) solid alloys. Experimental measurements and the radial heat flow apparatus are given in (Niven, 1905; Powell, 1939; McElroy& Moore, 1969; Gündüz& Hunt, 1985; Saatçi et al., 2006; Meydaneri et al., 2011; Meydaneri et al., 2010; Terada et al., 1999). The values of the thermal conductivity of Sn- (x) wt. % Al (x= 0.5, 2.2, 25, 50, 75) alloys with temperature and composition is shown in Figs. 1-2.

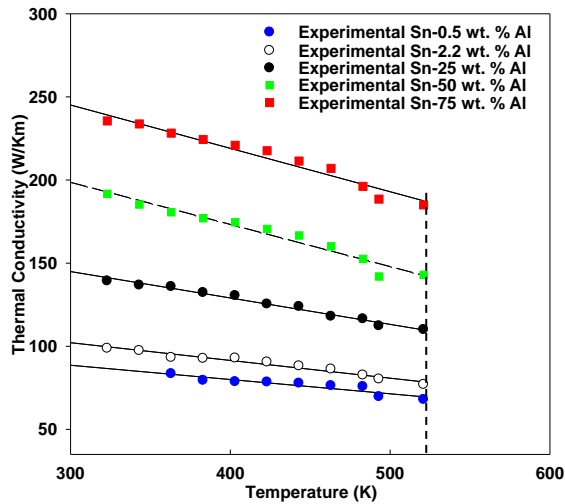


Fig. 1 Thermal conductivity of Sn-(x) wt.% Al (x= 0.5, 2.2, 25, 50, 75) alloys vs. temperature.

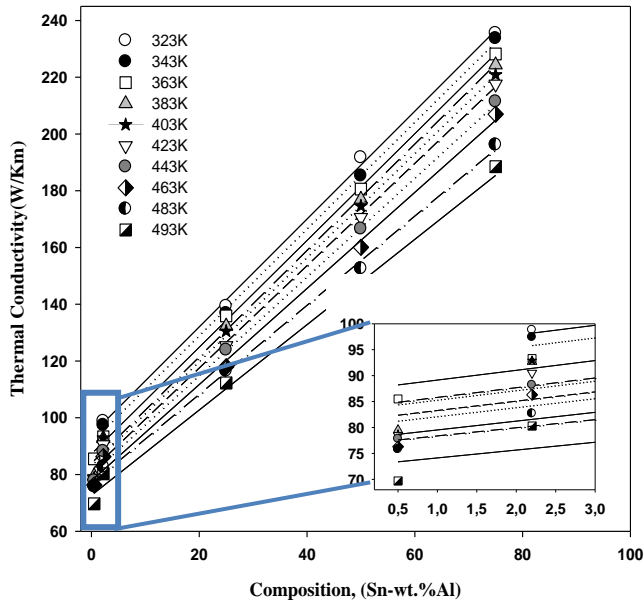


Fig. 2 Thermal conductivity of Sn-(x) wt.% Al (x= 0.5, 2.2, 25, 50, 75) alloys vs. composition.

2.2 Determination of the electrical conductivity and electrical resistivity

Conductivity and temperature coefficient of resistance are important electrical characteristics of any material. These two properties generally determine how the material is used in various electrical and electronic components, from wire to resistors, potentiometers, and many more. Electrons carry the current in metals without changing the chemical properties of metal. Electrical conductivity (EC), which is the ability to conduct an electric current, is one of the physical properties of materials (<http://www.rrcap.unep.org>). Electrical conductivity is affected by substances' chemical composition and the stress of crystalline structures. Therefore, electrical conductivity can be used to classify materials, determine the proper heat treatment for metals, and inspect for heat damage in some materials. Electrical conductivity is provided by free electrons, whereas both electrons and phonons play a role in thermal conductivity. The relation between thermal conductivity and electrical resistivity is explained by the Wiedemann-Franz-Lorenz law (Yamasue et al., 2003):

$$\frac{\kappa \rho_e}{T} = \frac{\pi^2 k^2}{3e^2} = L_0 = 2.445 \times 10^{-8} \text{W}\Omega\text{K}^{-2} \quad (1)$$

where k is the Boltzman constant, e is the electron charge, T is the absolute temperature and L_0 is Lorenz number. According to the Wiedemann-Franz law, the relation between the electrical conductivity and thermal conductivity is given as,

$$\sigma = \frac{\kappa_S}{LT} \quad (2)$$

where σ is the electrical conductivity, κ_S is the thermal conductivity of the solid phase at temperature T , and L is the Lorenz number. Wiedemann-Franz-Lorenz law can be modified to link thermal conductivity and electrical resistivity of complex alloys into the following form:

$$\kappa = A \frac{L_0 T}{\rho_e} + BT + C \quad (3)$$

where A , B , and C are empirical constant. Smith-Palmer (Smith&Palmer, 1935) suggested that the thermal conductivity of many alloys could be expressed by Eq.(3) if $A=0.904$, $B=0$ and $C=5.27$.

In the study, the variation of electrical conductivity with temperature and composition was determined from the Wiedemann-Franz law and Smith-Palmer equation. L seems constant and independent of the properties of materials. However, the value of L , which can be obtained in the letterure, depends on the properties of materials. They are well-known for pure materials, but they are unknown for alloys, L and κ_S are required to show electrical conductivity change with temperature and composition. The Lorenz numbers for pure Al and pure Sn are 2.24×10^{-8} and $2.49 \times 10^{-8} \text{W}\Omega/\text{K}^2$ (Sergent&Krum, 1998).

$$L_{alloy} = \sum_{n=1}^2 x_n L_n \quad (4)$$

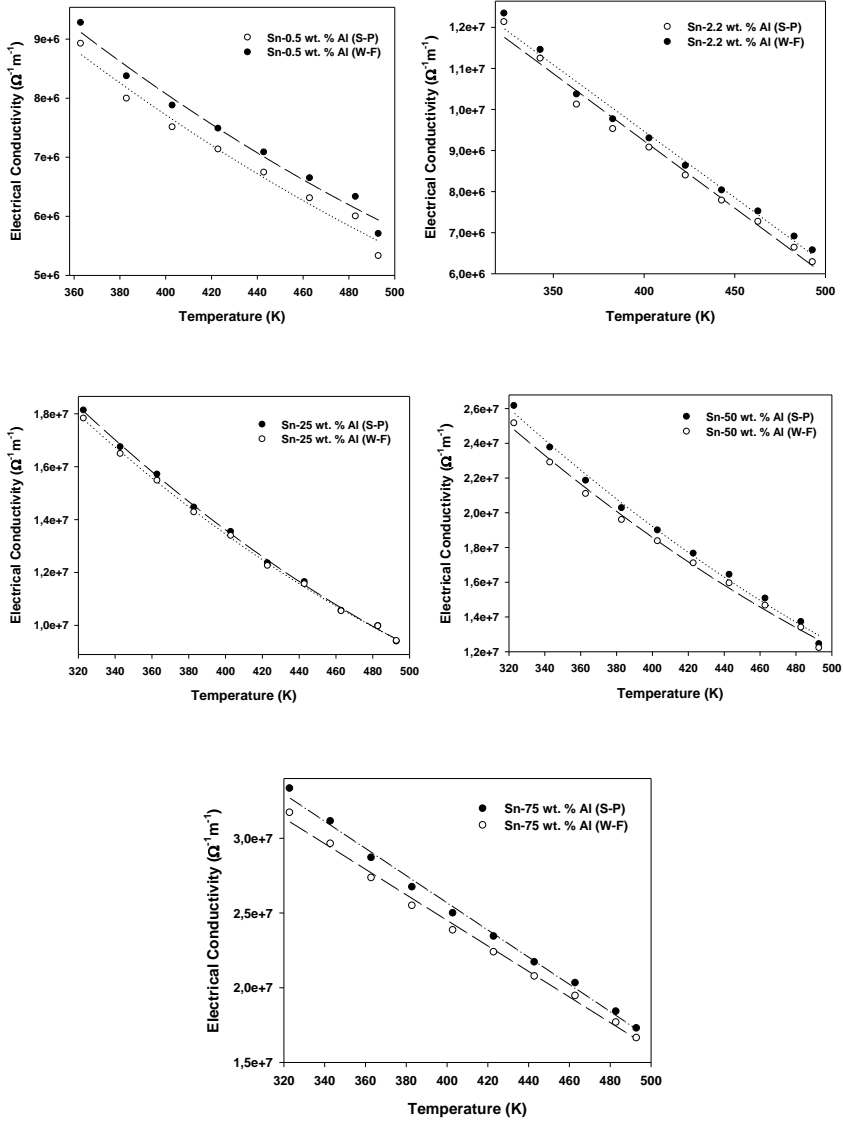


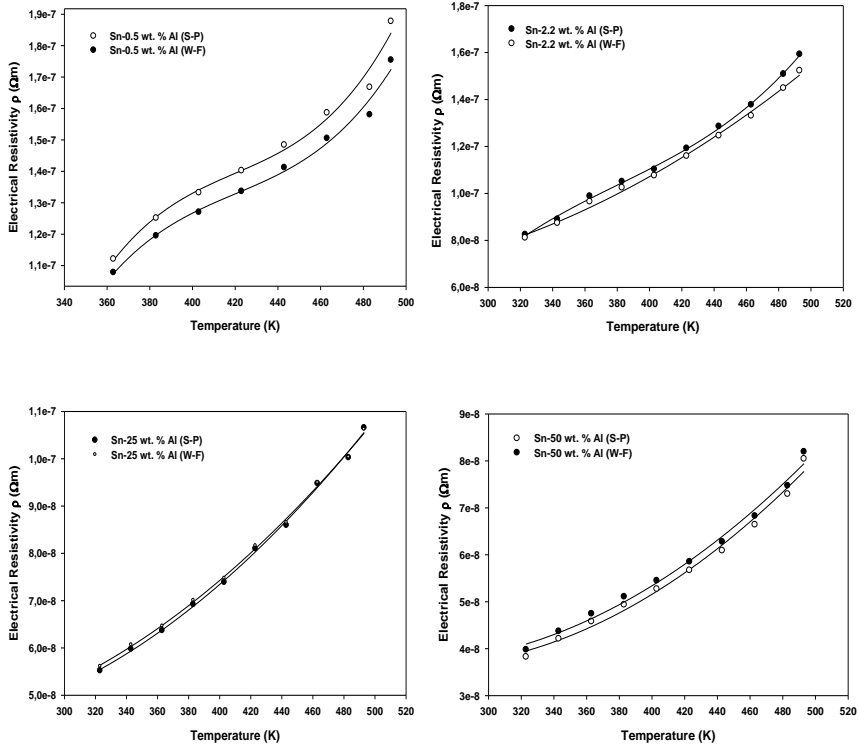
Fig. 3 Electrical conductivity of Sn-(x) wt. % Al (x= 0.5, 2.2, 25, 50, 75) alloys vs. temperature.

Lorentz values for Sn-Al binary alloys were calculated from Eq. (4). X_n is the percent by weight of the n^{th} component; L_n is the percent of the Lorentz value of the n^{th} component. Electrical conductivities of Sn-Al binary alloys changing with temperature and composition were determined by using L_{alloy} and κ_S . The variation of electrical conductivity

and electrical resistivity of Sn-(x) wt. % Al (x=0.5, 2.2, 25, 50, 75) alloys with temperature and composition are shown in Fig. 3-6. The relationship between electrical conductivity and temperature is often expressed as the slope of the electrical conductivity curve and can be depicted as:

$$\alpha_{ETC} = \frac{1}{\sigma_0} \frac{\Delta\sigma}{\Delta T} = \frac{\sigma - \sigma_0}{\sigma_0(T - T_0)} \quad (5)$$

where σ is the electrical conductivity of the solid phase at temperature T , σ_0 is the electrical conductivity at the initial temperature T_0 , and α_{ETC} is the electrical temperature coefficient. The electrical temperature coefficients for Sn-(x) wt. % Al (x=0.5, 2.2, 25, 50, 75) alloys were obtained from the graph of electrical conductivity vs. temperature and given in Table 1.



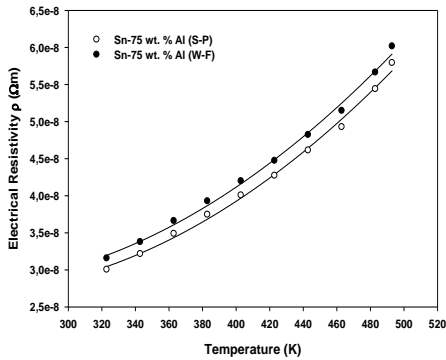


Fig. 4 Electrical resistivity of Sn-(x) wt. % Al (x= 0.5, 2.2, 25, 50, 75) alloys vs. temperature.

Table 1 Thermal and electrical properties of Sn-(x) wt. % Al (x=0.5, 2.2, 25, 50, 75) alloys.

| Sample | T ₀ [K] | T [K] | κ ₀ [W/Km] | κ [W/Km] |
|-----------------|-----------------------|-----------------------|-----------------------|-----------------------|
| Sn-0.5 wt. % Al | 363 | 493 | 83.50 | 69.70 |
| Sn-2.2 wt. % Al | 323 | 493 | 98.80 | 80.30 |
| Sn-25 wt. % Al | 323 | 493 | 139.30 | 112.30 |
| Sn-50 wt. % Al | 323 | 493 | 191.70 | 142.00 |
| Sn-75 wt. % Al | 323 | 493 | 235.50 | 188.50 |
| Sample | σ ₀ (W-F) | σ (W-F) | σ ₀ (S-P) | σ (S-P) |
| Sn-0.5 wt. % Al | 9.27x10 ⁶ | 5.70x10 ⁶ | 9.61x10 ⁶ | 5.82x10 ⁶ |
| Sn-2.2 wt. % Al | 12.33x10 ⁶ | 6.56x10 ⁶ | 12.91x10 ⁶ | 6.78x10 ⁶ |
| Sn-25 wt. % Al | 17.82x10 ⁶ | 9.41x10 ⁶ | 18.96x10 ⁶ | 9.92x10 ⁶ |
| Sn-50 wt. % Al | 25.14x10 ⁶ | 12.20x10 ⁶ | 27.05x10 ⁶ | 12.99x10 ⁶ |
| Sn-75 wt. % Al | 31.70x10 ⁶ | 16.62x10 ⁶ | 34.28x10 ⁶ | 17.87x10 ⁶ |
| Sample | ρ ₀ (W-F) | ρ (W-F) | ρ ₀ (S-P) | ρ (S-P) |
| Sn-0.5 wt. % Al | 10.7x10 ⁻⁸ | 17.5x10 ⁻⁸ | 10.4x10 ⁻⁸ | 17.1x10 ⁻⁸ |
| Sn-2.2 wt. % Al | 8.10x10 ⁻⁸ | 15.2x10 ⁻⁸ | 7.74x10 ⁻⁸ | 14.7x10 ⁻⁸ |
| Sn-25 wt. % Al | 5.61x10 ⁻⁸ | 10.6x10 ⁻⁸ | 5.27x10 ⁻⁸ | 10.0x10 ⁻⁸ |
| Sn-50 wt. % Al | 3.97x10 ⁻⁸ | 8.19x10 ⁻⁸ | 3.69x10 ⁻⁸ | 7.69x10 ⁻⁸ |

| | | | | |
|-----------------|---|---|-----------------------|-----------------------|
| Sn-75 wt. % Al | 3.15×10^{-8} | 6.01×10^{-8} | 2.91×10^{-8} | 5.59×10^{-8} |
| Sample | α_{ETC} (S-P) [K ⁻¹] | α_{ETC} (W-F) [K ⁻¹] | | |
| Sn-0.5 wt. % Al | 3.03×10^{-3} | 2.96×10^{-3} | | |
| Sn-2.2 wt. % Al | 2.79×10^{-3} | 2.75×10^{-3} | | |
| Sn-25 wt. % Al | 2.80×10^{-3} | 2.77×10^{-3} | | |
| Sn-50 wt. % Al | 3.05×10^{-3} | 3.02×10^{-3} | | |
| Sn-75 wt. % Al | 2.81×10^{-3} | 2.79×10^{-3} | | |

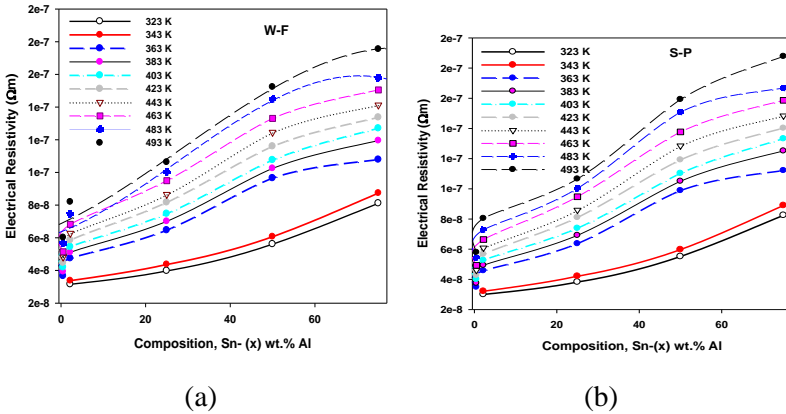


Fig. 5 (a) Electrical resistivity variations (W-F) (b) Electrical resistivity (S-P) of Sn-(x) wt.% Al (x=0.5, 2.2, 25, 50, 75) alloys vs. composition.

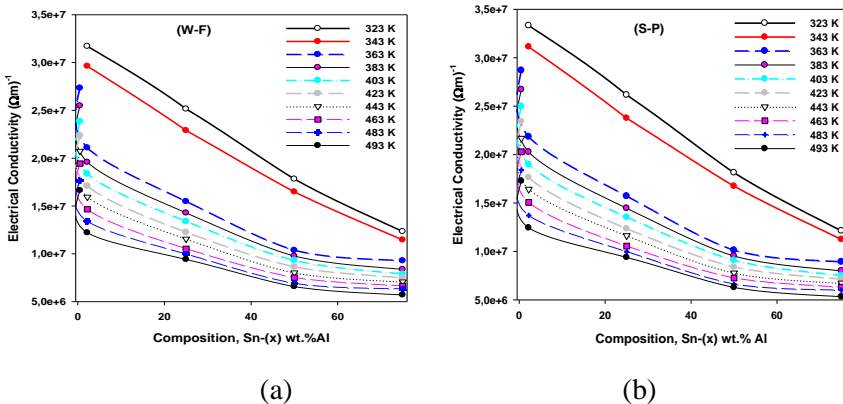


Fig. 6 (a) Electrical conductivity variations (S-P) (b) Electrical conductivity (W-F) of Sn-(x) wt. % Al (x=0.5, 2.2, 25, 50, 75) alloys vs. composition.

2.3 Measurement of enthalpy change and specific heat capacity

The molecular structure and phase determine the specific heat capacity of a material. The latent heat of phase transitions and the heat capacity should be known to understand phase transitions and the thermodynamics of a certain material. For most solids, the heat capacity is controlled by the vibrations of the atoms at temperatures far from the phase transitions.

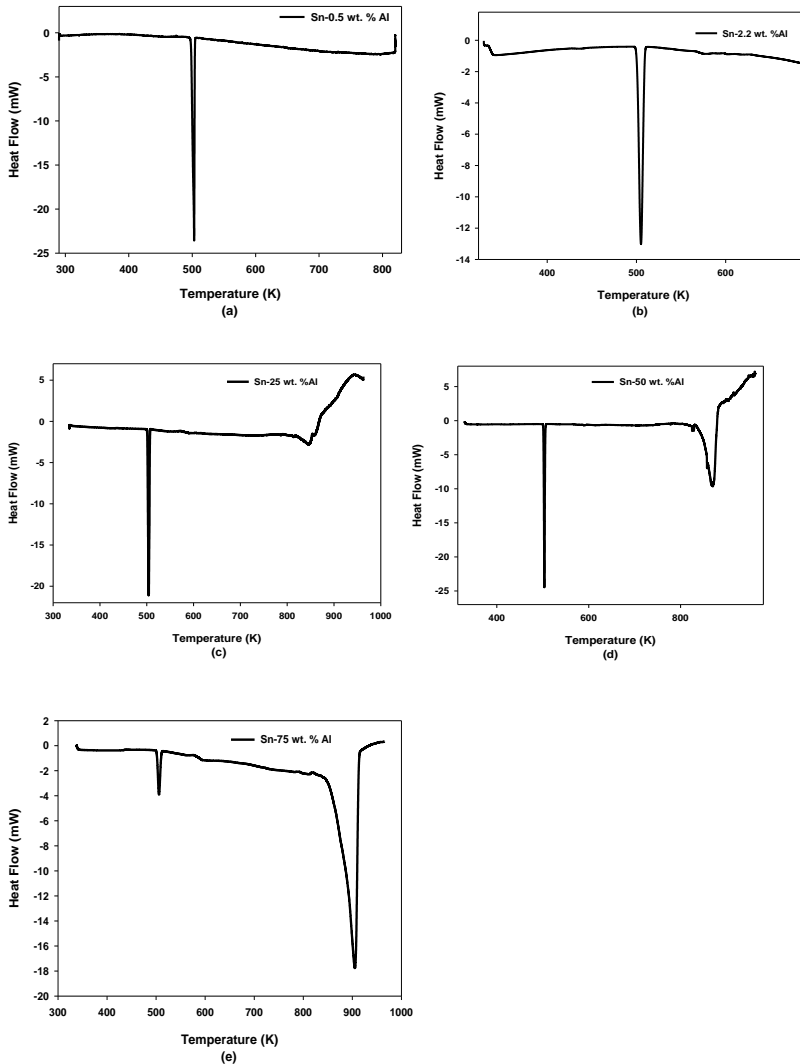


Fig. 7 Heat flow curves vs. temperature for Sn-(x) wt. % Al (x= 0.5, 2.2, 25, 50, 75) alloys.

C_p = Specific heat capacity at constant pressure,

$$C_p = \left(\frac{\partial H}{\partial T} \right)_p \quad (6)$$

The heat supplied to the system will not increase its melting temperature but will supply the enthalpy of fusion (the latent heat of melting) required for the passage from solid to liquid the enthalpy of fusion and specific heat capacity changes of Sn- (x) wt. % Al (x = 0.5, 2.2, 25, 50, 75) alloys were measured by DSC (Perkin Elmer Diamond model) in the temperature range of 300-800 K (27-527°C), with a heating rate of 1°C/min and under a constant flow of nitrogen at atmospheric pressure. The DSC curve of Sn-(x) wt. % Al (x=0.5, 2.2, 25, 50, 75) alloys are shown in Fig. 7. The enthalpies of fusion (ΔH) of the alloys were obtained from the area under the curve by the program of the DSC device. Specific heat change (ΔC_p) was determined by dividing it by the temperatures of the enthalpies of fusion (T_{peak}).

2.4 Investigation of microhardness and tensile strength

Mechanical properties such as hardness, tensile strength, wear properties, and fatigue resistance are related to the composition, microstructure, processing temperature, etc. (Frear et al., 1994). They are usually measured using tensile strength test, hardness test, ductility test, etc. Tensile strength test of solidified alloys gave inconsistent results with a wide scatter due to the strong dependence on material's surface properties/quality. Hence, they were measured by hardness testing, which is one of the easiest ways to determine the structure's mechanical properties at the different phases. The microhardness measurement was performed at room temperature using a hardness tester device (Q10 A + QNESS at Iron and Steel Institute). The microhardness measured by the Vickers method is defined as the ratio of the load applied (in kg) to the projected area of the indentation (in mm^2). Vickers hardness measurement was performed to clarify the relationship between microstructure and microhardness. Vickers hardness value was obtained as

$$H_V = \frac{2F \sin(\phi/2)}{d^2} \quad (7)$$

where ϕ is the indenter apex angle, F is the applied load, and d is the average length of diagonals. The pyramid on square base diamond indenter is attached to a metallurgical microscope. An optimum load of

10 g was chosen and applied for 10 seconds to the sample. Due to the variation of hardness, seven different spots on the sample were indented. The accuracy of the microhardness measurement was about $\pm 1\%$. The average microhardness was used to eliminate the variation in crystallographic orientations of the sample.

Tensile strength was calculated by dividing the maximum force carried by the sample during the test by the original cross-sectional area of the sample. The samples are prepared as cylinders of 55 mm length and 10 mm diameter. Tensile tests were applied by a testing machine (Zwick / Roell Z600 Universal Testing Device, KBU-MARGEM) to obtain elongation and tensile strength data. The speed of the test was set as 10 mm/min at room temperature. Tensile strength and microhardness according to composition are given in Table 2.

Table 2 Grain sizes, microhardness, and tensile test values of Sn-(x) wt. % Al (x=0.5, 2.2, 25, 50, 75) alloys.

| Samples | Max. Tensile (MPa) | Max. Elongation (%) | Elastic Tensile 2-7 Kgf-mm ² | |
|-----------------|---------------------------------------|--|---|--------|
| Sn-0.5 wt. % Al | 86.88 | 19.5671 | 164.497 | |
| Sn-2.2 wt. % Al | 82.27 | 19.0654 | 158.900 | |
| Sn-25 wt. % Al | 82.89 | 25.4727 | 58.5257 | |
| Sn-50 wt. % Al | 78.43 | 30.5673 | 39.9642 | |
| Sn-75 wt. % Al | 80.83 | 28.1994 | 52.9278 | |
| Samples | YS1 Strength 0.2% Kgf/mm ² | Vickers Micro hardness (Hv _{0.01}) | D, Grain Size (nm) D _{Al} D _{Sn} | |
| Sn-0.5 wt. % Al | 7.02992 | 33.73 | 42.62 | 154.03 |
| Sn-2.2 wt. % Al | 7.02034 | 34.7 | 49.46 | 124.08 |
| Sn-25 wt. % Al | 7.00974 | 66.86 | 54.3 | 96.00 |
| Sn-50 wt. % Al | 7.00604 | 60.4 | 60.10 | 38.98 |
| Sn-75 wt. % Al | 7.01166 | 66.20 | 92.41 | 29.58 |

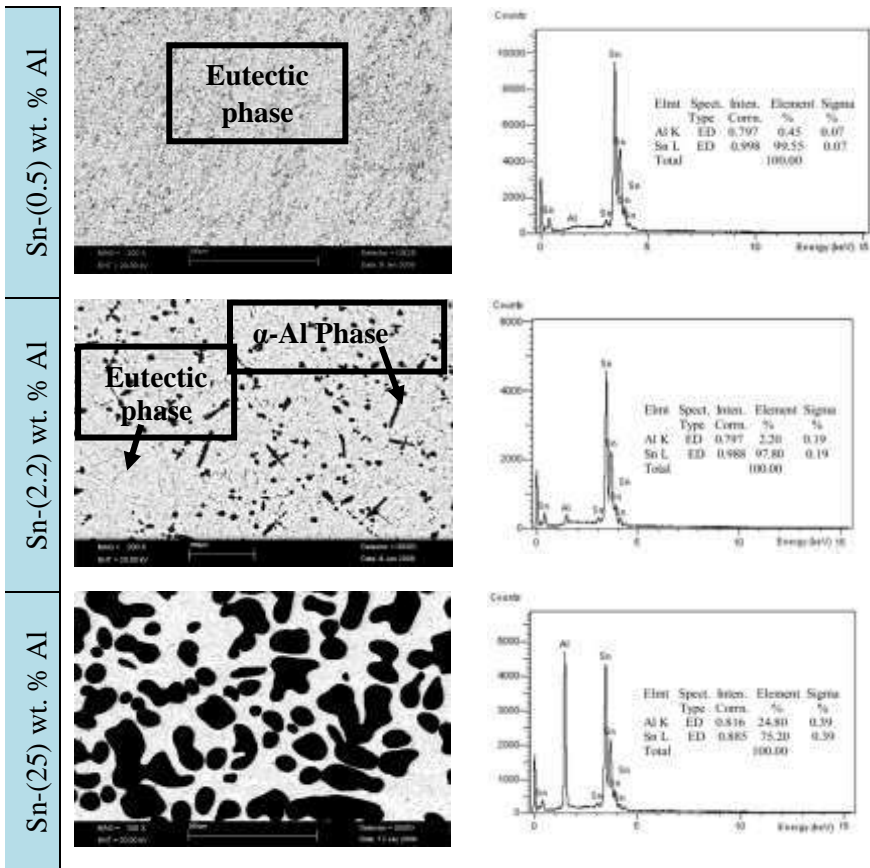
2.5 Surface morphology, composition analysis, and grain sizes

The surface morphology of the alloys was explored via a computer-controlled LEO 440 scanning electron microscope (SEM). The ratio of

chemical compositions was measured by an EDX spectrometer attached to the SEM. SEM images and EDX analyses were shown in Fig. 8. A Bruker AXS D8 Advance Model XRD diffraction device was used to determine the samples' diffraction patterns; the powder diffraction patterns were taken with a 40 mA current and 0.02 °/s scanning speed (CuK α 1 radiation). Grain sizes (D) was obtained by using Scherrer's formula (Mamazza et al., 2005):

$$D = \frac{0.9\lambda}{\beta \cos\theta} \quad (8)$$

where λ is the wavelength of X-ray used (1.5406 Å), β is the half-width of the peak with maximum intensities, θ is Bragg's angle.



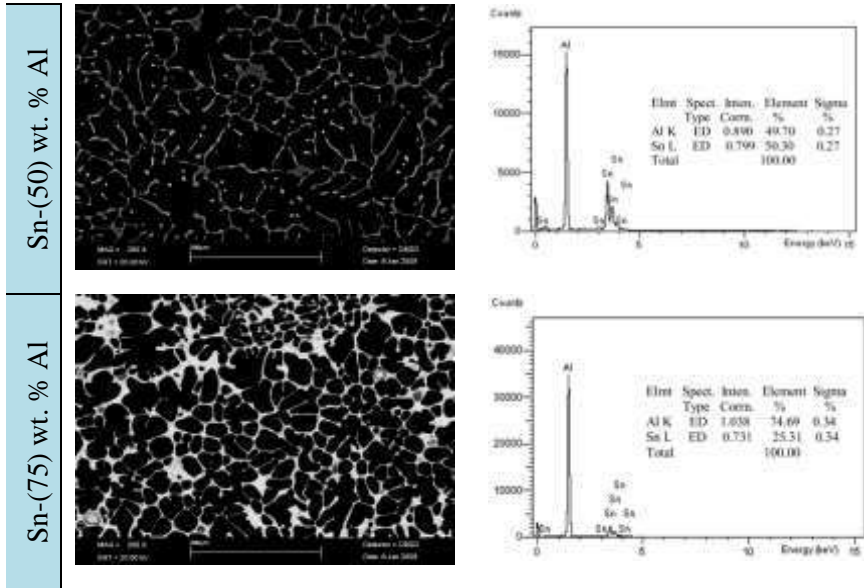


Fig. 8 SEM images and EDX analyses of Sn-(x) wt. % Al (x= 0.5, 2.2, 25, 50, 75) alloys.

3. Results and discussions

3.1 The thermal conductivity

The eutectic melting temperature of the Sn-Al binary system is about 501 K. The thermal conductivity of the solid phase of Sn-(x) wt. % Al (x=0.5, 2.2, 25, 50, 75) alloys (κ_S), versus temperature and composition is shown in Fig.1-2. According to the results, Sn-Al alloys' thermal conductivity linearly decreases with increasing temperature, but linearly increases with increasing Al's content for a given temperature. The thermal conductivities of Sn-(x) wt. % Al (x=0.5, 2.2, 25, 50, 75) alloys at their melting temperature and the values of κ_S in the literature were shown in Table 3, and they were similar (Cruz et al., 2008; Touloukian et al., 1970). The thermal conductivity κ_S is the sum of the contributions of phonons and electrons to heat transfer. The electronic component κ_{el} is negligible at low temperatures, but it accounts for up to 10-15 % of the conduction above 300 K (Chen& Savvides, 2010; Liu et al., 2011). Phonon-phonon and phonon-electron inelastic scattering at high temperatures are quite intense. Thermal conductivity differs depending on the bulk stoichiometry and structural defects of alloys. In other words, some alloy systems show only limited solubility at any temperature, while others exhibit complete solid solubility (e.g., Cu-Ni). Solubility

limits are expressed as a series of rules often called William Hume-Rothery Rules (Mizutani, 2011). According to these rules, Al-Sn is a simple eutectic system with limited solid solubility in the two-terminal solid solutions, Fcc (Al) and tetragonal (β -Sn). Pure Sn transforms from Bct (β -Sn) to diamond cubic structure (α -Sn) at low temperatures. Sn-Al solubility is limited because the Sn's atomic radius is higher than the Al's atomic radius, and their crystal structures and valences are different. Therefore, the crystal lattice is distorted; hence the thermal conductivity that decreases with temperature increases with the increase of Al composition.

Table 3 κ_s values of Sn-Al alloys obtained in this study and κ_s values of previous studies.

| Sample | Temperature [K] | Thermal conductivity κ_s [W/Km] |
|-----------------|-----------------|--|
| Sn-50 wt. % Al | 324.2 | 139.3(Touloukian et al., 1970) |
| Sn-40 wt. % Al | 324.2 | 125.5(Touloukian et al., 1970) |
| Sn-30 wt. % Al | 324.2 | 114.2(Touloukian et al., 1970) |
| Sn-20 wt. % Al | 324.2 | 95.0(Touloukian et al., 1970) |
| Sn-10 wt. % Al | 324.2 | 81.2(Touloukian et al., 1970) |
| Sn-90 wt. % Al | 324.2 | 186.2(Touloukian et al., 1970) |
| Sn-70 wt. % Al | 324.2 | 173.2(Touloukian et al., 1970) |
| Sn-80 wt. % Al | - | 183.8(Cruz et al., 2008) |
| Sn-70 wt. % Al | - | 169.2(Cruz et al., 2008) |
| Sn-60 wt. % Al | - | 154.6(Cruz et al., 2008) |
| Sn-0.5 wt. % Al | 501 | 69.70 [PW] |
| Sn-2.2 wt. % Al | 501 | 80.30 [PW] |
| Sn-25 wt. % Al | 501 | 112.30 [PW] |
| Sn-50 wt. % Al | 501 | 142.00 [PW] |
| Sn-75 wt. % Al | 501 | 188.50 [PW] |

3.2 The electrical properties

The variations of electrical conductivity and resistivity of Sn-Al alloys with temperature and composition are shown in Fig. 3-6. The electrical conductivity (σ_0 and σ) and electrical resistivity (ρ_0 and ρ) of the alloys at their initial (T_0) and melting (T) temperatures are given in Table 1. Electrical temperature coefficients (α_{ETC}) were obtained using W-F conductivities; S-P conductivities of the alloys are shown in Table 1. σ decreases with the temperature increase, whereas ρ increases with the

temperature increase. The electrical conductivity on the content of Al is linearly decreased as the composition of Al increases for a given temperature. However, the variations of electrical conductivity with the temperature decrease exponentially for pure Al. According to these results, the linear decrease of the electrical conductivities of Sn-Al alloys may be due to the transmission provided by the maximum number of electrons. The metals's electrical resistivity increases with temperature and electron-phonon interactivity can play a key role. The number of mobile charge carriers in a metal depends on the carrier's Fermi energy concentration. Free electron concentration in metals (at finite temperatures like room temperature) does not change with temperature increase since it is already too high to contribute new electrons. However, increasing temperature increases electrical resistance because of the electrons's collisions among themselves and with the lattice edge. The time between two collisions is called τ ; collision will increase quickly in metals with the temperature increase. As the number of imperfections in the atomic lattice structure increases with temperature, electron movements are impeded, which causes an increase in resistivity. These imperfections include dislocations, vacancies, interstitial defects, and impurity atoms (Onaran, 2009). The sample may contain both micro cracks and voids. In literature, electrical conductivity and electrical resistivity of Al and Sn are 3.5×10^7 and 9.17×10^6 (Ωm)⁻¹ and 2.82×10^{-8} and 1.09×10^{-7} (Ωm) [~at 293 K (20 °C)] https://en.wikipedia.org/wiki/Electrical_resistivity_and_conductivity (Accessed 10 April 2016), respectively. As given in Table 1, this study's electrical conductivity and electrical resistivity values are coherent with the literature.

3.3 Determination of enthalpy change and the specific heat

As can be seen from DSC analysis of Sn-(x) wt. % Al (x=0.5, 2.2, 25, 50, 75) alloys, Sn-Al solubility is limited because the Sn' atomic radius is larger than the Al's atomic radius, and their crystal structures and valences are different. Therefore, two peaks were observed as the amount of Al increases. The total area under these two peaks gives the fusion enthalpy of the alloy. For other pure and alloy systems, specific heat capacity change is calculated by dividing the fusion enthalpy values, the area under the curve, by the melting temperature that peaks occurred. The enthalpy of fusion (ΔH) of Sn-(x) wt. % Al (x=0.5, 2.2, 25, 50, 75) alloys were 62.96 J/g, 63.54 J/g, 126.85 J/g, 182.34 J/g, 301.68 J/g, respectively. Also, the change of specific heat (ΔC_p) for Sn-(x) wt. % Al (x=0.5, 2.2,

25, 50, 75) alloys were 0.124 J/gK, 0.126 J/gK, 0.250 J/gK, 0.360 J/gK and 0.596 J/gK, respectively. In literature, the enthalpy of fusion for Al and Sn are 398.7 and 58.9 J/g (Hultgren et al., 1963), respectively, and the specific heat change for pure Al and Sn are 0.427 and 0.117 J/gK (Aksöz et al., 2010; Ocak et al., 2010). The resulting ΔH and ΔC_p are consistent with the literature.

3.4 Mechanical properties

Microhardness of Sn-(x) wt. % Al (x= 0.5, 2.2, 25, 50, 75) alloys were calculated from the average microhardness measurements of Sn and Al phases and Sn-Al grain boundaries. Solidification conditions of Sn-(x) wt. % Al (x= 0.5, 2.2, 25, 50, 75) alloys were the same. However, depending on the composition, an increase is observed in microhardness from the eutectic Sn-0.5 wt. % Al alloy to Sn-25 wt. % Al alloy with the increase of Al ratio. In Sn-50 wt. % Al and Sn-75 wt. % Al alloys, the microhardness decreased with the increase of grain size or the decrease of grain boundaries (Hall-Petch equation). Average microhardness and grain sizes of Sn-(x) wt. % Al (x=0.5, 2.2, 25, 50, 75) alloys were given in Table 2. Inhomogeneous distribution of Sn phase along the grain boundaries had a softening effect. Different distributions of the Sn phase in the Al matrix result in different effects on hardness. Regarding the microhardness of Al-based alloys in the literature, (Liu et al., 2008) reported 63 ± 2 HRC for Al-20 wt. % Sn alloy is produced by mechanical alloying and sintering. (Pathak and Mohan,2003) obtained 33.2 (BHN) and 25.2 (BHN) microhardness for Al-based Al-20.3 Sn-1.1. Cu alloy and Al-20.6Pb-1.1 Cu, respectively. (Noskova et al., 2008) reported 34.8 kg/mm² for Al-%30 Sn alloy, 30.7 and 56.2 kg/mm² for Al+%5Sn+%35 Pb ternary alloy. The average microhardness of Sn-based Sn-1.2wt.% Cu (Çadırlı et al., 2009), Sn-3.5wt.%Ag (Meydaneri et al.,2013), Sn-2 wt.% Mg (Meydaneri&Saatçi,2014) and Sn-9Zn-0.5Al (Das et al., 2009) alloys were 11.36 kg/mm², 13.20 ± 0.6 kg/mm², 24.12 ± 1.2 kg/mm² and 18.3 kg/mm², respectively, and the values obtained in this study are consistent with the literature.

The growth of the grain size reduces the grain boundary. The different crystal orientation of grains naturally provides grain boundaries adjacent to another with different angles. During plastic deformation, slip, or dislocation movement, this common border is obstructed and changes the direction of movement from one side to the other. As the difference in the crystal orientation increases, the realization of this movement gets more difficult. Dislocations in grain boundaries with large-angle cannot cross

grain boundaries and are accumulated there. These accumulations result in cluster stress at the adjacent grain and produce new dislocations (in front of the slip plane). On the other hand, twin boundaries are highly effective in stopping the slip and increasing the material's strength. The boundaries between two different phases form a barrier against the movement of dislocations and play an important role in increasing of the alloy's strength. Strength and hardness increase occurs as the most natural indicators. The experimental results show that total elongation has increased, and tensile strength has decreased with the increase of Al amount. There is only a slight decrease in Sn-75 wt. % Al alloy. Hence, as the amount of Al increases, the toughness and ductility of the material get higher.

3.5 Surface and composition analysis

Surface morphologies of the alloys showed that the samples are homogeneous, without cracks or holes, and grain boundaries of the samples can be seen clearly. The composition analysis of the alloys was performed with EDX, and shown in Fig. 8. The eutectic sample is a fibrous microstructure with a small volume fraction of one phase (Al-99.5 % wt. Sn). A small Al increase grows the grain boundaries (black phase). Structural changes depending on the solidification circumstances and the Al alloys's content are very important. Different cooling rates, changes in temperature, time, and content may cause a change in crystallization kinetics. Overcooling eutectic $\alpha + \beta$ and α solid or β solid solutions affects crystallization, resulting in microstructure changes that determine mechanical and functional properties. In addition, the phase transition temperature and structural defects also affect these kinetics significantly. In the tests performed on this study, such as SEM, EDX, and DSC, the examination of morphologies cooled under the same conditions showed that eutectic fibrous particles are formed in eutectic compounds. In other samples, growths on island shape were observed with the increase of Al amount depending on diffusion rules. As seen in the Al-Sn phase diagram (Hansen & Anderko, 1985), grains have grown in the form of islands when the Al content is higher than 2 % wt., because the alloy shows no solution in each other; this is proceeding the diffusion of Al and Sn. It can be said that Al promoted the diffusion of Sn, and therefore prevented the growth of eutectic compounds. (Chen et al., 2008) also have shown the Al rate rule on diffusion kinetic of some elements and reported that Al promoted the diffusion of these elements. Therefore, an increase of Al prohibits the growth of eutectics.

4. Conclusions

The main outcomes of this research can be summarized as follows: The thermal conductivity of Sn-Al alloys was investigated by using a radial heat flow apparatus. The change of Sn-Al binary alloys' electrical conductivity/resistivity with composition was computed from the Wiedemann-Franz law and Smith-Palmer Equation using the thermal conductivity and L_{alloy} . Electrical temperature coefficients were determined from the electrical conductivity vs. temperature. The enthalpy of fusion (ΔH) and the specific heat change (ΔC_p) of Sn-(x) wt. % Al (x=0.5, 2.2, 25, 50, 75) alloys were obtained by DSC. Microhardness was determined, and mechanical measurements were performed depend on compositions. Microstructures shifted from tetragonal solid solution to orthorhombic solution phase and then single cubic phase. Lattice distortion increased because of the difference in radii. The grain boundaries between two different phases form a barrier against the movement of dislocations; hence the dislocations in the grain boundaries with large-angle are accumulated in the grain boundaries and play an important role in increasing the alloy's strength. So, the elongation, toughness, and ductility increase as the Al amount increases, and the material's tensile strength is very slightly decreased.

References

- Aksöz, S., Ocak, Y., Maraşlı, N., Çadırılı, E., Kaya, H., Büyük, U. (2010) Dependency of the thermal and electrical conductivity on the temperature and composition of Cu in the Al based Al-Cu alloys. *Exp. Therm. Fluid Sci.* 34, 1507-1516.
- Callendar, H.L., Nicolson, J.T. (1897) Experiments on the condensation of steam. Part I. A new apparatus for studying the rate of condensation of steam on a metal surface at different temperatures and pressures. *Br. Assoc. Adv. Sci., Rept. Ann. Meet.* 22, 418-422.
- Chen, J., Chen, Z., Yan, H., Zhang, F., Liao, K. (2008) Effects of Sn addition on microstructure and mechanical properties of Mg-Zn-Al alloys. *J. Alloy Compd.* 461, 209-215.
- Chen, H.Y., Savvides, N. (2010) High quality Mg₂Sn crystals prepared by RF induction melting. *J. Cryst. Growth.* 312, 2328-2334.

- Cruz, K.S., Spinelli, J.E., Ferreira, I.L., Cheung, N., Garcia, A. (2008) Microstructural development in Al-Sn alloys directionally solidified under transient heat flow conditions. *Mater. Chem. Phys.* 109, 87-98.
- Cruz, K.S., Meza, E.S., Fernandes, F.A.P., Quaresma, J.M.V., Casteletti, L.C. and Garcia A. (2010) Dendritic arm spacing affecting mechanical properties and wear behavior of Al-Sn and Al-Si alloys directionally solidified under unsteady-state conditions, *Metall. Mater. Trans. A*, 41A, 972-984.
- Çadırılı, E., Büyük, U., Engin, S., Kaya, H., Maraşlı, N.(2009) Variations of microhardness with the solidification processing parameters and thermo-electrical properties with the temperature in the Sn-Cu alloy. *Kovove Materialy - Metallic Materials*, 47, 381-387.
- Das, S.K., Sharif, A., Chan, Y.C., Wong, N.B., Yung, W.K.C. (2009) Influence of small amount of Al and Cu on the microstructure, microhardness and tensile properties of Sn-9Zn binary eutectic solder alloy. *J. Alloy Compd.* 481, 167-172.
- Gündüz, M., Hunt, J.D. (1985) The measurement of solid-liquid surface energies in the Al-Cu, Al-Si and Pb-Sn systems, *Acta Mater.* 33, 1651-1672.
- Frear, D., Morgan, H., Burchett, S., Lau, J. (1994) *The mechanics of solder alloy interconnects*. 1 edition, Van Nostrand Reinhold: New York, pp.60-63.
- Hansen, M. and Anderko, K. (1985) *Constitutions of binary alloys*. second ed., McGraw-Hill: New York, pp. 135.
https://en.wikipedia.org/wiki/Electrical_resistivity_and_conductivity
 (Accessed 10 April 2016)
<http://www.rrcap.unep.org>
- Hultgren, von R., Orr, R.L., Anderson, P.D., Kelley, K.K. (1963) *Selected values of thermodynamic properties of metals and alloys*. 1 edition, John Wiley & Sons: New York-London, pp.33-36.
- Kim, K.H., Slazhniev, M.A., Kim, S.W., Sim, H.S., Euh, K. (2015) Study on controlled segregation of Al-Sn alloys for bearings, 8th International Conference on Electromagnetic Processing of Materials, Cannes, France.
- Liu, X., Zeng, M.Q., Ma, Y., Zhu, M. (2008) Wear behavior of Al-Sn alloys with different distribution of Sn dispersoids manipulated by mechanical alloying and sintering. *Wear*, 265, 1857-1863.
- Liu, X., Zeng, M.Q., Ma, Y., Zhu, M. (2009) Melting behavior and the correlation of Sn distribution on hardness in a nanostructured Al-Sn alloy. *Mater. Sci. Eng. A*, 506, 1-7.

- Liu, X., Shan, D., Song, Y., Chen, R., Han, E. (2011) Influences of the quantity of Mg₂Sn phase on the corrosion behavior of Mg-7Sn magnesium alloy. *Electrochim Acta*. 56, 2582-2590.
- Mamazza Jr., Robert, Morel, Don L., Ferekides, Christos S. (2005) Transparent conducting oxide thin films of Cd₂SnO₄ prepared by RF magnetron co-sputtering of the constituent binary oxides. *Thin Solid Films*. 484, 26-33.
- McElroy, D.L., Moore, J.P. (1969) *Thermal conductivity*, vol. I, Academic Press: London, pp. 185-239.
- Meydaneri, F., Saatçi, B., Özdemir, M. (2010) Thermal Conductivities of Solid and Liquid Phases for Pure Al Pure Sn and Their Binary Alloys. *Fluid Phase Equilibr*. 298, 97-105.
- Meydaneri, F., Saatçi, B., Özdemir, M. (2011) Experimental determination of solid liquid interfacial energy for solid Sn in the Sn-Mg system. *Appl. Surf. Sci*. 257, 6518-6526.
- Meydaneri, F., Saatçi, B., Özdemir, M. (2013) Thermal, electrical, microstructure and microhardness properties of the eutectic Sn-3.5 wt.% Ag alloy. *Kovove Materialy - Metallic Materials*, 51, 173-181.
- Meydaneri, F., Saatçi, B. (2014) Thermal, electrical, microstructure and microhardness properties of the eutectic magnesium-tin. *The Arabian Journal for Sci. and Eng*. 39, 5815-5824.
- Mizutani, U. (2011) *The Hume-Rothery rules for structurally complex alloy phases*. 1 edition, CRC Press, Taylor and Francis Book: New York.
- Nassar, A., Taha, A.S., Labeeb, A. and Gouda, El Said A. (2015) Structure and Properties of the Al-Sn-Cu Bearing Alloy under Different Cold Rolling Conditions. *J. Mater. Sci. Eng. B*, 5, 298-304.
- Niven, C. (1905) On a method of finding the conductivity for heat. *Proc. Roy. Soc. A*76, 34.
- Noskova, N.I., Korshunov, L.G. and Korznikov, A.V. (2008) Microstructure and tribological properties of Al-Sn, Al-Sn-Pb, and Sn-Sb-Cu alloys subjected to severe plastic deformation. *Metal Science and Heat Treatment*. 12, 34-40.
- Ocak, Y., Aksöz, S., Maraşlı, N., Çadırılı, E. (2010) Dependency of thermal and electrical conductivity on temperature and composition of Sn in Pb-Sn alloys. *Fluid Phase Equilibr*. 295, 60-67.
- Onaran, K. (2009) *Material Science*. 11th edition, Science Technique Publisher: Istanbul/Turkey.
- Osorio, W.R., Spinelli, J.E., Cheung, N., Garcia, A. (2006) Secondary dendrite arm spacing and solute redistribution effects on the

- corrosion resistance of Al-10 wt% Sn and Al-20 wt% Zn alloys. *Mater. Sci. Eng. A*, 420, 179-186.
- Pathak, J.P. and Mohan, S. (2003) Tribological behaviour of conventional Al-Sn and equivalent Al-Pb alloys under lubrication. *Bull. Mater. Sci.* 26, 315-320.
- Powell, R.W. (1939) Further measurements of the thermal and electrical conductivity of iron at high temperatures. *Proc. Phys. Soc.* 51, 407.
- Saatçi, B., Arı, M., Gündüz, M., Meydaneri, F., Bozoklu M. and Durmuş S. (2006) Thermal and electrical conductivities of Cd-Zn alloys. *J. Phys: Condens. Mater.* 18, 10643-10653.
- Sergent, E.J., Krum, A. (1998) *Thermal management handbook: for electronic assemblies*. 1 edition, McGraw-Hill Professional: New York, p. 26.
- Smith, C.S., Palmer, E.W. (1935) Thermal and electrical conductivities of copper alloys. *Trans. AIME.* 117, 225-243.
- Terada, Y., Ohkubo, K., Mohri, T., Suzuki, T. (1999) Thermal conductivity in Pt-based alloys. *J. Alloy Compd.* 285, 233-237.
- Touloukian, Y.S., Powell, R.W., Ho, C.Y., Klemens, P.G. (1970) *Thermal conductivity metallic elements and alloys*, vol. 1, Plenum: New York, pp. 17a, 404, 7, 823, 483.
- Yamasue, E., Susa, M., Fukuyama, H., Nagata, K. (2003) Deviation from Wiedemann-Franz law for the thermal conductivity of liquid tin and lead at elevated temperature. *Int. J. Thermophys.* 24, 713-730.

CHAPTER VIII

MEASUREMENT OF THERMAL CONDUCTIVITIES WITH LASER FLASH METHOD AND ELECTRICAL, MECHANICAL, AND MICROSTRUCTURE CHARACTERIZATION OF Bi-Sn, Bi-Sn-Zn AND Bi-Sn-Sb EUTECTIC ALLOYS

Prof. Dr. Fatma MEYDANERİ TEZEL* and Prof. Dr. İbrahim UZUN**

*Department of Metallurgy and Materials Engineering, Faculty of Engineering, Karabük University, 78050, Karabük, Turkey,
E-mail: fatmameydaneri@karabuk.edu.tr, meydaneri@yahoo.com
ORCID ID: 0000-0003-1546-875X

**Department of Mechanical Engineering, Faculty of Engineering, Kırıkkale University, 71300, Kırıkkale, Turkey,
E-mail: uzun@kku.edu.tr, ibrahimuzun71@gmail.com,
ORCID ID: 0000-0001-9725-2009

1. Introduction

In recent years, increasing environmental and health concerns about the toxicity of lead combined with the strict legislation banning the use of lead-based solders have created an inevitable driving force for the development of lead-free solder alloys (Shen et al., 2005; Shen et al., 2005; Wei et al., 2009; Shen et al., 2006; Torres et al., 2012; Flandorfer et al., 2008; Çadırılı et al., 2011; Braga et al., 2007; Shalaby, 2013; Yang et al., 2008; Awe and Oshakuade, 2014; Miric and Grusd, 1998; Morando et al., 2014). The search for a global Pb-free replacement for Sn-Pb eutectic alloy has been evolving as the threat of a regional lead ban became a reality in July 2006. Over the twelve years from 1994 to 2006, the manufacturing, performance, and reliability criteria for Pb-free solder joints have become increasingly complex as relationships between the solder alloy, the circuit board materials and construction, and the component designs and materials have been revealed through widespread experiments of the companies, industrial consortia, and university researchers (Shen et al., 2005; Shen et al., 2005; Wei et al., 2009; Shen et al., 2006; Torres et al., 2012; Flandorfer et al., 2008; Çadırılı et al., 2011;

Braga et al., 2007; Shalaby, 2013; Yang et al., 2008; Awe and Oshakuade, 2014; Miric and Grusd, 1998; Morando et al., 2014; Manasijević et al., 2007). Researching and replacing conventional tin-lead (Sn-Pb) solders with Pb-free materials required examination of the basic properties of these alloy systems. These include physical, chemical, mechanical, and electrical features, as well as cost and manufacturability. Among these, the physical properties, such as surface tension, interfacial tension, copper as the base metal, and contact angles, are important because of their direct correlation with the wettability of the solder (Manasijević et al., 2007). A material's electrical conductivity is very important for developing electronic materials and interconnection technologies, especially in modern industry and microelectronics (Shen et al., 2006). In most cases, high-level mechanical properties are required for industrial applications. The hardness and strength of the alloys mainly depend on their microstructure; thus, numerous work has been accomplished on micromechanics to dissection the practice of these alloys (Braga et al., 2007; Manasijević et al., 2007; Zhang et al., 2014; Hu et al., 2009; Zou et al., 2009; Mei and Morris, 1992; Morris et al., 1993) The melting temperature of the Sn-Zn eutectic alloy, which is lead-free, is about to the Sn-Pb' melting point. Nevertheless, new solder alloys must provide economic, physical, and chemical properties and fulfil other conditions. The melting points of lead-free solder alloys developed in this respect should be close to the conventional Sn-Pb eutectic alloy; their strength and stability should be similar or superior. Also, in terms of production cost, the costs of newly developed alloys must be capable of competing with lead-containing alloys (Billah et al., 2011; Frear et al., 1994).

This work aims to explore the thermal, electrical, mechanical, and microstructure of Sn- 57 wt.% Bi, Bi-39 wt.% Sn-3 wt.% Sb and Bi-58.5 wt.% Sn-12.2 wt.% Zn eutectic alloys.

2. Experimental procedure and characterization

The amounts of Bi, Sn, Zn, and Sb were determined by the 2001 Model Seles Aptb457 balance with 0.001g sensitivity. They were melted in a graphite crucible of approximately 400 cm³ volumes, which does not interact physically or chemically with the samples, in a 1994 Model, Inductotherm induction furnace, with 250 kW power and 750 kg capacity. Dimensions of the mould cavity of the four-cavity permanent mould were Ø= 20 mm, h = 200 mm for each sample (Fig.1). The mould was heated to approximately 40 °C below the melting temperature on the

induction furnace before casting. Before the casting process, the mould is covered with green sand to prevent the liquid metal from leaking. 150 °C was taken as the sufficient melting temperature for casting Bi-Sn, Bi-Sn-Sb, and Bi-Sn-Zn alloys whose eutectic melting temperatures are 139 °C, 137 °C, and 134.8 °C, respectively. The samples were kept for approximately 30-45 minutes after each casting process to solidify. Due to the low molding temperature, the samples were placed in Protherm Brand, plf110/10 Model laboratory-type heat treatment oven. The oven temperature was fixed at 55 °C; they were left for about 45 min.s and released to cool to room temperature.



Fig. 1 The shape of the samples and the mould cavity.

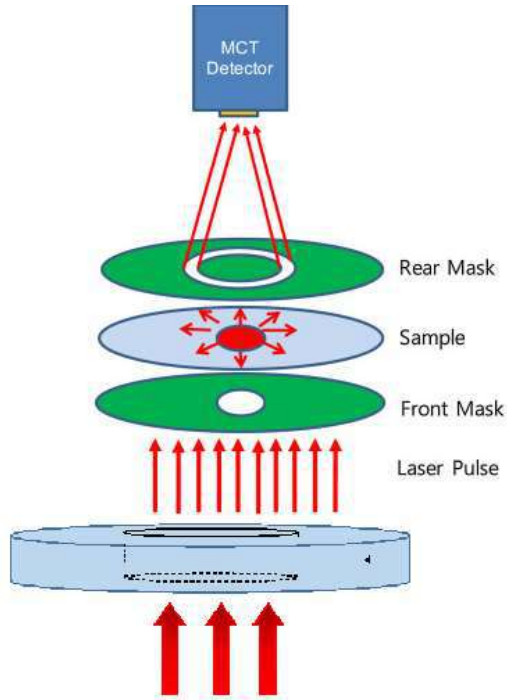


Fig. 2 Laser flash method.

Mechanical (tensile, Charpy impact), thermal, electrical, and structural properties of Bi-Sn-Sb and Bi-Sn-Zn eutectic alloys produced by adding Sb and Zn to Bi-Sn lead-free solder alloy were investigated. The alloys' structural and morphologic properties are researched by FESEM (Carl Zeiss Ultra Plus Gemini) and X-ray diffraction (Rigaku Ultra IV). The compositions of Bi-Sn binary eutectic alloy and Bi-Sn-Sb, Bi-Sn-Zn ternary eutectic alloys were supported by EDX. The alloys' fusion enthalpy and heat capacity changes were determined by (DSC 7000X Model). In addition, their thermal conductivities have been investigated by the laser flash method (Fig. 2). Vicker hardness was measured with a Qness hardness measuring device; tensile tests were performed with Shimadzu tensile device and notch-impact tests with Zwick/Roel Rkp450.

3. Results and discussion

3.1 Surface, compound and structural properties

The sample was cut transversely into ~ 2-4 mm sections to obtain the SEM images, and hot bakelite was taken with Struers Mark Citopress10 Model device. Transverse surfaces of samples were ground by Tegramin-30 model device with 800, 1000, 2400 grid SiC papers and mechanically polished via 6, 3, 1, and 1/4 μm diamond paste. Then, the etching procedure was also executed to obtain the microstructures on samples with 10 ml nitric acid and 90 ml water. The ratio of chemical compositions was analyzed by an EDX spectrometer attached to the FESEM. FESEM pictures and EDX mappings are depicted in Fig. 3. Sn-57 wt.% Bi, Bi-39 wt.% Sn-3 wt.% Sb and Bi-58.5 wt.% Sn-12.2 wt.% Zn eutectic alloys' XRD patterns are given in Fig. 4 and crystal structure parameters are in Table 1.

The Fig.3 displays that eutectic structures with Chinese script morphology are formed in Bi-Sn and Bi-Sn-Sb alloys. Regarding Bi-Sb binary phase diagram, they are completely dissolved in each other, and in the Bi-Sn binary phase diagram, Bismuth is dissolved about 21% in the Sn phase. The light grey phase in Bi-rich showed Fishbone type orientations at the dark grey Sn-rich matrix phase' grain boundaries. Secondary lamellar and rod-like BiSn eutectic phase was formed in the Sn matrix phase, divided into dendrite branches. Despite 3% wt. Sb doped to Bi-Sn-Sb structure, Bi-Sn has not moved away from its eutectic structure (Torres et al., 2012). The coarse-grained Bi-rich phase has formed a fishbone structure at the irregular eutectic structure' grain boundaries with Chinese script morphology in its microstructure. These coarse Bi-rich phases surrounded the SnSb IMC phase. In the Sn matrix phase, which is divided into dendrite branches, a small point-shaped anomalous eutectic structure was formed in some regions, and a lamellar BiSnSb eutectic structure was formed in some others. Considering to the literature, the existence of small amounts of Sn and Sb in the coarse-grained Bi-rich phase is considered the quasi-peritectic phase (Zhang et al., 2014). In the Bi-Sn-Zn alloy, in addition to this, the Zn-rich phase is formed as thick rods and thin needle-like structures, and the Bi atoms are embedded along or inside the Sn grains. The dissolved Bi phase or BiSn intermetallic phase are formed as small dots in light grey and segregated. Solidification has begun around the needle-like structures, and tiny needle-like and coarse rod-like Zn phases provide the dislocation density,

which will increment the mechanical features as hardness and yield strength. These outcomes are convenient with the letterure (Çadrlı et al., 2011).

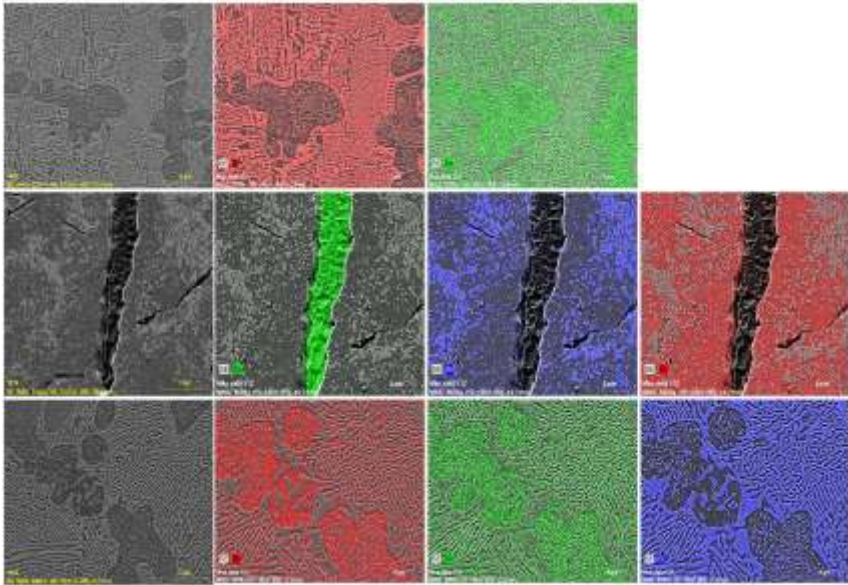


Fig. 3 Microstructures and EDX mappings of Bi-Sn, Bi-Sn-Zn and Bi-Sn-Sb alloys.

Accordingly, Sn- 57 wt.% Bi eutectic alloy has Sn, Bi, and Sn₉₅Bi₅ intermetallic compounds. There are four contents in the Bi-39 wt.% Sn-3 wt.% Sb alloy; these are Sn₂₀Sb₈₀ and Sn₉₅Bi₅, which form intermetallic phases with Bi and Sn. These results confirm the phases formed in the microstructure.

Table 1 Crystal structure parameters of Sn- 57 wt.% Bi, Bi-39 wt.% Sn-3 wt.% Sb and Bi-58.5 wt.% Sn-12.2 wt.% Zn eutectic alloys.

| Crystal Structure | 2 θ [°] | Miller Index (h k l) |
|---|----------------|----------------------|
| Bi (PDF Card No.: 01-071-4642) a=4.55 Å | 23.78 | (1 0 1) |
| | 27.16 | (0 1 2) |
| | 37.99 | (1 0 4) |
| | 39.58 | (1 1 0) |
| | 45.95 | (0 0 6) |
| | 48.67 | (2 0 2) |

| | | |
|---|-------|---------|
| b=4.55 Å c=11.84 Å Trigonal | 56.02 | (0 2 4) |
| | 59.42 | (1 0 7) |
| | 62.23 | (1 1 6) |
| | 71.81 | (3 0 0) |
| Bi ₉₅ Sn ₅ (PDF Card No.: 01-074-5514) a=b= 5.8570 Å c= 3.1900 Å Tetragonal | 30.50 | (2 0 0) |
| | 31.92 | (1 0 1) |
| | 44.73 | (2 1 1) |
| | 55.11 | (3 0 1) |
| | 54.30 | (3 2 1) |
| | 66.72 | (2 0 2) |
| | 79.19 | (3 1 2) |
| Sn (PDF Card No.: 01-071-3924) a=b=5.8318 Å c= 3.1819 Å Tetragonal | 30.63 | (2 0 0) |
| | 32.02 | (1 0 1) |
| | 43.87 | (2 2 0) |
| | 44.90 | (2 1 1) |
| Sn ₈₀ Sb ₂₀ (PDF Card No.: 01-077-3397) a=b= 5.8646 Å, c= 3.1798 Å Tetragonal | 43.62 | (2 2 0) |
| | 44.75 | (2 1 1) |
| | 66.89 | (2 0 2) |
| | 71.94 | (4 2 0) |
| Zn (PDF Card No.: 01-078-7027) a=b=2.6617 Å c= 4.9262 Å Hexagonal | 36.45 | (0 0 2) |
| | 39.04 | (1 0 0) |
| | 43.30 | (1 0 1) |
| | 54.47 | (1 0 2) |
| | 70.73 | (1 1 0) |

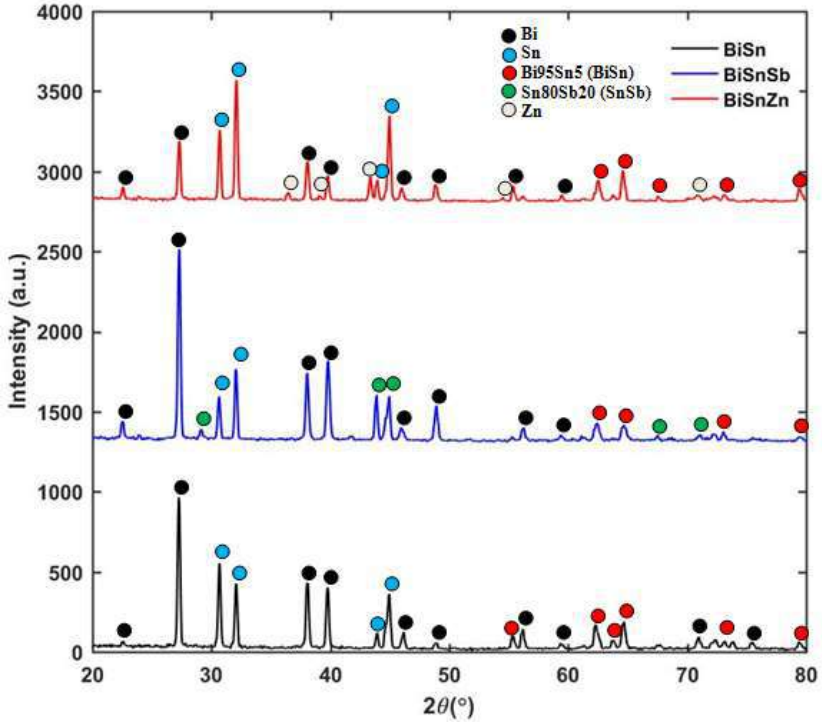


Fig. 4 XRD patterns of Bi-Sn, Bi-Sn-Zn and Bi-Sn-Sb eutectic alloys.

3.2 The fusion enthalpy and specific heat capacity variances

The materials' specific heat capacity depends on their phase composition and molecular vibrations. In order to understand the thermodynamic properties and phase transitions of a material, it is essential to know its heat capacity and latent heat.

Specific heat capacity at steady pressure (C_p),

$$C_p = \left(\frac{\partial H}{\partial T} \right)_p \quad (1)$$

The heat supplied to the system at the melting temperature will not increase its temperature but will be used to supply the enthalpy of fusion (the latent heat of melting) required to convert solid to liquid. For the transformation from solid-state to the liquid state, enthalpy change can be expressed as

$$\Delta H \approx \Delta C_p T_M \quad (2)$$

where T_M is the melting temperature and ΔC_p is the specific heat change.

The samples weighed for DSC analysis were placed in a 1 cm diameter aluminum container; the composition of each was distinct. Prepared samples were placed on a Hitachi Brand, DSC 7000X Model Differential Scanning Calorimeter. The temperature range of the device was set as 30-180 °C for each sample, with an increase of 2 °C per minute. The weighed sample amounts were also recorded on the instrument. The experiment was started after performing the last controls of the device. The DSC curves were obtained for Bi-Sn, Bi-Sn-Sb and Bi-Sn-Zn eutectic alloys and are depicted in Fig. 5. The peak temperatures indicate the transition of the alloy from the solid to the liquid. The areas under the graph gave the enthalpies of the alloys and were calculated by the DSC program. The enthalpy ratio to peak temperature determines the compositions' specific heat change. As a result, the heat capacitance change (ΔC_p) is determined by getting the rate of the fusion enthalpy (ΔH) and the peak temperature (T_p) under constant pressure. The enthalpy of fusion (ΔH) of Bi-Sn, Bi-Sn-Sb and Bi-Sn-Zn eutectic alloys were 46.2 J/g, 36.4 J/g, and 34.4 J/g, respectively. The peak temperatures of these alloys were 413.4 K, 419.4 K, and 408 K, respectively. Specific heat capacity changes were calculated as 0.111 J/gK, 0.086 J/gK, and 0.084 J/gK, respectively. As seen in the figure, regarding the effect of Zn and Sb on the Bi-Sn alloy, Zn decreased the phase transformation temperature; whereas Sb increased the phase transformation temperature because of the melting point of Zn (419.5 °C) is lower than Sb (630.8 °C). In the literature, enthalpy of fusion for Bi-Sn (Morando et al., 2014) and Bi-Sn-Zn (Çadırlı et al., 2011) alloys were 42.4 J/g and 54.5 J/g, respectively. The enthalpy of fusion obtained for the Bi-Sn eutectic alloy is in good agreement with this study, but it is quite higher for the Bi-Sn-Zn alloy. In the literature, higher results were obtained because of producing Bi-Sn-Zn alloy according to the solidification rate. However, the specific heat exchange is in line with the value determined by (Çadırlı et al., 2011). Specific heat changes for both Bi-Sn and Bi-Sn-Zn alloys are in very consistent with the DSC outcomes of Braga (Braga et al., 2007) and Kamal (Kamal et al., 2005). The enthalpy values for Bi-Sn-Sb alloy are given in the literature by the CALPAD method as a temperature-dependent theoretical functional formula (Awe and

Oshakuade, 2014; Manasijević et al., 2007); therefore, the outcomes of this work could not be compared with the literature.

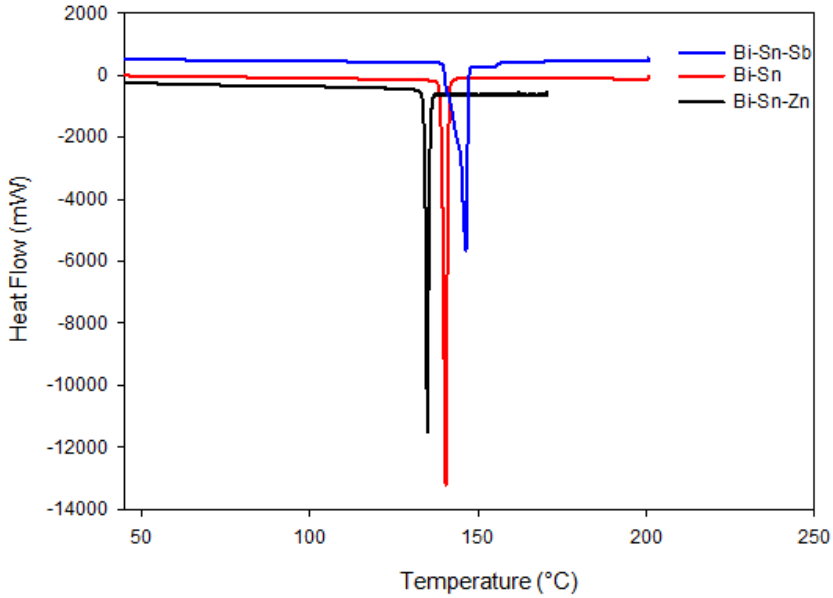


Fig. 5 DSC curves of Bi-Sn, Bi-Sn-Zn and Bi-Sn-Sb eutectic alloys.

3.3 The thermal and electrical conductivity, thermal- electrical temperature coefficient

The eutectic melting temperature of Bi-Sn, Bi-Sn-Sb and Bi-Sn-Zn eutectic alloys are 139 °C, 137 °C, and 134.8 °C, respectively. The thermal conductivities of the solid phase κ_s according to temperature were measured by laser flash device for Bi-Sn, Bi-Sn-Sb, and Bi-Sn-Zn alloys, and are shown in Fig. 6. The phonon is concerned with the vibration regulation in the crystal structure. Thermal conductivity is not a simple feature. It depends on the detailed structure of the material and the temperature. Phonon-phonon and phonon-electron inelastic scattering are more intense at high temperatures. The thermal conductivity differs depending on alloys' bulk stoichiometry and structural defects. The thermal conductivity, κ is the sum of the phonon's and electron's contributions to heat transport, and the electronic component κ_{el} is negligible at low temperatures. At high temperatures, the diffusion effect and lattice structure degradation caused the contribution of photon-phonon interactions to the heat transport to decrease, decreasing thermal conductivity. In this study, the thermal conductivities of Bi-Sn, Bi-Sn-Sb,

and Bi-Sn-Zn eutectic alloys at 10 °C below the approximate melting temperatures were 28.45 W/Km, 33.88 W/Km, and 80.83 W/Km, respectively. The thermal temperature coefficients of the solid phases according to temperature are calculated by equation (3). Aksöz et al. found the thermal conductivity for Bi-21wt.% Sn alloy as 25.7 W/Km (Aksöz et al., 2010) and Demir et al. for Sn -10wt.% Bi alloy as 34.73 W/Km (Demir et al., 2014). They found α_{TTC} values for the same alloys as $2.9 \times 10^{-4} \text{ K}^{-1}$ and $9.1 \times 10^{-4} \text{ K}^{-1}$, respectively. Although the experimental method is different, the thermal conductivity values are compatible with this study. For the Sn-32 wt.% Bi-3 wt.% Zn alloy, the thermal conductivity measured by the radial heat flow method was found to be 38.71 W/Km, and the α_{TTC} was found to be $2.21 \times 10^{-3} \text{ K}^{-1}$ (Aksöz et al., 2010). The thermal conductivity for this alloy is dramatically lower than the value acquired in this work, but the α_{TTC} value is quite compatible. It is owing to the difference in the alloys' contents and the experimental method. The thermal conductivity of the Bi-Sb-Sn alloy could not be compared with the literature.

$$\alpha_{TTC} = \left(\frac{1}{\kappa_1}\right)\left(\frac{\Delta\kappa}{\Delta T}\right) \quad (3)$$

where κ_1 is the thermal conductivity at the initial temperature T_1 , α_{TTC} is the temperature coefficient of thermal conductivity according to the temperature between $\Delta T = T_2 - T_1$. $\Delta\kappa = \kappa_2 - \kappa_1$, κ_1 and κ_2 are the thermal conductivity at T_1 and T_2 . In this study, the thermal temperature coefficients (α_{TTC}) of Bi-Sn, Bi-Sn-Zn and Bi-Sn-Sb eutectic alloys were 2.20×10^{-3} , 4.14×10^{-3} and $2.90 \times 10^{-3} \text{ K}^{-1}$, respectively.

The electrical and thermal conductivity of metals and alloys in solid and liquid states mainly results from free electrons. Therefore, the Wiedemann-Franz law explains the relation between thermal conductivity and electrical resistivity (Yamasue et al., 2003):

$$\frac{\kappa \rho_e}{T} = \frac{\pi^2 k^2}{3e^2} = L_0 \quad (4)$$

k is the Boltzman constant, e is the electron charge, and T is the absolute temperature. Lorenz constant, L_0 , is $2.445 \times 10^{-8} \text{ W}\Omega\text{K}^{-2}$.

The graph of Bi-Sn, Bi-Sn-Zn and Bi-Sn-Sb eutectic alloys' electrical conductivity according to temperature is given in Fig.7. Accordingly, the electrical conductivity of Bi-Sn-Zn and Bi-Sn-Sb eutectic alloys

decreased significantly. Nevertheless, there advents to be a small reduce for the Bi-Sn alloy, although it seems to be stable. The electrical conductivity of Bi-Sn, Bi-Sn-Zn, and Bi-Sn-Sb eutectic alloys were 4.62×10^{11} , 5.84×10^{11} , and 1.39×10^{12} (Ωm)⁻¹, respectively.

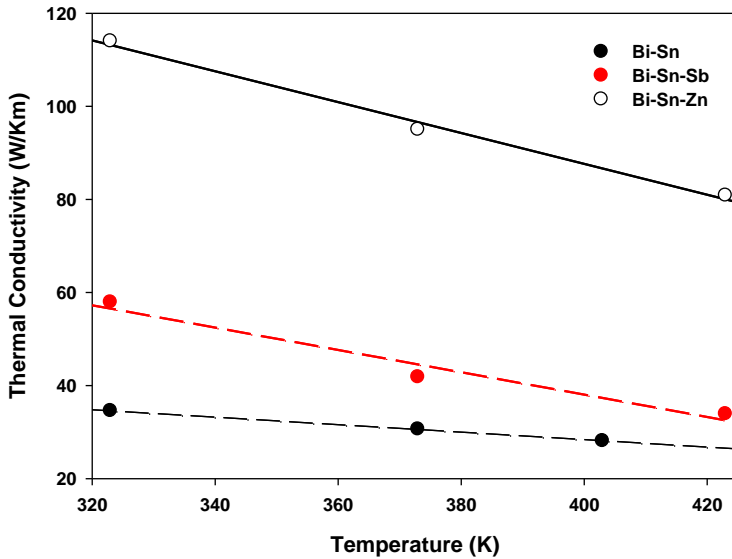


Fig. 6 Thermal conductivity vs temperature for Bi-Sn, Bi-Sn-Zn and Bi-Sn-Sb eutectic alloys.

The electrical conductivity of metals and metallic alloys decreases with temperature. Electron-electron scattering and electron-phonon interactions may play a key role. Moreover, the doping ratio and the elements' number of valence electrons are also very important in alloys. The doping ratio creates an impurity effect in the structure; the formed phases' structure (especially IMC structures) triggers scatter by collision, significantly reducing the electrical conductivity. Elements with more conduction electrons have a higher probability of collision, so the free path they take will decrease, and consequently, the conductivity will decrease. Aksöz et al. found the electrical conductivity values for Bi-21wt.% Sn alloy as 26×10^{11} (Ωm)⁻¹ (Aksöz et al., 2010) and Demir et al. found the electrical conductivity values for Bi-10wt.% Sn alloy as 33.3×10^{11} (Ωm)⁻¹ (Demir et al., 2014); both are higher than the values determined in this work. They found α_{ETC} for the same alloys as 3.4×10^{-3} K⁻¹ and 3.19×10^{-3} K⁻¹, respectively. The electrical conductivity of Sn-32 wt.% Bi-3 wt.% Zn alloy was found to vary between 1.52×10^6 (Ωm)⁻¹ and

$1.39 \times 10^6 (\Omega\text{m})^{-1}$ depending on temperature, and α_{ETC} was $1 \times 10^{-3} \text{ K}^{-1}$ (Aksöz et al., 2010). The electrical conductivity of this alloy is dramatically lower than the value calculated in this work. Çadırılı et al. (Çadırılı et al., 2011) reported that the electrical conductivity as a function of temperature for Sn-23 wt.% Bi-5 wt.% Zn alloy varied between $4.52 \times 10^6 (\Omega\text{m})^{-1}$ and $3.33 \times 10^6 (\Omega\text{m})^{-1}$. They found α_{ETC} of this alloy as $2.97 \times 10^{-3} \text{ K}^{-1}$, which is fit in line with the value determined in this work. It is slightly lower than the $3.9 \times 10^{-3} \text{ K}^{-1}$ found by Kamal for the SnZn₉Bi₁ alloy (Kamal et al., 2005). It results from the factors such as composition differences of the alloys, experimental/or theoretical calculations, and temperature ranges. The thermal conductivity of the Bi-Sb-Sn alloy could not be contrasted with the literature.

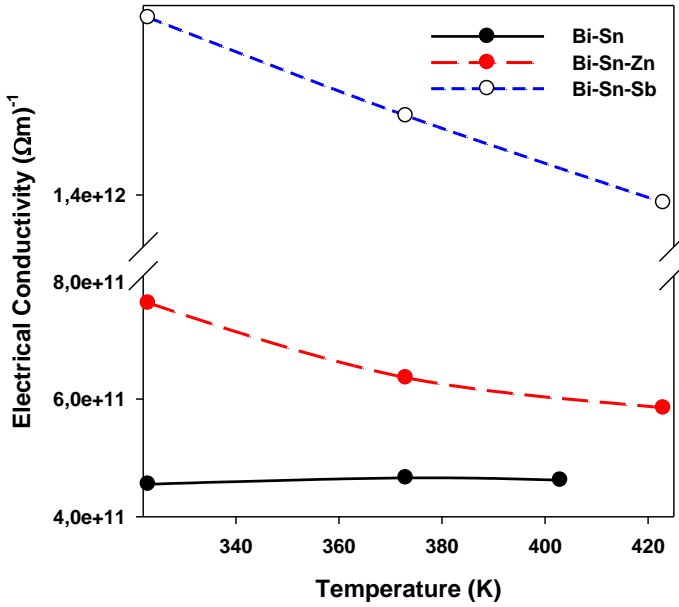


Fig. 7 Electrical conductivity vs temperature for Bi-Sn, Bi-Sn-Zn and Bi-Sn-Sb eutectic alloys.

The temperature-dependent electrical conductivity coefficient α_{ETC} is calculated using equation 5.

$$\alpha_{ETC} = \frac{\sigma - \sigma_0}{\sigma_0(T - T_0)} \quad (5)$$

σ is the solid phase' electrical conductivity at the temperature T , σ_0 is the electrical conductivity at the initial temperature T_0 , and α_{ETC} is the

electrical temperature coefficient. In this study, α_{ETC} values for Bi-Sn, Bi-Sn-Zn and Bi-Sn-Sb eutectic alloys were calculated as 1.88×10^{-4} , 2.33×10^{-3} and $7.13 \times 10^{-4} \text{ K}^{-1}$, respectively.

3.4 Examination of mechanistic features

The mechanistic features such as micro hardness depend on the composition, microstructure, processing temperature, etc. (Frear et al., 1994). The mechanistic features of any solidified material are usually obtained by tensile strength test, hardness test, and ductility test. Due to the strong correlation between the solidified sample's surface quality and the tensile strength test, the results are scattered in a wide range. Therefore, the mechanistic features were observed via hardness testing, which is the easiest ways to determine the mechanistic features of the structure's different phases. The Vickers micro hardness measurement was actualized at room temperature via hardness tester device Qness. In the hardness measurement, a load of 50 grams was applied to the samples for 20 seconds. Five hardness prints were taken on each sample, and the average was calculated. The hardness obtained for Bi-Sn, Bi-Sn-Zn, and Bi-Sn-Sb eutectic alloys were 20.7, 22.8, and 21.4 Hv, respectively. Zn gave more hardness to the Bi-Sn alloy than Sb. The micro hardness values for Bi-Sn, Bi-Sn-Zn and Bi-Sn-Sb alloys with different compositions were 22 (Hwang, 1989), 23.2 (Çadırılı et al., 2011), and 25.5 (Torres et al., 2012), respectively, and are almost consistent with the values measured in this work.

In this work, in order to apply the tensile test to the samples, first of all, the material turned into tensile test samples with (d_0) = 9.3 mm, cross-sectional area (A_0) = 67.916 mm^2 , length (L_t) = 180 mm. The tensile test of the samples prepared according to the standards was performed at room temperature by the Goodwy Brand Gls-200 Model CNC tensile tester. The test standard is TS EN ISO 6892-2: 2011; the test speed is 1 mm/min. Stress-strain curves of Bi-Sn, Bi-Sn-Sb and Bi-Sn-Zn alloys are given in Fig.8.

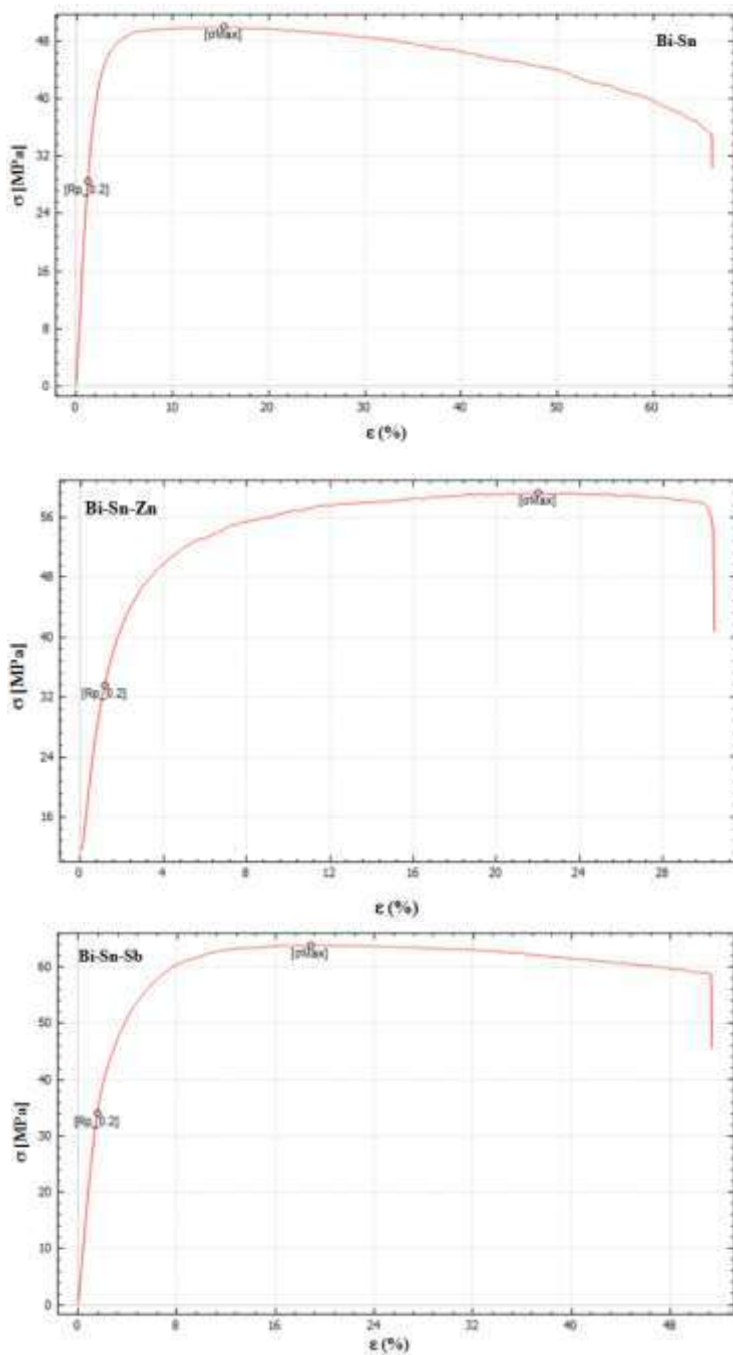


Fig. 8 Stress-strain curves of Bi-Sn, Bi-Sn-Zn and Bi-Sn-Sb eutectic alloys.

The values of yield and tensile strength, elongation, elasticity modulus (E) of Bi-Sn, Bi-Sn-Zn and Bi-Sn-Sb eutectic alloys were calculated from stress-strain graphs and are exhibited in Table 2.

Table 2 The mechanistic features of the alloys.

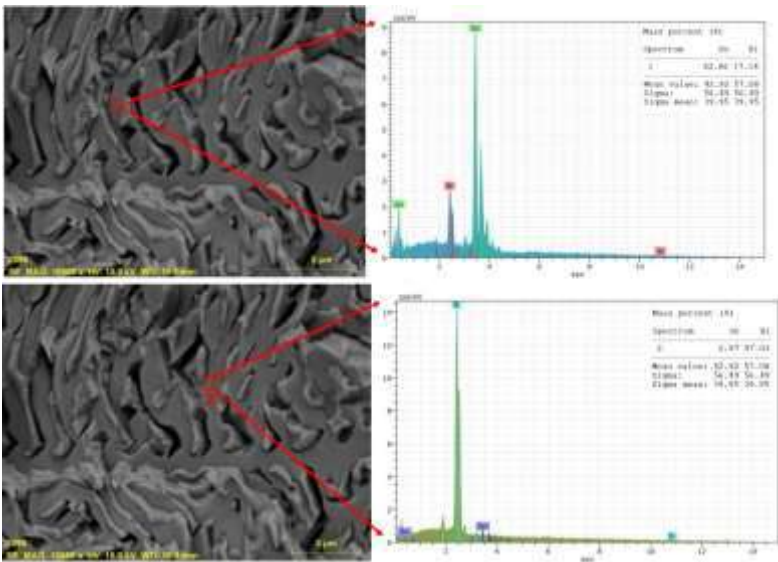
| Samples | Force [kN] | Tension [N/mm ²] | Elongation [%] | Yield [N/mm ²] | Elasticity modulus |
|----------|---------------|---------------------------------|-------------------|-------------------------------|-----------------------|
| Bi-Sn | 3.395 | 49.99 | 66.29 | 28.57 | 31.5747 |
| Bi-Sn-Sb | 4.333 | 63.80 | 51.61 | 34.01 | 25.2780 |
| Bi-Sn-Zn | 4.025 | 59.26 | 30.69 | 33.60 | 25.4410 |

Based on these data; Compared to Zn, Sb increased the Bi-Sn alloy' yield and tensile strengths while decreasing the elongation percentage. At the same time, adding Sb to the Bi-Sn alloy increased the strength and decreased the elasticity, that is, the toughness. Bi-Sn-Sb alloy is more ductile and tougher than Bi-Sn-Zn alloy. The elastic modules (E) of Bi-Sn-Sb and Bi-Sn-Zn alloys are slightly close to each other. Shalaby (Shalaby, 2013) found the elastic modulus for the Bi-Sn eutectic alloy as 45.23, which is dramatically higher than the value determined in this work. The tensile stress of 59.26 MPa obtained for Bi-Sn-Zn alloy in this study is much smaller than 89.1 MPa, 89 MPa and 72 MPa reported by Çadırılı et al. (Çadırılı et al., 2011), Soares et al. (Soares et al., 2003) and El-Daly et al. (El-Daly et al., 2009), for similar ternary alloy. Shen et al. (Shen et al., 2014) reported a mean tensile strength of 73.24 MPa for Sn-58Bi solder. Ma and Wu (Ma and Wu, 2015) added Zn to the Sn-58Bi solders. The UTS of the Sn-58Bi solder after adding Zn ranging from 0.0 to 2.0 wt.% was increased from 59 MPa to 63 MPa. Sakuyama et al. (Sakuyama et al., 2009) found that adding 0.5 wt.% Cu and Sb changed the tensile strength slightly. In addition, the elongation was improved by 140% and 320%, respectively. Adding 0.5 wt.% Zn weakened the tensile strength of the Sn-58Bi solder, which decreased to 68 MPa, and changed the elongation slightly. Hwang (Hwang, 1989) found the tensile strength of Sn-Bi-3wt.% Sb alloy to be 65 MPa, which is fit in line with this work. According to the charpy impact test performed at room temperature, adding Zn increased the toughness partly, which was expected, confirmed by Vickers hardness values and tensile strength. The charpy impact test' results are demonstrated in Table 3.

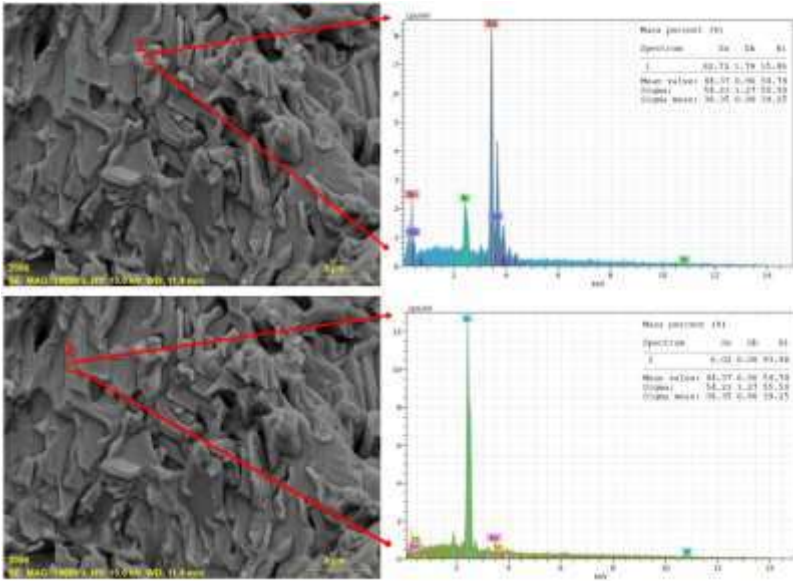
Table 3 The charpy impact test' results.

| Samples | Applied Load [kg] | Working Capacity [J] | Width [mm] | W [J] |
|----------|-------------------|----------------------|------------|---------|
| Bi-Sn | 32.85 | 450.25 | 10 | 0.92929 |
| Bi-Sn-Zn | 32.85 | 450.25 | 10 | 1.00726 |
| Bi-Sn-Sb | 32.85 | 450.25 | 10 | 0.92929 |

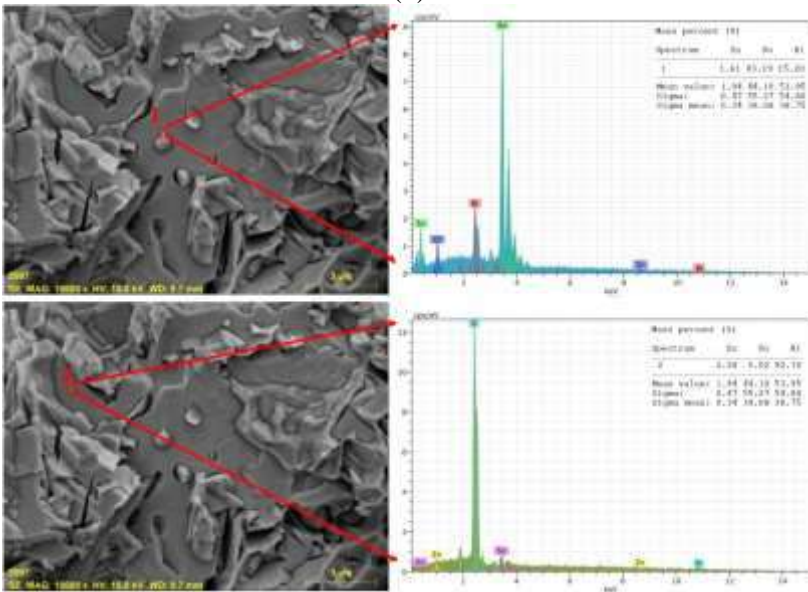
The surface of the fractured samples formed after the tensile test was examined with FESEM. The objective of examining fractured surfaces is to investigate whether the samples have a ductile or brittle structure and find the correlation between their mechanical properties and the dopings. The fractured surfaces are depicted in Fig. 9. Fractured surfaces have an indented opaque surface. These indentations and projections indicate that shear fracture occurs due to the shifting of atomic planes. The formation of very few dimples and a fibrous appearance between these indentations and protrusions indicates ductile fracture and is coherent with the tensile test results.



(a)



(b)



(c)

Fig. 9 Fracture surfaces of a) Bi-Sn, b) Bi-Sn-Sb c) Bi-Sn-Zn eutectic alloys.

4. Conclusion

Structural and micro structural features and surface morphologies of Sn- 57 wt.% Bi, Bi-39 wt.% Sn-3 wt.% Sb and Bi-58.5 wt.% Sn-12.2 wt.% Zn eutectic alloys manufactured by residual mould casting were investigated. Bi-Sn and Bi-Sn-Sb alloys formed chinese script eutectic structures, and fishbone structures developed at grain boundaries. The Bi-Sn-Sb ternary alloy has not moved away from the Bi-Sn binary alloy structure. In the Bi-Sn-Zn alloy, on the other hand, solidification started to occur around the primary-Zn phase, and the coarse rod-like and tiny needle-like Zn-rich phases were dispersed into the structure. Thermal conductivities of the alloys were measured via laser flash device, and thermal conductivity decreased with increasing temperature due to the contributions of electrons and phonons. The electrical conductivity, calculated by the Wiedeman-Franz law using the thermal conductivity coefficients, decreased with temperature increase. To better understand the vibrations of atoms and the thermodynamics of phases in phase transformations, fusion enthalpy and specific heat changes were determined using DSC results. Composition differences affecting mechanical properties were discussed through the tensile test, charpy impact test and Vickers micro hardness test results. BiSn and SnSb IMC structures and Zn-rich phases increased the strength of the alloys. Analysis of the fractured surfaces showed that these alloys indicate a ductile fracture.

References

- Aksöz, S., Ocak, Y., Keşlioğlu, K. and Maraşlı, N. (2010) Determination of Thermo-Electrical Properties in Sn-Based Alloys. *Met. Mater. Int.* 16, 507-515.
- Awe, O.E., Oshakuade, O.M. (2014) Theoretical prediction of thermodynamic activities of all components in the Bi-Sb-Sn ternary lead-free solder system and Pb-Bi-Sb-Sn quaternary system. *Thermochimica Acta.* 589, 47-55.
- Billah, Md. M., Alam, T., Hossain, M. A., Sharif, A. and Islam, S. M. K. N. (2011) Effect of Al Addition on the thermal and mechanical behavior of Sn-9Zn eutectic Pb-Free solder alloy. *Proceedings of the International Conference on Mechanical Engineering, Dhaka, Bangladesh, AM-016.*

- Braga, M.H., Vizdal, J., Kroupa, A., Ferreira, J., Soares, D., Malheiros, L.F. (2007) The experimental study of the Bi-Sn, Bi-Zn and Bi-Sn-Zn systems. *CALPHAD*. 31, 468-478.
- Çadırlı, E., Büyük, U., Kaya, H., Maraşlı, N. (2011) Determination of mechanical, electrical and thermal properties of the Sn-Bi-Zn ternary alloy. *Journal of Non-Crystalline Solids*. 357, 2876-2881.
- Demir, M., Aksöz, S., Öztürk, E. and Maraşlı, N. (2014) The Measurement of Thermal Conductivity Variation with Temperature for Sn-Based Lead-Free Binary Solders, *Metallurgical and Materials Transactions B*, 45, 1739–1749.
- El-Daly, A.A., Swilem, Y., Makled, M.H., El-Shaarawy, M.G., Abdraboh, A.M. (2009) Thermal and mechanical properties of Sn-Zn-Bi lead-free solder alloys. *Journal of Alloys and Compound*. 484, 134-142.
- Flandorfer, H., Sabbar, A., Luef, C., Rechchach, M., Ipser, H. (2008) Enthalpies of mixing of liquid Bi-Cu and Bi-Cu-Sn alloys relevant for lead-free soldering. *Thermochimica Acta*. 472, 1-10.
- Frear, D., Morgan, H., Burchett, S., Lau, J. (1994) The mechanics of solder alloy interconnects. Van Nostrand Reinhold, New York, pp.1-40.
- Hu, L., Zeng, M., Shen, B. (2009) Research of Sn-Bi lead-free solder. *Modern Electronics Technique*. 32, 164-167.
- Hwang, J. S. (1989) Solder Paste in Electronics Packaging. Van Nostrand Reinhold, New York, NY 10003, p. 115.
- Kamal, M., Meikhail, M.S., El-Bediwi, A.B., Gouda, E.S. (2005) Study of structural changes and properties for Sn-Zn₉ lead-free solder alloy with addition of different alloying elements. *Radiation Effects and Defects in Solids*. 160, 45-52.
- Ma D.-L. and Wu, P. (2015) Effects of Zn addition on mechanical properties of eutectic Sn-58Bi solder during liquid-state aging. *Transactions of Nonferrous Metals Society of China (English Edition)*, 25, 1225-1233.
- Manasijević, D., Vřešťál, J., Miniš, D., Kroupa, A., Živković, D., Živković, Ž. (2007) Phase equilibria and thermodynamics of the Bi-Sb-Sn ternary system. *Journal of Alloys and Compounds*. 438, 150–157.
- Mei, Z., Morris, J. W. (1992) Characterization of eutectic Sn-Bi solder joints. *Journal of Electronic Materials*. 21, 599-607.

- Miric, A.Z., Grusd, A. (1998) Lead-free alloys. *Soldering & Surface Mount Technology*. 10, 19-25.
- Morando, C., Fornaro, O., Garbellini, O., Palacio, H. (2014) Thermal properties of Sn-based solder alloys. *J Mater Sci: Mater Electron*. 25,3440-3447.
- Morris, J. W., Goldstein, J. L., Mei, Z. (1993) Microstructure and mechanical properties of Sn-In and Sn-Bi solders. *Journal of Electronic Materials*. 7, 25-27.
- Sakuyama, S., Akamatsu, T., Uenishi, K. and Sato, T. (2009) Effects of a third element on microstructure and mechanical properties of eutectic Sn-Bi solder. *Transactions of the Japan Institute of Electronics Packaging*. 2, 98-103.
- Shalaby, R. M. (2013) Effect of silver and indium addition on mechanical properties and indentation creep behavior of rapidly solidified Bi-Sn based lead-free solder alloys. *Materials Science and Engineering: A*. 560, 86-95.
- Shen, J., Liu, Y.C., Gao, H.X., Wei, C., Yang, Y.Q. (2005) Formation of bulk Ag_3Sn intermetallic compounds in Sn-Ag lead-free solders in solidification. *J. Electron. Mater.* 34, 1591-1597.
- Shen, J., Liu, Y.C., Han, Y.J., Zhang, P.Z., Gao, H.X. (2005) Formation of bulk intermetallic compound Ag_3Sn in slowly-cooled lead-free Sn-4.0 wt pct Ag solders. *J. Mater. Sci. Technol.* 21, 827-830.
- Shen, J., Liu, Y.C., Han, Y.J., Gao, H.X., Wei, C., Yang, Y.Q. (2006) Effects of cooling rates on microstructure and microhardness of lead-free Sn-3%Ag solders. *Trans. Nonferr. Met. Soc. China*. 16, 59-64.
- Shen, J., Pu, Y., Yin, H., Luo, D. and Chen, J. (2014) Effects of minor Cu and Zn additions on the thermal, microstructure and tensile properties of Sn-Bi-based solder alloys. *Journal of Alloys & Compounds*. 614, 63-70.
- Soares, D., Vilarinho, C., Barbosa, J., Silva, R., Pinho, M., Castro, F. (2003) Effect of the Bi content on the mechanical properties of a Sn-Zn-Al-Bi solder alloy. II International Materials Symposium, XI Encontro da Sociedade Portuguesa de Materiais (SPM), 14-16 April, Costa da Caparica, Portugal.
- Torres, A., Hernández, L., Domínguez, O. (2012) Effect of Antimony Additions on Corrosion and Mechanical Properties of Sn-Bi Eutectic Lead-Free Solder Alloy, *Materials Sciences and Applications*, 3, Article ID:19815, 8 pages.

- Wei, C., Liu, Y., Gao, Z., Xu, R., Yang, K. (2009) Effects of aging on structural evolution of the rapidly solidified Sn-Ag-Zn eutectic solder. *Journal of Alloys and Compounds*. 468, 154-157.
- Yamasue, E., Susa, M., Fukuyama, H., Nagata, K. (2003) Deviation from Wiedemann-Franz law for the thermal conductivity of liquid tin and lead at elevated temperature. *Int. J. Thermophys.* 24, 713-730.
- Yang, C.-F., Chen, F.-L., Gierlotka, W., Chen, S.-W., Hsieh, K.-C., Huang, L.-L. (2008) Thermodynamic properties and phase equilibria of Sn-Bi-Zn ternary alloys. *Materials Chemistry and Physics*. 112, 94-103.
- Zhang, C., Liu, S.-D., Qian, G.-T., Zhou, J., Xue, F. (2014) Effect of Sb content on properties of Sn-Bi solders. *Trans. Nonferrous Met. Soc. China*. 24, 184-191.
- Zou, H. F., Zhang, Q. K., Zhang, Z. F. (2009) Eliminating interfacial segregation and embrittlement of bismuth in SnBi/Cu joint by alloying Cu substrate. *Scripta Materialia*. 61, 308-311.

CHAPTER IX

EFFECT OF PLUG PARAMETERS ON THICKNESS VARIATION OF A THERMOFORMED PRODUCT USING PLUG ASSIST THERMOFORMING

Dr. Olcay EKŞİ* and MSc. Ertuğ CABBAR**

*Kırklareli University, Kırklareli, Turkey, e-mail: olcayeksi@klu.edu.tr
<https://orcid.org/0000-0002-2433-6700>

**Department of Maintenance and Repair at Hamitabat Natural Gas
Combined Cycle Power Plant, Kırklareli, Turkey, e-mail: cabbarertug@gmail.com
<https://orcid.org/0000-0001-7983-5788>

1. Introduction

Thermoforming technology, involves heating and forming of a sheet or film in to the desired shape. Mostly amorphous engineering thermoplastics (Acrylonitrile butadiene styrene-ABS, Polystyrene-PS, Polyvinyl chloride-PVC and Polyethylene terephthalate glycol-PETG) are used in thermoforming due to their wide forming temperature range. Sometimes, semi-crystalline thermoplastics such as Polypropylene-PP and Polyethylene-PE are used in thermoforming applications, although they are though to shape due to their narrow melting temperature range. Forming process is called depending on the thickness and form of the material to be thermoformed. If the plastic material is flexible and fed as rolls, process is called Roll-fed thermoforming. If the material to be thermoformed is a sheet which is cut and prepared with predetermined dimensions, thermoforming process is called as Cut-sheet thermoforming. Also thermoforming machines are called according to plastic material feeding types (Ashter, 2014; Morris, 2017; Schwarzmann, 2019a; Selke et al., 2021; Tempelman et al., 2014; Throne, 2017).

Initially, the sheet or film to be thermoformed is fixed in such a way as to provide sealing. Clamping frame is employed to provide better sealing between mould and thermoformed material. Plastic sheet is heated to a temperature which depends upon the type of thermoplastic material. The forming temperature is chosen below the melting temperature and above the glass transition temperature. Heating can be performed using different methods. Contact heating, convection heating and Infrared radiation heating are some of these techniques(Schwarzmann, 2019b).

Positive or negative air pressure is utilized to force the sheet to take the shape of the mould effectively. In some thermoforming operations plug assist may be required to provide better thickness distribution along the mould surface. If only vacuum is applied, the process is called vacuum forming. After plug is employed in thermoforming, process is called Plug Assisted Thermoforming (Hosseini et al., 2006).

Studies over the past two decades have provided important information on the effect of variation of thermoforming process parameters on final product properties. Chen et al. 2008, investigated the effects of processing parameters such as mold temperature, film preheating temperature, plug speed, plug holding time, and plug depth on the dimensional variation and thickness distribution. They observed that an increase in the thermoforming depth will cause wrinkling and multiple-step thermoforming may reduce the residual stress of the final thermoformed product. Morales et al. 2014, investigated the effect of the thermoforming process parameters on the sheet friction coefficient. It has been found out that coefficient of friction increases with an increase in sheet temperature. They showed that it was not possible to detect a significant coefficient of friction variations depending upon the plug material. Several attempts have been made to show the importance of thermoforming process for other industries. Even production of microelectronics and planar optical waveguides(Hoffmann et al., 2020; Shen et al., 2022; Zulfiqar et al., 2021). Also, some simulation studies have been reported on production and forming of different composites(Harhash et al., 2021; Nardi & Sinke, 2021; Ning et al., 2009; O'Connor et al., 2013; Sun et al., 2021). Additionally, heating methods and simulation in thermoforming have been studied by many researchers using Computer Aided Engineering (CAE) packages(Erchiqui, 2018; Schmidt et al., 2003). Some literature studies have focused alternative thermoforming materials and their deformation behavior during thermoforming(Mohammadian-Gezaz et al., 2006; Sánchez et al., 2022; Takaffoli et al., 2020).

Thickness distribution is an increasingly important area in thermoformed part manufacturing. Because, thickness variation can simply affect the outer appearance of the product. Especially for the thermoformed packages; color, light transmittance, air and gas permeability is one of the most critical factors. Additionally, thickness distribution is one of the factors which influences the packages rigidity and strength.

In this study, effect of variation of plug depth and diameter on thickness distribution of semi-finished thermoformed part, was investigated comparatively. PVC sheets were utilized in thermoforming operations. Initially, a plug which has a constant diameter (40 mm) were used in thermoforming operation by changing the plug depth in a conical female mould. Then, thermoforming operations were repeated using plugs which have different diameters, for a constant plug depth. Thickness variations for each case were examined comparatively. Thickness change in sidewall and bottom of the thermoformed product was studied via graphical method.

2. Materials and Methods

In this study, Petvinil S 23/59 (Petkim, Türkiye) extruded PVC sheets were used in thermoforming operations. All sheets to be thermoformed have a thickness of 0.45 mm. A conical aluminum female mould was employed during thermoforming experiments. The mould was fixed on a Lab-scale thermoforming machine (Figure 1). The thermoforming machine was designed and built for laboratory experiments only. This machine consists of heating system, mould, clamping frame, sealing element, air compressor, plug equipment, vacuum pump and a vacuum comparator. The heating system has 3 infrared ceramic heaters. Using control panel, each heater was adjusted to be 300 °C. When the temperature of heaters reached 300 °C, the sheet to be thermoformed was heated for 1 minute. With this heating system, sheet temperature cannot be adjusted. But after 1 minute heating time, sheet's temperature distribution was detected with a thermal imaging cam (Testo 875-i). Appropriate temperature distribution was determined by trial-and-error method under the melting temperature of Petvinil S 23/59.

First, square sheets in dimensions of 150 mm were cut and prepared before thermoforming. A sheet was placed on to the mould correctly. Then it was fixed using the clamping unit. At this time, the plug and its parts were assembled. Selected plug depth was adjusted using different depth control bushings. After the sheet temperature reached to the minimum temperature which is sufficient to form, plug assist was utilized for first deformation stage. It took approximately one second. Vacuum was applied and plug returned to its original position. Vacuum was measured as 700-720 mmHg using a vacuum comparator during thermoforming operations. After vacuum was turned off, clamping unit was disassembled. The thermoformed product cooled and solidified in 5 or 6 seconds. It

released from the mould and a cycle was completed. Each forming operation repeated 3 times. In this study, five different plug diameters were considered and aluminum plugs with diameters of 30, 35, 40, 45 and 50 mm were manufactured by machining (Figure 2). Also, five plug depth values were considered as 25, 30, 35, 40 and 45 mm (Figure 2). Plug diameters and plug depths were determined by considering the dimensions of the female mould. Thermoforming operations repeated for two cases. First one is constant plug diameter case. For this case, plug diameter was selected as 40 mm. A plug with 40 mm diameter was utilized using five different plug depth values during thermoforming. Second one is constant plug depth case. Five plugs with different diameters were used in thermoforming operations using a constant 35 mm plug depth. 30 thermoformed conical semifinished samples were obtained at the end of the experimental procedure.

Thickness distribution of all thermoformed samples was obtained by experimental procedure. A sample was cut and divided in to two pieces. Starting from the center of the bottom of the sample, thickness measurements were made at 28 points on the sidewall and flange. The thickness value at each point was determined by averaging the three measurement values.



Fig. 1 Lab-scale thermoforming machine



Fig. 2 a) Plugs with 30, 35, 40, 45 and 50 mm diameters, b) Bushings for 25, 30, 35, 40 and 45 mm plug depths

Results and Discussion

Initially, thermoforming temperature for the Petvinil S23/59 was obtained using thermal images which were recorded during heating. Forming temperature was determined as about 165 °C (Figure 4, Figure 7). From Figure 3, it is understood that temperature changes between 150 and 175 °C. Also, temperature values taken in the P1 and P2 directions are quite different from each other. The difference in the temperature distribution, causes the thickness distribution to be different in the two perpendicular directions (P1, P2). Thanks to its amorphous structure, the PVC sheets could be thermoformed at temperatures between 150 and 175 degrees (Figure 3).

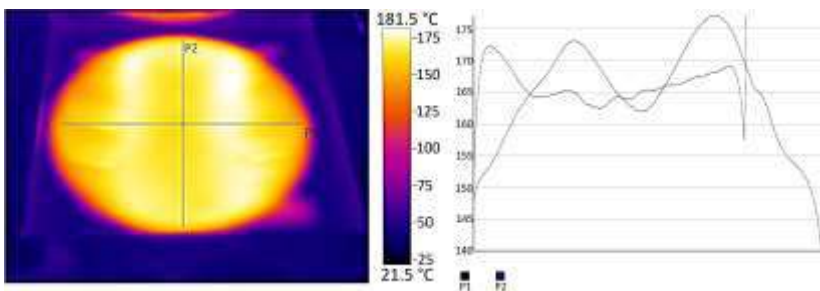


Fig. 3 Temperature distribution of the Petvinil S23/59 before thermoforming (constant plug diameter).

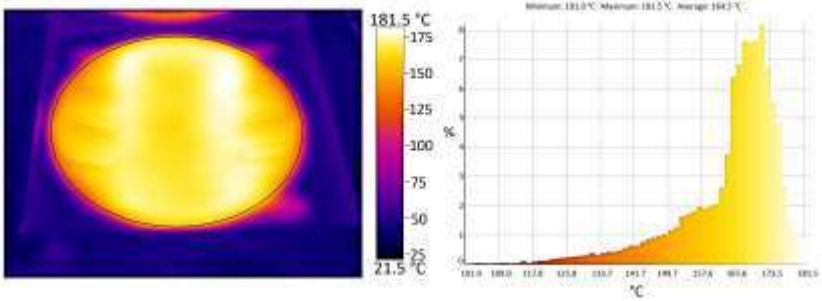


Fig. 4 Forming temperature of Petvinil S23/59 (constant plug diameter).

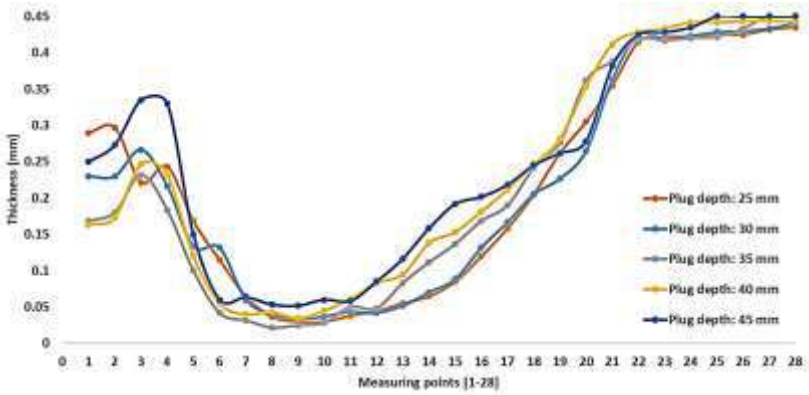


Fig. 5 Thickness values of samples which were formed via plug assisted thermoforming with constant plug diameter.

40 mm was chosen as plug diameter and thermoforming operations were performed for the 25, 30, 35, 40 and 45 mm plug depths. Figure 5 shows average thickness distribution for each plug depth. The thickness increased for almost all plug depth values from point 1 to point 4. The first 10 points whose thickness is measured are located at the base of the sample. Especially, points 9 and 10 are located on the radius at the base. Nearly the lowest thicknesses were measured at these points. Also, thickness variation showed a decreasing trend between the points 4 and 10. Between points 11 and 19 (sidewall of the sample), the thickness increased as the plug depth value increased. Additionally, thickness increased from point 19 to point 22. However, the thickness value did not change significantly from point 23 to point 28. Because points from 23 to 28 are on the flange part of the

sample. These points were mostly undeformed and remained close to the initial sheet thickness (0.45 mm).

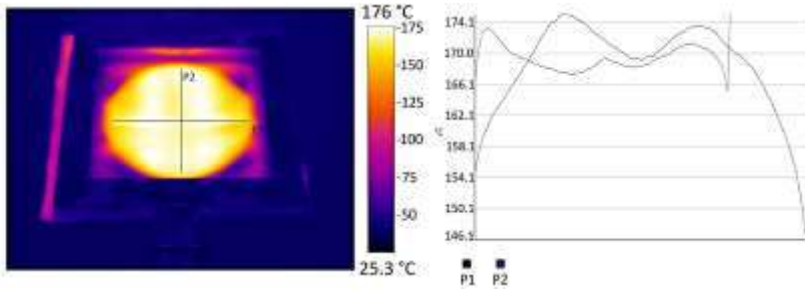


Fig. 6 Temperature distribution of the Petvinil S23/59 before thermoforming (constant plug depth).

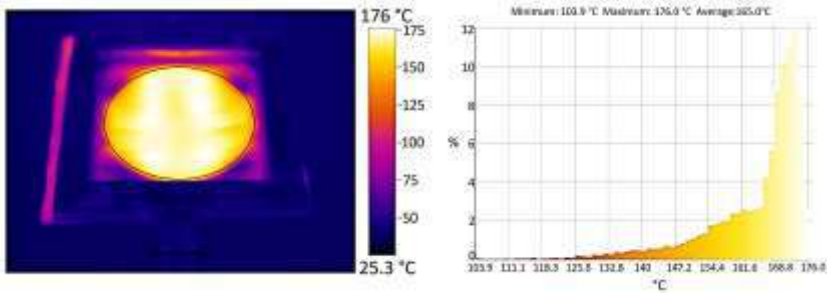


Fig. 7 Forming temperature of Petvinil S23/59 (constant plug depth).

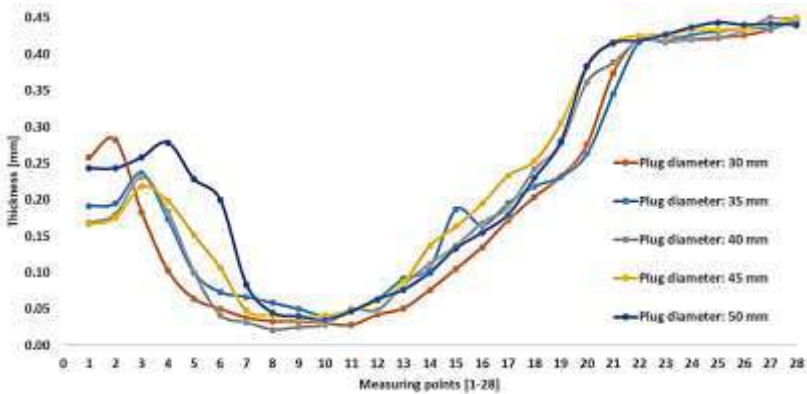


Fig. 8 Thickness values of samples which were formed via plug assisted thermoforming with constant plug depth.

From Figure 6 and 7, maximum and minimum temperatures were measured as 176 °C and 155 °C on the heated sheet respectively. Due to differences in temperatures measured in the P1 and P2 directions (Figure 6), non-uniform temperature distribution occurred on the heated PVC sheet. Also, average forming temperature was obtained as 165 °C. Figure 8 shows the thickness variation in the sample for 35 mm plug depth. Starting from the center of the base of sample (points from 1 to 10), along the sidewall of the sample (points from 11 to 22) and through the flange (points from 23 to 28), thickness was measured. In figure 8, thickness increased at first 3 measuring points for almost all plug diameter cases. For a plug diameter of only 30 mm, the thickness decreased after the 2nd measurement point. This decrease in the thickness distribution continued until the 11th measurement point. Considering the variation between the 11th and 22nd measurement points, a significant correlation could not be established between the plug diameter and the thickness distribution. Between the 23rd and 28th measurement points, the thickness remained almost constant, taking values close to the initial sheet thickness of 0.45 mm.

3. Conclusions

The main goal of the current study was to determine the effect of plug parameters such as plug diameter and plug depth, on final thermoformed product's properties. Particularly, thickness variation of the product was examined with the varying plug diameters and depths. From figure 5, a clear correlation could not be obtained between the change of plug depth and the thickness distribution of the thermoformed product. Only between the 11th and 19th measurement points, sidewall thicknesses increased with increasing plug depths. The greater the plug depth, the more stretched the thermoformed sheet. The more biaxial stretching of the thermoformed sheet provided a more uniform thickness distribution on the sidewalls. Thickness remained nearly the same as the initial sheet thickness at the flange part of the product. In figure 8, especially between the 1st and 10th measurement points; The thickness values measured for the 50 mm plug diameter are greater than the measured thickness values for the 30 mm plug diameter. From figure 8, as the plug diameter increased, the contact surface between the thermoformed sheet and the plug increased, so more material solidified and accumulated in the center of the base of the product.

4. Acknowledgements

This study is a part of the Master of Science thesis entitled “Investigation of the effect of thermoforming parameters for plastic-based sheets on thermoformed product's final thickness distribution” and written by Ertuğ CABBAR in 2021.

References

- Ashter, S. A. (2014). Introduction to Thermoforming. *Thermoforming of Single and Multilayer Laminates*, 1–12. <https://doi.org/10.1016/B978-1-4557-3172-5.00001-3>
- Chen, S. C., Huang, S. T., Lin, M. C., Chien, R. der. (2008). Study on the thermoforming of PC films used for in-mold decoration. *International Communications in Heat and Mass Transfer*, 35(8), 967–973. <https://doi.org/10.1016/j.icheatmasstransfer.2008.04.008>
- Erchiqui, F. (2018). Application of genetic and simulated annealing algorithms for optimization of infrared heating stage in thermoforming process. *Applied Thermal Engineering*, 128, 1263–1272. <https://doi.org/10.1016/j.applthermaleng.2017.09.102>
- Harhash, M., Fischer, T., Grubenmann, M., Hua, W., Heingärtner, J., Kuhtz, M., Gude, M., Hora, P., Ziegmann, G., Palkowski, H. (2021). Top-hat crashboxes of thermoplastic fibre-metal-laminates processed in one-step thermoforming: Experimental and numerical study. *Composites Part B: Engineering*, 226. <https://doi.org/10.1016/j.compositesb.2021.109367>
- Hoffmann, G. A., Wienke, A., Reitberger, T., Franke, J., Kaieler, S., Overmeyer, L. (2020). Thermoforming of planar polymer optical waveguides for integrated optics in smart packaging materials. *Journal of Materials Processing Technology*, 285. <https://doi.org/10.1016/j.jmatprotec.2020.116763>
- Hosseini, H., Berdyshev, B. V., Mehrabani-Zeinabad, A. (2006). A solution for warpage in polymeric products by plug-assisted thermoforming. *European Polymer Journal*, 42(8), 1836–1843. <https://doi.org/10.1016/j.eurpolymj.2006.03.020>
- Mohammadian-Gezaz, S., Ghasemi, I., Karrabi, M., Azizi, H. (2006). Investigation on the thermoformability of polyolefin blends by hot

- tensile and rheological tests. *Polymer Testing*, 25(4), 504–511.
<https://doi.org/10.1016/j.polymertesting.2006.02.002>
- Morales, R. A., Candal, M. v., Santana, O. O., Gordillo, A., Salazar, R. (2014). Effect of the thermoforming process variables on the sheet friction coefficient. *Materials and Design*, 53, 1097–1103.
<https://doi.org/10.1016/j.matdes.2013.08.009>
- Morris, B. A. (2017). Thermoforming, Orientation, and Shrink. *The Science and Technology of Flexible Packaging*, 401–433.
<https://doi.org/10.1016/B978-0-323-24273-8.00011-3>
- Nardi, D., Sinke, J. (2021). Design analysis for thermoforming of thermoplastic composites: prediction and machine learning-based optimization. *Composites Part C: Open Access*, 5, 100126.
<https://doi.org/10.1016/j.jcomc.2021.100126>
- Ning, H., Pillay, S., Vaidya, U. K. (2009). Design and development of thermoplastic composite roof door for mass transit bus. *Materials and Design*, 30(4), 983–991.
<https://doi.org/10.1016/j.matdes.2008.06.066>
- O'Connor, C. P. J., Martin, P. J., Sweeney, J., Menary, G., Caton-Rose, P., Spencer, P. E. (2013). Simulation of the plug-assisted thermoforming of polypropylene using a large strain thermally coupled constitutive model. *Journal of Materials Processing Technology*, 213(9), 1588–1600. <https://doi.org/10.1016/j.jmatprotec.2013.02.001>
- Sánchez, E., Nájera, A., Sotomayor, O. (2022). Numerical study of the viscoelastic mechanical response of polystyrene in the process of thermoforming through the generalized Maxwell model. *Materials Today: Proceedings*, 49, 107–114.
<https://doi.org/10.1016/j.matpr.2021.07.480>
- Schmidt, F. M., le Maout, Y., Monteix, S. (2003). Modelling of infrared heating of thermoplastic sheet used in thermoforming process. *Journal of Materials Processing Technology*, 143–144(1), 225–231.
[https://doi.org/10.1016/S0924-0136\(03\)00291-7](https://doi.org/10.1016/S0924-0136(03)00291-7)
- Schwarzmann, P. (2019a). Basic principles and terminology in thermoforming. *Thermoforming*, 5–34.
<https://doi.org/10.3139/9781569907092.002>

- Schwarzmann, P. (2019b). Temperature control for thermoforming tools. *Thermoforming*, 411–436. <https://doi.org/10.3139/9781569907092.022>
- Selke, S. E. M., Culter, J. D., Auras, R. A., Rabnawaz, M. (2021). Thermoforming. *Plastics Packaging*, 275–292. <https://doi.org/10.3139/9781569908235.010>
- Shen, L., Yu, X., Fu, H., Wei, S., Shan, W., Yang, Y. (2022). Sustained-release capsules coated via thermoforming techniques. *European Journal of Pharmaceutical Sciences*, 168. <https://doi.org/10.1016/j.ejps.2021.106050>
- Sun, C., Gergely, R., Okonski, D. A., Min, J. (2021). Experimental and numerical investigations on thermoforming of thermoplastic prepregs of glass fiber reinforced nylon 6. *Journal of Materials Processing Technology*, 295. <https://doi.org/10.1016/j.jmatprotec.2021.117161>
- Takaffoli, M., Hangalur, G., Bakker, R., Chandrashekar, N. (2020). Thermo-visco-hyperelastic behavior of polycarbonate in forming of a complex geometry. *Journal of Manufacturing Processes*, 57, 105–113. <https://doi.org/10.1016/j.jmapro.2020.06.019>
- Tempelman, E., Shercliff, H., van Eyben, B. N. (2014). Thermoforming. *Manufacturing and Design*, 157–170. <https://doi.org/10.1016/B978-0-08-099922-7.00009-3>
- Throne, J. (2017). Thermoforming. *Applied Plastics Engineering Handbook: Processing, Materials, and Applications: Second Edition*, 345–375. <https://doi.org/10.1016/B978-0-323-39040-8.00016-X>
- Zulfiqar, S., Saad, A. A., Sharif, M. F. M., Samsudin, Z., Ali, M. Y. T., Ani, F. C., Ahmad, Z., Abdullah, M. K. (2021). Alternative manufacturing process of 3-dimensional interconnect device using thermoforming process. *Microelectronics Reliability*, 127. <https://doi.org/10.1016/j.microrel.2021.114373>

CHAPTER X

THE EVALUATION OF STUDENT AWARENESS IN THE NEW BUILDING DESIGN STUDIO TEACHING PRACTICES IN HISTORICAL ENVIRONMENT

Asst. Prof. Dr. İlknur ACAR ATA* and Asst. Prof. Dr. Merve ÖZKAYNAK**

*Nigde Omer Halisdemir University, Nigde, Turkey, acaratailknur@gmail.com

Orcid no:<https://orcid.org/0000-0002-6080-1307>

**Amasya University, Amasya, Turkey, merve.ozkaynak@hotmail.com

Orcid No:<https://orcid.org/0000-0002-1423-6749>

1. Introduction

Architects are one of the most important occupational groups that ensure the sustainability of the concept of conservation of historical environment professionally. The sensitivity of the architects on the subject of designing the living environment is increasing with the input of the historical environment. While the analysis and synthesis studies for the design in architectural education are valuable in terms of putting out the structure suitable for the place of mind, the awareness revealed in designing the new structure in the historical environment is important in terms of putting out the original designs.

The environment, which has been described as historical, comes from the whole of the natural and built environment that able to sustain its day-to-day inheritance from past civilizations. Historical environments with a lot of knowledge and accumulation of past life, culture, architecture, art and economy can be redesigned to meet the needs of today's conditions and provide continuity with new constructions or modern additions to historical textures. According to Duralı (2007), this change in the historical environment must be controlled and directed, and protection begins at this stage.

The social, cultural and architectural accumulation of historical surroundings must be maintained and preserved by adapting to today's contemporary conditions. In order for this to happen, it is important that the society has access to a sense of its value and a certain conservation consciousness, which only takes place through education (Duralı, 2007). One of the areas of the architectural discipline, the lessons in the undergraduate degree in preserving the historical environment, have a very

big significance at this point. Architects are one of the professional groups that have the most influence on society with the skill of designing the space. In the student's years, architects should have the awareness of preserving the historic environment and designing for it to enable them to realize their awareness in the future city. For this purpose, in the Architecture Department of Selçuk University, students in the fifth and sixth semesters in the Architecture Department scope of studio training were asked to design new structures in Sille suitable for historical environment and texture. At the end of the semester, students' projects were assessed by the awareness model with the criteria determined by the course instructors on the project they intended to act with this awareness.

1.1. Purpose and Scope of the Study

It's aimed to study to provide undergraduate students awareness of designing a new building in the historical environment, it is important to bring a solution proposal to the problems related to this texture. In Sille, which has a great history in past, it was chosen as a free space project area situated close to the rock carving caves, the Aya Eleni Church, and having traditional Sille view. This studio teaching practice targets to create design awareness in accordance with the new building design criteria within the historical texture of Sille.

1.2. Research Methods

The theoretical information and practical architectural studio teaching process within the scope of the research was divided into five-step (Figure 1):



Fig. 1 Method flow diagram

Firstly, students were informed about historical environment and conservation concepts and new building design criteria in the historical environment. During the preparatory process for the project, the students investigated these concepts and evaluated their domestic and foreign examples made in the historical environment in accordance with the planned new function of the design, and students were provided with discussions about the subject in the workshop environment. 15 weeks of education planning was carried out by two instructors in Architectural Design and Restoration Department and the students were required to have investigated about the historical environment and the new structure in 3

weeks. The students were informed about the relevant definitions, examples, and presentations.

The second step is the analysis of the natural, built, and social environment for the students in the historical neighborhood, which are directed towards tissue analysis. Sille was not considered as a historical neighborhood, the analyzes were made in connection with the city center of Konya. Because the state of designing a new structure within the historical texture has an approach that requires an analysis of touching at the urban scale. In this sense, various methods are used to read historical textures. Karatosun (2010); some of these methods have been classified as an urban image analysis technique, urban texture analysis, morphological/typological analysis, space syntax research, space geometry analysis, visual perception analysis. With a technical trip organized in Sille, historical churches, mosques, baths, rock-carved caves, re-functional buildings, and pottery workshops reflecting Sille's culture were visited. It was expected that the analysis would be made for the surrounding area and for the design, such as occupied space, street, courtyard, square, floor elevations, transportation, and social environment.

In the third step, each student has identified new structure approaches (harmony, contrast, imitation) in accordance with Sille's historical texture and the chosen plot, the scenario and main ideas for this have been shaped.

At the fourth step, students who adopt any of the new building design criteria, conduct stain study in the context of their chosen criterion and transfer their decisions to the site plan. During the nine-week period until the end of the semester, the students reflected this to their project, trying to stay connected to the main course they had taken for the historical site in their site plan, floor plans, sections, and especially facade studies.

At the last step, the projects of the students were evaluated with the determined criteria in accordance with the awareness criteria in designing the new building in the historical environment at the end of the planned training.

1.3 Theoretical context: New Building Design Approaches in Historical Environment

Approaches to historical cities and preservation of structures should be dealt with by analyzing the relationship between old and new construction. Day (2011) seeing the historical architectural texture as a cultural resource emphasizes that the new designs are both an important factor in the sustainability of the historical districts, as they are both of a nature that sheds light on modern times and refers to historical textures. When this situation is reversed, Velioglu (1992) argues that new constructions lead to

old texture crushes, and that these environments are deteriorating with clarity, perceptual awareness and continuity. According to Warren (1998), while designing new structures in historical surroundings; the awareness of historical events and the responsibility for historical evidence must be acknowledged.

Designers and theoreticians have put forward many methods and principles for the new construction at the point of the contribution of the historical circle to the life of the modern world and decisions have been taken in the congresses on the international platform. In Italy, the ICOMOS (1931) Carte Del Restauro Declaration focused on additions at historical textures and buildings at the first time. Annex 1 of ICOMOS (1931) states that the new structure to be built around historical buildings is required to respect the historical structure of materials, texture and colour. In the Charter of Athens (1933) it was emphasized that the new construction in historical surroundings is in harmony with the old structure of texture, texture and colour, but it should be avoided from imitation the old structure in terms of design.

In Annex 5 of the UNESCO (1976); meeting in Nairobi, it has been argued that improper restoration and renewal in the context of growth and modernization in the world has damaged historical fabric. According to this meeting, any intervention to be done in the historic areas should be in accordance with the scientific principles and care should be paid to the architectural features such as position, height, roof type, material, façade type, environment relation and so on.

The principles to be taken into consideration in the design of new structures in historical surroundings; to approach the existing built environment with respect, to use the historical landscape as a design data in design decisions, to analyze height, settlement texture, material, color, mass and environment relation, to have easily distinguishable features reflecting the characteristics of the age (Duralı, 2007). Dibner and Dibner-Dunlap (1985) discusses such approaches, such as Copy/Imitate, Contrast, Analogy, Contextual Conformity, Connection/Transition Location, etc. In this study, students who designed new structures in Sille basically used the methods of harmony, contrast and imitation.

1.3.1. Harmony Approach

Adaptation to the environment in the concept and terminology of art is defined as a situation in which an architectural product does not contradict the urban or natural environment in which it lies (Sözen and Tanyeli, 1986). In this study, new building design criteria in historical environment; the method of harmony is categorized as analogy, ineffectiveness and interpretation and examined in subheadings.

In the analogy method, the new structure to be built on the historical texture is designed by taking advantage of the same or similar façade and mass effects as the traditional texture (Duralı, 2007). Erginoğlu (1996) has determined the criterion used in the method of analogy in his work as proportions of entrance axes, material relations, color-tissue similarities, roof constructions and slopes and the elements of adjoining historical building are to be interpreted in a new context and its repetition of space occupancy rates, rituals, mass and plan articulations defense of repeatability. The designer who uses the analogy method should not imitate the old texture, should produce the differences that reveal the contemporary of the new structure.

In the neutralization method, while creating a neutral image against the historical construction, it would prevent the deterioration of environmental integrity (Aydın, 1998). Düzgün (2010), this attitude is obtained by applying reflection/transparency, underground construction, cloaking/camouflage methods, and it does not perceive directly in the environment where the new structure is located. The newly designed structure creates a neutral frontal effect in the traditional texture, and it does not disrupt the integrity of the tissue (Duralı, 2007).

The method of interpretation is a new design approach that clearly states its own period and attitude while emphasizing the features of the historical landscape to be included in the new structure, reinterpreting the escapes and making new ones (Akın and Batur, 2003). According to Demiri (2013), the relationship between the new architecture and the historical context is determined by the significance of the architectural heritage and the modern interpretation. Duralı (2007) stated that the significance of this method is to be a part of the chain of historical-cultural continuity, to understand the environment that exists in the design phase, and to interpret the past with a contemporary understanding.

1.3.2. Contrast Approach

Erginoğlu (1996), classified the mirror surface, transparency, and existing texture as methods of contrasting (in contrast, removing contemporaneity completely to the foreground) in the design practices of the historical texture made by contrast method. In this method, success requires a long work and accumulation process aiming at realizing and realizing the characteristics of creating the environment and evaluating the "contrast" that is to be designed within the frame of this information (Akın and Batur, 2003). Contradiction must not be a random one, it must be composed of rhythmic surfaces, which are integral in itself, supported by materials and contrasts in the eye, and the new structure must be distinguishable from the past (Sparks, 2011, Aydın, 1998). A design

approach that includes the richness of differences between the old and new structure is composed of a more stringent method (Cullinan, 2011).

1.3.3. Imitation/Copy Approach

When designing a new one, it is an application in which the past is imitated under the name of conformity, where utilization of the past is exaggerated and transformed into copying (Düzgün, 2010). This attitude, which the old and the new seemed to be different from each other, was completely abandoned by the 1964 Treaty of Venice and the 1964 Venice Constitution (Aydın, 1998). The imitation structure is only the formal imitations of historical structures; but as they are in the historical building, they do not carry past cultural values, they have no emotional significance (Konyalı, 1964). By using contemporary construction techniques appropriate to the conditions of the time, the designs made by avoiding imitation of old are made to be read on the historical texture.

2. Case Study

As the project design area, Selçuklu district of Konya province was selected as Sille neighborhood. Students are aimed to create their concept by adhering to one of the new building design approaches in the historical texture with the design inputs introduced by this historical area.

2.1. Project Design Area: Sille Historical Texture

Sille is an old settlement located at a distance of 8 km from the city center in Konya, connected to the Selçuklu District, and was established in the valley of the creek. In the past, Christians and Muslims lived together in Sille's valley and carved on the southern slopes of rock-carved churches are the first settlement areas. Sille which is an important settlement centre during Hittites, Phrygians in B.C. and Romans, Byzantines, Seljuks, Karaman sons, Ottomans in A.D. has a historical background of at least 5700 years which draws attention with its different culture, beliefs, traditions and geographical structure (Konyalı, 1964). After the death of Jesus Christ, two of the twelve apostles, St. Barnabas and St. Paul, came to Ikonian (Konya) when they were traveling to Cappadocia with the first Christians who believed in them to get rid of the intense and violent oppression of radical Jews. and putt-worshippers have instilled Christianity (Konyalı, 2007). However, due to the Jewish community pressures in the city, after a while Christians abandoned Konya and the mountainous region in the northwest was withdrawn. The first rock churches were built in the of Sille valleys out of public gaze (Küçük, 2001). During the process, Sille became an important settlement on the holy pilgrimage route in the Roman-Jerusalem area during the Christian era (Özönder, 1998).

Although Sille has been in the scene of some Muslim-Arab influences, Konya and its close control of the Muslim Turks encounters with the Seljuk period. The Greeks in Konya in the Seljuk period were removed from the castle settlement and placed in Sille (Aklanoğlu, 2009).



Fig. 2 Relation between important structures in Sille and project design area (Prepared by Merve Ozkaynak)

In Sille there are religious buildings for Christians and Muslims due to their coexistence (Figure 2). In order to fulfill Christians' worship in the past, Komise Tes Panagias Church (Rock Carving Churches), Ak Monastery, Aya Eleni Church, Tepe Chapel were made. Karatas Mosque, Mormi Mosque, Mezaryaka Mosque, Haci Ali Aga Bath, Subaşı Hamami and many other fountains were built as the Muslim population started to live in the region (Figure 3). In Sille the bulk settlement is concentrated on the northern slope of the valley. In Sille, where a sloping topography is located, inclination has developed parallel to the east and west direction of both sides of the creek bed.



Fig. 3 Aya Eleni Church and Rock Carving Churches in Sille (From Merve Ozkaynak's personal archive, 2017)

Sille traditionally settled in terraced houses that did not interfere with each other's viewing and sunbathing narrow streets between them. Sille stone and wood are used as traditional building material (Figure 4). It is one of the advantages of terraces in typical rectangular or rectangular houses. It uses the roof of a house as an entrance and terrace for other houses. The dwellings are flat-dipped and generally have two floors.



Fig. 4 Examples of Structures from Traditional Sille Texture (From İlknur Acar Ata's personal archive, 2017)

There are Aya Eleni Church in the west, Komesis Tes Panagias Church on the south and mosques, baths and civil architectural works forming the traditional Sille texture on the north of the selected area (Figure 2). There is a historical environment for students to work in the historical environment in the context of new building design criteria (Figure 5). According to the wind direction dominated by the Hagia Sophia Church in the vicinity of the design area, the settlement in the north-west direction is considered as an example for the optimum environmental conditions in the designed projects.

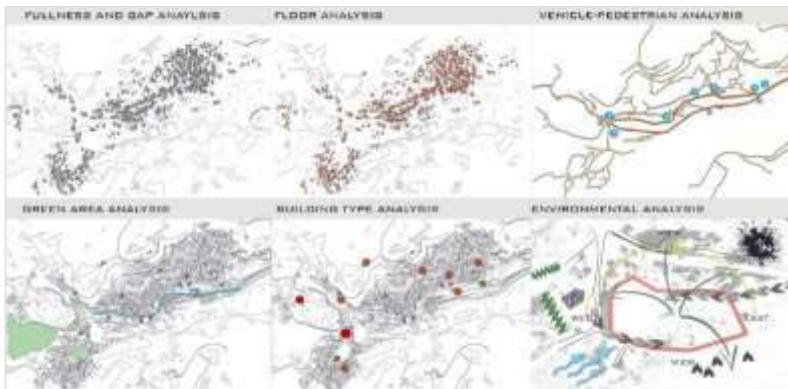


Fig. 5 Examples of Students' Analysis for Sille Historical Texture, 2017

2.2. The studio teaching practice: Evaluation Part

In the evaluation of the projects designed by architect students in-studio education; a new awareness assessment criteria have been developed on the basis of the criteria that Day (2011) sets out in the synergy between the

old structure and the new structure, and on the basis of Capon (1999) 's assumption that it can be handled according to the category of contextual data. Firstly, the contextual relationship of the adaptation, contrast and imitation methods with the historical texts of the new methods of building in the historical environment is presented with ten criteria (Table1).

Table 1 Criteria for Awareness Assessment in Designing New Buildings in Historical Environment

| Criteria | Score Interval |
|--|-----------------------|
| The new structure contributes to the historical value and sustainability of the place where it is designed. | 0-5 points |
| The new structure has a design in the context of human being in the historical environment, which is directed towards identity, local and cultural values. | 0-5 points |
| The new structure introduces new ways to "deal", "watch", "experience" and "read" in the historical context. | 0-5 points |
| The new structure has qualities that are appropriate for the time of the year, respecting the "legibility" of the surrounding area, staying away from imitation. | 0-5 points |
| The new structure, construction methods and materials and reminiscent/interpretive of local craft methods in the historical context. | 0-5 points |
| With the possibilities that the new project has, it is making sentiments about the historical context in terms of open-closed spaces, recreation, interpretive attitude towards the environment. | 0-5 points |
| The new building provides visual appropriateness by adhering to the building criterion (harmony-contrast-imitation) that it deals within its environmental context. | 0-5 points |
| The new building is in communication with the old building in the context of the place. | 0-5 points |
| The new building possesses a functional appearance with a vision of historical context. | 0-5 points |
| In the new structure form, mass, scale, appearance, rhythm factors are used appropriately in the context of historical texture/tissue. | 0-5 points |

The studio instructors working in the field of Architectural Design and Restoration evaluated the student projects between 0-5 points according to their suitability for these items and the awareness of the student about the new environment design in the historical environment was assessed according to the determined score range (Table 2).

Each criterion has a score between 0 and 5. If the total point value is x;

Table 2 Awareness Point Evaluation Interval

| Score Interval | Assessment of Awareness |
|---------------------|---|
| $0 \leq x < 20$ | The awareness of the student is weak according to the awareness criteria in designing new structures in historical environment. |
| $20 \leq x < 35$ | The awareness of the student is moderate according to the awareness criteria in designing new structures in historical environment. |
| $35 \leq x \leq 50$ | The awareness of the student is successful according to the criteria of awareness in designing new structure in historical environment. |

After the projects were categorized according to the new building approaches in the historical environment that the students had adopted in the designs, they were evaluated with the schedules prepared for each of them (Table 3-4-5).

Table 3 Evaluation Sample Chart of Student Projects Adopting the Approach of Harmony According to the Criteria of Awareness in Designing New Structures in Historical Environment

| EVALUATION CHART-1 | | | | | | | | | | | | | | | | | | | | | |
|--------------------|----------|---|---|---|---|---|--|---|---|---|---|---|---|---|---|---|---|---|---|---|---|
| HARMONY APPROACH | | | | | | | | | | | | | | | | | | | | | |
| | | Student 1 | | | | | Student 2 | | | | | | | | | | | | | | |
| | |  | | | | |  | | | | | | | | | | | | | | |
| | | <p>The concept of "Cittaslow Sille", which will be a part of the boutique hotel, has been adopted. With this principle, the preservation of the existing traditional texture and the restoration of the ruined ones are considered. In order to protect crafts and crafts belonging to the region and to be passed on to future generations, new pottery workshops should be added instead of existing pottery workshops, and active training should be given to these workshops. The local food shops that serve the public in the boutique hotel are also considered.</p> | | | | | <p>The main idea of the boutique hotel has been the design point where the art is designed to be taken out of the closed and customized art spaces and into daily life. Designed as the city's new focal point with Sille Art concept, the Art Hotel has arts and workshops that bring people together and make them feel free. It is aimed to integrate the art and landscape with the amphitheater for social activities in the hotel recreation area and to ensure architectural integrity.</p> | | | | | | | | | | | | | | |
| | |  | | | | |  | | | | | | | | | | | | | | |
| | | <p>The student who defended the idea that Sille's existing historical texture, traditional architecture, would provide integrity, was the design of the boutique hotel designed in Sille according to the harmony approach in the new surroundings.</p> | | | | | <p>The student who adopted the harmony in the new building design in the historical environment and interprets the existing traditional texture according to the era has considered this in the topography placement of the hotel units, in the use of materials and in the facade arrangement.</p> | | | | | | | | | | | | | | |
| Resu It | Po in | a | b | c | d | e | f | g | h | i | j | a | b | c | d | e | f | g | h | i | j |
| | od | 5 | 5 | 5 | 5 | 5 | 5 | 5 | 5 | 5 | 5 | 5 | 5 | 5 | 5 | 5 | 5 | 5 | 5 | 5 | 5 |
| | | 50 Successful | | | | | 50 Successful | | | | | | | | | | | | | | |

Table 4 Evaluation Sample Chart of Student Projects Adopting the Approach of Contrast According to the Criteria of Awareness Model in Designing New Structures in Historical Environment

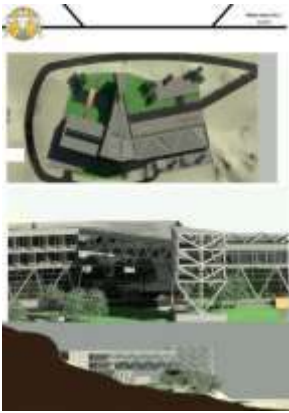
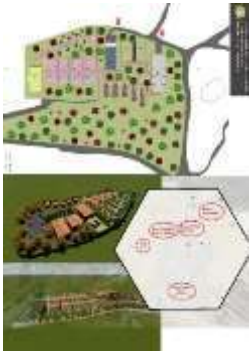
| EVALUATION CHART-2 | | | | | | | | | | | | | | | | | | | | |
|--|---|----------|----------|----------|--|--|----------|----------|----------|----------|----------|----------|----------|----------|----------|----------|----------|----------|----------|----------|
| | Student 3 | | | | | Student 4 | | | | | | | | | | | | | | |
| CONTRAST APPROACH |  | | | | |  | | | | | | | | | | | | | | |
| | <p>The concept of the student project is the notion of the inner street in the traditional texture. The boutique hotel, consisting of accommodation for the Sille scenery on the inner side of the main street, which is basically composed of two masses, is enriched with viewing terraces and floor gardens.</p> | | | | | <p>The student project was designed not only for the tourists who came to Sille but also for the tourists coming to Konya, with the amenities and comfort conditions and being an icon belonging to its own age. The viewing tower for the scenery has separated the accommodation units and the social units from each other.</p> | | | | | | | | | | | | | | |
| |  | | | | |  | | | | | | | | | | | | | | |
| <p>The student who planned to design the main mass as having the qualities required by the modern age adopted the contrast approach.</p> | | | | | <p>The student adopted the contrast approach, which aims to make the hotel feel itself in the historical texture of the hotel, which has a large clear-cut transparent surface provided by modern construction technique steel construction.</p> | | | | | | | | | | | | | | | |
| Result Point Code | a | b | c | d | e | f | g | h | i | j | a | b | c | d | e | f | g | h | i | j |
| Result Point | 4 | 4 | 4 | 5 | 5 | 4 | 5 | 4 | 4 | 3 | 4 | 5 | 4 | 4 | 0 | 5 | 5 | 5 | 4 | 3 |
| Result | 42 Successful | | | | | 39 Successful | | | | | | | | | | | | | | |

Table 5 Evaluation Sample Chart of Student Projects Adopting Imitation Approach According to Awareness Model Criteria in Designing New Structure in Historical Environment

| EVALUATION CHART-3 | | | | | | | | | | | | | | | | | | | | |
|--------------------|--|---|---|---|---|---|---|---|---|---|---|---|---|---|---|---|---|---|---|---|
| IMITATION APPROACH | Student 5 | | | | | | | Student 6 | | | | | | | | | | | | |
| |  | | | | | | |  | | | | | | | | | | | | |
| | <p>The student considered the morphological and typological characteristics of the Sille constructions which are suitable for the topography by interpreting the historical traditional texture of Sille. The student has designed workshops that overlook Sille scenery for both the Sille community and hotel guests as common areas of use.</p> | | | | | | | <p>The boutique hotel, which is designed according to the concept, will contribute to the Sille silhouette but will not disrupt the texture. In design, the streets of Sille traditional texture, rock caves near the working area are used as a recreation area.</p> | | | | | | | | | | | | |
| |  | | | | | | |  | | | | | | | | | | | | |
| | <p>The student adopted the imitation approach which uses the morphological features of Sille texture in the construction of local materials. The rhythm, shape and mass scales in the buildings are designed to copy the existing texture.</p> | | | | | | | <p>The student adopted the imitation approach of the new building design criteria in the historical environment, designed the hotel with units that resemble material features and a 1-2 storey terrace home-building system that leads to the scenery.</p> | | | | | | | | | | | | |
| Code | a | b | c | d | e | f | g | h | i | j | a | b | c | d | e | f | g | h | i | j |
| Point | 3 | 4 | 1 | 2 | 4 | 3 | 3 | 3 | 3 | 3 | 4 | 4 | 4 | 0 | 3 | 4 | 3 | 3 | 2 | 3 |
| Result | 29 Medium Level | | | | | | | 30 Medium Level | | | | | | | | | | | | |

Targets determined at the end of the education period; scores attained by the students according to the awareness evaluation criterion

codes, the approaches they had considered throughout the design process in the project, and the numerical values obtained as a result of the awareness assessment were documented (Table 6).

Table 6. The Assessment Chart of The Students in Studio 5-6.

| Student Number | Awareness criterion code-Score | | | | | | | | | | Total Points | Evaluation | |
|----------------|--------------------------------|---|---|---|---|---|---|---|---|---|--------------|--------------------|--------------|
| | a | b | c | d | e | f | g | h | i | j | | Approach | Level |
| 1 | 5 | 5 | 5 | 5 | 5 | 5 | 5 | 5 | 5 | 5 | 50 | Harmony Approach | Successful |
| 2 | 5 | 5 | 5 | 5 | 5 | 5 | 5 | 5 | 5 | 5 | 50 | Harmony Approach | Successful |
| 3 | 5 | 4 | 4 | 5 | 5 | 5 | 5 | 5 | 5 | 5 | 48 | Harmony Approach | Successful |
| 4 | 5 | 5 | 5 | 4 | 4 | 4 | 5 | 4 | 4 | 5 | 45 | Harmony Approach | Successful |
| 5 | 4 | 5 | 5 | 5 | 4 | 5 | 3 | 4 | 2 | 5 | 42 | Harmony Approach | Successful |
| 6. | 4 | 4 | 5 | 4 | 2 | 3 | 3 | 2 | 3 | 4 | 34 | Harmony Approach | Medium Level |
| 7 | 3 | 3 | 4 | 3 | 0 | 3 | 5 | 4 | 4 | 4 | 33 | Harmony Approach | Medium Level |
| 8 | 4 | 4 | 5 | 3 | 1 | 3 | 2 | 3 | 3 | 2 | 30 | Harmony Approach | Medium Level |
| 9 | 3 | 4 | 4 | 4 | 0 | 4 | 3 | 2 | 3 | 2 | 29 | Harmony Approach | Medium Level |
| 10 | 2 | 4 | 3 | 4 | 1 | 2 | 3 | 2 | 2 | 2 | 25 | Harmony Approach | Medium Level |
| 11 | 4 | 4 | 4 | 5 | 5 | 4 | 5 | 4 | 4 | 3 | 42 | Contrast Approach | Successful |
| 12 | 4 | 5 | 4 | 4 | 0 | 5 | 5 | 5 | 4 | 3 | 39 | Contrast Approach | Successful |
| 13 | 4 | 2 | 4 | 4 | 2 | 4 | 4 | 2 | 4 | 4 | 34 | Contrast Approach | Medium Level |
| 14 | 3 | 3 | 4 | 4 | 2 | 5 | 2 | 2 | 2 | 1 | 28 | Contrast Approach | Medium Level |
| 15 | 2 | 1 | 2 | 3 | 3 | 3 | 4 | 3 | 2 | 2 | 25 | Contrast Approach | Medium Level |
| 16 | 3 | 1 | 3 | 3 | 0 | 2 | 2 | 2 | 3 | 2 | 21 | Contrast Approach | Medium Level |
| 17 | 2 | 2 | 3 | 3 | 0 | 2 | 3 | 0 | 2 | 2 | 19 | Contrast Approach | Weak |
| 18 | 1 | 3 | 2 | 0 | 2 | 3 | 0 | 3 | 1 | 2 | 17 | Contrast Approach | Weak |
| 19 | 4 | 4 | 4 | 0 | 3 | 4 | 3 | 3 | 2 | 3 | 30 | Imitation Approach | Medium Level |
| 20 | 3 | 4 | 1 | 2 | 4 | 3 | 3 | 3 | 3 | 3 | 29 | Imitation Approach | Medium Level |
| 21 | 0 | 1 | 2 | 3 | 0 | 3 | 1 | 1 | 1 | 1 | 13 | Uncertain | Weak |
| 22 | 0 | 0 | 1 | 3 | 1 | 2 | 2 | 1 | 1 | 1 | 12 | Uncertain | Weak |
| 23 | 0 | 3 | 3 | 2 | 0 | 1 | 0 | 1 | 1 | 1 | 12 | Uncertain | Weak |

3. Conclusions

In architectural education, studio lessons take place with the active participation of the student as opposed to theoretical lessons. It is important that students reflect on the theoretical knowledge they have obtained from specialized courses on the conservation of the historical environment to their design projects. The purpose of this study is to assess student awareness in designing a new building in the historical environment in the studio courses.

In this study, architectural students in studio 5 and 6 courses were introduced with the concept of new building design criteria in a historical environment. The awareness that each student who designed a new building design in the Sille Quarter was evaluated by the studio instructors with a new method. At the beginning of the educational period, the studio instructor of the Restoration and Architectural Design Department set the lesson plan and the data for creating awareness within the process of designing in a historical environment. When these data are set as a joint study area, a need program, a course schedule, students are allowed to choose new methods of construction in the historical environment, one of the design inputs.

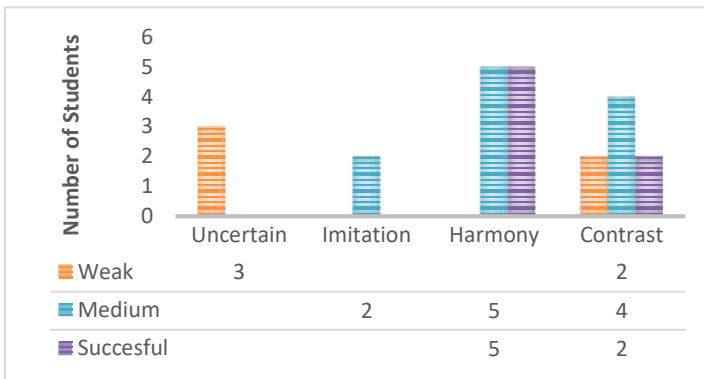
In the assessment of the students' projects, the awareness determined by the studio instructors was used. In the historical environment, the criteria for model evaluation were established/determined to assess the awareness of new building design. While these criteria are being developed, Day and Capon have been interpreted on the basis of their work on the old and new synergy of the environment and context.

In the awareness assessment at research the students are expected to contribute to the design of the historical neighborhood by contributing and sustainable approach, identity, having a design input for the local culture, dealing with the historical wisdom, introducing new ways to experience, watching, reading, to be reminded of local craft methods, to adhere to new building criteria, to communicate with old buildings and to have a visionary function. As a result of the assessment, the student was grouped at three levels as weak, medium level and successful by scoring awareness of the new building design criteria in the historical environment.

At the end of the semester, 23 students who took Studio 5 and 6 courses design a new structure in a historical environment, 43% adhered to harmony, 35% contrast, 9% imitation method and 13% were uncertain. According to the criteria that assess awareness in designing new structures in a historical environment, it has been determined that 30% of the students are successful, 48% of them have medium level and 22% have weak awareness.

When the relationship between the assessment criteria of the model created in the study and the approach taken by the students is evaluated, it is seen that the awareness of the three students who do not adopt the approach is weak, the two students who imitate are medium level, half of the ten students who adopt harmony approach is at the middle level and the other half is the successful and the eight students who accept the contrast approach, two of them are weak, two of them are the medium level and the four of them are successful (Figure 6).

Fig. 6 The Success Relation Between Students' Approach and Awareness Assessment



At the end of this study, the project of twenty-three learners were evaluated by the awareness evaluation model and it was revealed how much the end-of-term was achieved by the numerical data and the targeted consciousness. In architectural studio education, in project courses that have the characteristic of new building design in a historical environment, aiming to fulfill the developed criteria, a basis for project executives has been established.

We anticipate that this study; the awareness assessment method that we have revealed is not only a proposal that assesses and increases the student awareness of the new building design in the historical environment but also it can be developed as a criterion to be applied by the local governments for the new buildings to be built in the historical texture.

References

- Akın, N. & Batur, A. 2003. Kentsel Korumada Cephe Sürekliliği: Konuralp Örneği. *Mimarist*, 10, 68.
- Aklanoğlu, F. 2009. Geleneksel Yerleşmelerin Sürdürülebilirliği ve Ekolojik Tasarım: Konya-Sille Örneği. Phd. Thesis, Ankara University.
- Athens, C. O. 1933. IV International Congress of Modern Architecture.
- Aydın, E. 1998. Tarihi Çevre İçindeki Yeni Yapılaşmaların Uygulama Sonuçları. Master Thesis, Mimar Sinan University.
- Capon, D. S. 1999. *Architectural Theory* New York, John Wiley & Sons.
- Cullinan, E. 2011. Contributing to historic settings without kow-towing. In: WARREN, J. & WORTHINGTON, J. (eds.) *Context: new buildings in historic settings*. Oxford: Architectural Press.
- Day, S. 2011. *Synergisms: Building Modern in the Context of Historic, USA*, Common Ground Publishing.
- Demiri, K. 2013. New Architecture as Infill in Historical Context. *Architecture and Urban Planning* 7, 44-50.
- Dibner, D. R. & DIBNER-DUNLAP, A. 1985. *Building Additions Design*, ABD, McGraw-Hill Book Company.
- Duralı, İ. K. 2007. Tarihi Çevrede Yeni Yapılaşma Uygulamalarının İrdelenmesi. Master Thesis, Mimar Sinan Fine Arts University.
- Düzgün, H. 2010. Tarihi Çevrelerde Yeni Yapı Tasarımında Kabuk - Bağlam İlişkisinin Temel ve Güncel Tasarım Kavramları. Master Thesis, Yıldız Technical University.
- Erginoğlu, K. 1996. Tarihi Çevrede Yeni Yapı Tasarımı. Master Thesis, Mimar Sinan University.
- ICOMOS 1931. Carta Del Restauro Declaration. <http://www.icomos.org.tr/?Sayfa=Tuzukler2&dil=tr>.
- Karatosun, M. B. 2010. Geleneksel Dokularda Yeni Yapı Tasarımı: Alaçatı Örneğinin İncelenmesi. *Ege Mimarlık*, 75, 32-35.
- Konyalı, İ. H. 1964. *Abideleri ve Kitabeleri ile Konya Tarihi*, Konya, Yeni Basım Kitapevi.
- Konyalı, İ. H. 2007. *Konya Tarihi*, Konya, Konya Büyükşehir Belediyesi Yayınları.
- Küçük, M. 2001. Mevlana Sille'ye Uğradı. *Popüler Tarih*, 82-86.
- Özönder, H. 1998. *Sille: Tarih, Kültür, Sanat*, Konya, Merhaba Basımevi.
- Sözen, M. & Tanyeli, U. 1986. *Sanat kavram ve terimleri sözlüğü*, İstanbul, Remzi Kitabevi.

- Sparks, L. 2011. Historicism and the public perception In: WARREN, J. & WORTHINGTON, J. (eds.) Context: new buildings in historic settings. Oxford: Architectural Press.
- UNESCO 1976. Records of the General Conference Nineteenth Session Nairobi. Nairobi.
- Veliöglu, A. 1992. Tarihi çevre içinde mimari tasarım ve süreci üzerine bir çalışma. Phd. Thesis, Karadeniz Technical University.
- Warren, J. 1998. The historic context: principles and philosophies. In: WARREN, J. & WORTHINGTON, J. (eds.) New buildings in historic settings. Oxford: Architectural Press.